ABSTRACT

Title of dissertation: TOWARD THE FLUXONIUM QUANTUM PROCESSOR

Long Bao Nguyen, Doctor of Philosophy, 2020

Dissertation directed by: Professor Vladimir Eduardovich Manucharyan
Department of Physics

This thesis reports recent achievements toward scalable quantum computing with fluxonium, a superconducting artificial atom with rich energy spectrum and selection rules similar to those found in natural atoms. We show how such spectral properties can be harnessed to protect the qubit from energy relaxation and dephasing. At half integer flux quantum bias, we show that fluxonium's $|0\rangle \rightarrow |1\rangle$ qubit transition has high coherence by design, with T_1, $T_2 \approx 500\ \mu$s in one device, the highest reported in superconducting circuits so far. Yet, the qubit exhibits the same level of addressability found in more conventional superconducting qubits ($T_{\mathrm{gate}} < 50$ ns). In addition, a controlled-Z gate can be implemented by sending a short 2π-pulse at a frequency near the $|1\rangle \rightarrow |2\rangle$ transition of the target qubit. Preliminary results suggest that this gate can be used to entangle two fluxonium qubits with high fidelity. We also discuss experimental techniques employed to characterize the qubits, and present a perspective on future fluxonium-based quantum technologies.

TOWARD THE FLUXONIUM QUANTUM PROCESSOR

by

Long Bao Nguyen

Dissertation submitted to the Faculty of the Graduate School of the
University of Maryland, College Park in partial fulfillment
of the requirements for the degree of
Doctor of Philosophy
2020

Dissertation Committee:
Professor Vladimir E. Manucharyan, Advisor
Professor Thomas M. Antonsen, Co-Advisor
Professor Steven M. Anlage
Professor Cheng Gong
Professor Frederick C. Wellstood
Professor Benjamin S. Palmer
Professor Andrew M. Childs, Dean's Representative

Acknowledgement

Physics isn't the most important thing. Love is.

Richard P. Feynman

I would like to begin by expressing gratitude to my advisor, Prof. Vladimir Manucharyan, for giving me the opportunity to learn about quantum computing and superconducting circuits under his guidance. I still remember the first time I visited the lab, when it was an empty space surrounded by four walls, like it was only yesterday. I also recall the first time I came to see Vlad, he stopped whatever he was doing and started deriving the fluxonium Hamiltonian on the white board. Together we began building the lab from the ground up, overcoming broken devices, short coherence times, bad equipment, and administrative hassles. Being more of a brother figure than a boss, Vlad has also given me useful advice on teamwork and giving talks.

I owe my enthusiasm in scientific research to my academic advisor, Prof. Thomas Antonsen Jr., who also supervised my master thesis work. Tom not only inspires me with his combination of ingenuity and patience, but also encourages me to get out of my comfort zone and live my dream. I am especially fond of the few times we played tennis together. I have not only learned how to solve problems from first principles, but also how to survive academic life from him. The love he shows toward his students is unparalleled, either in this universe or another.

I thank Prof. Steven Anlage for teaching me everything I know about superconductivity. Our characterization of microwave components up to 50 GHz was done using the vector

network analyzer in his lab. It's an interesting coincidence that many of my friends from the same cohort decided to work with Steve, and our discussions throughout the years have inspired me to take an interest in superconductivity research.

I thank the other committee members, Prof. Benjamin Palmer, Prof. Frederick Wellstood, Prof. Cheng Gong, and Prof. Andrew Childs for overseeing this dissertation work and the defense. Comments and suggestions from Ben and Fred helped me tremendously in editing the manuscript.

The person whom I spent the most amount of time working with is undoubtedly Prof. Yen-Hsiang Lin, who taught me everything I know about cryogenic engineering, machining, overcoming difficult people, Asian food, and raising kids. I appreciate his patience and easy-going temperament. Whenever there was a problem with the fridge, I could count on Yen-Hsiang to come to the lab and fix it, be it in the middle of a winter storm or at 3 AM in the morning. Detecting leaks and chatting about life during those times were memorable. Yen-Hsiang also influenced me with the concept of *academic brother*, which we now use to refer to each other.

I am indebted to my academic twin sister Natalia Pankratova (née Solovyeva) for her love and support. Natalia not only works hard to ensure a friendly working environment, she also goes the distance to make sure I live a life outside the lab. Thanks to her, I had the chance to enjoy the cherry blossoms, go to the beach, and attend many school events with other fellow graduate students. I am sure that the series of birthday parties Natalia organizes will leave every lab member with happy memories. Our conversations throughout the years have helped me manage the stress and beyond.

I thank Jonathan San Miguel for making the first half of my time in the lab so enjoyable. Jon is not only a genius, but also a fun guy to be around with. Every single time I exchanged an idea with Jon, it bounced back being a better sounding idea. Outside the lab, we became gym partners and good friends. I also owe Jon my excitement and enthusiasm in coding as well as in solving riddles and puzzles.

Although he spent only one year at the University of Maryland, Dr. Nathanaël Cottet helped us tremendously with our understanding on quantum measurement and detection. The fluorescence experiment he started has given us the opportunity to learn so much about open quantum systems. I thank him for all the illuminating discussions about circuits and readout, and for letting me sleep on the bed during our March Meeting trip. I also appreciate Nat's friendship and encouragement throughout the years.

We could measure so many fluxonium devices only because of the hard work from Aaron Somoroff. Aaron has tirelessly fabricated device after device, made dose test after dose test, to come up with the right qubits. I also thank Aaron for sharing his life experience outside the lab, and for cheering me up in time of duress. Partnering up with Aaron and learning fab from him in the final stretch of my graduate student life was fun and memorable.

The recent achievements in fluorescence shelving readout came from the hard work of Haonan Xiong. His willingness to learn and discuss science in details is inspiring. I also thank Haonan for simulating the new cavity and waveguide designs. Haonan took no time learning about fluxonium, and I have no doubt he will achieve great success with future fluxonium experiments.

I haven't been fortunate enough to work in the same project with Dr. Roman Kuzmin, but his methodological approaches, persistence, and discipline in scientific research have never failed to impress me. For every problem that I have ever discussed with Roman, he could always come up with a foolproof solution. Despite his intense focus on research, he never refused to give us a hand when other problems arose in the lab. I especially miss his rare but ingenious jokes. In short, Roman is the scientist that I aspire to become one day

I thank Dr. Ivan Pechenezhskiy for his encouragement inside and outside the lab. I would never have the courage to ski black diamond trails without his instructions and companionship. Ivan not only taught me so many things about circuits, but also motivated me to code cleaner python scripts and write better job applications. I owe him many great advice on financial investments, future career paths, and professional life. Our discussions

about big pictures in research are especially helpful and memorable.

For a long time, optimizing the readout was not our primary concern, and we only began to realize its importance at the start of the two-qubit entangling gate experiment. Fortunately, Dr. Quentin Ficheux arrived and started a revolution on our readout setup just on time. He has also helped us tremendously with his experience in cQED. I appreciate the time he spent solving problems from first principles and motivated us to be rigorous. Quentin has definitely made me become a better scientist.

I haven't had the chance to work exclusively on the same project with everyone in the lab, but I appreciate the camaraderie from Nicholas Grabon, Raymond Mencia, Nitish Mehta, Christiane Ebongue, and Hanho Lee. I will remember dearly the early morning trip to Dunkin Donuts with Nick, the cookout at Nitish and Ray's house, going for lunch with Chris, and discussion about K-pop with Hanho.

Outside the lab, I would like to first thank our theory collaborators Dr. Konstantin Nesterov and Prof. Maxim Vavilov for teaching me the physics behind multi-fluxonium systems. I thank Prof. Chen Wang and his students, Dario Rosenstock and Ebru Dogan, for allowing me to visit their nicely setup lab and learn from them. I am grateful to Prof. Rajamani Vijayaraghavan for helping me understand the readout and initialization techniques in multi-qubit systems, and for discussing the details of our experiments. I have come to enjoy Vijay's wonderful insight in life and physics, and I hope to learn more from him in the future. I thank Prof. William Oliver for giving me the chance to visit his lab and have fruitful discussion with his group during the crucial stage of the two-qubit project. I thank Prof. Michel Devoret for his feedback on my talks.

I thank the administrative staff in both the ECE and Physics departments for their help and assistance throughout the years. From the ECE graduate office, I thank Melanie Prange, Heather Stewart, Dorothea Brosius, Tracy Chung, Vivian Lu, Bill Churma, and Maria Hoo. From the Physics department, I thank Lorraine DeSalvo, Paulina Alejandro, Pauline Rirksopa, Margaret Lukomska, Melissa Britton, and Kelly Phillips.

Without my teachers' endless encouragement and belief in me, I would never be able to get out of my comfort zone and start living the dream. I am especially grateful to Ms. Huong, Ms. Loan, Mr. Thanh, and Mr. Nghe for their guidance and advice, both inside and outside the classroom. I thank Prof. Lawrence Overzet and Prof. Daisuke Ogawa for patiently introducing me to experimental science. I am glad to have received their love and encouragement despite the fact that I have never been the brightest or most obedient student in the class. The devotion they give to generations after generations of students has never failed to inspire me.

The old friends still willing to meetup and listen to my old jokes have made graduate school more tolerable. From my school days, I thank Khoa, Tung, Nha, Long, Khang, and Tien for living the past, present, and future all at once with me every time we meet. I thank Misa for all her love and support when she was alive. Our conversations throughout the years, from the very first one in the exam room to the very last one in the hospital, were encouraging and inspiring. Her positive attitude in life was a tour de force that always motivates me to go further and do better in my ventures. I thank Dai and Kim for dissipating my nostalgia and creating important retrospection points in my life. From my college years, I thank Tra and Ngan for visiting and keeping me grounded with their recommendations of fun things to do.

I am fortunate to have met many amazing friends in graduate school. I especially thank Dr. Hyun Jung for introducing me to the Korean study group who helped me survive the qualifying exam and the brutal first year, Dr. Tao Gong for his friendship and inspiration, Dr. Aydin Cem Keser for motivating me to learn quantum physics and introducing me to Vlad, Dr. Dmitry Kashin for getting me into distance running, Dr. Tao Cai and Dr. Dakang Ma for sharing their interest in tennis and photography, and Dr. Setiawan Wenming for introducing me to the world of Majorana physics. I thank the group of friends including Monica Gutierrez, Dr. Vikram Un, Dr. Elizabeth Tennyson, Sarthak Subhankar, Sabyasachi Barik, and Swarnav Banik for hanging out and diversifying my graduate school experience.

Most importantly, I would like to thank my family, especially my mom Loan and my great-grandma Xinh, for their endless love and encouragement, which have allowed my curiosity and creativity to thrive. I thank my cousin Anna for visiting and checking on my well-being. Finally, for accompanying me on this journey, I thank Anna Fin, the love of my life and the apple of my eye.

Contents

List of Figures

List of Tables

Nomenclatures

Abbreviations

ADC	Analog to digital converter
AWG	Arbitrary waveform generator
BCS	Bardeen-Cooper-Schrieffer
CNOT	Controlled-NOT gate
CP	Carr-Purcell
CPB	Cooper-pair-box
CPMG	Carr-Purcell-Meiboom-Gill
CQED	Cavity quantum electrodynamics
cQED	Circuit quantum electrodynamics
CU	Controlled-Phase gate
CW	Continuous wave
CZ	Controlled-Z gate
DAC	Digital to analog converter

DRAG Derivative removal by adiabatic gate

DUT Device under test

IPA Isopropanol

IQ In-phase, Quadrature

JC Jaynes-Cummings

LO Local oscillator

MLE Maximum likelihood estimation

NMR Nuclear magnetic resonance

RB Randomized benchmarking

RF Radio frequency

RWA Rotating wave approximation

SNR Signal to noise ratio

SQUID Superconducting quantum interference device

SSB Single sideband

TWPA Traveling wave parametric amplifier

VNA Vector network analyzer

Greek Letters

α Coherence state phasor

β_{ij} Readout coefficients

χ_{ij} Dispersive shift between states i and j

Δ Detuning

ϵ Dielectric constant

Γ Relaxation rate of qubit

κ Coupling/relaxation rate of cavity

Ω' Effective Rabi frequency

Ω Rabi frequency

ω Cyclic frequency

ω_{ij} Qubit transition frequency between states i and j

ρ Density matrix

σ_I Pauli identity matrix

σ_X Pauli X matrix

σ_Y Pauli Y matrix

σ_Z Pauli Z matrix

Latin Letters

$a^\dagger, a$ Creation and annihilation operators

C Capacitance

C_Σ Total qubit capacitance

D Oscillator displacement operator

E_C	Electric charging energy
E_J	Josephson energy
E_L	Magnetic inductive energy
f	Frequency
g	Coupling constant
H	Hamiltonian
I	Pauli identity matrix
I_c	Junction critical current
J_C	Qubits' capacitive coupling constant
J_L	Qubits' inductive coupling constant
L	Inductance
L_J	Josephson inductance
M	Measurement operator
N	Number of energy quanta
n	Charge number operator
n_g	Gate charge
Q	Quality factor
$Q(\alpha)$	Husimi Q function
Q_{ext}	External quality factor

Q_{int}	Internal quality factor
R_i^θ	Rotation operator around axis i with angle θ
T_1	Relaxation time of qubit
T_2	Coherence time of qubit
T_2^*	Coherence time of qubit obtained from Ramsey measurement
T_2^{echo}	Coherence time of qubit obtained from echo measurement
X	Pauli X matrix
Y	Pauli Y matrix
$Y(\omega)$	Admittance
Z	Pauli Z matrix
$Z(\omega)$	Impedance

Physical Constants

$\hbar$	Reduced Planck constant, $1.054 \times 10^{-34}\,\mathrm{J \cdot s}$
Φ_0	Magnetic flux quantum, $2.067 \times 10^{-15}\,\mathrm{T \cdot m^2}$
c	Speed of light in a vacuum inertial frame, $299792458\,\mathrm{m/s}$
e	Electronic charge, $1.602 \times 10^{-19}\,\mathrm{C}$
h	Planck constant, $6.626 \times 10^{-34}\,\mathrm{J \cdot s}$
k_B	Boltzmann constant, $1.38 \times 10^{-23}\,\mathrm{J/K}$

Citations to Published Work

Parts of Chapters 6 and 7 have appeared in the following papers:

Y.-H. Lin, L. B. Nguyen, N. Grabon, J. F. San Miguel, N. A. Pankratova, V. E. Manucharyan, "Demonstration of Protection of a Superconducting Qubit from Energy Decay," Phys. Rev. Lett. **120**, 15, (2018)

L. B. Nguyen, Y.-H. Lin, A. J. Somoroff, R. A. Mencia, N. Grabon, V. E. Manucharyan, "High coherence fluxonium qubit," Phys. Rev. X **9**, 4, (2019)

Chapter 1

Introduction

There are only two ways to live your life.
One is as though nothing is a miracle.
The other is as though everything is a miracle.

Albert Einstein

1.1 The Second Quantum Revolution

In 1620, Francis Bacon argued in his philosophical and scientific work "The New Instrument" that knowledge gives us power and enables us to do new things. The idea sounds exceedingly simple, but the connection between science and technological renovation was in fact revolutionary at the time. Prior to the 16th century, science and technology were separate fields: new tools were usually discovered by craftsmen instead of scholars, and hardly any ruler or business person bothered financing research to gain power or wealth. Through trials and errors, people might have realized the usefulness of the circular wheel, come up with lightweight paper, or invented bricks to construct buildings. However, the spread of their usage was slow, innovations were few and far in between, and design and material used largely remained the same for centuries. The later marriage between science

and technology gave birth to the *Scientific Revolution*, which has changed our way of life forever [1].

The Scientific Revolution is a historical process in which humankind came to believe in the importance of scientific research, realizing that they could increase their capabilities through investment in such venture. It started with their willingness to admit their own ignorance, to realize that there are questions unanswered and problems unsolved. They then became inquisitive and set out to obtain answers through observation and mathematical tools, and subsequently gained new insights via their acquired knowledge. Wealthy and powerful people became willing to invest part of their resources in researches which they believed would give them the power to gain more resources.

Prior to the 1500s, people were used to the idea that the golden age was in the past, life was a zero-sum game, and the world was stagnant. For example, the conversion of energy depended primarily on muscle power for most of human history: the sun and nutrients in the soil give energy to plants, animals and human gain energy by eating plants or other animals, and energy is converted from food to work via metabolism. This process is inefficient, yet hardly anyone thought twice about improving the situation.

Modern culture, on the other hand, embraces the future, in technological innovations and scientific research. There has been plenty of evidence in recent history to support this belief in the future. In a short span of time, less than 0.1% of humankind's entire history, we have not only figured out how to convert energy much more efficiently, starting with the *Industrial Revolution*, but are also learning how to do it in more sustainable fashions. Within one century, humankind has not only built flying machines but also successfully commercialized the aviation industry. People can now routinely cross the Atlantic in just a few hours, a fact that would have startled Christopher Columbus and other early European explorers.

There is no doubt that the Scientific Revolution has resulted in tremendous progress

and unprecedented growth in the modern world. In fact, the modern economy relies significantly on technological advances, on unicorn startup companies and ingenious business ventures of tomorrow. Therefore, there is a constant need for humankind to acquire new knowledge and transform it to novel technologies.

The fundamental power human has over other species is our ability to store, communicate, and process information. In order to go from nomadic bands of foragers to kingdoms and empires, human progressively developed new tools and methods to obtain and analyze necessary data. While societies require the storage and processing of huge amount of information such as laws and taxes, the human brain is, unfortunately, not designed by nature to store and analyze information efficiently. The brain's capacity is limited, its lifespan is too short, and it is only adapted to store and process specific types of information. For example, hunters might only need to remember and identify animals' footprints, whereas gatherers had to distinguish between edible and poisonous vegetables. The arrival of writing systems, numbers, and algorithm-like information organization techniques helped change the game. Laws could be passed down, tax records could be kept and catalogued, large structures could be built with the help of trigonometry and algebra, and empires started popping up around the world. To build more powerful countries, stronger economies, and advance scientific frontiers further, we need more efficient computing devices and information processing techniques.

Humankind made a giant leap in the last century with the arrival of the modern computers. While sophisticated computing ideas had been developed at earlier times, with evidence dating back to as early as c. 1750 B.C., the knowledge was lost in the sands of time. The modern notion of computing as we know it took form in 1936, when Alan Turing constructed the model for a programmable computer now known as the *Turing machine*. He showed that the machine is *universal*, meaning that it is able to perform any computational task computable by any other device. This assertion is known as the *Church-Turing thesis*. It is this work that laid much of the foundation for modern computer science.

Soon after, the very first computers were built based on John von Neumann's model for the Turing machine. Despite the great breakthroughs, those first computing machines were hardly programmable, and they were bulky, often taking up the entire room. For example, the ENIAC (Electronic Numerical Integrator and Calculator) took up 1800 square feet, consisted of 18000 vacuum tubes, weighed 50 tons, and was used solely for calculating missiles' trajectories. Things really took off only after John Bardeen, Walter Brattain, and Williams Shockley invented the transistor in 1947, and accelerated after Jack Kilby and Robert Noyce invented the integrated circuit independently in 1958 and 1959, respectively. Computing power has been growing at an amazing pace ever since, a trend predicted by Gordon Moore in 1965, and neatly coined into what we now refer to as *Moore's law*. It states that computing power will double every other year at a constant cost. Interestingly, the law has held true until now. Today, a modern handheld device that fits in one's palm may wield tremendous power: it can perform billions of calculations per second, store valuable information, and moreover can connect the user to the internet and cloud services. Much of human knowledge, ranging from nutrition facts for sriracha sauce to machine learning algorithms, is just a mouse-click, or more conveniently, a tap on the phone, away.

Yet, there are computational problems that even these powerful machines cannot solve *efficiently*. What does "efficient" mean if the computers are so much faster than us anyway? Well, computers typically solve problems following sets of instructions or rules called *algorithms*. In *computational complexity* language, an efficient algorithm runs in time polynomial to the size of the problem, while an inefficient algorithm runs in time super-polynomial in time. Roughly speaking, there are problems that no existing algorithm can solve in time polynominal with respect to the size of the problems. Even if our computers become twice more powerful every other year, it will never be good enough to solve these hard problems efficiently! On top of that, Moore's law cannot hold true forever, and it is widely believed that we will soon be at the breaking point where it's impossible to scale the transistors smaller and pack more of them into a single chip [2].

So, can such hard problems be solved more efficiently at all? In the late 1960s and early 1970s, it seemed that a Turing machine was as powerful as any other possible computing device. This observation was codified as the *strong Church-Turing thesis*, which states that any computing process can be performed efficiently using a Turing machine. A major challenge to the thesis was *randomized algorithm*, which gives answers in a probabilistic, instead of deterministic, manner. This motivated David Deutsch to look into quantum mechanical laws to derive a stronger Church-Turing thesis. This led to the conception of the quantum circuit model, which is more generally known as gate-based quantum computing. In 1985, he showed a simple example, demonstrating what is now known as *Deutsch algorithm* [3], suggesting that a quantum computer may solve certain problems more efficiently than classical computers. This small first step was followed by a wave of enthusiastic researchers, culminating in Peter Shor's factorization algorithm in 1994 [4], which caused widespread excitement, first, because finding prime factors of a number could not be done efficiently by any known classical algorithm, and second, because implementing such algorithm would have far-reaching applications in modern cryptography and information security [5]. Another potential application for a quantum computer is optimization, spear-headed by Lov Grover. In 1995, he showed, via what is now known as *Grover's algorithm* [6], that unstructured search can be sped up by such computer. Although the algorithm only provides a quadratic speedup, this is still considerable when the size of the problem is large. A number of quantum algorithms have since been developed [7, 8].

The most intuitive application of quantum computers is to simulate quantum systems, as Richard Feynman first suggested in 1982. A system of N qubits interacting with each other must be described by a state living in a Hilbert space of dimension 2^N. Equivalently, simulating the dynamics of such state involves $2^N \times 2^N$ matrices, which is a hard task for conventional computers. Feynman suggested that a computer that functions according to the principles of quantum mechanics may allow us to complete this task more efficiently.

Following this hint, several researchers began working out approaches to simulate quantum systems using quantum computers and have shown that it is in fact possible to do so more efficiently than it would be on a classical computer. Ultimately, quantum simulations may have profound impact on our understanding of complex quantum systems and future discovery of new medicines and chemicals [9].

Why don't we have a quantum computer yet?

Let us first recall that the notion of quantum mechanics is not new, and physical properties resulted from quantum mechanical effects have been understood and utilized extensively in the modern technological world. Our ability to harness these quantum mechanical effects and use them to our advantage is often referred to as the *first quantum revolution*. The quintessential example is the transistor, which has made our experience with the computing world almost seamless. Everyday we use our phones, surf the internet, or write emails without thinking about the physics inside the transistors which made up the processing unit. Broadly speaking, all electronic equipment around us rely on various integrated circuits to function.

Quantum mechanics also gave us the laser. Until the 1960s, light was simply made of random waves. By exploiting stimulated emission in atomic systems, scientists could control the radiation precisely, being able to select the frequencies and intensity as desired, and laser technology was born. Lasers are used in a wide range of applications today, from transmitting signal in optical cables over long distances to controlling atomic quantum systems. With recent breakthroughs in photonic research, it is believed that further technological advances using lasers will occur [10].

Another important technology enabled by quantum mechanics is Nuclear Magnetic Resonance (NMR). The magnetic moments inside the atoms' nuclei, following quantum mechanical laws, are quantized. For a spin-half nuclei, the Z-projection of the spin can take only two different orientations: up or down. This can be controlled by an applied magnetic field and radio-frequency pulses. We are probably most familiar with this technology

through its application, the Magnetic Resonance Imaging (MRI) technique. During an MRI scan, a magnetic field is used to align the protons within the tissues of the patient. Radio-frequency pulses and field gradient are then applied, and the response from the nuclei is detected. The amount of energy released and the time it takes depend on the density of the protons and their environment, so the extracted data can be analyzed and used to reconstruct an image of our internal organs. This approach has been used widely to diagnose certain medical conditions and help countless patients [11]. NMR is important also because the techniques developed in NMR have been adapted to other quantum systems.

While machines whose working principles are based on quantum mechanical phenomena have been successfully constructed, what we need in order to build a quantum computer is the ability to coherently control individual quantum systems and their interactions, and the capability to measure them. To fulfill these challenging requirements, we must satisfy two seemingly contradicting conditions: keeping the qubits isolated from the noisy environment, and at the same time retaining a high degree of controllability of the quantum degrees of freedom. Moreover, as we scale up to a large number of computing elements, the level of coherence and addressability must be retained. With the technological advances in the last two decades, scientists around the world have gradually become more adept at this. Our demonstrated ability to coherently control quantum systems and their interactions is at the heart of the *second quantum revolution*, an era in which we seek to harness our knowledge to construct and operate useful quantum computers. A summary of notable advances in quantum hardware can be found in ref. [12].

1.2 Fluxonium Qubit: Preview

Among the currently available quantum systems, superconducting circuits based on Josephson tunnel junctions have become a leading platform in the pursuit of quantum computing. The history of these artificial atoms could be said to have started with the observation of

quantized energy levels in a macroscopic circuit in the 1980s [13, 14]. However, coherent control of Josephson circuit was achieved only in 1999 when Nakamura et al. successfully performed Rabi oscillation experiment in a Cooper-pair-box [15, 16]. This breakthrough was followed by various superconducting qubit designs [17, 18].

Superconducting circuits inherit certain advantages from other technologies. They can be printed on chips in large numbers [19, 20], wired together for strong interactions [21], and precisely manipulated and readout by radio-frequency electronics [22, 23]. The Josephson tunnel junction provides the necessary non-dissipative non-linearity required to turn linear electrical circuits into quantum bits and strong circuit-circuit coupling into fast logical operations. They inherit the advances in cryogenic technology and the robustness of superconductivity [18], both of which have a rich history of innovation. This platform has ushered in the era of noisy intermediate scale quantum processing [24] and quantum supremacy over classical computation [25, 26].

However, superconducting circuits also have some disadvantages. Since they are macroscopic in size, they can be surrounded by multiple noise sources and impurities [27, 28]. The most persistent problems come from dielectric loss [29, 30] and $1/f$ flux noise [31, 32, 33], which are due to microscopic two-level defects and the spin-$1/2$ impurities residing in the interface oxide layers around the device. These material imperfections persist even at low temperature and are challenging to get rid of. As a result, superconducting qubits have relatively short coherence times compared to microscopic quantum systems.

Decoherence is detrimental to quantum operations. It is a process through which the information about the quantum states is lost to the environment (see section 2.3), and is a fundamental barrier between the classical and the quantum worlds [34]. In quantum computing, decoherence introduces errors during gate operations [35] and constrains the number of qubits that can coherently tunnel in a quantum annealer [36, 37]. Improving coherence of superconducting qubits without sacrificing their controllability remains a central problem in the quest to build complex quantum processors [38, 39, 40, 41, 42, 43].

Material imperfections are the major obstacles in improving the coherence of superconducting qubits. Engineering circuit materials to improve performance is challenging [44, 45, 46, 47, 48]. Alternatively, coherence can be improved by designing noise-insensitive circuits. The most successful approaches to date all sacrifice qubit anharmonicity: the transmon qubit [49, 50, 51] and the C-shunt flux qubit [52, 53, 54] are derived from the Cooper-pair-box [15, 16] and the original flux qubit [55, 56, 57] by shunting the circuit with a large capacitance. The coherence was improved at the cost of a reduction in anharmonicity to about 5%. Such low anharmonicity adds challenges in scaling up the system. Since nonlinearity enables logic, reducing it too much will slow down gate operations. For example, exciting multiple qubits creates nearly resonant conditions for state leakage outside of the computational subspace [58], an error which is difficult to correct algorithmically.

This dissertation work describes progress in quantum computing with fluxonium superconducting artificial atoms [59]. The fluxonium qubit is designed to evade decoherence due to material imperfections without sacrificing non-linearity, flux-tunability, or microwave controllability [60, 61].

We report long relaxation time T_1 in the millisecond regime, enhanced by selection rules engineering, which is the equivalent of bit-flip quantum error correction at the hardware level [60]. At the flux symmetric point, coherence time T_2 in fluxonium approaches half a millisecond, still limited by energy relaxation (Fig. 1.1). This is the stepping stone for high performance quantum computing with fluxonium qubits [61]. Our results indicate that the current limit is due to our fabrication and material selection, implying that even longer coherence times are expected upon upgrading our fabrication techniques [30]. This achievement also sets the stage for further development of more complex superconducting circuit designs with additional protection from decoherence.

Finally, the thesis discusses our ongoing work on a fluxonium quantum processor constructed from two capacitively coupled qubits which can be entangled via a microwave-activated controlled-Z gate (see Fig. 1.2). We use the gate to create Bell states which are

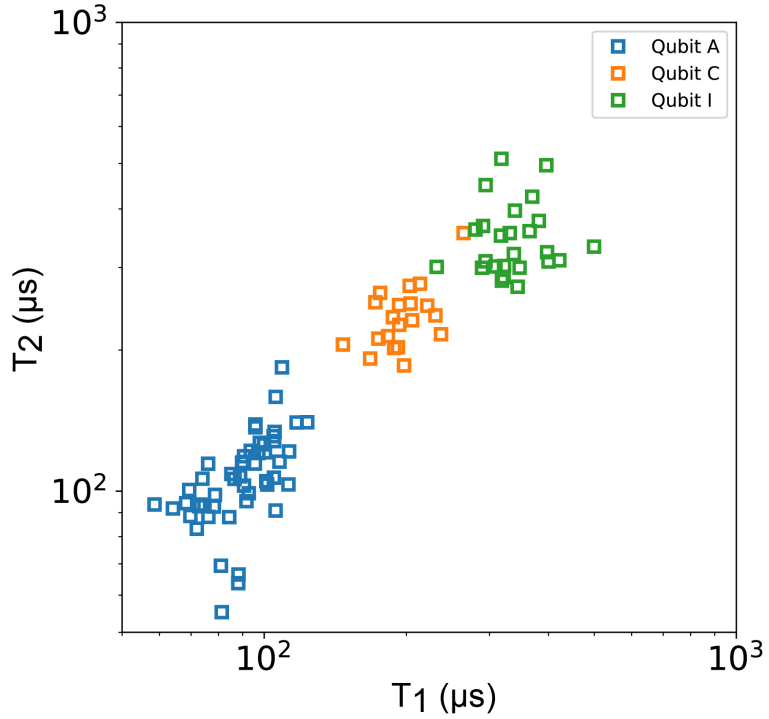

Figure 1.1: Coherence result highlight. Variations of coherence time T_2 and relaxation time T_1 of qubits A, C, and I (see table 6.1). The strong correlation suggests that improvement in T_1 would further enhance T_2.

highly entangled. Benchmarking of the gate shows that the fidelity is approaching the fault tolerant threshold, with the best fidelity $\mathcal{F}_{\mathrm{CZ}} \approx 0.975 \pm 0.015$ obtained from interleaved randomized benchmarking. With the tools developed and integrated into current experimental setup, we expect further optimization of the gate. This achievement is a necessary step toward constructing more complex, high performance fluxonium-based quantum architectures.

1.3 Thesis Outline

This thesis is organized as follows.

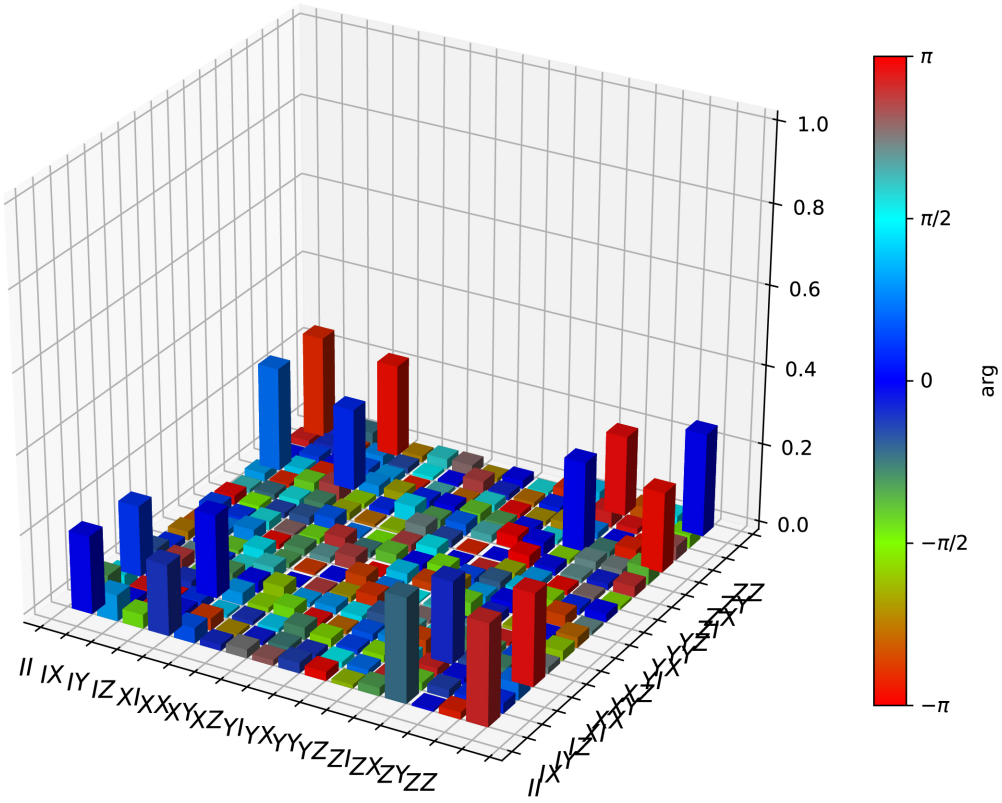

Figure 1.2: Two-qubit gate result highlight. Quantum process tomography χ matrix of the controlled-Z gate, with process fidelity $\mathcal{F} \approx 0.88$.

Chapter 2 introduces fundamental concepts in quantum computing, starting with the postulates of quantum mechanics in section 2.1. We then discuss in section 2.2 the simple yet ubiquitous theory of spins and springs, which we respectively use to model ideal two-level system and harmonic oscillator. We ends the chapter by discussing the formalism describing open quantum systems and decoherence processes in section 2.3.

Chapter 3 introduces the readers to the field of superconducting circuits. We start by reviewing in section 3.1 the physical concepts that allow these macroscopic quantum system to be treated as qubits, namely the phenomenon of superconductivity and the Josephson effects. Armed with this knowledge, we move on to review circuit quantization formalism.

Common decoherence mechanisms in superconducting qubits are discussed in section 3.2. The chapter ends with a brief description of quantum gates and readout techniques in superconducting circuits in section 3.3.

The rest of the thesis focuses on fluxonium qubits and the experiments done in the Superconducting Circuits Lab at the University of Maryland in the past six years. Chapter 4 establishes the theory which the experiments described in Chapter 6 are based on. We start with a discussion of fluxonium spectrum and selection rules in section 4.1. Specific decoherence mechanisms in fluxonium are analyzed in section 4.2, and dispersive readout with fluxonium is described in section 4.3. Relevant properties of coupled fluxonium circuits are discussed in section 4.4.

The quantum realm can only be explored if great care is taken to (i) isolate a quantum system from the environment, and at the same time (ii) retain coherent control of quantum degrees of freedom. We discuss the necessary experimental techniques to fulfill these requirements in Chapter 5, starting with cryogenic engineering concepts employed to setup the experiments in section 5.1. We follow with a discussion on cavity designs and simulation in section 5.2, and a description of our room temperature electronics in section 5.3. The chapter ends with an overview of relevant fabrication techniques in section 5.4.

Numerous experiments have been done throughout the course of this dissertation work. First, we discuss the tune up experiments done with aluminum cavities in section 6.1. The focus of the thesis are the coherence experiments, discussed in sections 6.2 and 6.3. We report our preliminary results on the microwave-activated controlled-Z gate in section 6.4. We conclude the chapter with a description of tune-up and auxiliary measurements in section 6.5.

Chapter 7 first discusses the importance of our experimental results in the context of quantum computing with superconducting circuits in section 7.1. We then present a perspective on quantum computing with fluxonium-based architectures in section 7.2.

Chapter 2

Concepts in Quantum Computing and Quantum Optics

Those who are not shocked when they first come across quantum theory cannot possibly have understood it.

Niels Bohr

This chapter serves as the introduction to fundamental and essential concepts that we will use in the rest of thesis. We first start with concepts from quantum computing and quantum information [2, 5] in section 2.1. We follow by discussing the simple yet ubiquitous physics of spins and springs [10] in section 2.2 to build our intuition for later chapters. Section 2.3 discusses the formal approach used to model open quantum systems and decoherence, ending with a brief discussion on quantum process tomography [5, 10].

2.1 Fundamental Concepts

2.1.1 State Space

An isolated quantum system is completely described by a *state vector*. A state vector is a unit vector that lives in an associated *state space*, which is a complex vector space, referred to as the Hilbert space of the system.

The basic building block of quantum computers is the quantum bit, or *qubit*. It is also the simplest isolated quantum mechanical system. A qubit lives in a two-dimensional state space. Suppose, using Dirac's notation, that the ground state $|0\rangle$ and excited state $|1\rangle$ form an orthogonal basis for the qubit's state space, then an arbitrary state vector in the state space can be written as

$$|\psi\rangle = a|0\rangle + b|1\rangle, \tag{2.1}$$

where a and b are complex numbers. The condition for the state vector $|\psi\rangle$ to be a unit vector is that it satisfies the *normalization condition*, $\langle\psi|\psi\rangle = 1$, which requires $|a|^2+|b|^2 = 1$. The states $|0\rangle$ and $|1\rangle$ are analogous to the classical bits 0 and 1 in a digital register. However, instead of being only in one state or the other, a qubit can be in any *superposition state* as generally described by Eq. 2.1. When the qubit is in a superposition state, it cannot be determined with certainty whether it is in one of its basis states. Instead, it has probability $|a|^2$ of being in $|0\rangle$ and probability $|b|^2$ of being in $|1\rangle$. Thus, a and b are referred to as probability amplitudes. For example, the state

$$\frac{|0\rangle + |1\rangle}{\sqrt{2}} \tag{2.2}$$

is a superposition of the basis states $|0\rangle$ and $|1\rangle$, with amplitudes $a = b = 1/\sqrt{2}$, which means there is a 50% probability for the state to be in $|0\rangle$ and a 50% probability for it to be in $|1\rangle$.

The state vector of a qubit can be conveniently visualized on a *Bloch sphere* (Fig. 2.1).

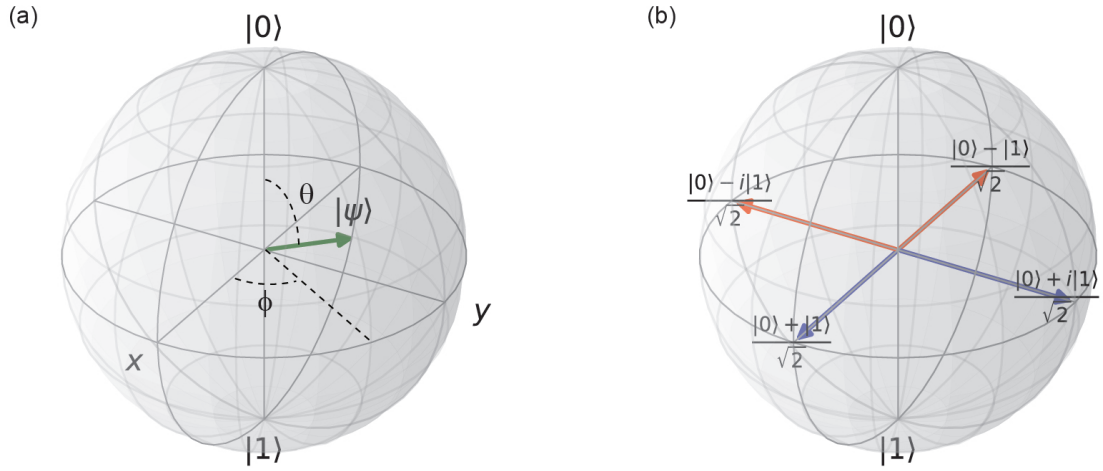

Figure 2.1: Bloch sphere visualization. (a) Bloch sphere with an arbitrary superposition state, where the state vector's end point lies on the surface of the sphere, its direction and polarization are defined by angles ϕ and θ. (b) Bloch sphere with superposition states aligned along the X and Y axes.

It is a sphere with unit radius, and the state vector of a qubit is represented as a unit vector with the tip lying on the surface of the sphere.

The state vector can then be rewritten in terms of the angles θ and ϕ as

$$|\psi\rangle = \cos\frac{\theta}{2}|0\rangle + e^{i\phi}\sin\frac{\theta}{2}|1\rangle, \tag{2.3}$$

which is very useful when we want to describe simple quantum operations on the qubit, although this visualization is limited to the single-qubit case, as there is no generalization for multiple qubits.

Note that the normalization condition is automatically satisfied with trigonometric identity of sine and cosine in Eq. 2.3. The factor $1/2$ for angle θ is chosen so that $\theta = 0$ corresponds to $|0\rangle$ state, $\theta = \pi$ corresponds to $|1\rangle$ state, and $\theta = 2\pi$ corresponds to $-|0\rangle$ state, so the qubit is actually 4π periodic. This *global phase* is, however, not important for the qubit, as it is not possible to probe it in a single qubit. For a single qubit, the important physical

quantity is the *relative phase* between the $|0\rangle$ and $|1\rangle$ components. We will confirm this after introducing the measurement postulate, and come back to the 4π periodicity in the case of multiple qubits coupled to each other, where this property allows us to do multi-qubit entangling gate.

2.1.2 Quantum Evolution and Gates

The evolution of an isolated quantum system from time t_i to time t_f is described by a *unitary operator* U,

$$|\psi(t_f)\rangle = U(t_i, t_f)|\psi(t_i)\rangle \tag{2.4}$$

The unitary operator U defined above is abstract. Its form depends on the particular system under consideration. An important practical consideration is how the state varies continuously in time, which is described by the *Schrödinger equation*:

$$i\hbar\frac{d|\psi\rangle}{dt} = H|\psi\rangle, \tag{2.5}$$

where $\hbar$ is the *Planck's constant*, and H is the *Hamiltonian* of the closed quantum system. If we know the Hamiltonian of a system, we can then understand its dynamics and predict its time evolution.

The Hamiltonian is a Hermitian operator with spectral decomposition

$$H = \sum_E E|E\rangle\langle E|, \tag{2.6}$$

with eigenvalues E and corresponding normalized eigenvectors $|E\rangle$. Physically, the states $|E\rangle$ are the energy eigenstates of the system with corresponding eigenenergies E. The eigenstate with the lowest eigenenergy is conventionally defined as the *ground state*. Eigenstates of a closed quantum system are also referred to as *stationary states* because their evolution in time is simply a change in phase, which can be readily deduced from Eq. 2.5

and Eq. 2.6,

$$|E(t)\rangle = \exp(-iEt/\hbar)|E(t=0)\rangle. \tag{2.7}$$

The unitary operator U that acts on a quantum state $|\psi\rangle$ to evolve it from time t_i to time t_f can be formally written in terms of the time-independent Hamiltonian as

$$U(t_f, t_i) = \exp\left(\frac{-iH(t_f - t_i)}{\hbar}\right). \tag{2.8}$$

In quantum computation and quantum information, we often work with abstract unitary operations, leaving the details of the Hamiltonian H to be determined separately. For example, in the quantum circuit model, the qubit can be manipulated using specific unitary gate operations which only take into account the initial and final states. To proceed further, let us introduce the Pauli operators in matrix forms. They are used extensively in quantum computation and quantum information. There are two equivalent notations frequently used in literatures written below,

$$\begin{aligned} \sigma_I \equiv I = \begin{pmatrix} 1 & 0 \\ 0 & 1 \end{pmatrix}, \quad \sigma_X \equiv X = \begin{pmatrix} 0 & 1 \\ 1 & 0 \end{pmatrix}, \\ \sigma_Y \equiv Y = \begin{pmatrix} 0 & -i \\ i & 0 \end{pmatrix}, \quad \sigma_Z \equiv Z = \begin{pmatrix} 1 & 0 \\ 0 & -1 \end{pmatrix}. \end{aligned} \tag{2.9}$$

The action of the Pauli matrices on a qubit state is straightforward. The identity operator I leaves the qubit state unchanged, while the other operators flip it around the respective axis. The Pauli matrices can further be used to describe arbitrary rotations around the X, Y,

Z axes via the *rotation operators*,

$$R_X(\theta) \equiv e^{-i\theta X/2} = \cos\frac{\theta}{2}I - i\sin\frac{\theta}{2}X, \tag{2.10}$$

$$R_Y(\theta) \equiv e^{-i\theta Y/2} = \cos\frac{\theta}{2}I - i\sin\frac{\theta}{2}Y, \tag{2.11}$$

$$R_Z(\theta) \equiv e^{-i\theta Z/2} = \cos\frac{\theta}{2}I - i\sin\frac{\theta}{2}Z. \tag{2.12}$$

Note that we have used the Pauli matrices identity $\sigma_i\sigma_j = \delta_{ij}I + i\epsilon_{ijk}\sigma_k$ after expanding the exponential in our derivation. In quantum computing, the angles $\theta = \pm\pi/2$ are often used to rotate the qubit onto and away from the X-Y plane, so we often write $R_X(\theta = \pm\pi/2)$ and $R_Y(\theta = \pm\pi/2)$ as $\pm X/2$ and $\pm Y/2$, respectively.

2.1.3 Measurement

Quantum measurements are described by a set of *measurement operators* $\{M_m\}$ acting on the state space of the system being measured. It is a complete set of operators which satisfies the completeness relation

$$\sum_m M_m^\dagger M_m = I. \tag{2.13}$$

If the state of the system is $|\psi\rangle$ before the measurement, then after the measurement, the system is left in

$$|\psi_m\rangle = \frac{M_m|\psi\rangle}{\sqrt{\langle\psi|M_m^\dagger M_m|\psi\rangle}} \tag{2.14}$$

with probability

$$p(m) = \langle\psi|M_m^\dagger M_m|\psi\rangle. \tag{2.15}$$

From the completeness relation, we can deduce that the probabilities sum up to one, $\sum_m p(m) = 1$. For many applications, we will be concerned with an important class of measurements known as *projective measurements*. In this case, the measurement operators M_m are orthogonal projectors, $M_m M_{m'} = \delta_{m,m'}M_m$. The measurement is then described

by an *observable* M with spectral decomposition

$$M = \sum_m m P_m, \tag{2.16}$$

where P_m is the projector onto the eigenspace of M with eigenvalue m. When measuring state $|\psi\rangle$, the probability of getting result m is

$$p(m) = \langle\psi|P_m|\psi\rangle. \tag{2.17}$$

For example, when measuring a qubit along the Z-axis, the observable is $\sigma_Z \equiv Z$. We can write

$$Z = |0\rangle\langle 0| - |1\rangle\langle 1|. \tag{2.18}$$

Thus, if we measure the superposition state $|\psi\rangle = (|0\rangle + |1\rangle)/\sqrt{2}$ along Z, we would get $(+1)$ with probability $\langle\psi|0\rangle\langle 0|\psi\rangle = 1/2$ and (-1) with probability $\langle\psi|1\rangle\langle 1|\psi\rangle = 1/2$.

We can also measure the qubit along X and Y. From Fig. 2.1, we can infer that we would get $\langle X\rangle = \langle\psi|X|\psi\rangle = 1$ and $\langle Y\rangle = \langle\psi|Y|\psi\rangle = 0$. Indeed, we can check by direct matrix multiplication that $\langle X\rangle = 1$ for superposition state ψ. More generally, we can define

$$|0\rangle_X = \frac{|0\rangle_Z + |1\rangle_Z}{\sqrt{2}}, \qquad |1\rangle_X = \frac{|0\rangle_Z - |1\rangle_Z}{\sqrt{2}}, \tag{2.19}$$

so it's also possible to write the superposition state $\frac{|0\rangle_Z+|1\rangle_Z}{\sqrt{2}}$ in the Z-basis as $|0\rangle_X$ in the X-basis. While the decomposition of a state vector varies according to the different bases, the measurement is independent of the choice for the bases.

A practical problem in quantum computing is to determine the observables X and Y when the system can only be measured along Z. To accomplish this, we simply perform $\pm\pi/2$ rotations right before the projection measurement. This transformation converts what we measure along Z to the expectation values $\langle X\rangle$ and $\langle Y\rangle$, as shown in Table 2.1.

Table 2.1: Qubit rotations and Z-projection measurements to determine expectation values of Pauli matrices.

Rotate	Measure
I	$\langle Z \rangle$
X/2	$\langle Y \rangle$
Y/2	-$\langle X \rangle$
-X/2	-$\langle Y \rangle$
-Y/2	$\langle X \rangle$

We can now examine the importance of the global phase and the relative phase of a qubit state. Consider two different states $|\psi\rangle$ and $e^{i\phi}|\psi\rangle$. Suppose that we measure it with an arbitrary observable corresponding to the measurement operator M_m. The expectation value of such observable for these states are $\langle\psi|M_m^\dagger M_m|\psi\rangle$ and $\langle\psi|e^{-i\theta}M_m^\dagger M_m e^{i\theta}|\psi\rangle$, which are equivalent. Thus, it is not possible to tell these states apart by any kind of measurement. We may say that they are equivalent states.

It's quite a different story with the relative phase. For example, consider the states

$$|0\rangle_X = \frac{|0\rangle_Z + |1\rangle_Z}{\sqrt{2}}, \qquad |1\rangle_X = \frac{|0\rangle_Z - |1\rangle_Z}{\sqrt{2}}. \tag{2.20}$$

The probabilities of the two available expectation values when we measure the states in the Z basis are the same, and we cannot tell them apart. However, the relative phase difference in the Z basis is equivalent to a different state in the X basis, and we can measure the difference when we determine $\langle X \rangle$, with $|0\rangle_X$ giving 0 and $|1\rangle_X$ giving 1. Thus, the relative phase is basis-dependent, and the difference between the phases in one basis can result in physically distinguishable states in another basis. Therefore, states with different relative phases are not physically equivalent.

2.1.4 Composite Systems

When multiple individual systems are prepared separately and used to construct a composite system, the state space of such a composite system is the tensor product of the state spaces of the component systems. The joint state of the total system can be written as the *tensor product* of the constituent state vectors

$$|\psi\rangle = |\psi_1\rangle \otimes |\psi_2\rangle \otimes ... \otimes |\psi_n\rangle. \tag{2.21}$$

In this case, any manipulation on one part does not affect the others. Unitary operations on composite system when the operation is applied to only one of the individual systems can simply be written as the tensor product as well. For example, when we flip the first qubit of a two-qubit system while leaving the other qubit untouched, the corresponding unitary can be written as

$$U = X \otimes I. \tag{2.22}$$

However, it is not always possible to write the state vector representing a composite system as the tensor product of the state vectors of individual systems. For instance, it's not possible in the case where two systems are allowed to interact and form an *entangled state*. As an example, let us consider the two-qubit state

$$|\psi\rangle = \frac{|00\rangle + |11\rangle}{\sqrt{2}}. \tag{2.23}$$

We can readily check that there are no single-qubit states $|\psi_1\rangle$, $|\psi_2\rangle$ such that $|\psi\rangle = |\psi_1\rangle \otimes |\psi_2\rangle$.

Such entangled states play a crucial role in quantum physics, quantum computation, and quantum information. Unlike product composite states, when we measure one constituent qubit, we also project the other qubit onto the respective basis. For example, if we measure the first qubit in $|\psi\rangle$ and project it onto $|0\rangle$ (with 50% probability), then the second qubit

collapses onto $|0\rangle$ with certainty (100% probability).

The state defined in Eq. 2.23 is called a *Bell state*. There are four of them:

$$\begin{aligned} |\beta_{00}\rangle &= \frac{|00\rangle + |11\rangle}{\sqrt{2}}, \\ |\beta_{01}\rangle &= \frac{|00\rangle - |11\rangle}{\sqrt{2}}, \\ |\beta_{10}\rangle &= \frac{|01\rangle + |10\rangle}{\sqrt{2}}, \\ |\beta_{11}\rangle &= \frac{|01\rangle - |10\rangle}{\sqrt{2}}. \end{aligned} \tag{2.24}$$

Just as there are non-trivial (non-product) composite states, there are also non-trivial unitary operations which cannot be written as the tensor products of individual unitary gates of constituent systems. These are called multi-qubit entangling gates, and they are required to construct universal sets of quantum gates. A universal set of gates is required to synthesize any arbitrary operation on a quantum computer. A set composed of any two-qubit entangling gate and all single-qubit gates is universal [2].

A two-qubit gate is an entangling gate if for some input product state, the output after applying the gate is an entangled state. An important entangling gate is the controlled-NOT (CNOT) gate, defined by the unitary matrix

$$U_{\text{CNOT}} = \begin{pmatrix} 1 & 0 & 0 & 0 \\ 0 & 1 & 0 & 0 \\ 0 & 0 & 0 & 1 \\ 0 & 0 & 1 & 0 \end{pmatrix}. \tag{2.25}$$

We can easily check its action on the basis states: the gate flips the state of the second qubit if the first qubit state is $|1\rangle$. Thus, the first qubit is referred to as the *control qubit* and the

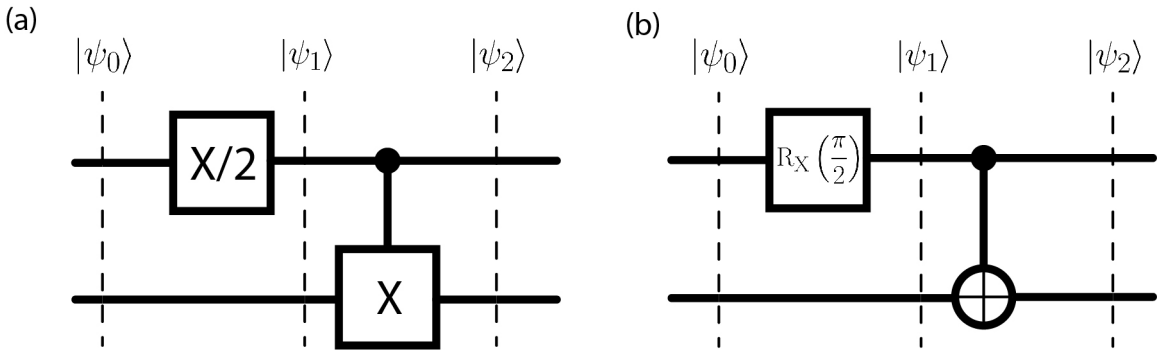

Figure 2.2: Quantum circuit to create Bell states using CNOT gate. (a) Quantum circuit diagram showing the creation of Bell states using a single-qubit gate and the controlled-NOT two-qubit gate. If the initial state $|\psi_0\rangle$ is $|00\rangle$, then the final state $|\psi_2\rangle$ is the Bell state $|\beta_{00}\rangle$. Other Bell states can be created starting from different initial states (see Table 2.2). (b) Equivalent representation of the single-qubit gate $X/2$ and the CNOT gate in a quantum circuit.

second qubit is referred to as the *target qubit*,

$$\begin{aligned} U_{\mathrm{CNOT}}|00\rangle &= |00\rangle, \\ U_{\mathrm{CNOT}}|01\rangle &= |01\rangle, \\ U_{\mathrm{CNOT}}|10\rangle &= |11\rangle, \\ U_{\mathrm{CNOT}}|11\rangle &= |10\rangle. \end{aligned} \tag{2.26}$$

The CNOT gate can be used together with single-qubit gates to generate entangled states, as shown in Fig. 2.2. The circuit shown is often referred to as *quantum circuit diagram*, the input and output are quantum states, and the gates are drawn as rectangular blocks. Two different representations of the gates are shown. The state of the system is changed by the gates as follows,

$$|\psi_0\rangle = |00\rangle,\ |\psi_1\rangle = \frac{|00\rangle + |10\rangle}{\sqrt{2}},\ |\psi_2\rangle = \frac{|00\rangle + |11\rangle}{\sqrt{2}} = |\beta_{00}\rangle. \tag{2.27}$$

Other Bell states can be created depending on the initial states, as shown in Table 2.2.

Table 2.2: Creation of Bell states from different initial states using the quantum circuit diagram in Fig. 2.2.

Initial state	$\|00\rangle$	$\|01\rangle$	$\|10\rangle$	$\|11\rangle$
Final state	$\|\beta_{00}\rangle$	$\|\beta_{10}\rangle$	$\|\beta_{01}\rangle$	$\|\beta_{11}\rangle$

Another important two-qubit gate is the controlled-Phase (CU) gate, defined by the unitary matrix

$$U_{\mathrm{CU}} = \begin{pmatrix} 1 & 0 & 0 & 0 \\ 0 & 1 & 0 & 0 \\ 0 & 0 & 1 & 0 \\ 0 & 0 & 0 & e^{i\theta} \end{pmatrix}. \tag{2.28}$$

When $\theta = \pi$, $e^{i\theta} = -1$, the CU gate becomes what we often call the controlled-Z (CZ) gate,

$$U_{\mathrm{CZ}} = \begin{pmatrix} 1 & 0 & 0 & 0 \\ 0 & 1 & 0 & 0 \\ 0 & 0 & 1 & 0 \\ 0 & 0 & 0 & -1 \end{pmatrix}. \tag{2.29}$$

The action of the CU (and CZ) gate is also straightforward. If the two-qubit state is $|11\rangle$, the unitary U_{CU} would apply a phase factor $e^{i\theta}$ to it.

$$\begin{aligned} U_{\mathrm{CU}}|00\rangle &= |00\rangle, \\ U_{\mathrm{CU}}|01\rangle &= |01\rangle, \\ U_{\mathrm{CU}}|10\rangle &= |10\rangle, \\ U_{\mathrm{CU}}|11\rangle &= e^{i\theta}|11\rangle. \end{aligned} \tag{2.30}$$

The CZ gate can also be combined with single-qubit gates to create entangled states. For

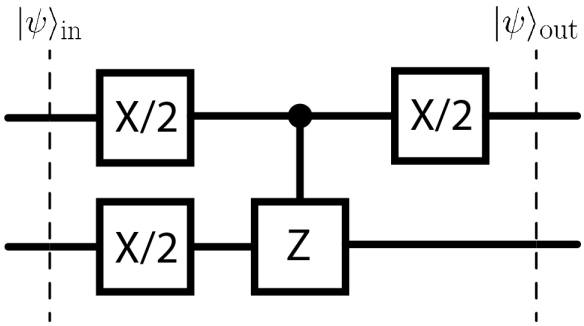

Figure 2.3: Quantum circuit to create Bell states using CZ gate. Quantum circuit diagram showing the creation of Bell states using single-qubit gates and controlled-Z two-qubit gate. Different Bell states can be created starting from different initial states, as summarized in Table 2.3.

Table 2.3: Creation of Bell states based on different initial states using the quantum circuit diagram in Fig. 2.3.

Initial state	$\|00\rangle$	$\|01\rangle$	$\|10\rangle$	$\|11\rangle$
Final state	$\|\beta_{10}\rangle$	$\|\beta_{11}\rangle$	$\|\beta_{01}\rangle$	$\|\beta_{00}\rangle$

example, we can create different Bell states using the quantum circuit shown in Fig. 2.3. The circuit's input-output relations are summarized in Table 2.3.

2.2 Spin and Mass On A Spring

Cavity quantum electrodynamics (CQED) physics is elegant and ubiquitous. Part of its appeal comes from the simplicity of the model: a two-level system is represented as a spin, and a quantum field is described as a mass on a spring. Despite its simplicity, the model displays a wide variety of phenomena, the breadth of which can be explored in references such as [10]. This section introduces the basic concepts which have been adopted for use in superconducting circuits to give birth to the field of *circuit quantum electrodynamics* (cQED) [22, 62]. We will explore cQED physics in more details in section 3.1.

Realistic quantum systems can often be simplified to include just two states, with complications from other states eliminated by appropriate approximation. The physics involved is then reduced to two-level system configuration, which can be effectively modeled as a spin-half, with the spin pointing up representing one state and the spin pointing down representing the other state. The dynamics of the spin obeys the Bloch equations [10].

When many quanta of energy are involved, a mass on a spring model is better suited to capture the physics. A harmonic oscillator with its Hamiltonian quadratic with respect to the system's conjugate coordinates provides a good description of low lying states in such system. Note that interactions which are too strong can introduce non-linear phenomena, and the approximation fails. Therefore, we shall not consider that regime here.

In this section, we start with a description of the two-level system as a spin, and review how it can be manipulated by an external field. We then move on to analyze the Hamiltonian of a quantum harmonic oscillator which models an electromagnetic field, and define the state of a driven oscillator in equilibrium. Finally, we explore the coupled spin-spring system in the dispersive limit. This formalism is expanded to explore gates and readout for superconducting circuits in section 3.3.

2.2.1 The Spin System

A two-level system with eigenstates $|0\rangle$ and $|1\rangle$ is equivalent to a spin one-half aligned along the Z-axis. Let the difference in its eigenenergies be $\hbar\omega_{01}$, then the Hamiltonian for this system can be written as

$$H_s = -\frac{\hbar\omega_{01}}{2}\sigma_Z. \tag{2.31}$$

With this definition, $|0\rangle$ and $|1\rangle$ correspond to the ground and excited states with eigenenergies $-\hbar\omega_{01}/2$ and $\hbar\omega_{01}/2$, respectively. Let us introduce the raising and lowering operator $\sigma_\pm$, defined as

$$\sigma_+ = |1\rangle\langle 0|, \qquad \sigma_- = |0\rangle\langle 1|, \tag{2.32}$$

which can be written in terms of the Pauli matrices $\sigma_{X,Y}$ as

$$\sigma_{\pm} = \frac{1}{2}(\sigma_X \mp i\sigma_Y). \tag{2.33}$$

We can attempt to drive the two-level system with a classical oscillating field written as

$$\vec{E} = E_d \left(\vec{\epsilon_d} e^{-i(\omega_d t + \phi_d)} + \vec{\epsilon_d}^* e^{i(\omega_d t + \phi_d)} \right), \tag{2.34}$$

where E_d is the amplitude of the field, ω_d is the angular frequency, ϕ_d is the phase, and $\vec{\epsilon_d}$ is the complex polarization vector. The field can be coupled to the spin via a dipole moment

$$\vec{D} = d\left(\vec{\epsilon_s}\sigma_+ + \vec{\epsilon_s}^*\sigma_-\right), \tag{2.35}$$

where d is the dipole matrix element and $\vec{\epsilon_s}$ is the spin's polarization. The coupling Hamiltonian can then be written as $H_d = \vec{E} \cdot \vec{D}$, with $H = H_s + H_d$. We can simplify the driving scheme by letting $\vec{\epsilon_d} \cdot \vec{\epsilon_d}^* = 1$. We can then use the *rotating wave approximation* in the *interaction representation* to get the interaction Hamiltonian of the system rotating at the field's frequency ω_d [10],

$$\begin{aligned} H_I &= \frac{\hbar\Delta}{2}\sigma_Z + \frac{\hbar\Omega}{2}(e^{-i\phi_d}\sigma_+ + e^{i\phi_d}\sigma_-) \\ &= \frac{\hbar\Delta}{2}\sigma_Z + \frac{\hbar\Omega}{2}\left(\cos(\phi_d)\sigma_X + \sin(\phi_d)\sigma_Y\right) \end{aligned} \tag{2.36}$$

where $\Delta = \omega_{01} - \omega_d$ is the spin-field detuning, and $\Omega = 2dE_d/\hbar$ is the *Rabi frequency* of the driven system, which is intuitively proportional to the matrix element of the spin d and the amplitude of the field E_d. However, that is not always the exact rotation frequency of the spin, due to the finite detuning between the drive and the transition frequency. In general,

we can write the driven Hamiltonian as

$$H_I = \frac{\hbar\Omega'}{2}\vec{\sigma}\cdot\vec{n}, \tag{2.37}$$

where

$$\Omega' = \sqrt{\Delta^2 + \Omega^2} \tag{2.38}$$

is the effective Rabi frequency, and

$$\vec{n} = \frac{\Delta\vec{u}_Z + \Omega\cos\phi_d\vec{u}_X + \Omega\sin\phi_d\vec{u}_Y}{\Omega'} \tag{2.39}$$

is a unit vector in the Bloch sphere, the direction of which is determined by the ratio between the detuning Δ and the Rabi frequency Ω.

The Hamiltonian in Eq. 2.37 thus describes the Larmor precession around an effective axis along $\vec{n}$ at frequency Ω'. This is also known as *Rabi oscillation*. The time evolution of the spin on the Bloch sphere under the driving field can be visualized by simulating Eq. 2.5 in the rotating frame,

$$i\hbar\frac{\partial}{\partial t}|\psi\rangle_I = H_I|\psi\rangle_I. \tag{2.40}$$

Time evolution of the spin in different detuning scenarios is plotted in Fig. 2.4. For simplicity, we can set $\phi_d = 0$, and vary the detuning Δ. In the resonant case, the spin vector rotates around the X-axis. In the detuned case, the axis of rotation is tilted away from the X-axis by an angle that increases with the detuning. From Eq. 2.39, we can deduce that the tangent of this angle is equal to Δ/Ω.

Rabi oscillation provides a simple way to prepare the qubit in any arbitrary state. The most important cases are for rotation angles of π and $\pi/2$, where a combination of the field amplitude E_d and the interaction time is tuned to rotate the spin precisely by these angles.

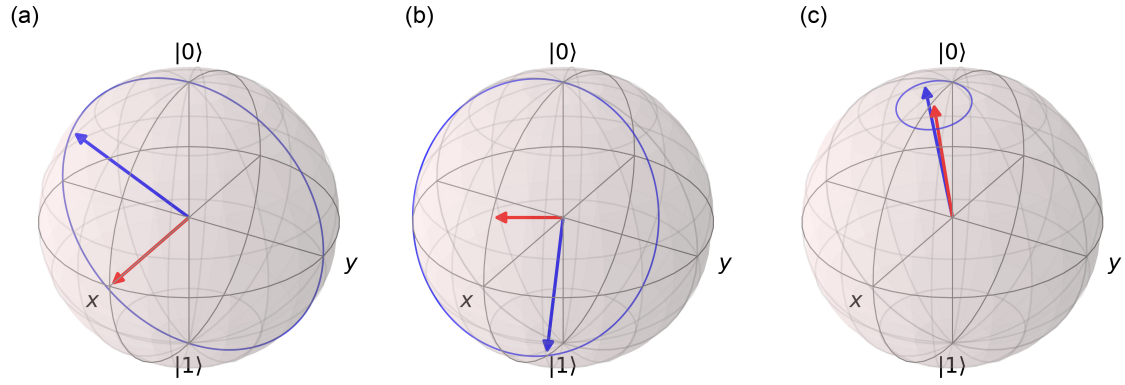

Figure 2.4: Qubit rotation. A qubit rotating in the drive's frame when the drive is (a) on resonant with qubit's frequency $\Delta = 0$, (b) somewhat off-resonant $\Delta = \Omega/2$, and (c) far-detuned from qubit's frequency $\Delta = 4\Omega$. The qubit's trajectory is described by the blue arrow tracing the blue line. The red arrow represents the axis of rotation.

2.2.2 The Field Oscillator

Generally speaking, harmonic motion can be characterized by a particle of mass m moving in a 1D quadratic potential $V(x) = m\omega^2 x^2/2$. The motion of the particle in a phase space of complex variable $x + ip$ is a rotation at angular frequency ω. In quantum physics, the position and momentum are operators satisfying the commutation relation $[x, p] = i\hbar$, and the Hamiltonian of the system can be written as

$$H = \frac{m\omega^2 x^2}{2} + \frac{p^2}{2m}. \tag{2.41}$$

Next, we can introduce the natural units for x and p as [10]

$$x_0 = \sqrt{\frac{\hbar}{2m\omega}}, \quad p_0 = \sqrt{\frac{m\omega\hbar}{2}}, \tag{2.42}$$

then normalize $x' = x/2x_0$, $p' = p/2p_0$ to get

$$H = \hbar\omega(x'^2 + p'^2). \tag{2.43}$$

Quantum harmonic oscillator formalism can be conveniently and elegantly written in terms of the *ladder operators*, namely the annihilation operator $a = x' + ip'$ and its complex conjugate $a^\dagger$. The commutation relation between x and p leads to $[a, a^\dagger] = I$, and the spring's Hamiltonian can be written as

$$H = \hbar\omega \left(a^\dagger a + \frac{1}{2} \right), \tag{2.44}$$

where $N \equiv a^\dagger a$ is the number operator satisfying $[a, N] = a$, $[a^\dagger, N] = -a^\dagger$, and the term $\hbar\omega/2$ represents the vacuum fluctuation energy. We can check that $\langle x^2 \rangle = x_0^2$ and $\langle p^2 \rangle = p_0^2$ (or $\langle x'^2 \rangle = \langle p'^2 \rangle = 1/4$) satisfy the vacuum condition $N = 0$, $H = \hbar\omega/2$. Thus, x_0 and p_0 are also referred to as *zero point* position and momentum r.m.s. fluctuations, respectively. We shall use this formalism in deriving the corresponding zero point coordinates for an LC oscillator in section 3.1.

Within a constant vacuum energy $\hbar\omega/2$, the eigenvalues of the Hamiltonian of an oscillator are then $\hbar\omega N$, with denoted eigenstates $|n\rangle$, where n is a non-negative integer. These are called *Fock states* of the harmonic oscillator, such that $N|n\rangle = n|n\rangle$. The ladder operators' effect on the Fock states is to move the system up or down in the ladder (see Fig. 2.5(b)),

$$a|n\rangle = \sqrt{n}|n-1\rangle, \qquad a^\dagger|n\rangle = \sqrt{n+1}|n+1\rangle. \tag{2.45}$$

An electric field in a cavity can be expressed as a linear combination of the creation and annihilation operators,

$$\vec{E}(\omega, t) = E_0 \left(\vec{f} a e^{-i\omega t} - \vec{f}^* a^\dagger e^{i\omega t} \right), \tag{2.46}$$

where E_0 is the electric field amplitude, and $\vec{f}$ describes the position dependence of the field, obeying fields equation and boundary conditions.

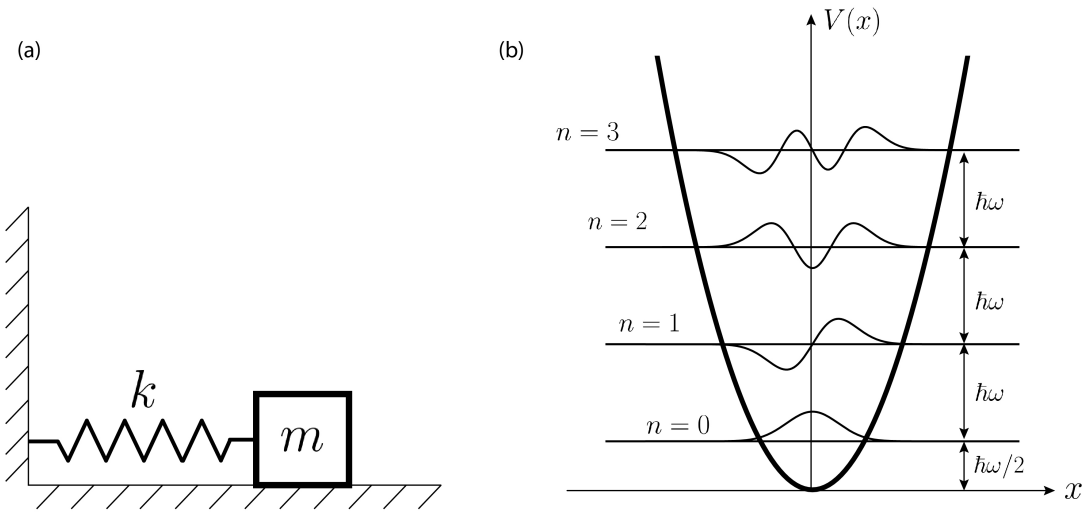

Figure 2.5: Harmonic oscillator concepts. (a) A harmonic oscillator is represented as a mass m connected to a spring with spring constant k. Its resonant frequency is $\omega = \sqrt{k/m}$. (b) Energy spectrum ladder of a harmonic oscillator. The levels are equally spaced, with the lowest state having the vacuum energy of $\hbar\omega/2$.

Since the Fock states are equidistant in the energy space, the electric field has an indefinite phase and does not correspond to an oscillator excited by a classical field. When an oscillator is driven by a classical field, it is instead put into a state described by well-defined amplitude and phase. For example, we can drive a mechanical oscillator into such state by giving it a momentum kick p, while for an LC oscillator, we can drive it with a current or voltage source. We call the resulting state *coherent state* $|\alpha\rangle$, defined as

$$|\alpha\rangle = D(\alpha)|0\rangle, \tag{2.47}$$

where $D(\alpha) = e^{(\alpha a^\dagger - \alpha^* a)}$ is the displacement operator, satisfying $D^\dagger(\alpha) = D(-\alpha)$ and $D(0) = I$. The coherent state can be expressed in terms of Fock states using the expression

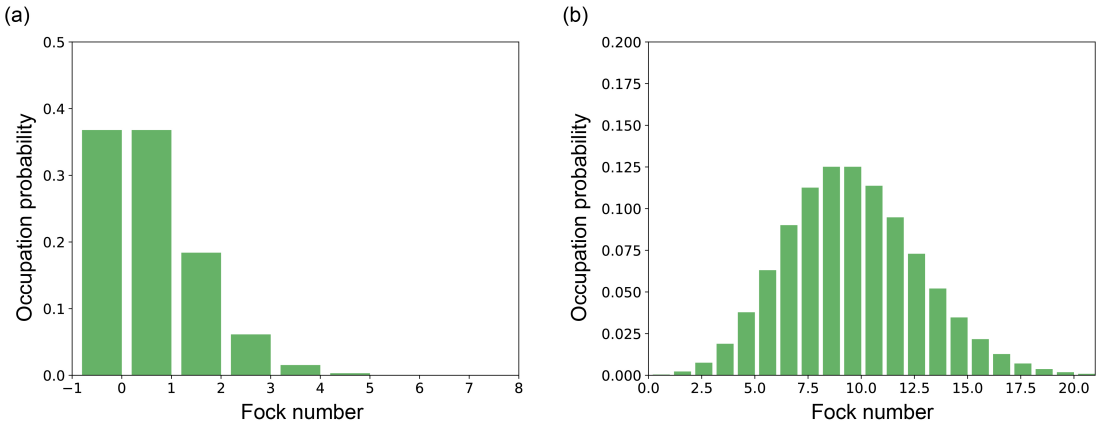

Figure 2.6: Fock state representation of coherent state. Coherent states represented by the Poisson number distribution (Fock basis) for an average of (a) 1 photon, and (b) 10 photons.

$D(\alpha) = e^{|\alpha|^2/2} e^{\alpha a^\dagger} e^{-\alpha^* a}$. Explicitly writing out $a^{\dagger n}|0\rangle$, we get

$$|\alpha\rangle = e^{|\alpha|^2/2} \sum_n \frac{\alpha^n}{\sqrt{n!}} |n\rangle. \tag{2.48}$$

The square of the probability amplitude gives the probability of finding the excitation number n as $p_\alpha(n) = |c_n|^2$, which has Poisson statistics,

$$p_\alpha(n) = e^{-|\alpha|^2} \frac{|\alpha|^{2n}}{n!}. \tag{2.49}$$

From this, we can deduce that a driven harmonic oscillator is in a superposition of number states, with the average number of excitations $\bar{n} = |\alpha|^2$, and standard deviation $\Delta n = \sqrt{\langle n^2 \rangle - \langle n \rangle^2} = \sqrt{\bar{n}}$ [10].

Figure 2.6 shows the probability distribution in the number states basis for 1 and 10 quanta of excitation on average. Note that the relative width of the distribution, $\Delta n/\bar{n}$ becomes progressively smaller as the amplitude of the field increases. This is consistent with our definition. The coherent state is ill-defined for a harmonic oscillator in vacuum state, and becomes more classical as we increase the driving strength.

2.2.3 Coupled Spin-Spring System

From the derivations of spin and field mode previously explored, we can now write the atom-cavity coupling Hamiltonian as

$$H_{\text{coupling}} = -d\left(\vec{\epsilon}_s\sigma_+ + \vec{\epsilon}_s^*\sigma_-\right)\cdot E_0\left(\vec{\epsilon}_c a + \vec{\epsilon}_c^* a^\dagger\right). \tag{2.50}$$

Terms like $\sigma_- a$ and $\sigma_+ a^\dagger$ correspond to highly non-resonant processes and play a minor role compared to the other two terms $\sigma_+ a$ and $\sigma_- a^\dagger$, which correspond to photon emission and absorption processes. Neglecting those non-resonant terms, we can approximate the coupling Hamiltonian as

$$H_{\text{coupling}} = \hbar g(a\sigma_+ + a^\dagger\sigma_-), \tag{2.51}$$

where $g = dE_0|\vec{\epsilon}_s^* \cdot \vec{\epsilon}_c|$ is the vacuum Rabi frequency, which represents the strength of the atom-cavity field coupling. It is proportional to the dipole moment of the atom, the amplitude of the field across the atom, and the polarization alignment between the atom and the field. The first term describes the absorption of energy by the atom from the cavity, and the second term describes the emission of energy from the atom to the cavity. The Hamiltonian describing the coupled system is called the *Jaynes-Cumming Hamiltonian*,

$$H_{\text{JC}} = \hbar\omega_c\left(a^\dagger a + \frac{1}{2}\right) + \hbar\frac{\omega_s}{2}\sigma_Z + \hbar g(a\sigma_+ + a^\dagger\sigma_-). \tag{2.52}$$

The first term represents the energy of the electromagnetic field inside the cavity, the second describes a spin one-half, and the last term is the coupling given by Eq. 2.51. Physical phenomena involving this atom-cavity coupled system has been investigated in atom and superconducting circuit systems [22, 62, 63, 64].

Dispersive Case

When the detuning between the atom and the cavity is large, $\Delta = |\omega_c - \omega_s| \gg g$, there is negligible energy exchange between the subsystems. This regime is called the *dispersive limit* of the Jaynes-Cumming model. Expanding the Jaynes-Cumming Hamiltonian in powers of g/Δ to second order gives

$$H \approx \hbar \left(\omega_c + \frac{g^2}{\Delta}\sigma_Z\right)\left(a^\dagger a + \frac{1}{2}\right) + \hbar\frac{\omega_s}{2}\sigma_Z \tag{2.53}$$

The first term describes a harmonic oscillator with resonant frequency dependent on the state of the atom, $\omega_c' = \omega_c \pm g^2/\Delta$. This frequency shift is called the *dispersive shift*. It can be used to measure the state of the spin in a Quantum Non-Demolition (QND) fashion [10]. This physics has been utilized to realize cavity quantum electrodynamics paradigm in superconducting circuits [22, 23, 62], where a spring (cavity) is used to probe a spin (qubit). Note that the dispersive approximation is only valid at sufficiently low photon number. If the number of cavity excitation exceeds the critical value $n_c = \Delta^2/4g^2$, this approximation breaks down.

The Hamiltonian can also be written to emphasize the dependence of the spin on the number of excitations in the cavity,

$$H \approx \hbar\omega_c\left(a^\dagger a + \frac{1}{2}\right) + \frac{\hbar}{2}\left(\omega_s + \frac{2g^2}{\Delta}a^\dagger a + \frac{g^2}{\Delta}\right)\sigma_Z. \tag{2.54}$$

The spin's effective frequency is dependent on the Lamb shift g^2/Δ and the Stark shift $2g^2n/\Delta$. The Stark shift depends on the number of photons in the cavity, which leads to measurement-induced dephasing in qubits [63, 65]. Moreover, under the dispersive strong condition where the dispersive shift $2g^2/\Delta$ is larger than the qubit's spectroscopy linewidth and dephasing rate, we can use the qubit to query exactly how many photons are in the cavity [64]. This allows QND measurement of the photon number [66].

2.3 Open Quantum Systems

So far we have only discussed ideal, isolated systems for which we have complete knowledge. The state of the system is then said to be a *pure state*. However, that is not always the case, as the system can have interaction with the outside world, and its coherence can be destroyed via the leakage of information to the environment. In this case, the system is in a so-called *mixed state*.

In this section, we discuss the formalism to describe open quantum systems. We first introduce the *density operator*, also known as the *density matrix*, and its properties. The formalism is completely equivalent to the state vector approach, and provides a convenient language to describe a more general quantum state.

2.3.1 The Density Matrix

The density operator language provides a convenient means for describing quantum system that we do not have complete knowledge about. If we have an ensemble of pure quantum states $|\psi_i\rangle$ with corresponding probabilities p_i, then the density operator for the system can be defined as

$$\rho \equiv \sum_i p_i |\psi_i\rangle\langle\psi_i|. \tag{2.55}$$

If the state is known exactly to be in state $|\psi\rangle$, then the density operator can be simply written as $\rho = |\psi\rangle\langle\psi|$. This can also be done by rewriting Eq. 2.55 with one of the p_i equal to 1. Otherwise, when $p_i < 1$, the system is in a mixture of states. The decomposition of ρ in Eq. 2.55 also requires ρ to be positive and have unit trace,

$$\mathrm{Tr}(\rho) = 1. \tag{2.56}$$

We can show that $\mathrm{Tr}(\rho^2) = \sum p_i^2 \leq 1$, with the equality condition only satisfied when ρ is a pure state.

Other important notions in quantum mechanics can be rephrased in density operators language in complete analogy to the state vector approach. The evolution of a system following the unitary operator U obeys

$$\rho = \sum_i p_i |\psi_i\rangle\langle\psi_i| \rightarrow \rho(t) = \sum_i p_i U|\psi_i\rangle\langle\psi_i|U^\dagger = U\rho U^\dagger. \tag{2.57}$$

A measurement following operator M_m will give result m with probability

$$p(m) = \mathrm{Tr}(M_m^\dagger M_m \rho), \tag{2.58}$$

leaving the system in a state described by a density matrix

$$\rho_m = \frac{M_m^\dagger M_m \rho}{\mathrm{Tr}(M_m^\dagger M_m \rho)}. \tag{2.59}$$

If we have multiple quantum systems prepared in state ρ_i, then the joint state of these can be described by the density matrix $\rho = \rho_1 \otimes \rho_2 \otimes ... \otimes \rho_n$. Now, suppose we have physical systems A and B, and the state of the composite system is $\rho_{AB} = \rho_A \otimes \rho_B$. The subsystem A can be analyzed through the reduced density operator ρ_A defined via the partial trace

$$\rho_A \equiv \mathrm{Tr_B}(\rho_{AB}), \tag{2.60}$$

where the partial trace $\mathrm{Tr_B}$ is defined as

$$\mathrm{Tr_B}(\rho_A \otimes \rho_B) = \rho_A \mathrm{Tr_B}(\rho_B) = \rho_A. \tag{2.61}$$

Density Matrix of a Qubit

Let's consider the case of a two-level system with basis states $|0\rangle$ and $|1\rangle$. The density matrix is then a 2×2 Hermitian matrix which generally takes the form

$$\rho = \begin{pmatrix} \rho_{00} & \rho_{01} \\ \rho_{10} & \rho_{11} \end{pmatrix}. \tag{2.62}$$

Its real positive diagonal terms ρ_{00} and ρ_{11}, called *populations*, are the probabilities of finding the qubit in $|0\rangle$ and $|1\rangle$, and thus sum up to unity $\rho_{00} + \rho_{11} = 1$. The off-diagonal terms ρ_{01} and $\rho_{10} = \rho_{01}*$, called *coherences*, are important in determining whether the state is pure or mixed.

The density matrix of a qubit can be expanded onto the Pauli basis as

$$\rho = \frac{1}{2}(I + \vec{r} \cdot \vec{\sigma}), \tag{2.63}$$

where $\vec{r}$ is the Bloch vector for state ρ. Following the definition of a pure state, $\mathrm{Tr}(\rho^2) = 1$, we can deduce that $||\vec{r}|| \equiv (r_x^2 + r_y^2 + r_z^2)^{\frac{1}{2}} = 1$ only for pure states and $||\vec{r}|| < 1$ for mixed states. Thus, the tip of the Bloch vector lies on the surface of the Bloch sphere for pure states, and inside the Bloch sphere for mixed states. The center of the Bloch sphere would then correspond to the maximally mixed state $\rho = I/2$.

While the Bloch sphere is a great way to visualize the state of a qubit, it is not possible to generalize it to multiple qubits. An alternative approach is to plot the density matrix of the system in a *matrix histogram*, as shown in Fig. 2.7 for single-qubit and Fig. 2.8 for two-qubit states. *Hinton* diagrams are also used to describe matrices in the literature. We show some examples of Hinton diagrams in Fig. 2.9, where the density matrices correspond to the four Bell states.

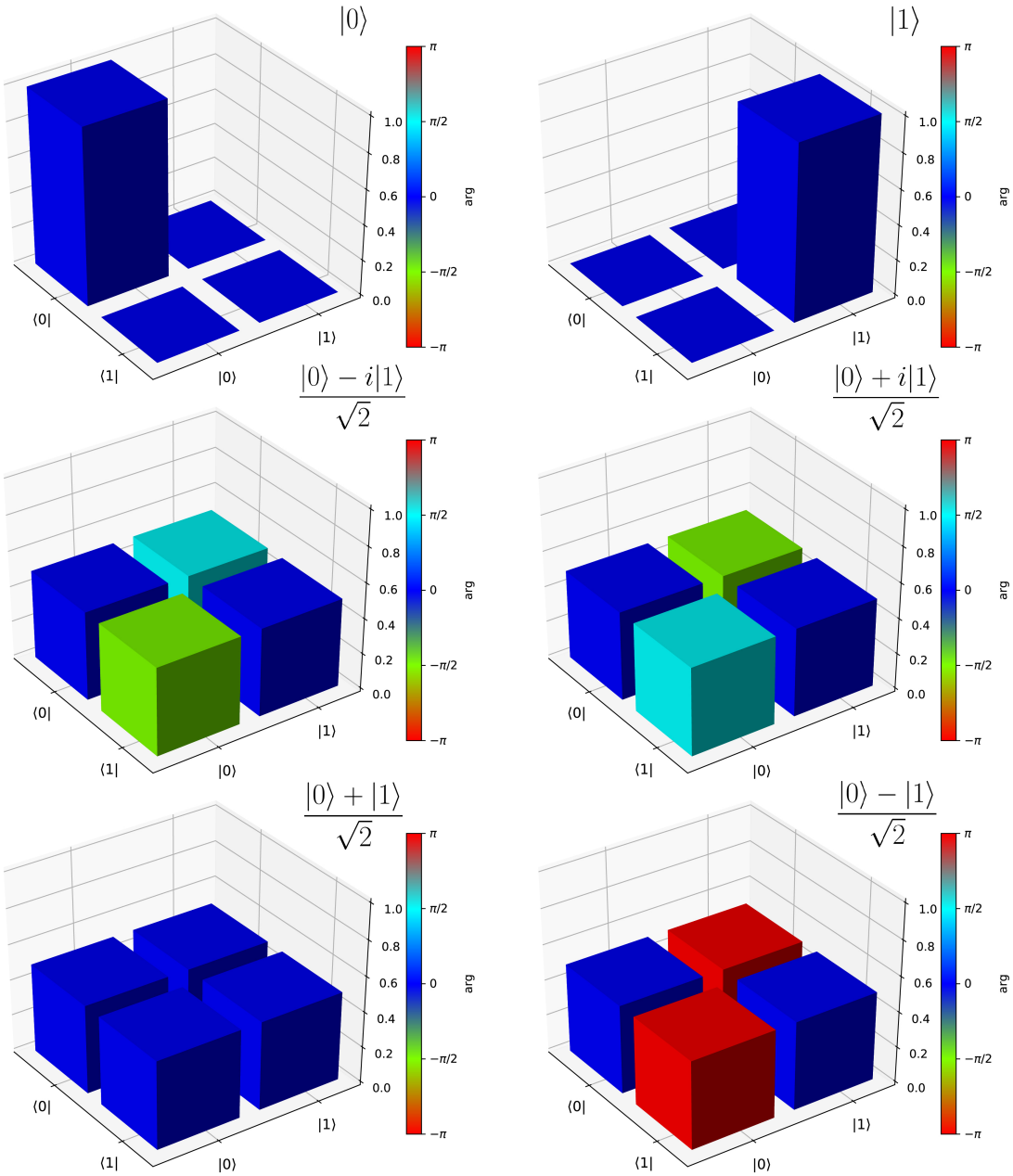

Figure 2.7: Visualizations of single-qubit density matrices. Amplitude and phase of density matrix's entries are presented as the height and color of the bars.

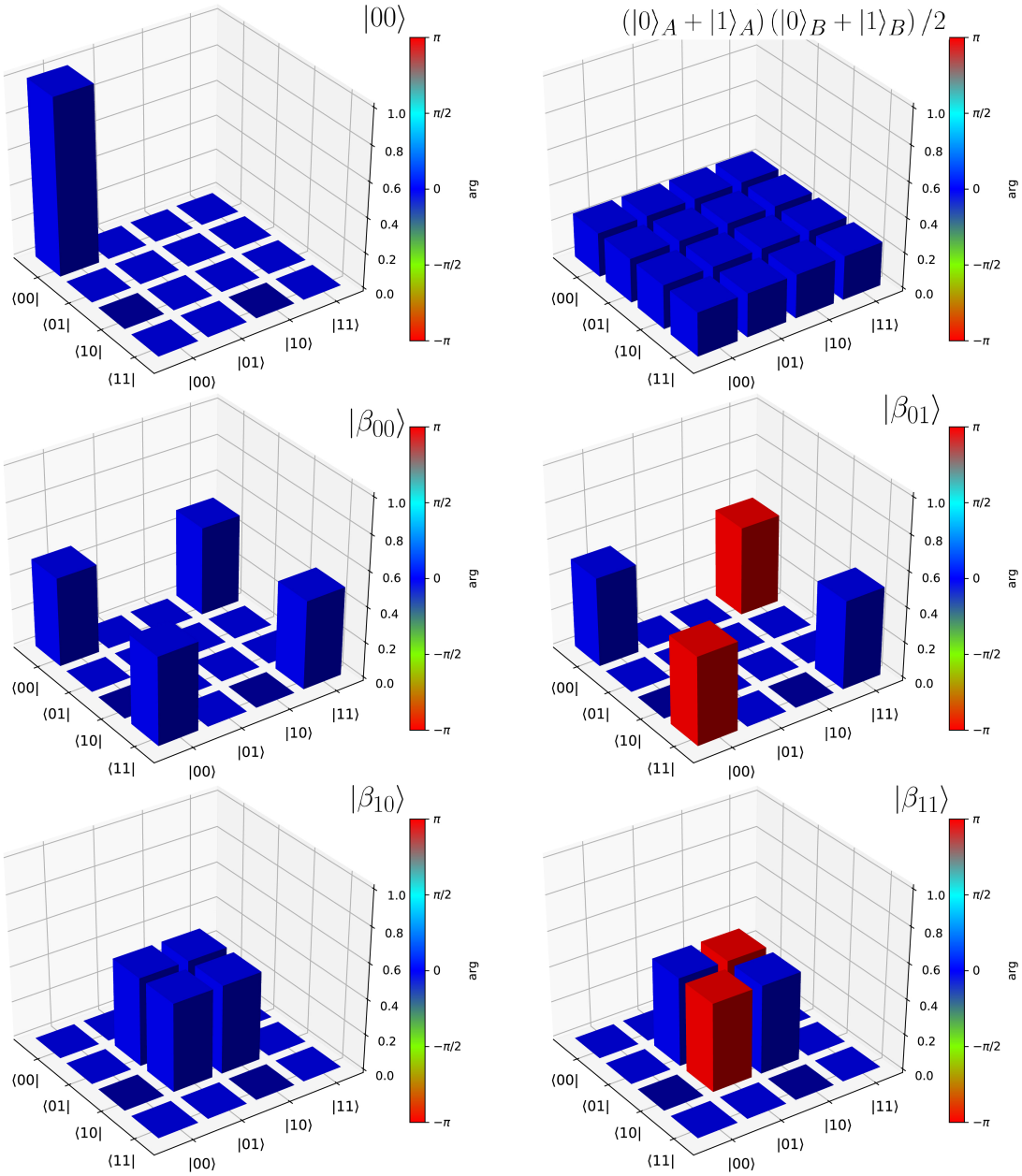

Figure 2.8: Visualizations of two-qubit density matrices. Amplitude and phase of density matrix's entries are presented as the height and color of the bars.

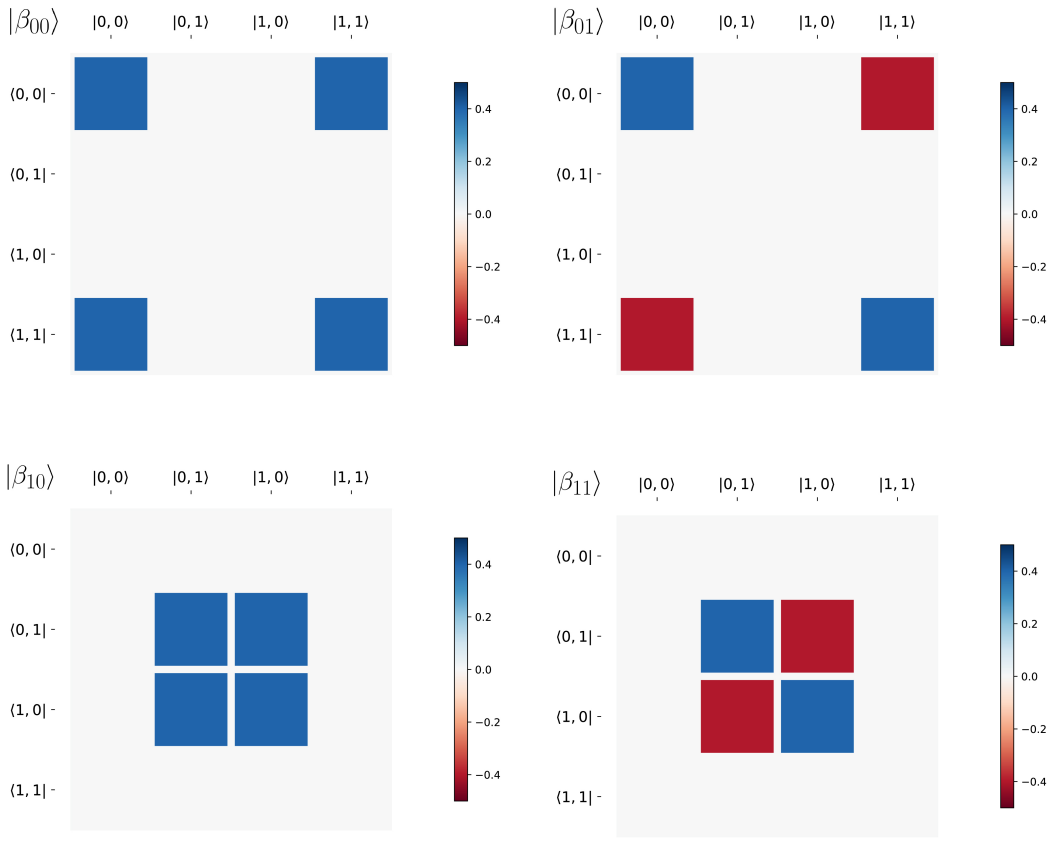

Figure 2.9: Gallery of Hinton diagrams for Bell states. Visualization of qubit states using Hinton diagrams. The opaqueness and colors represent the amplitude and phase of the density matrix' entries. Hinton plots are used interchangeably with the matrix bar plots in the literature.

Quantum State Tomography

Quantum state tomography is the procedure of determining the state of an unknown quantum system via the construction of its density matrix ρ. If we are given just a single copy of ρ then it would be impossible to determine it because we can only measure along one axis at a given time. On the other hand, if we prepare a large ensemble of identical matrices ρ's, then we can perform different measurements along orthogonal axes and determine the ensemble averages of the relevant observables.

For example, we can rewrite the density matrix for the two-level system given in Eq. 2.63 as

$$\rho = \frac{1}{2}\left(I + \langle X\rangle X + \langle Y\rangle Y + \langle Z\rangle Z\right), \tag{2.64}$$

where the expectation values of observables X, Y, Z are obtained by repeating the measurement along the respective axis, given that $\langle\sigma\rangle = \mathrm{Tr}(\sigma\rho)$. In principle, the density matrix of a two-level system has four entries, with one constraint $\mathrm{Tr}(\rho) = 1$, so we have to perform three different measurements to reconstruct ρ.

This formalism can be extended to an n-qubit system,

$$\rho = \frac{1}{2^n}\sum_{\vec{\sigma}}(\langle\vec{\sigma}_1 \otimes \vec{\sigma}_2 \otimes \cdots \otimes \vec{\sigma}_n\rangle\vec{\sigma}_1 \otimes \vec{\sigma}_2 \otimes \cdots \otimes \vec{\sigma}_n). \tag{2.65}$$

For example, the two-qubit density matrix can be written as

$$\begin{aligned}\rho = \frac{1}{4}(&II + \langle IX\rangle IX + \langle IY\rangle IY + \langle IZ\rangle IZ\\ &+ \langle XI\rangle XI + \langle XX\rangle XX + \langle XY\rangle XY + \langle XZ\rangle XZ\\ &+ \langle YI\rangle YI + \langle YX\rangle YX + \langle YY\rangle YY + \langle YZ\rangle YZ\\ &+ \langle ZI\rangle ZI + \langle ZX\rangle ZX + \langle ZY\rangle ZY + \langle ZZ\rangle ZZ).\end{aligned} \tag{2.66}$$

In practice, the measured expectation values are converted from physical measurements, and at least 15 rotations on the pair of qubits must be performed, together with the constraint $\mathrm{Tr}(\rho) = 1$, or $\langle II\rangle = 1$, to reconstruct the two-qubit density matrix. The experimental procedure to reconstruct density matrices is discussed in section 6.4.

Generally, ideal tomography plots, such as those shown in Fig. 2.7 and Fig. 2.8, can be used to compare with experimental data. However, a more rigorous approach is needed to check how close a prepared state and the ideal state are [5]. The first number developed to

measure this closeness between two quantum states ρ and σ is the *trace distance*, defined as

$$D(\rho, \sigma) = \frac{1}{2}\mathrm{Tr}|\rho - \sigma|, \tag{2.67}$$

which is ideally zero for two identical states. The second measure is the *fidelity*. For two quantum states ρ and σ, the fidelity is defined as

$$F(\rho, \sigma) = \mathrm{Tr}\sqrt{\rho^{1/2}\sigma\rho^{1/2}}. \tag{2.68}$$

We note that it is more common in the literature to write the fidelity as

$$F(\rho, \sigma) = \left(\mathrm{Tr}\sqrt{\rho^{1/2}\sigma\rho^{1/2}}\right)^2. \tag{2.69}$$

It is therefore a good idea to clearly state the formula used wherever a fidelity value is quoted. In either case above, we can check that the fidelity for two identical states is 1, and for two orthogonal states is 0.

Eq. 2.68 can be simplified if one of the states is a pure state, which is usually the case when we compute the fidelity. The fidelity between a pure state $|\psi\rangle$ and an arbitrary state ρ can be written as

$$F(\rho, |\psi\rangle) = \sqrt{\langle\psi|\rho|\psi\rangle}. \tag{2.70}$$

Finally, it follows that the trace distance and the fidelity between two quantum states are related,

$$1 - F(\rho, \sigma) \leq D(\rho, \sigma) \leq \sqrt{1 - F(\rho, \sigma)^2}. \tag{2.71}$$

For the special case when one of the states is pure, we get

$$1 - F(|\psi\rangle, \sigma)^2 \leq D(|\psi\rangle, \sigma). \tag{2.72}$$

2.3.2 The Lindblad Master Equation

To describe the evolution of a quantum system described by the density matrix ρ in the presence of a noisy environment, we use the Lindblad master equation [5, 10]:

$$\frac{d\rho}{dt} = -\frac{i}{\hbar}[H, \rho] + \sum_{\mu} \left(L_\mu \rho L_\mu^\dagger - \frac{1}{2} L_\mu^\dagger L_\mu \rho - \frac{1}{2} \rho L_\mu^\dagger L_\mu \right), \tag{2.73}$$

where H is the Hamiltonian describing the quantum system in isolation, and L_μ is the operator describing the effect of the environment on the system.

The derivation of the master equation is based on the Kraus-sum formulation of quantum maps, and the Markov approximation [10]. The Markovian limit assumes that the evolution is local in time, $\langle \rho(t)\rho(t+dt) \rangle = 0$. Let the characteristic timescale of the environment be τ_c, the typical time after which the environment 'forgets' about the information that it has acquired from the system, and subsequent information exchanged between the system and the environment is considered uncorrelated. The other time scale of importance is the long time T_r during which the system evolves. Markovian approximation is then valid for time step τ in which $\tau_c \gg \tau \gg T_r$. In other words, the equation is valid during a time coarse enough for the evolution of the system to be insensitive to any fast environmental fluctuations, but fine enough to describe a quantum evolution over the long time scale of interest.

Equation 2.73 provides a convenient method to simulate and understand the effect of relaxation and decoherence mechanisms on the evolution of a quantum system. First, let's examine a two level system undergoing relaxation from the excited state to the ground at rate $\Gamma_1 = 1/T_1$. The corresponding jump operator is $L_1 = \sqrt{\Gamma_1}\sigma_-$. The master equation

thus becomes

$$\frac{d\rho}{dt} = -i\frac{\omega_{01}}{2}[\sigma_Z, \rho] + \frac{\Gamma_1}{2}\left(2\sigma_-\rho\sigma_+ - \sigma_+\sigma_-\rho - \rho\sigma_+\sigma_-\right). \tag{2.74}$$

Inspecting individual matrix elements of ρ, we find

$$\frac{d\rho_{00}}{dt} = \Gamma_1\rho_{11}, \quad \frac{d\rho_{11}}{dt} = -\Gamma_1\rho_{11}, \quad \frac{d\rho_{10}}{dt} = -i\omega_{01}\rho_{10} - \frac{\Gamma_1}{2}\rho_{10}. \tag{2.75}$$

Hence, during the relaxation process, the qubit's population transfers from the excited state to the ground state at rate Γ_1, and the off-diagonal coherences decay at rate $\Gamma_1/2$. The decay rate Γ_1 can be obtained via *Fermi's golden rule*, which is discussed in more details in Appendix A.

In general, a qubit can undergo both emission and absorption processes in a thermal environment, both of which induce relaxation to equilibrium, which is a mixed state of $|0\rangle$ and $|1\rangle$ with populations in each state determined by the effective temperature of the bath. The jump operators can be modified as $L_\downarrow = \sqrt{\Gamma_\downarrow}\sigma_-$ and $L_\uparrow = \sqrt{\Gamma_\uparrow}\sigma_+$ to describe the relaxation by emission and excitation by absorption processes, respectively. The rates $\Gamma_\uparrow$ and $\Gamma_\downarrow$ must obey the detailed balance relation,

$$\Gamma_\uparrow = \Gamma_\downarrow e^{-\hbar\omega_{01}/k_B T_{\text{eff}}}. \tag{2.76}$$

We can check that the resulting master equation now includes two jump processes, one corresponding to relaxation with rate $\Gamma_\downarrow$ described by Eq. 2.74, and the other correspond to excitation process with rate $\Gamma_\uparrow$. Combination of these gives a decay rate $\Gamma_1 = \Gamma_\uparrow + \Gamma_\downarrow = \Gamma_\downarrow\left(1 + e^{-\hbar\omega_{01}/k_B T_{\text{eff}}}\right)$, the rate at which an excited qubit returns back to equilibrium. The relaxation rate Γ_1 corresponds to depolarization along the qubit quantization axis, as depicted in Fig. 2.10(a).

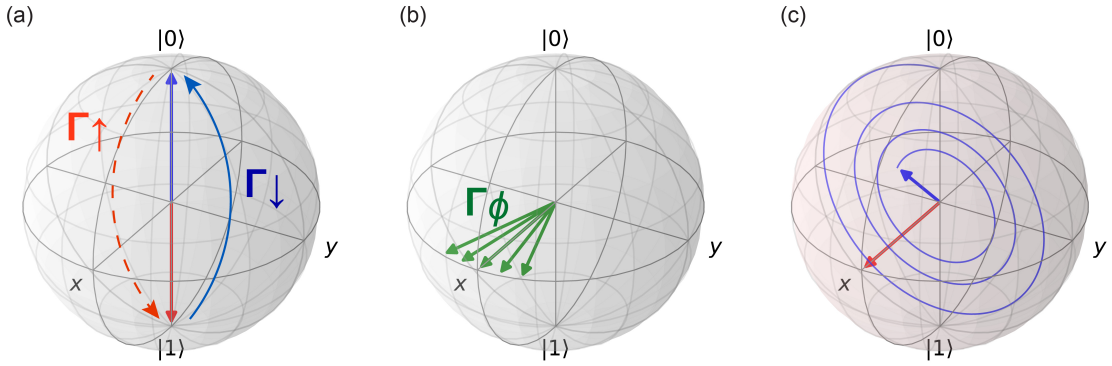

Figure 2.10: Decoherence processes. (a) Relaxation is the process in which the state of the qubit is flipped. At finite temperature, the qubit effectively relaxes to an equilibrium mixture of $|0\rangle$ and $|1\rangle$. (b) Pure dephasing is the process during which we lose track of the phase of the state vector due to the fluctuation of the qubit's parameters. The resulted averaged state vector after dephasing will have amplitude less than unity, its tip lying inside the Bloch sphere. (c) Rabi oscillation when there is decoherence.

The qubit may also undergo a pure dephasing process, corresponding to the jump operator $L_\phi = \sqrt{\Gamma_\phi/2}\sigma_Z$. As depicted in Fig. 2.10(b), this process happens because we lose track of the qubit's information over a certain time scale at rate Γ_ϕ, due to the fluctuations of the qubit transition frequency in time. When we average the fluctuations, the resulting Bloch vector will have a reduced amplitude with its tip lying inside the Bloch sphere. The master equation for this case can be written as

$$\frac{d\rho}{dt} = -i\frac{\omega_{01}}{2}[\sigma_Z, \rho] + \frac{\Gamma_\phi}{2}\left(\sigma_Z\rho\sigma_Z - \rho\right), \tag{2.77}$$

resulting in

$$\frac{d\rho_{01,10}}{dt} = \mp i\omega_{01}\rho_{01,10} - \Gamma_\phi\rho_{01,10}. \tag{2.78}$$

The coherence of the qubit thus decays at rate Γ_ϕ. Under both relaxation and pure dephasing, the resulting decoherence rate can be written as the sum of both processes, $\Gamma_2 = \Gamma_1/2 + \Gamma_\phi$.

The effect of decoherence on gate operations can be visualized as follows. As shown in

Fig. 2.10(c), due to our losing track of the qubit's trajectory, the applied drive does not rotate the qubit in a circle anymore. Rather, the state vector's amplitude becomes progressively smaller, until all the information about it is lost, and the state becomes completely mixed. That's primarily how decoherence introduces error during gate operation. Dephasing of qubits in the rotating frame is discussed in ref. [67].

Quantum Process Tomography

An important task in experimental quantum physics is to characterize quantum processes. Assume that we are given information on the input and output states coming in and out of a quantum circuit, how should we proceed to determine what has been done inside this circuit? The answer can be obtained following a procedure called quantum process tomography [68, 69].

A quantum operation is a linear map $\mathcal{E}$ describing the change of the quantum system such that

$$\rho \to \mathcal{E}(\rho). \tag{2.79}$$

In the operator-sum representation, the quantum map $\mathcal{E}$ can be written as

$$\mathcal{E}(\rho) = \sum_i E_i \rho E_i^\dagger, \tag{2.80}$$

where $\{E_i\}$ completely takes in account the state changes, with $\sum_i E_i^\dagger E_i = I$. To relate $\{E_i\}$ to measurable parameters, we can consider an equivalent description of $\mathcal{E}$ using $\{\tilde{E}_i\}$ which form a basis set of operators. $\{E_i\}$ can be expanded on the $\{\tilde{E}_i\}$ basis, $E_i = \sum_m e_{im}\tilde{E}_m$, and we can write

$$\mathcal{E}(\rho) = \sum_{mn} \tilde{E}_m \rho \tilde{E}_n^\dagger \chi_{mn}, \tag{2.81}$$

where $\chi_{mn} = \sum_i e_{im} e_{in}^*$ are complex entries of a matrix, simply called the χ *matrix*. The

central task we must accomplish in quantum process tomography is to determine χ. The reason is because the quantum map $\mathcal{E}$ in the operator basis $\{\tilde{E}_i\}$ can be fully described by this χ matrix.

A general linear map between two $d \times d$ complex matrices is described by d^4 independent parameters. However, there are d^2 constraints from the completeness relation $\sum_i E_i^\dagger E_i = I$, so χ contains $d^4 - d^2$ independent parameters ($d = 2^n$, where n is the number of qubits).

Mathematically, χ can be computed for any unitary operation using Eq. 2.81. We can simply expand the operation on the operator basis, and find χ using the complex coefficients e_{im}. Experimentally, we determine χ by first preparing a set of linearly independent input states, $\{\rho_j\}$, then applying the quantum map $\mathcal{E}$ on the input states to get $\mathcal{E}(\rho_j) = \rho'_j$. Finally, we can determine the output states ρ'_j using quantum state tomography. Then, we can reconstruct χ using linear algebra techniques.

The first step is to expand ρ'_j as a linear combination of the basis states,

$$\rho'_j = \sum_k \lambda_{jk} \rho_k, \tag{2.82}$$

from which the coefficients λ_{jk} can be extracted experimentally, $\lambda_{jk} = \mathrm{Tr}(\rho_k \rho'_j)$. Next, we may write

$$\tilde{E}_m \rho_j \tilde{E}_n = \sum_k \beta_{jk}^{mn} \rho_k, \tag{2.83}$$

where β_{jk}^{mn} are complex numbers which can be extracted using the trace operation. We can then write

$$\sum_{mn} \beta_{jk}^{mn} \chi_{mn} = \lambda_{jk}, \tag{2.84}$$

from which the χ matrix can be reconstructed. We can compute λ as a vector, β as a $d^4 \times d^4$ matrix with columns indexed by mn and rows by jk, then invert $\kappa = \beta^{-1}$ to get $\chi = \kappa \cdot \lambda$. This gives χ as a vector, which, in the final step, can be reshaped into a $d^2 \times d^2$ matrix.

Ideal χ matrices for single-qubit gates based on the $\{I, X, Y, Z\}$ operator basis are shown

in Fig. 2.11(a, b). In addition to unitary operation, we can simulate the output density matrix resulted from energy relaxation and pure dephasing by utilizing the master equation (Eq. 2.73). The results are shown in Fig. 2.11(c-f).

Process tomography χ matrices for two-qubit CNOT and CZ entangling gates based on the $\{\{I, X, Y, Z\}^{\otimes 2}\}$ operator basis are shown in Fig. 2.12. To reconstruct χ for two-qubit gates, a set of 16 input states are prepared, and each resulting output state can be determined by quantum state tomography. Linear inversion of Eq. 2.84 results in a χ vector with length equal to $d^2 = 256$, which is then reshaped into a 16×16 matrix.

Similar to state fidelity, we can write the process fidelity based on the experimentally obtained χ matrix and the expected χ_{ideal} matrix as

$$F(\chi, \chi_{\text{ideal}}) = \left(\text{Tr}\sqrt{\chi^{1/2}\chi_{\text{ideal}}\chi^{1/2}} \right)^2. \tag{2.85}$$

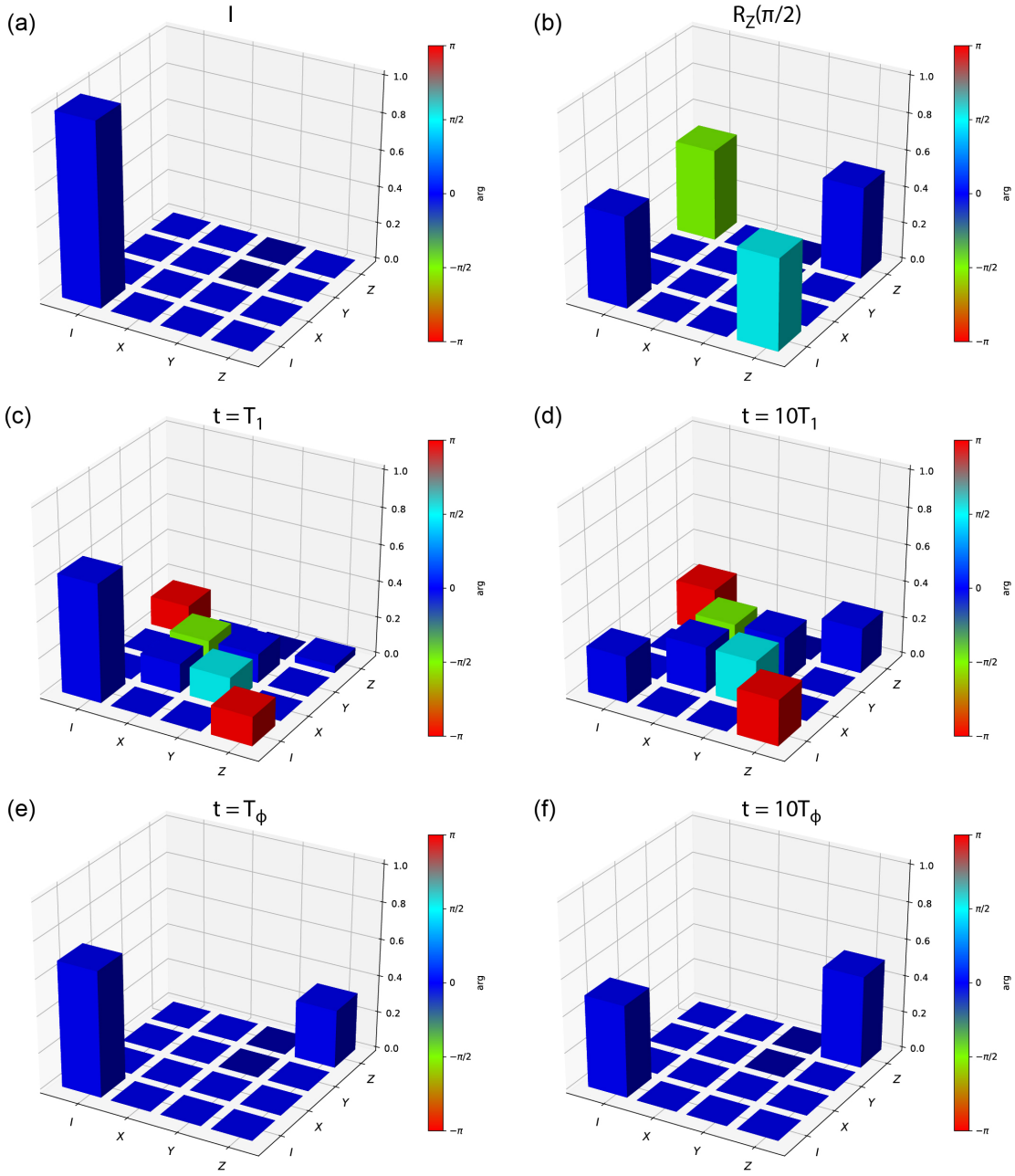

Figure 2.11: χ matrices for single-qubit gates. Quantum process tomography χ matrix corresponding to (a) identity gate, (b) $R_Z(\pi/2)$ gate, (c) relaxation process at $t = T_1$, (d) relaxation process at $t = 10T_1$, (e) pure dephasing process at $t = T_\phi$, (f) pure dephasing at $t = 10T_\phi$. The χ matrices are based on the {I,X,Y,Z} operator basis.

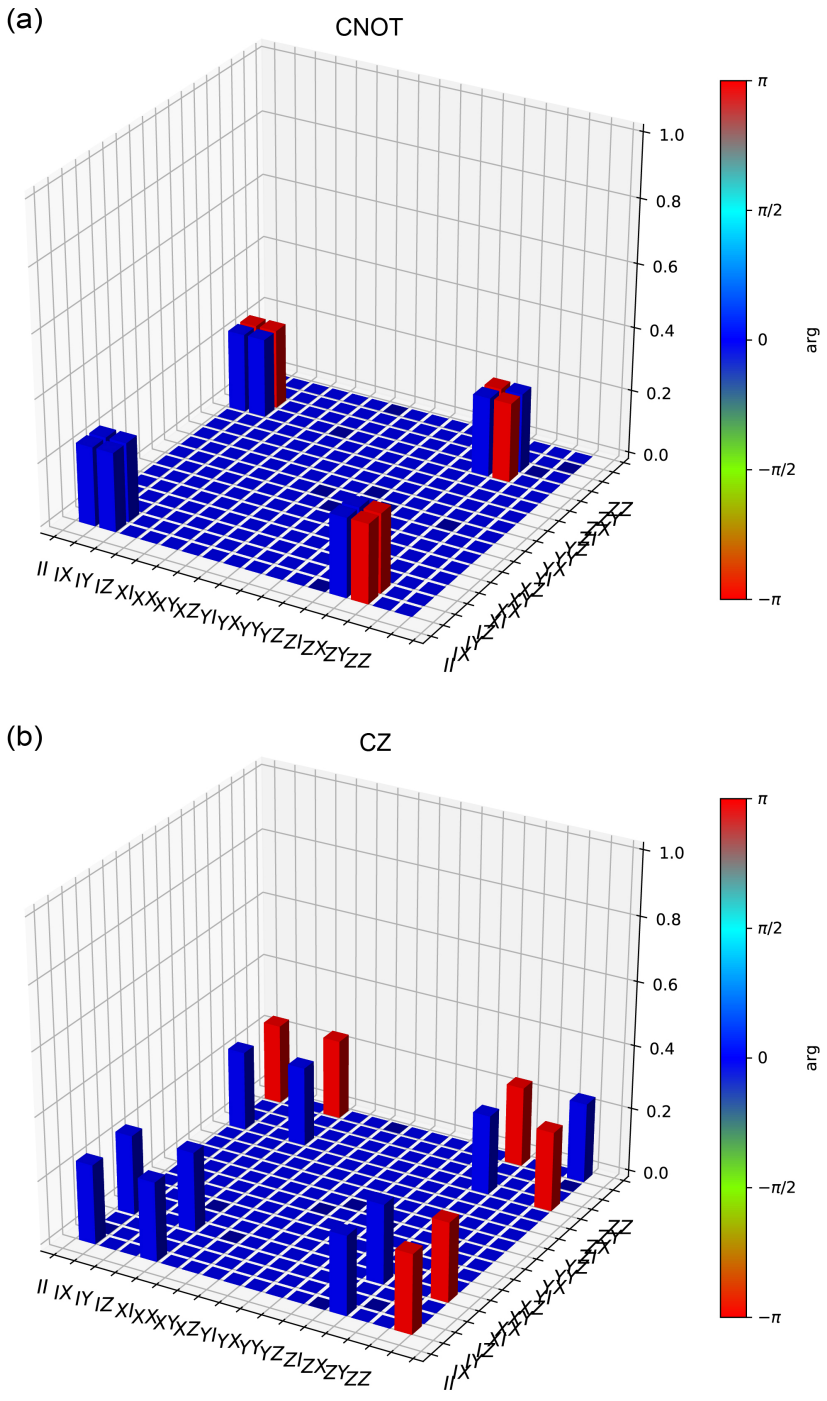

Figure 2.12: χ matrices for two-qubit gates. (a) χ matrix for CNOT gate. (b) χ matrix for CZ gate. Both are based on the $\{\{I, X, Y, Z\}^{\otimes 2}\}$ operator basis.

Chapter 3

Superconducting Circuits: Macroscopic Artificial Atoms

Many years later, as he faced the firing squad, Colonel Aureliano Buendia was to remember that distant afternoon when his father took him to discover ice.

Gabriel Garcia Marquez

In the previous chapter, we introduced cavity quantum electrodynamics in an abstract manner. The formalism can be applied to construct powerful quantum machines whose degrees of freedom are described by quantum operators. Now, we are going to explore specific realization of atoms and photons. Our artificial atoms are made of macroscopic circuit elements , inductors and capacitors, plus a special ingredient: the Josephson junction.

Superconducting circuits are much larger than the usual microscopic atoms, with circuits' dimensions in the μm to mm scale, compared to the ytterbium atom's Van der Waals radius of 228 pm. Although these circuits are usually visible to the naked eye, their currents and voltages, behave like quantum mechanical variables [70]. These circuits can be

designed and fabricated at will to create different kinds of resonators that store microwave photons and artificial atoms that have specific quantized energy levels. With breakthroughs in circuit designs, lithography techniques, and clever engineering in microwave readout and control, quantum processors based on superconducting circuits have been successfully constructed [71, 72] and their performances, quantified by *quantum volume* [73], have been continuously improved. Recently, a claim was made that *quantum supremacy* has been achieved in a programmable superconducting quantum processor [42, 43, 26].

The chapter is organized as follows. We first review the basics of superconductivity and the Josephson effects in section 3.1. We discuss common decoherence processes in superconducting circuits in section 3.2. The chapter ends with a brief discussion of quantum gates and readout in section 3.3.

3.1 Constructing Superconducting Circuits

3.1.1 Superconductivity

Upon thinking about building electrical circuits, the first element that may come to one's mind is the resistor. However, with resistance comes dissipation, which would cause energy relaxation and destroy the coherence property of qubits. In order to reveal the quantum nature of electrical circuits, we have to get rid of resistance in the circuits as much as possible.

Fortunately, superconductivity was discovered at the beginning of the last century, a phenomenon in which the resistance of certain metals vanishes at low temperatures. In 1911, while studying the temperature dependence of mercury's resistivity, the research group leaded by Heike Kamerlingh Onnes at Leiden Laboratory discovered that at a certain temperature $\mathrm{T_c} \approx 4$ K, the resistance of the mercury sample dropped to zero and could not be measured at any temperature below $\mathrm{T_c}$. At first, it was thought to be a fluke due to some broken equipment, but repeated measurements yielded consistent results, and

the same phenomenon was found in other metals soon after: superconductivity was real. Materials exhibiting superconductivity are called *superconductors* [74].

It was found later that superconductivity depends not only on the temperature of the sample, but also on the magnetic field around it, the critical value of which is denoted as $\mathrm{H_c}$. When the field amplitude is higher than $\mathrm{H_c}$, superconductivity is destroyed. Interestingly, when a magnetic field with an amplitude less than the critical value is applied to a bulk type I superconductor cooled down to $\mathrm{T} < \mathrm{T_c}$, the said field is expelled from the sample, regardless of the field condition in which the sample is cooled down. This is the Meissner-Ochsenfeld effect [75].

There is yet another profound magnetic field effect associated with superconductors. Consider a superconducting ring cooled down through its critical temperature in the presence of a magnetic field. Since the current can persist in an infinitely long time, it can sustain a permanent magnetic flux. If we switch off the magnetic field after, such current can keep the field going through the loop at the initial level. However, it turns out that the resulting magnetic flux can only take on values that are an integer multiples of the *magnetic flux quantum* $\Phi_0 = h/2e \approx 2.067 \times 10^{-15}\ \mathrm{T} \cdot \mathrm{m}^2$. The physical quantities h and e are the Planck's constant and electron charge, respectively.

Explaining these phenomena proved to be challenging. Early phenomenological equations proposed by the London brothers could describe perfect conductivity and the Meissner effect [76]. However, later attempts to explain superconductivity at a fundamental level were unsuccessful, including those by prominent scientists [77]. The most successful theory so far is the BCS theory, named after John Bardeen, Leon Cooper, and John Schrieffer [78]. It shows that weak attractive interaction between electrons mediated by electron-phonon interaction results in the formation of bound pairs of electrons having equal and opposite momentum and spin. These so-called *Cooper pairs* are the long-anticipated superconducting charge carriers [75]. The BCS theory explains superconductivity in aluminum which is largely used to fabricate superconducting qubits.

3.1.2 Circuit Quantization

With resistance in the circuit naively taken care of by superconductivity, let us consider a circuit constructed from an inductor and a capacitor in parallel. We can assume the lumped element limit, i.e. the physical size of the circuit (sub-mm) is much smaller than the wavelength of electromagnetic waves of interest, namely of the resonant modes of the circuit under consideration (cm).

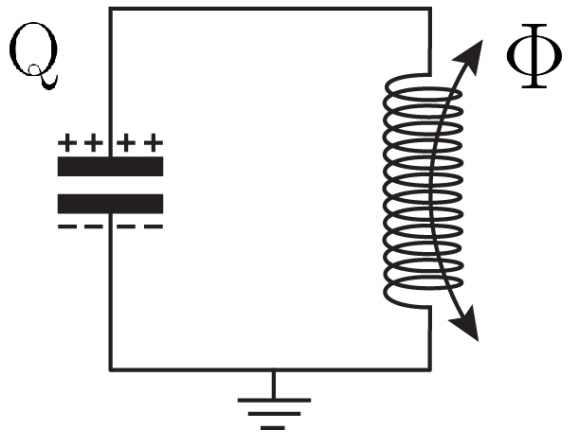

Figure 3.1: LC circuit diagram. The two dependent degrees of freedom are the electric charge accumulated on the capacitor and the magnetic flux threading the inductor.

The classical current-flux relation for an inductor and voltage-charge relation for a capacitor are

$$LI = \Phi, \quad CV = Q. \tag{3.1}$$

Also note that the time derivative of flux and charge are voltage and current, respectively,

$$\dot{\Phi} = V, \quad \dot{Q} = I. \tag{3.2}$$

The magnetic inductive energy E_L stored inside an inductor with inductance L can be found

from the electrical power P,

$$dE_L = Pdt = VIdt = \dot{\Phi}\frac{\Phi}{L}dt = \frac{\Phi}{L}d\Phi, \tag{3.3}$$

so by integration in flux, we get $E_L = \Phi^2/2L$. Similarly, for a capacitor with capacitance C,

$$dE_C = \frac{Q}{C}\dot{Q}dt = \frac{Q}{C}dQ, \tag{3.4}$$

SO the electric charging energy stored is $E_C = Q^2/2C = C\dot{\Phi}^2/2$. For now, we relate the electric energy and magnetic energy in an LC oscillator to the kinetic energy and potential energy in a mechanical oscillator, respectively. The convenience of this choice will become clear later. We can then write the Lagrangian of the oscillator as

$$\mathcal{L} = \frac{C\dot{\Phi}^2}{2} - \frac{\Phi^2}{2L}. \tag{3.5}$$

Comparing Eq. 3.5 with the Lagrangian of a mechanical oscillator,

$$\mathcal{L}_{\text{mech}} = \frac{m\dot{x}^2}{2} - \frac{kx^2}{2}, \tag{3.6}$$

we can interpret the capacitance C as an effective mass m, and the inductor L as the inverse of an effective spring constant k. The classical Hamiltonian can be derived using the Legendre transformation,

$$Q = \frac{\partial\mathcal{L}}{\partial\dot{\Phi}} = C\dot{\Phi}, \qquad H = \dot{\Phi}\frac{\partial\mathcal{L}}{\partial\dot{\Phi}} - \mathcal{L} = \frac{Q^2}{2C} + \frac{\Phi^2}{2L}. \tag{3.7}$$

To describe a quantum LC oscillator, we have to promote the charge and flux variables to quantum operators. By analogy, $\hat{p} \to \hat{Q}$, $\hat{x} \to \hat{\Phi}$, the proper commutation relation is [70]

$$\left[\hat{\Phi}, \hat{Q}\right] = i\hbar. \tag{3.8}$$

We can also check that the classical coordinates satisfy the Poisson bracket $\{\Phi, Q\} = 1$. In the rest of the thesis, charge and flux are quantum operators, and the hat above the notations is omitted for simplicity.

For convenience, we define here the unit-less quantum operators *reduced flux* $\phi \equiv 2\pi\Phi/\Phi_0$ and *charge number* $n = Q/2e$. We proceed to write the charging energy as $E_C = e^2/2C$ and the inductive energy as $E_L = (\phi_0)^2/L$, where $\phi_0 = \Phi_0/2\pi = \hbar/2e$ is the *reduced flux quantum*. The new operators satisfy the commutation relation $[\phi, n] = i$. The Hamiltonian then takes the form

$$H = 4E_C n^2 + \frac{1}{2}E_L\phi^2. \tag{3.9}$$

Following the procedure introduced in section 2.2, we can write the Hamiltonian and operators of an LC oscillator in terms of the creation and annihilation operators. Let us introduce

$$\begin{aligned} \Phi_{\text{ZPF}} &= \sqrt{\frac{\hbar Z}{2}} = \phi_o \left(\frac{2E_C}{E_L}\right)^{\frac{1}{4}}, \\ Q_{\text{ZPF}} &= \sqrt{\frac{\hbar}{2Z}} = e \left(\frac{E_L}{2E_C}\right)^{\frac{1}{4}}. \end{aligned} \tag{3.10}$$

One can check that $\langle 0|\Phi^2|0\rangle = \Phi^2_{\text{ZPF}}$, $\langle 0|Q^2|0\rangle = Q^2_{\text{ZPF}}$, and $\Phi_{\text{ZPF}}Q_{\text{ZPF}} = \hbar/2$. We can write

$$\begin{aligned} \Phi &= \Phi_{\text{ZPF}}\left(a^\dagger + a\right), \\ Q &= iQ_{\text{ZPF}}\left(a^\dagger - a\right), \\ H &= \frac{Q^2}{2C} + \frac{\Phi^2}{2L} = \hbar\omega\left(a^\dagger a + \frac{1}{2}\right). \end{aligned} \tag{3.11}$$

Since we will primarily use the reduced flux ϕ and charge number n operators expressions,

it is useful to write them explicitly as well,

$$\begin{aligned} \phi &= \frac{1}{\sqrt{2}} \left(\frac{8E_C}{E_L} \right)^{\frac{1}{4}} (a^\dagger + a), \\ n &= \frac{i}{\sqrt{2}} \left(\frac{E_L}{8E_C} \right)^{\frac{1}{4}} (a^\dagger - a). \end{aligned} \tag{3.12}$$

Although the circuit is quantum, when we drive such a harmonic oscillator with a field on resonant with $\omega = 1/\sqrt{LC}$, the oscillator is put in a superposition of number-basis states called the coherent state, no matter how small the field amplitude is, as shown in section 2.2. In order to realize a two level system and control a single quantum of energy, some non-linear element is needed to build up anharmonicity in the circuit.

3.1.3 Josephson Effects

1962 was a remarkable year, witnessing the birth of Walmart, Kmart, Spiderman, Motel 6, Evander Holyfield, Demi Moore, Jodie Foster, and others. Within a short time span of 12 months, the first men were put into space, Launcher IV crashed on the moon surface, Brazil won the World Cup the second time in a row, and plastic surgeons performed silicone breast implant for the first time. However, in our opinion, the most significant event taking place that year was the submission of a theoretical paper by Brian Josephson to Physics Letters [79]. The paper predicted the Josephson effects, which we briefly review below.

Consider a thin layer of insulator sandwiched between two slabs of superconductors. A supercurrent can flow through the junction, given by

$$I(\phi) = I_c \sin(\phi), \tag{3.13}$$

where I_c is the maximum current the junction can sustain, and ϕ is defined formally as the gauge-invariant superconducting phase difference between the two superconducting islands. For all practical purposes, it can be interpreted as the normalized flux we defined

previously, hence the same notation. This is the DC Josephson effect [79].

If a voltage V is maintained across the junction, the phase difference ϕ would obey the relation

$$V = \frac{\Phi_0}{2\pi}\frac{d\phi}{dt}, \tag{3.14}$$

This is the AC Josephson effect. By taking the time derivative of Eq. 3.13 and expressing $d\phi/dt$ in terms of V using Eq. 3.14, we can show that the junction acts as if it has an inductance,

$$L(\phi) = \frac{V}{dI/dt} = \frac{\Phi_0}{2\pi I_c \cos\phi} = \frac{L_J}{\cos\phi}. \tag{3.15}$$

Thus, the Josephson junction can be modeled as a non-linear inductor which varies as a function of ϕ with amplitude $L_J = \Phi_0/2\pi I_c$. The energy associated with this circuit element can be found as if it is associated with an inductor,

$$E = \int_t IV\,dt = \frac{I_c\Phi_0}{2\pi}\int_\phi \sin\phi d\phi = -E_J\cos\phi. \tag{3.16}$$

In Eq. 3.16, we have omitted the constant term after the integration step. In practice, this constant energy is not important because we can only probe the difference between energy levels. Here, $E_J = \frac{I_c\Phi_0}{2\pi}$ is called as the *Josephson energy*.

In a circuit, the Josephson junction is visualized as shown in Fig. 3.2(b). Note that a physical junction has a self-shunting capacitance due to electric field in the tunnel oxide, so it is more often interpreted as a parallel circuit consisting of a capacitor and a Josephson element discussed above.

We can write the Hamiltonian for a circuit consisting of an inductor, a capacitor, and a Josephson junction in parallel as

$$H = 4E_C n^2 + \frac{1}{2}E_L\phi^2 - E_J\cos(\phi + \phi_{\text{ext}}), \tag{3.17}$$

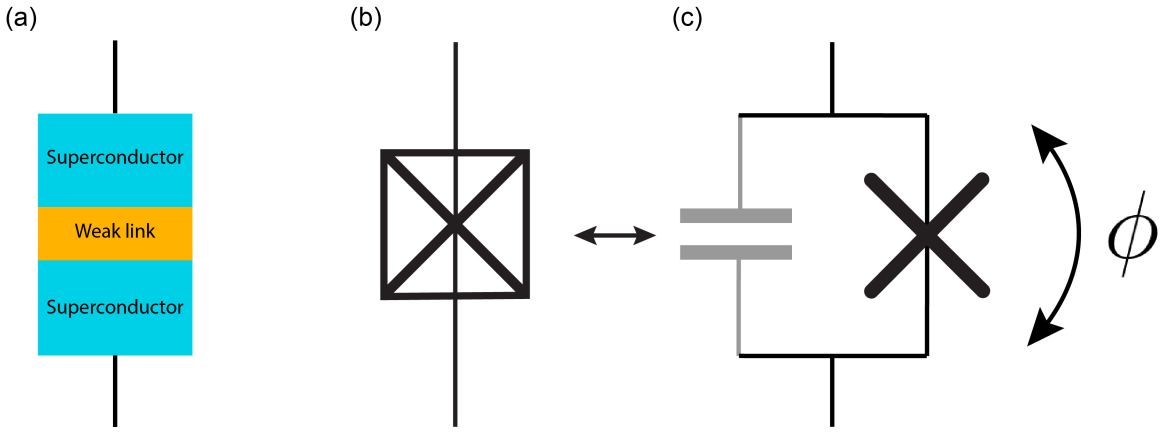

Figure 3.2: Josephson junction. (a) A tunneling junction is constructed from a weak link sandwiched between two superconductors. (b) Circuit representation of a Josephson junction: a cross surrounded by a box. (c) In practice, a Josephson junction has a small self-capacitance, so it can be interpreted as a parallel circuit consisting of a capacitor with a Josephson element.

where $\phi_{\text{ext}} = 2\pi \frac{\Phi_{\text{ext}}}{\Phi_0}$ is the reduced external flux achieved by threading the circuit with a magnetic field. It is of course only available in circuits with a closed loop. The three parameters E_C, E_L, E_J can be adjusted by changing the geometry of the circuit elements. Different combinations of these parameters correspond to various species of superconducting qubits with distinct properties [18, 80].

3.2 Decoherence in Superconducting Circuits

Superconducting circuits are macroscopic in size, and hence they are typically surrounded by more impurities and coupled to noise sources more strongly compared to microscopic ions and atoms, leading to relatively lower coherence times. This section discusses common decoherence mechanisms in superconducting circuits and how to model their effects on qubit performances. We also briefly review relevant methods to mitigate 1/f noise [81, 54].

3.2.1 Energy Relaxation

Dielectric Loss

Dielectric loss is attributed to material imperfections in the dielectric materials near the qubit. It is believed that the relaxation process occurs via the qubit's coupling to two level fluctuators present in the oxide surface interfaces between different layers of the circuit [30]. This material imperfection can be modeled by introducing a capacitor with complex dielectric constant $\epsilon = \epsilon' + i\epsilon''$. A quantity called *dielectric loss tangent* can be defined as $\tan\delta_d = \epsilon''/\epsilon'$. For example, an electromagnetic wave that propagates along x in a lossy material with finite loss tangent has a complex wave number $k = k_r + ik_i$. The wave decays as $e^{-k_i x} = e^{-k_r \tan\delta_d x}$, so the smaller the loss tangent, the further it can propagate.

A cavity resonator filled with a lossy material having permittivity $\epsilon = \epsilon' + i\epsilon''$, and suffering no other loss, would have a quality factor equal to the inverse of the dielectric loss tangent, $Q = \tan^{-1}\delta_d$ [82]. If the cavity is only partially filled with a lossy medium, then only the electric field inside the material contributes to energy loss. This is the case for a resonator or qubit with a thin layer of oxide on top of the metal surface. The effective quality factor Q_{diel} is then [30]

$$\frac{1}{Q_{\text{diel}}} = \sum_i \frac{p_i}{Q_i}, \tag{3.18}$$

where p_i is the *participation ratio* of material i with quality factor $Q_i = \frac{1}{\tan\delta_i}$. The relaxation time T_1 is directly related to the effective quality factor Q_{diel}, so we shall only consider this quantity in our general analysis of dielectric loss.

Relaxation process corresponding to a lossy shunting admittance model [70, 83] is derived using Fermi's golden rule in Appendix A,

$$\Gamma_{ij}^{\alpha} = \frac{1}{\hbar^2}|\langle j|\hat{O}|i\rangle|^2 S_\alpha(\omega_{ij}),$$

where $\hat{O}$ is the quantum operator that couples the system to the noise, and $S_\alpha(\omega_{ij})$ is the

noise spectral density of noise α that causes the decay at qubit transition frequency ω_{ij},

$$S_\alpha(\omega) = \hbar\omega \mathrm{ReY}_\alpha(\omega)\left[\coth\left(\frac{\hbar\omega}{2k_BT}\right)+1\right]. \tag{3.19}$$

To model the admittance $\mathrm{Y_{diel}}$ associated with dielectric loss, consider a capacitor filled with lossy dielectric medium. The complex dielectric constant gives rise to a complex effective capacitance $C_{\mathrm{eff}} = C(1+i\tan\delta_d)$, with the capacitance C related to the charging energy, $\mathrm{E_C} = e^2/2C$. The admittance of the capacitor can be written as $Y_{\mathrm{diel}} = i\omega C(1+i\tan\delta_d)$, from which we have

$$\mathrm{ReY_{diel}} = \frac{\omega C}{Q_{\mathrm{diel}}}. \tag{3.20}$$

The decay rate of transition $i \to j$ at zero temperature $T = 0$ can thus be written as

$$\Gamma_{ij}^{\mathrm{diel}} = \frac{2}{\hbar}|\phi_o\langle j|\phi|i\rangle|^2\frac{\omega_{ij}^2 C}{Q_{\mathrm{diel}}}. \tag{3.21}$$

Flux Noise Dissipation

It has been reported that flux noise with 1/f spectrum is responsible for energy relaxation in flux qubits at low frequencies [54, 84]. The noise couples to the qubit via the persistent current $I_p = \Phi/L$ and would cause the qubit to decay at a rate [84]

$$\begin{aligned}\Gamma_{ij}^{\Phi} &= |\langle j|I_p|i\rangle|^2 S_\Phi(\omega_{ij}) \\ &= \frac{1}{2e^2}\frac{1}{L^2}|\langle j|\phi|i\rangle|^2 S_\Phi(\omega_{ij}).\end{aligned} \tag{3.22}$$

Since the inductance in fluxonium is three orders of magnitude higher than in flux qubits ($L = 100-200$ nH compared to $L \approx 0.5$ nH) , this loss mechanism has negligible effect on fluxonium.

Quasiparticle Loss

Relaxation in superconducting qubit can be induced by quasiparticles tunneling across the Josephson junction, absorbing energy from the qubit. Quasiparticle dynamics in superconducting qubit have been actively investigated [85, 86, 87, 88, 89]. Below we follow refs. [90, 91] to summarize the general theory for a single junction.

From Fermi's golden rule, we can write the the relaxation rate corresponding to quasiparticle tunneling across a junction as

$$\Gamma_{ij}^{\mathrm{qp}} = \left| \langle j | \sin \frac{\phi}{2} | i \rangle \right|^2 S_{\mathrm{qp}}(\omega_{ij}), \tag{3.23}$$

where the noise spectral density S_{qp} describes the quasiparticle environment,

$$S_{\mathrm{qp}}(\omega) = \omega \mathrm{Re} Y_{\mathrm{qp}}(\omega)/\pi g_K, \tag{3.24}$$

with

$$\mathrm{Re} Y_{\mathrm{qp}}(\omega) = \frac{1}{2} x_{\mathrm{qp}} g \left(\frac{2\Delta}{\hbar\omega} \right)^{3/2}, \tag{3.25}$$

where $x_{\mathrm{qp}} = \frac{n_{\mathrm{qp}}}{2\nu_o \Delta}$ is the quasiparticle density normalized by the density of Cooper pairs, g is the junction conductance. We can write $E_J = g\Delta/8g_K$, where $g_K = e^2/h$ is the conductance quantum and Δ is the superconducting gap.

So for a single junction, the quasiparticle spectral density is inversely proportional to the square root of frequency. We can then write the relaxation rate explicitly as

$$\Gamma_{ij}^{\mathrm{qp}} = \left| \langle j | \sin \frac{\phi}{2} | i \rangle \right|^2 \times \frac{8E_J}{\pi\hbar} x_{\mathrm{qp}} \sqrt{\frac{2\Delta}{\hbar\omega_{ij}}} \tag{3.26}$$

Although BCS theory predicts that the quasiparticle density would vanish at the temperature of the mixing chamber in a dilution fridge, many experiments have confirmed a finite x_{qp} value [86, 87]. The effect are thus believed to be due to non-equilibrium quasiparticles

[88]. Recent experimental results indicate that these non-equilibrium quasiparticles may come from high energy noise reaching the qubit inside the dilution fridge [89, 92].

3.2.2 Pure Dephasing

Modeling Noise and Dephasing

Pure dephasing can be viewed semi-classically as a process in which the qubit transition fluctuates in time, and a random phase accumulates between states $|0\rangle$ and $|1\rangle$ (see section 2.3), destroying the coherence. The frequency of this process is much lower than the transition frequency, resulted from the slow fluctuation in time of qubit parameters.

To understand pure dephasing, we may consider a simple two-level system with an effective Hamiltonian that fluctuates in time,

$$H = \frac{1}{2}(\omega_{eg} + \delta\omega_{eg}(t))\sigma_Z, \tag{3.27}$$

where $\delta\omega(t)$ is a fluctuation caused by classical noise. Such function can be treated stochastically, where we consider an ensemble of individual fluctuations and assign a probability and distribution function to $\delta\omega$. Each run of the experiment is affected by one part of this ensemble. We can further look at the system in the rotating frame with respect to ω_{eg} with $H_I = \delta\omega(t)\sigma_Z/2$, considering only the variation of the transition energy in time.

Assuming the fluctuation is small, we can Taylor expand the change in frequency as

$$\delta\omega_{eg}(t) = \sum_{\{\lambda\}} \frac{\partial\omega_{eg}}{\partial\lambda}\delta\lambda(t) + O(\delta\lambda^2), \tag{3.28}$$

where $\{\lambda\}$ is the set of qubit parameters, and $\frac{\partial\omega_{eg}}{\partial\lambda}$ can be viewed as the sensitivity of the qubit transition to the respective parameter λ. The accumulated frequency drift at time T

to first order in $\delta\lambda$ is then

$$\delta\omega_{eg}(T) = \sum_{\{\lambda\}} \frac{\partial\omega_{eg}}{\partial\lambda} \int_0^T dt\delta\lambda(t). \tag{3.29}$$

We make a further simplifying assumption that the noise is Gaussian distributed, such that the parameter fluctuation has zero average, $\langle\delta\lambda(t)\rangle = 0$, and can be described by a correlation function $\langle\delta\lambda(t)\delta\lambda(t')\rangle = G_\lambda(t-t')$. The free induction decay from fluctuation of parameter λ follows the exponential of the mean-squared phase noise, $\langle e^{i\delta\omega_{eg}}\rangle = e^{-\langle\delta\omega_{eg}^2\rangle/2}$, with

$$\langle\delta\omega_{eg}^2\rangle_\lambda = \left(\frac{\partial\omega_{eg}}{\partial\lambda}\right)^2 \left\langle \int_0^T dt \int_0^T dt'\delta\lambda(t)\delta\lambda(t') \right\rangle. \tag{3.30}$$

Using relation A.9, we can write

$$\langle\delta\omega_{eg}^2\rangle_\lambda = \left(\frac{\partial\omega_{eg}}{\partial\lambda}\right)^2 \int_{-\infty}^{\infty} \frac{d\omega}{2\pi} S_\lambda(\omega) W_T(\omega), \tag{3.31}$$

where $W_T(\omega)$ is the window function,

$$W_T(\omega) = \left| \int_0^T dt e^{-i\omega t} \right|^2 = \frac{\sin^2(\omega T/2)}{(\omega/2)^2}. \tag{3.32}$$

For noise that is roughly constant with amplitude S_λ in the interval $[0, 2\pi/\tau_c]$, we can use the relation $\int_{-\infty}^{\infty} dx \frac{\sin^2 x}{x^2} = \pi$ to write $\langle e^{i\delta\omega_{eg}}\rangle = e^{-\Gamma_2 T}$ where

$$\Gamma_2 = \left(\frac{\partial\omega_{eg}}{\partial\lambda}\right)^2 \frac{S_\lambda}{2}. \tag{3.33}$$

Generally speaking, in order to define a 'dephasing rate', we must consider an evolution that is '*filtered*' in the time window of the measurement [93].

Dynamical Decoupling

There are certain techniques developed within the NMR community to mitigate noise that has long correlation time [81]. One such strategy is to use the spin echo sequence [94], in which a short π-pulse is used to flip the spin in mid-evolution. Then, the effect of slow-drift in the time interval $[0, T/2]$ is reversed and canceled out in the second half of the evolution $[T/2, T]$. This modifies the window function as

$$\begin{aligned} W_T(\omega) &= \left| \int_0^{T/2} dt e^{-i\omega t} - \int_{T/2}^{T} dt e^{-i\omega t} \right|^2 \\ &= \frac{1}{\omega^2} \left| 2e^{i\omega T/2} - e^{i\omega T} - 1 \right|^2 \\ &= \tan^2(\omega T/4) \frac{\sin^2(\omega T/2)}{(\omega/2)^2}. \end{aligned} \tag{3.34}$$

From Eq. 3.34, we see that the spin echo sequence filters out the low frequency part of the noise spectrum $S_\lambda(\omega)$ via the factor $\tan^2(\omega T/4)$, so we can think of $W_T(\omega)$ as a filter function which depends specifically on the sequence of pulses we use to manipulate the qubit. As shown in Fig. 3.3, the spin echo technique cancels out the very slow drift accumulated during the long measurement. Therefore, coherence time measured using echo is the most important T_2 time.

The spin echo technique can be generalized to include an odd-number $2N-1$ of π-pulses during the otherwise free induction decay. By inspecting the $2N$ integrals and canceling out the repeating terms, we can generalize Eq. 3.34 to

$$\begin{aligned} W_T(\omega) &= \frac{1}{\omega^2} \left| 2e^{i\omega T/2N} - e^{i\omega T} - 1 \right|^2 \\ &= \tan^2(\omega T/4N) \frac{\sin^2(\omega T/2)}{(\omega/2)^2}. \end{aligned} \tag{3.35}$$

If the correction pulses are in the same quadrature as the $\pi/2$-pulses, the sequence is called Carr-Purcell (CP) [95], and if they are in the quadrature orthogonal to the $\pi/2$-pulses,

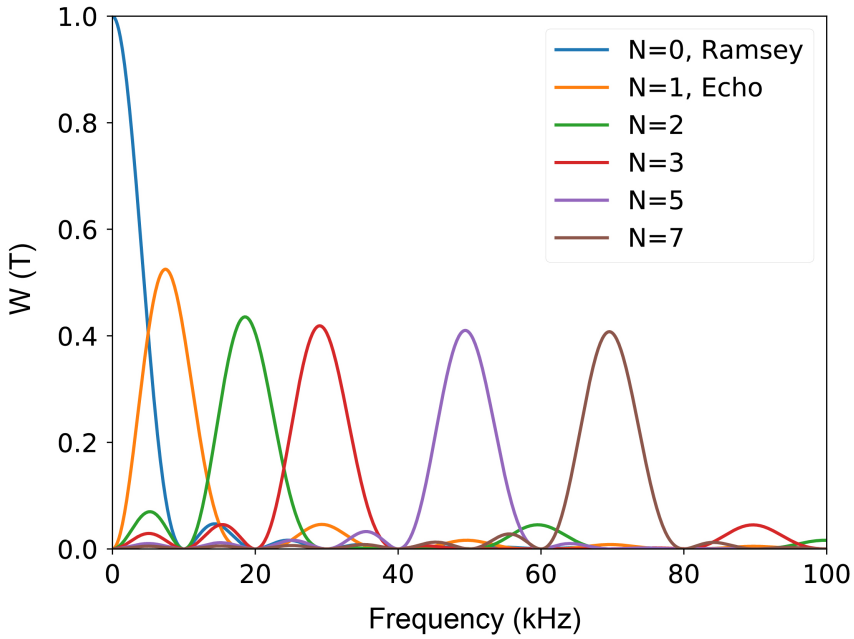

Figure 3.3: Window function. $W_{T=100\ \mu s}(\omega)$ for free induction (N=0), echo (N=1), and CPMG with 3, 5, and 7 refocusing pulses.

the sequence is called Carr-Purcell-Meiboom-Gill (CPMG) [96]. These techniques have been applied to flux qubits to enhance coherence times limited by slow drift [81, 54]. In practice, the pulses have finite length and are imperfect, hence beyond an optimal number, the refocusing pulses may contribute to the qubit's dephasing.

1/f Noise

Various noise sources in solid state systems display a somewhat similar 1/f behavior [97, 32, 98, 31, 33]. Prediction of decoherence due to this type of noise is complicated due to its long correlation time. The measurement frequency band is limited, for instance by the finite measurement time t_m, so during the measurement, the noise source may not reach equilibrium. In addition, $1/f$ noise cannot be generally assumed to be stochastically Gaussian. Some deviations from this assumption have been reported in refs. [99, 100]. Analytical

model regarding this type of noise typically involves the 'spin fluctuator' approach, which can be solved exactly under general conditions. From this model, 'weakly' coupled fluctuators can be approximated as a Gaussian process. Averaging over an ensemble of such fluctuators yields a $1/f$ spectral density. Fluctuators with frequency $< 1/t_m$ are considered strong and slow, and hence not effective. We will work within this approximation, and consider the noise spectral density for 1/f flux noise as

$$S(\omega) = \frac{2\pi A^2}{|\omega|^\mu}, \tag{3.36}$$

with noise amplitude $A = 10^{-6} - 10^{-5}\Phi_o$ [32, 33] and power $0.8 < \mu < 1.3$ [54].

The 1/f law does not need to be valid spanning across the entire frequency spectrum. We can merely assume it holds in the range of relevant frequency in our experiments $\omega_{\text{low}} < \omega < \omega_{\text{high}}$. The limiting frequencies depend on the specific architecture and experimental setup. In our measurements, ω_{low} is defined by the total measurement time $\omega_{\text{low}} = 2\pi/T_{\text{meas}} \approx 2\pi \times 0.1$ rad Hz, and ω_{high} by the total free induction time $\omega_{\text{high}} = 2\pi/T_{FI} \approx 2\pi[10^6 - 2\times 10^4]$ rad·Hz . The mean square phase variation is then

$$\langle \delta\omega_{eg}^2 \rangle_\lambda = \left(\frac{\partial \omega_{eg}}{\partial \lambda}\right)^2 A^2 \int_{-\infty}^{\infty} \frac{d\omega}{|\omega|^\mu} W_T(\omega). \tag{3.37}$$

For free induction decay W_T, we can write

$$\langle \delta\omega_{eg}^2 \rangle_\lambda = 2\left(\frac{\partial \omega_{eg}}{\partial \lambda}\right)^2 A^2 T^2 \int_{0}^{\infty} \frac{d\omega}{\omega^\mu} \text{sinc}^2(\omega T/2). \tag{3.38}$$

In the limit $T \gg 1/\omega$, we can use the static approximation $\text{sinc}(\omega T/2) \approx 1$. This happens when the noise spectrum has a peak at low frequency. In the simple case $\mu = 1$, the qubit phase decays following a Gaussian profile in time, $e^{-(\Gamma_\phi T)^2}$, with a dephasing rate Γ_λ

corresponding to noise source λ,

$$\Gamma_\lambda = \left(\frac{\partial \omega_{eg}}{\partial \lambda}\right)\sqrt{S_\lambda^\Sigma}, \tag{3.39}$$

where the noise spectral density can be approximated as

$$S_\lambda^\Sigma \approx A^2 \int_{\omega_{\rm low}}^{\omega_{\rm high}} \frac{d\omega}{\omega} = A^2 \ln\frac{\omega_{\rm high}}{\omega_{\rm low}}. \tag{3.40}$$

On the other hand, for a wideband 1/f noise at $T > 2\pi/\omega_{\rm high}$, we replace the higher limit with $1/T$ and get

$$S_\lambda^\Sigma \approx A^2 \int_{\omega_{\rm low}}^{1/T} \frac{d\omega}{\omega} = A^2 \ln\frac{2\pi}{\omega_{\rm low} T}. \tag{3.41}$$

The pure dephasing time can be defined as $T_\phi = 1/\Gamma_\phi$, where $\Gamma_\phi = \sum_\lambda \Gamma_\lambda$.

Equation 3.41 shows that if we want to obtain a nice signal for a Ramsey (free induction) decay by increasing the averaging time, we will get a logarithmically shorter coherence time. Empirically, averaging many decaying oscillations at different frequencies would result in a faster decay. Hence, a long Ramsey measurement shows a time scale that is actually lower than the realistic coherence time T_2.

As shown in Fig. 3.4, a Gaussian curve seems to decay faster in time compared to an exponential. Hence, fitting the data that follows a Gaussian profile to an exponential would give an incorrect dephasing time.

The use of echo decoupling sequence introduces a $\tan$ term to the window function [98], hence we get

$$\begin{aligned}\langle \delta\omega_{eg}^2 \rangle_\lambda &= 2\left(\frac{\partial \omega_{eg}}{\partial \lambda}\right)^2 A^2 T^2 \int_0^\infty \frac{d(\omega T/4)}{(\omega T/4)^3}\sin^3(\omega T/4) \\ &= 2\left(\frac{\partial \omega_{eg}}{\partial \lambda}\right)^2 A^2 T^2 \ln 2,\end{aligned} \tag{3.42}$$

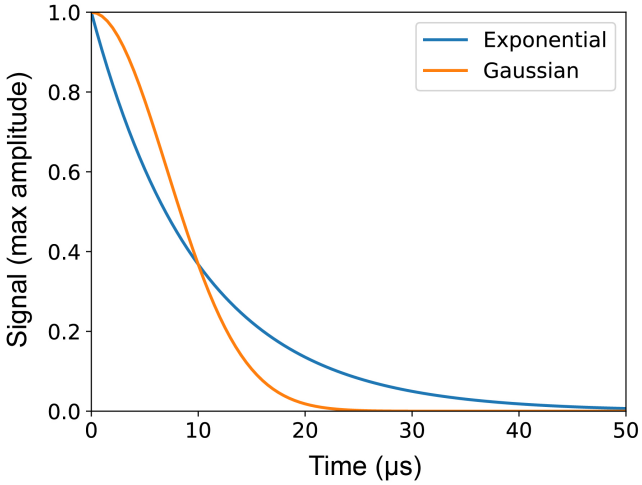

Figure 3.4: Exponential versus Gaussian decay. For the same time constant $T_\phi = 10\ \mu$s, the Gaussian curve shows a faster decay compared to an exponential function. We should therefore choose the right function to fit the data to extract the correct coherence time.

and the dephasing rate can be written analytically as

$$\Gamma_\lambda = \left(\frac{\partial \omega_{eg}}{\partial \lambda}\right) A\sqrt{\ln 2}. \tag{3.43}$$

This formula is exact and can be conveniently used to estimate flux noise amplitude when the dominant dephasing source is 1/f noise.

1/f Noise: Second Order Effect

At the symmetry bias point, for example when the flux threading the loop in fluxonium is at half integer flux quantum, superconducting qubits are first-order insensitive to the respective noise [33]. Such bias point is referred to as sweet spot. However, the qubit is still sensitive to higher order noise effect. Here we consider how the second-order noise may dephase the qubit.

The second order term that was left out of Eq. 3.28 can be written as

$$\delta\omega_{eg}^{(2)}(T) = \sum_{\{\lambda\}} \frac{1}{2}\frac{\partial^2\omega_{eg}}{\partial\lambda^2}\int_0^T dT(\delta\lambda(T))^2, \tag{3.44}$$

and the dephasing can be approximated in the low ($\omega_{\text{low}} < \omega < 2\pi/T$) and high ($\omega_{\text{high}} > \omega > 2\pi/T$) frequency limits using linked-cluster series expansion [98, 101], $e^{\langle i\delta\omega_{eg}^{(2)}(T)\rangle} = f^{lf}f^{hf}$. The contribution from the low frequency part is given as

$$f_\lambda^{lf}(T) = \frac{1}{\sqrt{1 - 2i(\partial^2\omega_{eg}/\partial\lambda^2)A^2T\ln(2\pi/\omega_{\text{low}}T)}}. \tag{3.45}$$

For the high frequency part at long times, we can approximate $T \gg [(\partial^2\omega_{eg}/\partial\lambda^2)A^2/2]^{-1}$ and find

$$f_\lambda^{hf}(T) = \exp\left(-\frac{\pi}{2}\frac{\partial^2\omega_{eg}}{\partial\lambda^2}A^2T\right). \tag{3.46}$$

So the resulting decay follows the combination of a power law at short time and an exponential law at long time. Note that only the real part of f^{lf} should be considered in practice.

For the echo decay, assuming a sharp cutoff at ω_{high}, we get

$$f_E(T) = \frac{1}{\sqrt{1 + (1/8)(\partial^2\omega_{eg}/\partial\lambda^2)^2A^4\omega_{\text{high}}^2\ln(1/\omega_{\text{low}}T)T^4}}. \tag{3.47}$$

These equations seem daunting, but there is a timescale that we can prescribe as the coherence time due to second order noise effect $T_\phi^{(2)}$ at long time. The corresponding dephasing rate in Eq. 3.46 can be written as

$$\Gamma_{\lambda,1/f}^{(2)} \approx \frac{\partial^2\omega_{eg}}{\partial\lambda^2}A^2. \tag{3.48}$$

It is a good approximation in our system to treat the time decay in a typical echo measurement to be exponential, assuming the lower frequency part is efficiently filtered out by a π-pulse. The easiest way to check if this is a good approximation is to compare the frequency dependence of the window function for the echo characterized by $T = 100\ \mu$s with $\Gamma^{(2)}_{\lambda,1/f}$.

More importantly, we can estimate the dephasing time limit corresponding to second-order noise using Eq. 3.48. To accomplish this, we have to compute the second-order sensitivity $\frac{\partial^2 \omega_{eg}}{\partial \lambda^2}$, and extract the noise amplitude A by measuring the coherence time away from the sweet spot (see Fig. 6.13(a), for instance).

Photon Noise

When dispersive readout is used in cQED [22, 62], the number of photons at the cavity frequency can shift the effective qubit frequency. For example, consider the Jaynes-Cumming Hamiltonian in the dispersive limit $\Delta \gg g$ (Eq. 2.54). In this case, the qubit transition frequency is shifted by $n\chi$, where n is the cavity photon number and $\chi = 2g^2/\Delta$ is the dispersive shift. As n fluctuates in time, it changes the qubit frequency randomly, and hence dephasing occurs.

In an ideal scenario with the cavity in thermal equilibrium at 10 mK, we expect the average number of thermal photons at the resonant frequency $f_r \sim 10$ GHz to be very small (see Fig. 3.5), following the Boltzmann distribution

$$n_{\text{th}} = \frac{1}{e^{\hbar\omega_r/k_B T} - 1} = O(10^{-21}). \tag{3.49}$$

So, we may naively expect almost no photons in the the cavity at 10 mK. However, due to a combination of imperfect shielding, isolation, and thermalization, there exists a finite photon population which can dephase the qubit.

Following refs. [102, 103], the thermal photon dephasing rate for cavity-qubit system

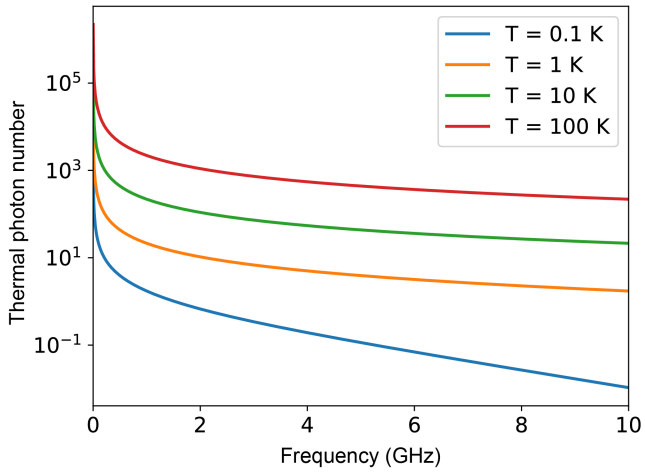

Figure 3.5: Effective thermal photon number. Thermal photon number $n_{\rm th}$ as a function of frequency (in GHz) at 100 K, 5 K, 1 K, and 100 mK.

with dispersive shift χ_{01} is given by

$$\Gamma_{\rm th} = \frac{\kappa_{\rm tot}}{2}{\rm Re}\left[\sqrt{\left(1+\frac{i\chi_{01}}{\kappa_{\rm tot}}\right)^2+\frac{4i\chi_{01}n_{\rm th}^{\rm eff}}{\kappa_{\rm tot}}}-1\right]. \tag{3.50}$$

In the small photon number limit, the rate is reduced to

$$\Gamma_{\rm th} = \frac{n_{\rm th}^{\rm eff}\kappa\chi_{01}^2}{\kappa^2+\chi_{01}^2}. \tag{3.51}$$

For large $\kappa_{\rm tot}/\chi$ ratio, Eq. 3.50 simplifies to

$$\Gamma_{\rm th} = \frac{\chi_{01}^2 n_{\rm th}^{\rm eff}}{\kappa_{\rm tot}}\left(n_{\rm th}^{\rm eff}+1\right), \tag{3.52}$$

and for large $\chi/\kappa_{\rm tot}$, it saturates to

$$\Gamma_{\rm th} = \kappa_{\rm tot} n_{\rm th}^{\rm eff}. \tag{3.53}$$

Critical Current Noise

Finally, since superconducting qubits are built from artificial Josephson junctions, certain properties within the junctions themselves can change over time, resulting in dephasing [104, 105, 106]. For instance, some change in the tunneling conductance directly causes fluctuation in the critical current, and thus E_J and E_L.

Following ref. [106], the critical current noise spectrum obeys the phenomenological relation

$$\frac{S_{E_J}}{E_J^2} = \frac{S_{R_n}}{R_n^2} = \frac{S_{I_c}}{I_c^2} \approx \frac{1}{A/\mu\mathrm{m}^2}\frac{T}{1K}\frac{1}{f}10^{-13}\mathrm{Hz}^{-1}, \tag{3.54}$$

exhibiting a 1/f dependency, scaling proportionally with temperature and inversely with junction area. However, their measurement is limited to the range around 1 Hz and temperature around 315 mK.

At the time of writing of this manuscript, little is understood about critical current noise at low temperatures, and contradicting results have been reported for circuits at kelvin-range temperatures [104, 105, 106]. Future experiments in which qubit coherence is not limited by other mechanisms may open the door to more rigorous investigation on junction noise.

3.3 Quantum Gates and Readout

3.3.1 Qubit Control

From Eq. 2.36, we can come up with a convenient method to perform X and Y control of superconducting qubits. Denoting $I = \epsilon_d \cos(\phi_d)$ as the *in-phase* and $Q = \epsilon_d \sin(\phi_d)$ as the *quadrature* components of the applied microwave field with amplitude ϵ_d, the resonant ($\Delta = 0$) driving Hamiltonian in the rotating frame takes the form

$$H_d = \frac{\hbar\Omega}{2}(I\sigma_X + Q\sigma_Y), \tag{3.55}$$

such that an in-phase signal rotates the qubit around the X-axis, and a quadrature signal rotates the qubit around the Y-axis. In microwave electronics, this is accomplished by using an IQ mixer to multiply the carrier signal at the qubit frequency and the pulse generated by an arbitrary waveform generator (AWG). Note that the choice of absolute phases of I and Q components is arbitrary, and only the phase difference between them is important.

Since superconducting circuits are not perfect two-level systems, other eigenstates can be excited by the applied microwave signal. An important technique to mitigate this problem is to turn on the applying field slowly by using an I or Q pulse with an envelope $s(t)$, which is typically Gaussian. This effectively reduces the spectral width of the pulse (see Fig. 5.11(a)). The effective rotating angle is thus

$$\theta(t) = \Omega \int_0^t s(t')dt' \tag{3.56}$$

A Rabi experiment (section 6.5) is performed by varying either the pulse's width or amplitude to find the correct rotation angles. Another experiment to tune the gate parameters can be done by measuring the qubit after applying a sequence consisting of an odd-number of $\pi/2$-pulses on the qubit. This allows us to determine which is the best gate configuration that minimizes over- and under-rotation. When short pulses are desired, pulse shaping techniques such as Derivative Removal by Adiabatic Gate (DRAG) [107, 108, 58] can be used to minimize gate errors from other energy levels.

Z-control of a qubit can be done using a sequence of gates, either by applying an off-resonant X or Y pulses, or by implementing a virtual-Z gate as shown in ref. [109].

3.3.2 Readout

In this thesis, we use the standard dispersive readout technique using a cavity coupled to a qubit system [22, 62, 63]. The dispersive shifts depend on the specific qubits, but the principle is essentially described by Eq. 2.53. For a general discussion here, we assign

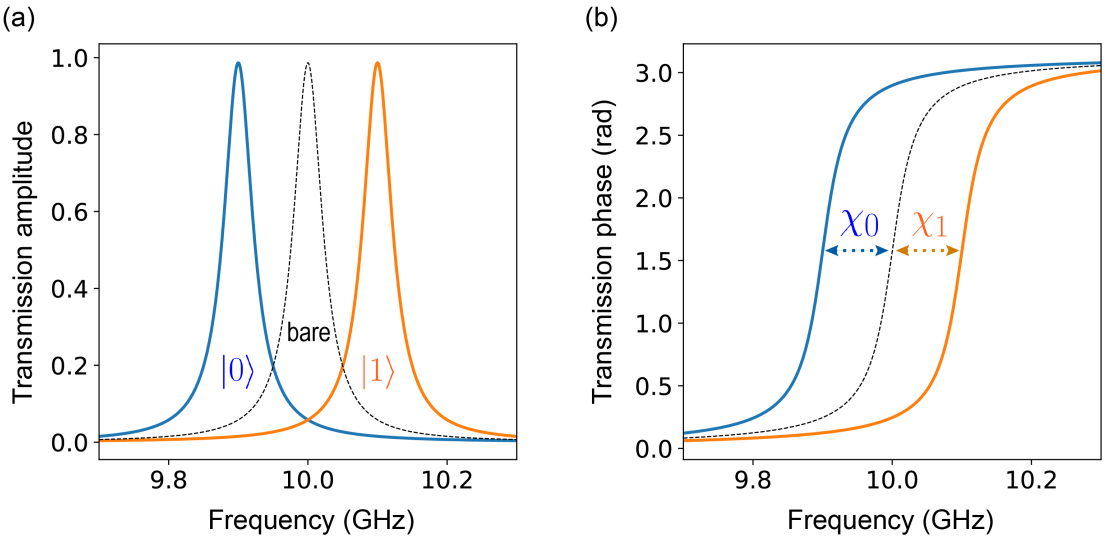

Figure 3.6: Dispersive readout. (a) Transmission amplitude and (b) phase of cavity signal across the resonance. The cavity is shifted by $\chi_0 = -\chi/2$ when qubit is in ground state $|0\rangle$, and by $\chi_1 = \chi/2$ when qubit is in excited state $|1\rangle$.

$\chi_0 = -\chi/2$ and $\chi_1 = \chi/2$, such that $\chi_{01} = \chi$. The readout scheme is illustrated in Fig. 3.6. The qubit shifts the cavity resonance differently when it is in the ground or the excited states. By probing the cavity at a frequency near its resonance, we can infer the state of the qubit.

Generally speaking, a multi-level system shifts the cavity by χ_i when it is in level i, such that the cavity resonance is modified as $\omega_c \to \omega_c + \chi_i$. The different shifts can be used to readout different states of a single qubit [110] or multiple qubits [111, 112]. As discussed in section 6.4, we have experimentally demonstrated this principle with a two-qubit device.

Rigorous description of superconducting qubit readout and amplification can be found in refs. [83, 113]. We describe our IQ demodulation technique in more details in section 5.3.

Chapter 4

Fluxonium Theory

Nothing is ever so expensive as what is offered for free.

Viet Thanh Nguyen

This chapter provides a theoretical background for the experimental discussion in Chapter 6. First, in section 4.1, we discuss the range of parameters E_J, E_C, E_L that defines fluxonium and inspect the typical spectra and matrix elements. We then follow up with decoherence analysis in section 4.2 and dispersive readout using cavity-fluxonium system in section 4.3. Finally, we discuss coupled fluxonium qubits and the microwave-activated controlled-Z gate in section 4.4.

4.1 Spectrum and Selection Rules

4.1.1 Fluxonium with a Single Small Junction

Fluxonium circuit consists of a Josephson junction with energy E_J shunted by a capacitance with charging energy E_C and inductance with inductive energy E_L. Let us recall that the

Hamiltonian for this circuit (see Eq. 3.17) can be written as

$$H = 4E_C n^2 + \frac{1}{2}E_L\phi^2 - E_J\cos(\phi + \phi_{\text{ext}})$$

where n and ϕ are the charge number (or normalized charge) and phase (or normalized flux) operators, respectively. In the harmonic oscillator basis, they can be written as (see Eq. 3.12)

$$\phi = \frac{1}{\sqrt{2}}\left(\frac{8E_C}{E_L}\right)^{\frac{1}{4}}(a^\dagger + a),$$
$$n = \frac{i}{\sqrt{2}}\left(\frac{E_L}{8E_C}\right)^{\frac{1}{4}}(a^\dagger - a).$$

The parameters must satisfy $E_J/E_L \gg 1$ and, opposed to the previous experiments [59, 85], $E_J/E_C \approx [1, 10]$. The energies ratios distinguish fluxonium from other inductively shunted junction devices. To satisfy the requirement on the small inductive energy, a superinductance with inductance per unit length of $10^4\ \mu_0$ constructed from a chain of $N \approx 10^2$ Josephson junctions with area of approximately $1\ \mu\text{m}^2$ is used. One can thus interpret fluxonium as an inductively shunted charge qubit which is insentitive to charge noise, or a generalized flux qubit with decreased sensitivity to flux noise, where the first- and second- order coupling to flux noise is suppressed as $1/N$ and $1/N^2$, respectively.

There are certain physical constraints on the circuit parameters. First, it is hard to make the charging energy E_C larger than 10 GHz because of the stray capacitance from the junction leads. Likewise, it is hard to reduce the Josephson energy E_J below 2 GHz, since we cannot fabricate junctions with arbitrarily small area reliably. In our experiments, the small junction's size goes from $90\ \text{nm} \times 90\ \text{nm}$ to $150\ \text{nm} \times 150\ \text{nm}$, corresponding to E_J ranging from 2 to 7 GHz. Note that E_J also depends on the oxidation conditions. The typical inductive energy E_L in high coherence fluxonium is around $0.5 - 1$ GHz.

In this section, the superinductor is treated as a lumped circuit element [59, 114]. With this assumption, the circuit is analogous to a particle in a box, where E_C sets the magnitude

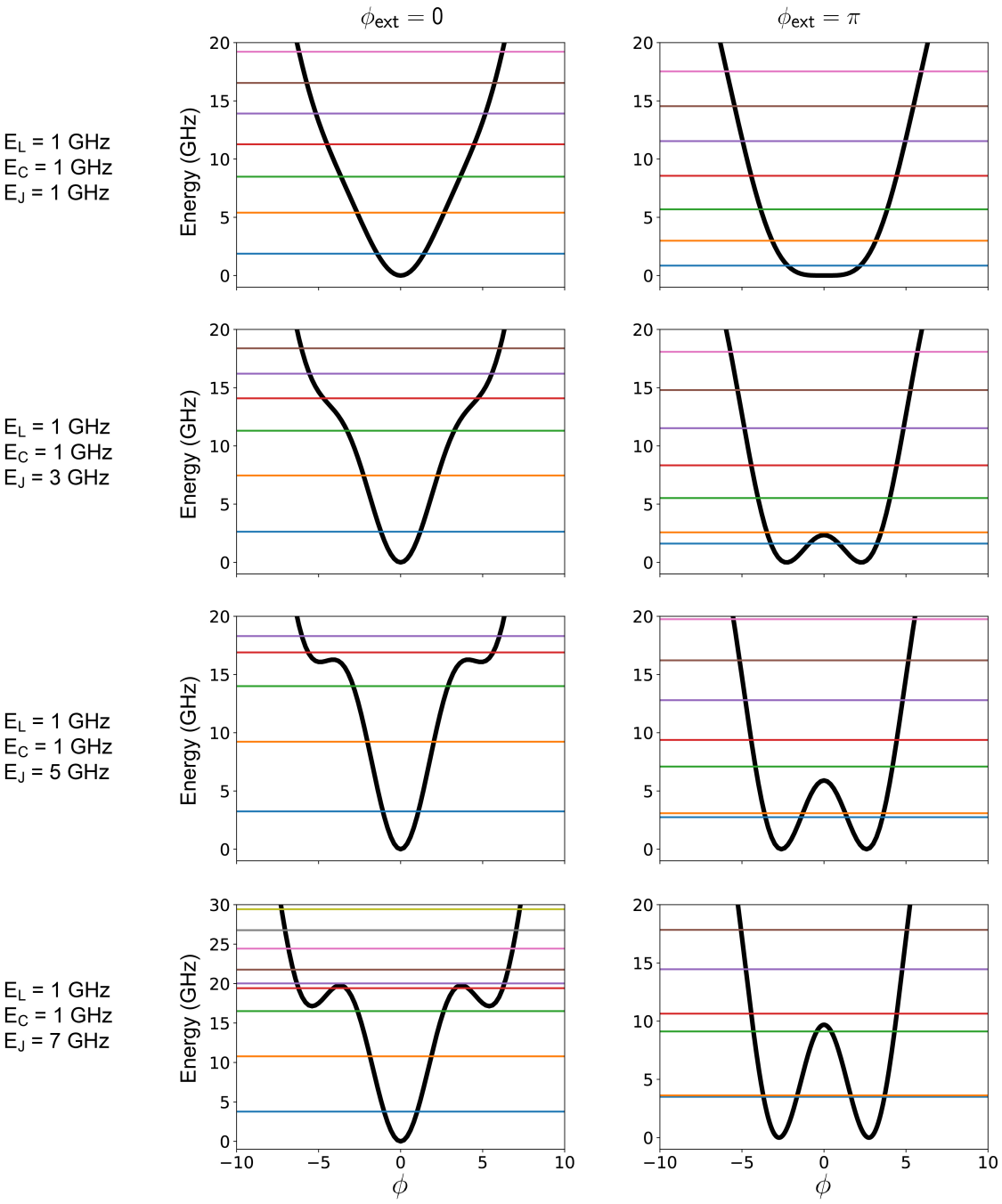

Figure 4.1: Eigenenergies and potential energy for different E_J values. Adjusted eigenenergies (horizontal lines) and potential energy (thick lines) for different E_J values, showing the more characteristic fluxonium properties at high E_J values: high anharmonicity, low $0 \rightarrow 1$ splitting at half flux quantum bias.

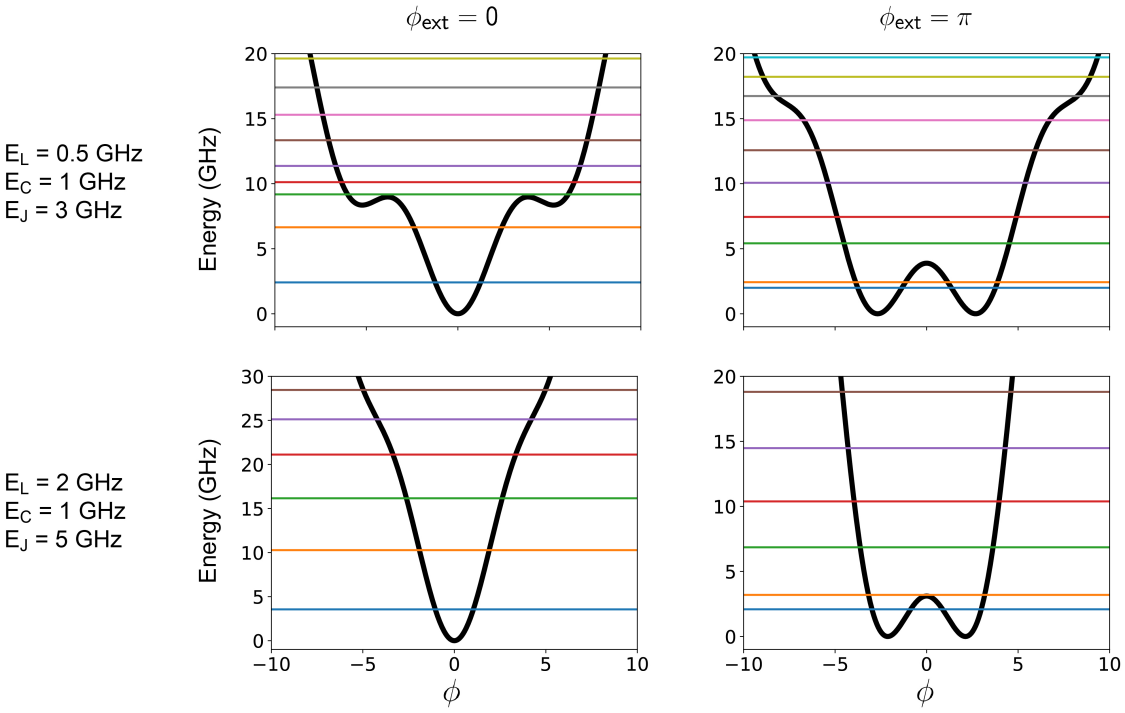

Figure 4.2: Eigenenergies and potential energy for different E_L values. Adjusted eigenenergies (horizontal lines) and potential energy (thick lines) for different E_L values.

of the kinetic energy, while E_J and E_L shape the potential energy, with the ratio E_J/E_L determining the number of localized wells. In addition, the external flux can be used to tune the relative position of the neighboring wells. We can gain intuition about the system by inspecting the potential wells and energy levels when the circuit is biased at integer and half-integer flux quantum. The results here were simulated numerically using QuTip [115, 116]. A more rigorous approach with analytical formulas can be found in refs. [117, 118].

We first consider the impact of the Josephson energy E_J. Since it is the non-linear term, the higher E_J, the more anharmonic the system becomes, and the higher the potential wall between the wells is. This subsequently makes the energy splitting between otherwise degenerate states decrease with increasing E_J, as shown in Fig. 4.1.

The inductive energy E_L, on the other hand, decreases the splitting at higher values, as shown in Fig. 4.2. This suggests that the ratio E_J/E_L plays a more important role than

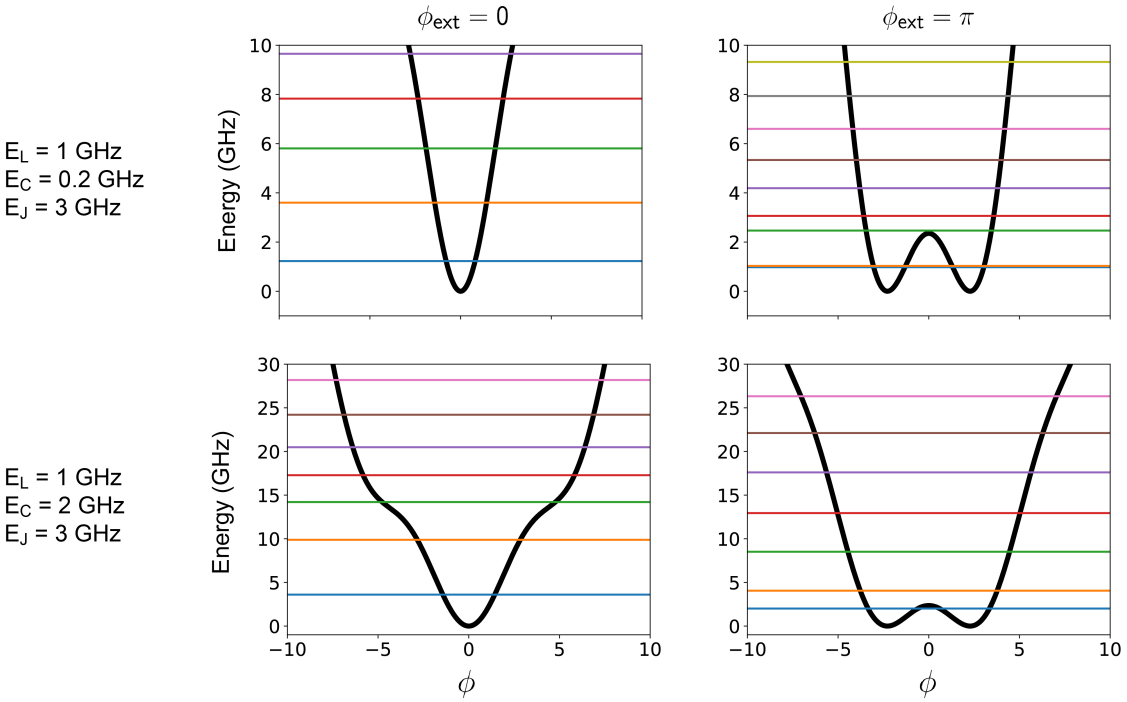

Figure 4.3: Eigenenergies and potential energy for different E_C values. Small E_C makes fluxonium similar to transmon at integer flux, and to flux qubit at half-integer flux.

each energy parameter's absolute value.

Finally, the charging energy E_C sets the overall scale for the kinetic energy. It determines the plasma frequency scale ω_p, affects the tunneling rate across the potential well [118], and also sets the anharmonicity of the system at integer flux [49]. On one hand, the small transition frequency between the two lowest states depends strongly on the E_J/E_C ratio, because the tunneling rate is exponentially sensitive to this ratio, as predicted by the WKB approximation. On the other hand, the higher levels are separated by the *plasmon gap*, roughly given by $\sqrt{8E_JE_C}$, and reside at much higher energies.

In general, there are two types of transitions in fluxonium when we move across the spectrum in flux, as shown in Fig. 4.4. The first type is called *plasmon*, since it is simply a plasma oscillation between states localized in the same potential well, and is thus associated with a large matrix element. The second type is called *fluxon*, because it is associated with

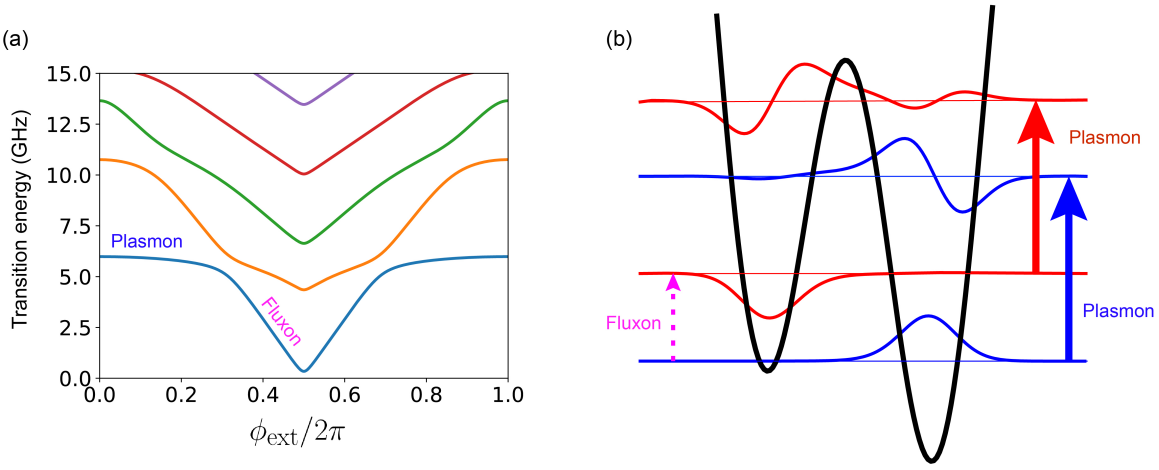

Figure 4.4: Plasmon and fluxon transitions. (a) Typical transition frequency spectrum of a device with $E_J = 5$ GHz, $E_C = 1$ GHz, and $E_L = 1$ GHz. Plasmon transitions are relatively flux-independent, while fluxon transitions are strongly flux-dependent. (b) Wavefunctions and potential energy showing plasmon (blue to blue and red to red) transitions and fluxon transition (blue to red or vice versa). A plasmon is just plasma oscillation between states localized in the same well, hence it is allowed, whereas a fluxon transition happens through the tunneling across the potential barrier, and is thus almost forbidden.

flux tunneling between states localized in adjacent wells. For $E_J \gg E_C$, the tunneling amplitude is exponentially small, and the fluxon transition is nearly forbidden away from the half-integer flux bias.

We simulate the charge and phase matrix elements and plot the results in Fig. 4.5. Note the vanishing of the $0 \to 2$ matrix elements at the symmetric flux bias (interger and half-integer flux quantum). This is due to symmetry of the potential seen by the ϕ variable. In fact, any even-number quanta of energy exchange is forbidden at the symmetry point, including any $|i\rangle \to |i+2\rangle$, qubit-cavity sideband transitions, and qubit-qubit double excitations such as $|00\rangle \to |11\rangle$. It is possible to use higher order process, such as two-photon excitation or Raman driving, to manipulate these forbidden transitions.

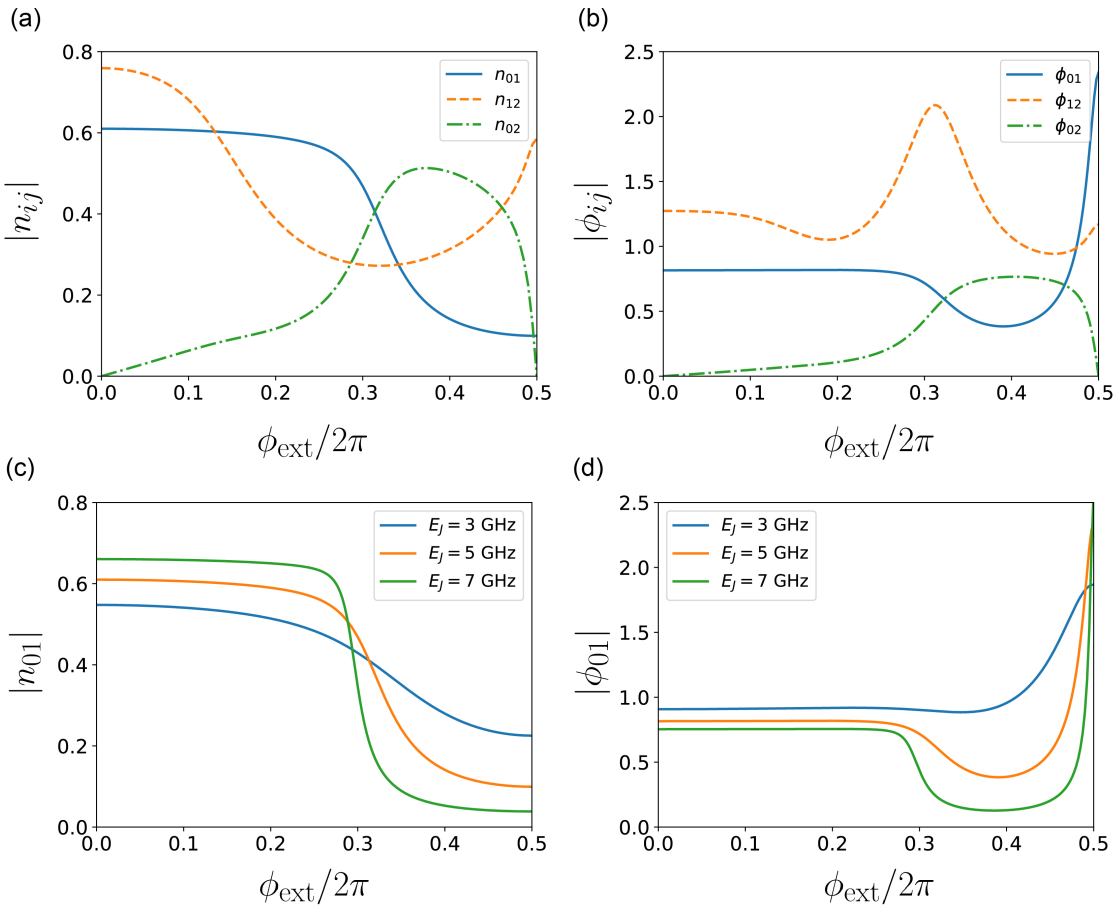

Figure 4.5: Simulations of matrix elements. (a) Charge number matrix elements for $0 \to 1$, $1 \to 2$, and $0 \to 2$ transitions in a fluxonium circuit with $E_J = 5$ GHz, $E_C = 1$ GHz, $E_L = 1$ GHz. The $0 \to 1$ transition dipole is flat for the plasmon region, declines sharply in the fluxon region, and reaches a constant around the symmetric flux point at half-integer flux quantum. The $0 \to 2$ dipole vanishes at the symmetry flux bias due to selection rules. (b) Phase matrix elements for the same circuit. The $0 \to 1$ phase matrix element also declines sharply around the fluxon region, but reaches a maximum at the half-integer flux quantum bias, due to strong overlapping at low frequency between the hybridized states. The $0 \to 2$ phase matrix elements also vanish at symmetric flux due to selection rules. (c) $0 \to 1$ charge matrix elements in the same circuit but for different E_J values. The dipole moment for the fluxon is smaller for higher E_J. The plasmon, however, has a larger charge matrix element for higher E_J values. (d) $0 \to 1$ phase matrix element in the same circuit but for different E_J values. The fluxon transition matrix element again becomes smaller for higher E_J. The phase matrix element rises sharply at the symmetry flux point for higher E_J due to stronger hybridization.

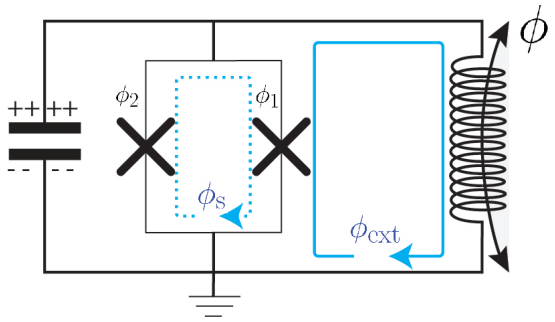

Figure 4.6: Split-junction fluxonium circuit. Circuit diagram showing a fluxonium with two parallel tunnel junctions. The phases across them are labeled ϕ_1 and ϕ_2, whereas the phase across the inductor is labeled ϕ.

The small fluxon dipole moments produced by increasing E_J is intriguing. It suggests an experiment where we can simply tune E_J and see if the matrix elements vanish. This can be accomplished by introducing a SQUID loop (split-junction) [49]. The experiment [60] is discussed in section 6.2. We develop the theory for the split-junction fluxonium below.

4.1.2 Split-Junction Fluxonium

It turns out that we can employ a SQUID loop in fluxonium to effectively tune the Josephson energy E_J. The circuit now consists of two loops, as depicted in Fig. 4.6. Let $\phi_{1,2}$ be the phase differences across the right and left junctions respectively, we can write the Hamiltonian as

$$H = 4E_C n^2 + \frac{1}{2}E_L\phi^2 - E_{J_1}\cos(\phi_1) - E_{J_2}\cos(\phi_2). \tag{4.1}$$

The magnetic fluxes Φ_s and Φ_{ext} threading the SQUID loop and the main circuit loop impose the constraints on the phase differences accordingly,

$$\begin{aligned} \phi_1 - \phi_2 &= 2\pi\frac{\Phi_s}{\Phi_o} = \phi_s, \\ \phi - \phi_1 &= 2\pi\frac{\Phi_{\text{ext}}}{\Phi_o} = \phi_{\text{ext}}. \end{aligned} \tag{4.2}$$

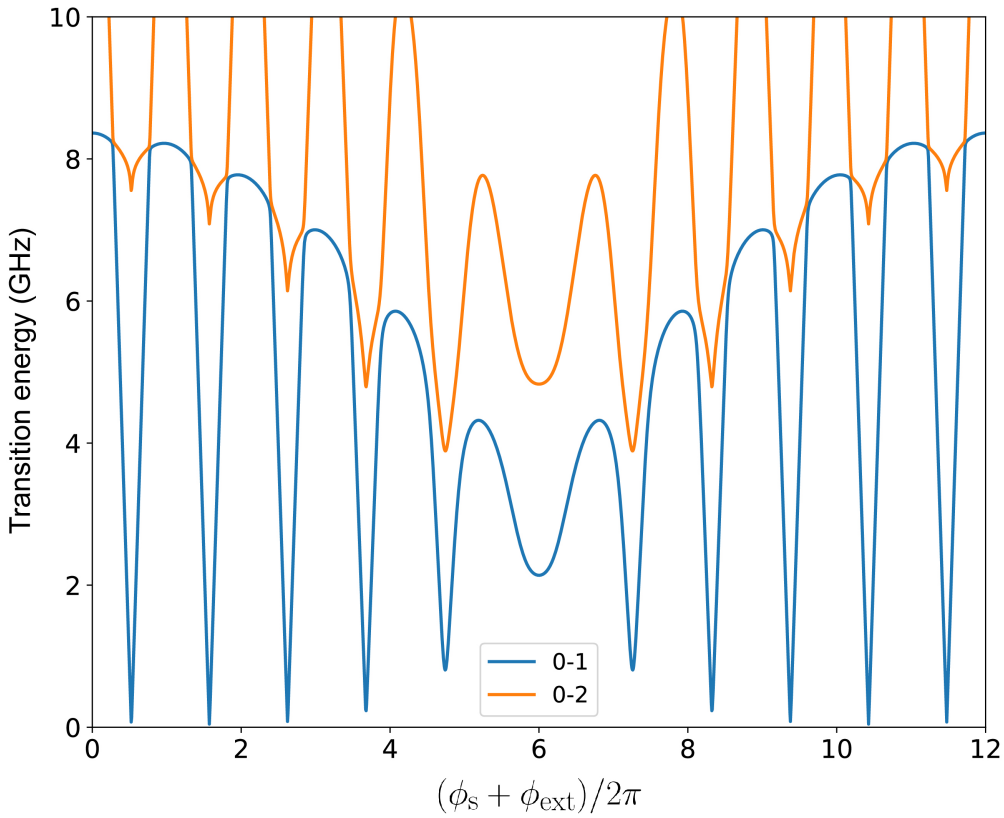

Figure 4.7: Split-junction fluxonium spectrum. Transition energy spectrum of a split-junction fluxonium circuit with $E_{J\Sigma} = 10$ GHz, $E_C = 1$ GHz, $E_L = 1$ GHz, $E_{J1} - E_{J2} = 1$ GHz, and the flux through the SQUID is 10 times smaller than the flux through the main loop at any total flux bias, $\phi_{ext} = 10 \times \phi_s$. Note that the anti-crossing between plasmon and fluxon becomes larger as the flux through the SQUID reduces the effective E_J.

Figure 4.7 shows an example spectrum of split-junction fluxonium circuit with $E_{J\Sigma} = E_{J1} + E_{J2} = 10$ GHz, $E_C = 1$ GHz, $E_L = 1$ GHz, $E_{J1} - E_{J2} = 1$ GHz. In this circuit, the flux through the small loop is 10 times smaller than the flux through the big loop at any total flux bias, $\phi_{ext} = 10 \times \phi_s$. We can observe that the anti-crossings between plasmon and fluxon become larger when the flux through the SQUID reduces the effective E_J.

The corresponding charge number and phase matrix elements are plotted in Fig. 4.8.

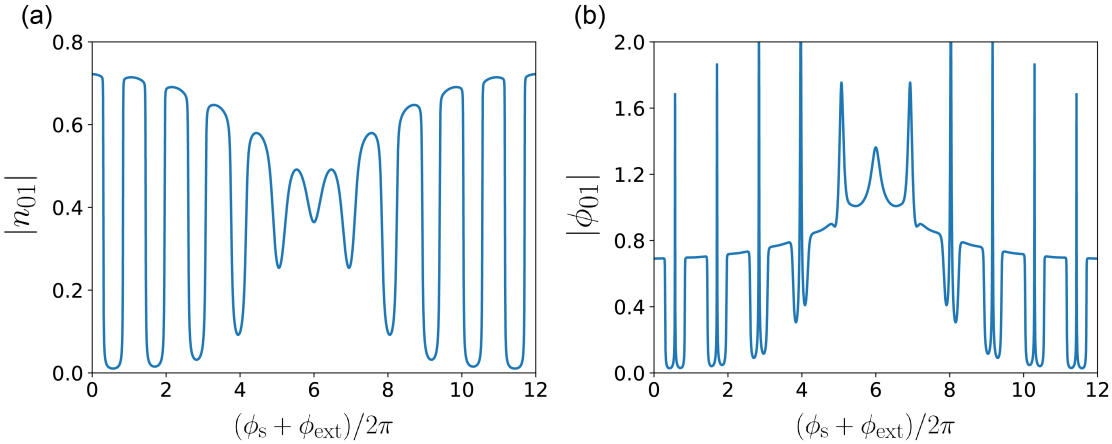

Figure 4.8: Split-junction fluxonium matrix elements. (a) The charge number and (b) phase matrix elements of the $0 \rightarrow 1$ transitions in the split-junction device. As the effective Josephson energy becomes smaller toward the symmetry flux point, both the charge and flux couplings for the fluxon transition become larger. The charge coupling for the plasmon transition also becomes smaller, consistent with Fig. 4.5(c).

When the effective Josephson energy E_J becomes smaller, the fluxon's matrix elements become larger as the transition becomes less forbidden. On the other hand, the plasmon charge matrix element becomes smaller, consistent with the single tunneling junction fluxonium analysis (see Fig. 4.5(c)).

4.2 Decoherence Mechanisms in Fluxonium

In this section, we develop the theoretical tools to model different decoherence effects in fluxonium qubits, starting with relaxation mechanisms. Flux noise is discussed separately in section 3.2. We end the section by describing briefly relevant parameters in our experiments related to thermal photon noise.

4.2.1 Dielectric Loss

We begin by applying Fermi's golden rule (see Appendix A) to a superconducting circuit at finite temperature T and write the relaxation rate as

$$\Gamma_{ij}^{\text{diel}}(\omega_{ij}) = \frac{\hbar\omega_{ij}^2}{4E_C Q_{\text{diel}}(\omega_{ij})} |\langle i|\phi|j\rangle|^2 \left| \coth\left(\frac{\hbar\omega_{ij}}{2k_B T}\right) + 1 \right|, \tag{4.3}$$

where $Q_{\text{diel}}(\omega_{ij}) = 1/\tan\delta_C$ is the effective quality factor of the lossy capacitance, and E_C is the charging energy of the circuit.

There are two obvious ways to reduce the dissipation rate: first, by de-coupling it from the noise source, which we demonstrate in section 6.2, and second, by increasing the effective dielectric quality factor. To reduce $\tan\delta_C$, we can turn to either material engineering [44, 46], or antenna design [30]. Another approach is to tune the qubit to work in the low frequency regime where relaxation is slowed down, which we demonstrate in section 6.3. Quantitatively, this comes from the quadratic frequency term in Eq. 4.3. We simulate T_1 limited by dielectric loss and show the results in Fig. 4.9.

It's also worth noting that at low frequency, the dielectric quality factor is likely better [119], which gives additional advantage to low frequency qubits if the loss is dominated by dielectric loss. To account for this effect, we model the quality factor to have a small frequency dependence accordingly,

$$\frac{\tan\delta_C(\omega)}{\tan\delta_C(\omega = 2\pi \times 6\ \text{GHz})} = \left(\frac{\omega}{2\pi \times 6\ \text{GHz}}\right)^{\epsilon}, \tag{4.4}$$

where the larger the ϵ power, the better it is for fluxonium.

Chain Dielectric Loss

An additional feature of fluxonium circuit compared to other superconducting qubits is the inductor, which we have so far treated as a lumped circuit element. In our devices, the

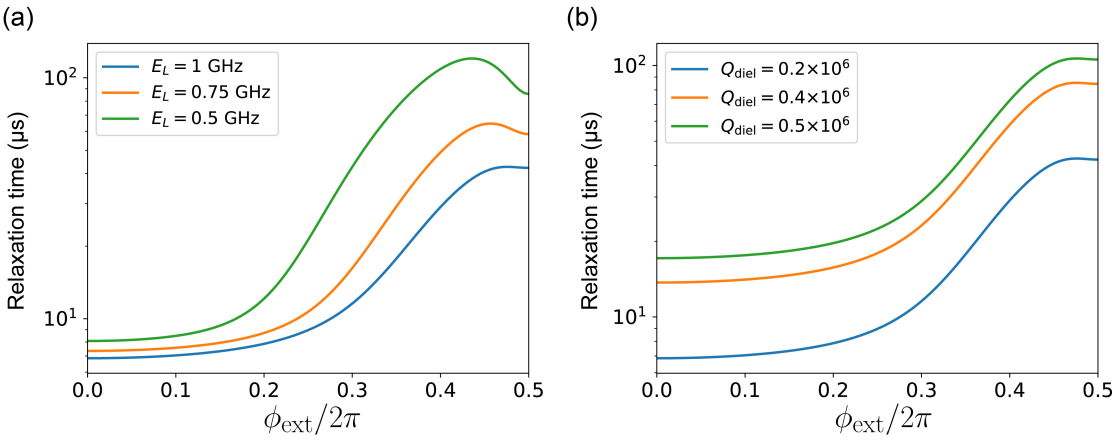

Figure 4.9: Simulation of T_1 limited by dielectric loss. Relaxation time limited by dielectric loss simulation results for (a) different E_L values which mostly affect the qubit's frequency, and (b) different effective dielectric quality factors.

inductor is a chain of junctions with metal parts covered with dielectric, so it inevitably introduces additional shunting capacitances with finite loss tangent. Below we consider two types of possibly lossy spurious capacitors associated with the chain, and discuss how they may contribute to relaxation.

First, we can approximate the loss from the self-capacitance of a chain of junctions by applying Eq. 4.3 to the junctions in the chain. Denoting the array using subscript A, we can write

$$\begin{aligned}\Gamma_{ij}^{\mathrm{diel_A}}(\omega_{ij}) &= \sum_i^N \frac{\hbar\omega_{ij}^2}{4E_{CA}Q_{\mathrm{A}}(\omega_{ij})}|\langle i|\frac{\phi}{N}|1\rangle|^2\left|\coth\left(\frac{\hbar\omega_{ij}}{2k_BT}\right)+1\right| \\ &= \frac{\hbar\omega_{ij}^2}{4NE_{CA}Q_{\mathrm{A}}(\omega_{ij})}|\phi_{01}|^2\left|\coth\left(\frac{\hbar\omega_{ij}}{2k_BT}\right)+1\right|,\end{aligned} \tag{4.5}$$

which is inversely proportional to the number of junctions in the chain. In our fluxonium devices, all the chain junctions have dimensions $0.4\ \mu\mathrm{m} \times 2\ \mu\mathrm{m}$, giving $C_{JA} \approx 36$ fF, using the empirical formula $C_J \approx 45\ \mathrm{fF}/\mu\mathrm{m}^2$. From our relaxation data, we can extract the bound for loss tangent of the junction oxide layer, which we assume to be $\tan\delta_A = \tan\delta_C/N$. These values are much smaller than the value reported in literature ($\tan\delta_{\mathrm{AlOx}} \approx 10^{-3}$)

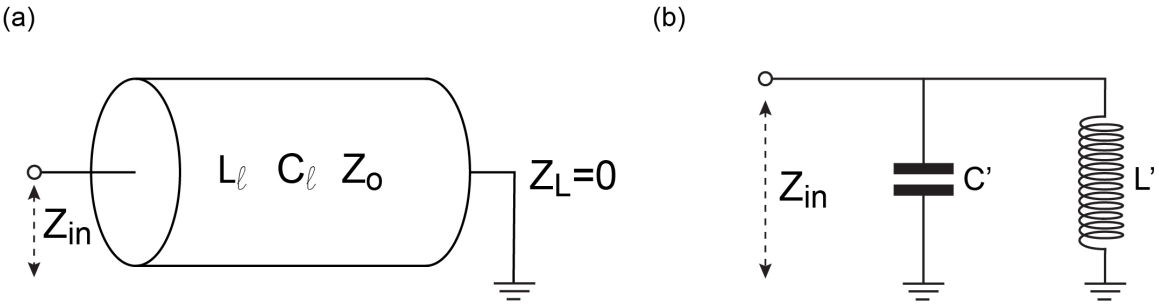

Figure 4.10: Modeling the shunting capacitance of the array. (a) Infinite transmission line terminated by a short is a good model of the array of Josephson junctions. (b) Equivalent circuit of an inductor in parallel with a capacitor. The capacitor C' effectively contributes to the total shunting capacitance of fluxonium circuit.

(see Table 6.1), indicating that the junction oxide is not as lossy as commonly believed at frequencies < 1 GHz.

Another dielectric loss channel in the Josephson junction array comes from the ground capacitance between the parallel conductors. To model this, let's first consider an infinite and lossless transmission line terminated by a short (see Fig. 4.10(a)), which roughly models the array. A transmission line having inductance and capacitance per unit length L_l and C_l, respectively, has a characteristic impedance $Z_o = \sqrt{L_l/C_l} = \sqrt{L/C}$, where $L = L_l \times l$, $C = C_l \times l$. The input impedance of the transmission line is then

$$Z_{\text{in}} = jZ_o \tan(\beta l), \tag{4.6}$$

where $\beta \equiv \omega\sqrt{L_l C_l}$ is the wave number. Expanding $\tan x = x + \frac{x^3}{3} + O(x^5)$ in Eq. 4.6, we get

$$Z_{\text{in}} \approx j\omega L \left(1 + \frac{\omega^2 LC}{3}\right). \tag{4.7}$$

Next, we consider the simple effective circuit in Fig. 4.10(b), where the shunting capacitance is C'. The input impedance for this circuit is

$$Z_{\text{in}} = \frac{i\omega L'}{1-\omega^2 L'C'} \approx j\omega L'(1+\omega^2 L'C'), \tag{4.8}$$

where we assume the circuit's resonance is much higher than the frequency range of interest, i.e. $\omega^2 \ll 1/L'C'$. From Eq. 4.6 and Eq. 4.8, we get $L' = L$ and $C' = C/3$. In our fluxonium circuits, the chain is made up of N junctions divided into two parallel lines (see Fig. 6.10), with the shunting capacitance per array junction $C_g \approx 36$ aF, determined from measurement of chain modes [120, 121]. The effective total capacitance is thus $C = NC_g/2$ for the transmission line, and $C' = NC_g/6$ for the effective circuit model. For a typical array consisting of 100 junctions, the estimated shunting capacitance from the chain is thus $C' \approx 0.6$ fF.

In our fluxonium designs, $C_{\text{shunt}} \approx 20$ fF $\gg C'$, where C_{shunt} is the shunting capacitance of the antenna. This tells us that the chain has a very small effect on the total capacitance. The ratio C'/C_{shunt} gives us a limit on the effective dielectric quality factor associated with the array. While the exact quantitative value of the array's participation ratio has not been determined, we can safely conclude that (i) the chain's effective dielectric loss must be > 20 times worse than the antenna's to degrade the circuit's performance, (ii) improving the circuit material should also increase the array's effective quality factor, and (iii) contribution from the array can be mitigated by constructing fewer junctions or making wider chain which has lower C_g.

4.2.2 Stimulated Emission

When the qubit transition frequency is low, we have to take the effect of temperature into account. As discussed in Appendix A, a resistor at finite temperature can produce stimulated emission and absorption, namely, it can relax and excite the qubit. In other words, it not

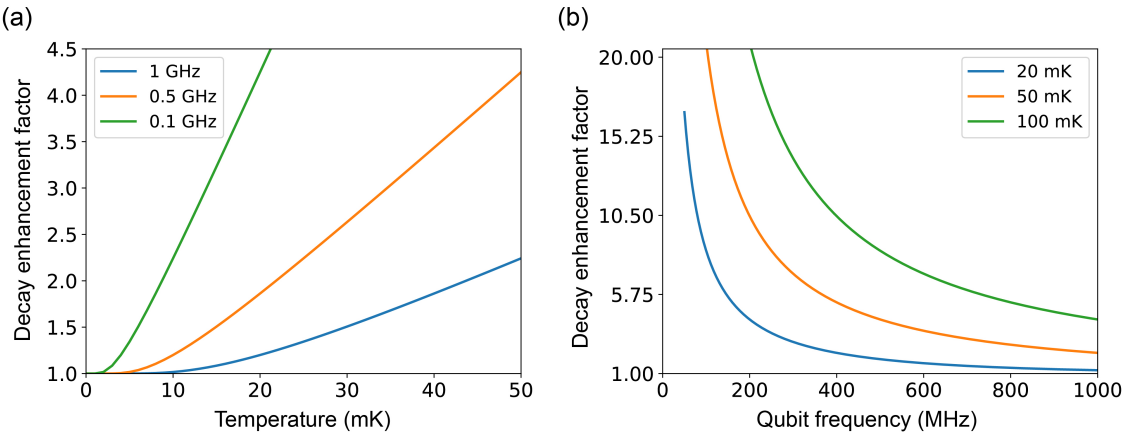

Figure 4.11: Effect of temperature on energy relaxation. The decay enhancement factor $\mathcal{E}_{\text{th}}$ in Eq. 4.9 is plotted for (a) Different qubit frequencies as a function of temperature, and (b) Different temperatures as a function of qubit frequency. As long as the qubit frequeny is in the 0.5-1 GHz range and the temperature is kept reasonably low, thermal effects on relaxation rate remain minimal.

only increases the relaxation rate, but also introduces an excitation rate. Both excitation and relaxation contribute to the decay to equilibrium $\Gamma_1 = \Gamma_\uparrow + \Gamma_\downarrow$. A hot qubit that has a low transition frequency will thus be a bad qubit.

We can examine the effect of temperature by considering the quantity

$$\mathcal{E}_{\text{th}} = \left(\left| \coth\left(\frac{\hbar\omega_{ij}}{2k_B T}\right) + 1 \right| + \left| \coth\left(\frac{-\hbar\omega_{ij}}{2k_B T}\right) + 1 \right| \right) /2, \tag{4.9}$$

where the factor of 2 corresponds to the case when temperature is zero. This can be considered as the *enhancement factor*. It is plotted in Fig. 4.11. This shows that if the qubit frequency is not too low (0.5 GHz is the typical threshold), the adverse effect from a finite temperature of 20 mK is minimal, and we can gain a quadratic improvement in relaxation time T_1 by operating at low frequency.

To account for temperature effects, the relaxation rate in Eq. 4.3 is analyzed at temperature $T = 20$ mK. It's likely that the effective temperature of the qubit is higher. Note that this can be compensated in our analysis by increasing the power factor ϵ of the dielectric

loss tangent in Eq. 4.4.

4.2.3 Quasiparticle Tunneling

Quasiparticles have been reported to affect the coherence of various types of superconducting circuits [87, 85, 88, 89, 54]. For the quasiparticles tunneling across the small junction, the corresponding relaxation rate using Eq. 3.23 is

$$\Gamma_{ij}^{\mathrm{qp}} = \left| \langle j | \sin \frac{\phi}{2} | i \rangle \right|^2 \times \frac{8E_J}{\pi\hbar} x_{\mathrm{qp}} \sqrt{\frac{2\Delta}{\hbar\omega_{ij}}}. \tag{4.10}$$

Notably, the matrix element coupling the qubit to quasiparticle tunneling is suppressed at the half-integer flux quantum bias, and fluxonium qubit becomes insensitive to this quasiparticle tunneling across the small junction (Fig. 4.12(a)).

We can extend Eq. 4.10 to account for quasiparticle tunneling across the chain junctions. Consider the general case in which $M+1$ junctions separating $M+1$ islands form a loop. When the inductance from the lead is much smaller than L_J, the phases across the junctions obey the flux quantization constraint:

$$\sum_{\beta=0}^{M+1} \phi_\beta = 2\pi k \frac{\Phi_e}{\Phi_o}, \tag{4.11}$$

where k takes non-zero integer values. The transition rate then follows from Eq. 3.23:

$$\Gamma_{ij}^{\mathrm{qp}} = \sum_{\beta=0}^{M+1} \left| \langle j | \sin \left(\frac{\phi_\beta}{2} \right) | i \rangle \right|^2 S_{\mathrm{qp}}(E_{J_\beta}, \omega_{ij}), \tag{4.12}$$

In fluxonium, an array of identical junctions of large Josephson energy $E_{J_1} = E_{J_2} = \ldots = E_{J_{M+1}}$ is connected to a weaker junction $E_{J_0} \ll E_{J_1}$. This gives $E_L \equiv E_{J_1}/M$. Here, we use the convention that $\beta = 0$ corresponds to the small tunneling junction. It is safe to assume that the phases across the array junctions are equal $\phi_{\beta\neq 0} = (\phi_o - 2\pi\Phi_e/\Phi_o)/M$.

Since individual phases across large array junctions are small, we can linearize the $\sin$ function for $\phi_{\beta\neq 0}$. We further approximate that the quasiparticle density on the array junctions are identical, so the relaxation rate due to quasiparticles in the array is

$$\Gamma_{ij}^{\mathrm{qp,array}} = \left|\langle j|\frac{\phi}{2}|i\rangle\right|^2 S_{\mathrm{qp}}(E_L, \omega_{ij}), \tag{4.13}$$

with $S_{\mathrm{qp}}(E_L, \omega_{ij})$ calculated by replacing E_J with E_L, starting from Eq. 4.10. In deriving Eq. 4.14, we use the property $\langle j|2\pi\Phi_e/\Phi_o|i\rangle = 0$ for $i \neq j$. We can write the explicit formula as

$$\Gamma_{ij}^{\mathrm{qp,array}} = \left|\langle j|\frac{\phi}{2}|i\rangle\right|^2 \frac{8E_L}{\pi\hbar} x_{\mathrm{qp}} \sqrt{\frac{2\Delta}{\hbar\omega_{01}}}. \tag{4.14}$$

In contrast to a single junction, the relaxation from quasiparticles in the array scales quadratically with the matrix element ϕ_{ij}, which is maximal at half-integer flux quantum for the $0 \to 1$ transition (Fig. 4.12(c)). We note that for the same T_1 limit, the quasiparticle density x_{qp} in the array has to be much less than that around the small junction.

Interestingly, the $0 \to 2$ transition is maximally sensitive to quasiparticles tunneling across the small junction (Fig. 4.12(b)) but insensitive to quasiparticle effect in the array (Fig. 4.12(d)). In addition, we can recall that $0 \to 2$ linear decay is suppressed due to selection rules. Thus, measuring T_1 for both $0 \to 1$ and $0 \to 2$ simultaneously in fluxonium would allow us to test for quasiparticle effects more rigorously.

A double loop fluxonium is an excellent testing device for quasiparticles. The $\sin \frac{\phi_{\{1,2\}}}{2}$ matrix elements never reach vanishing values simultaneously when we sweep the flux due to the finite value of flux through the small loop, as shown in Fig. 4.13. Interestingly, when the flux through the small loop reaches half-integer flux quantum value, the phases across the two small junctions are different by π, and one matrix element reaches a maximum, while the other reaches a minimum. As we move away from this flux bias, the situation

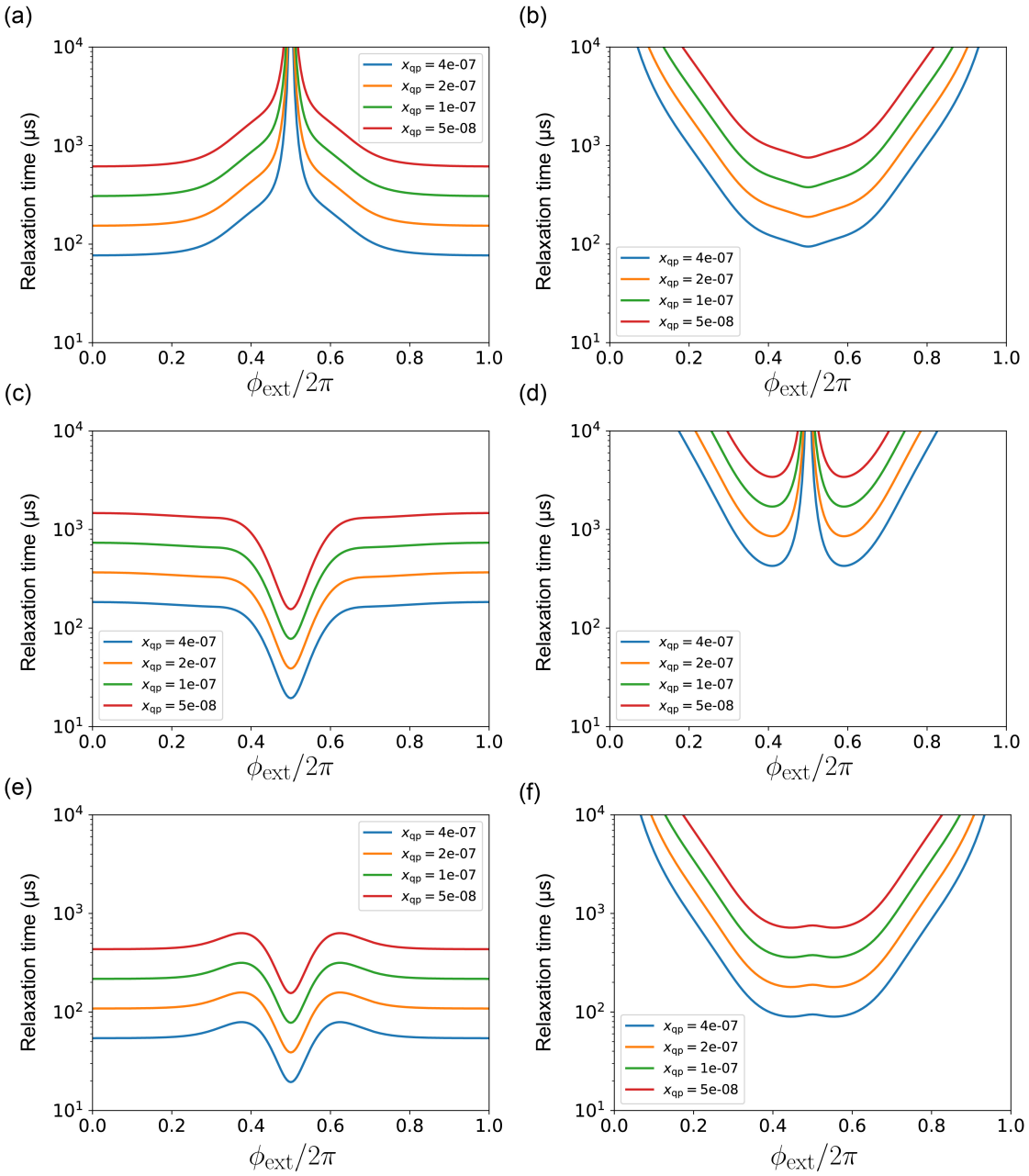

Figure 4.12: Simulation of T_1 limited by quasiparticle. Simulations performed using circuit parameters $E_C = 1$ GHz, $E_L = 1$ GHz, and $E_J = 3$ GHz. (a) $T_1^{0\to1}$ limited by quasiparticles tunneling across the small junction. (b) $T_1^{0\to2}$ limited by quasiparticles tunneling across the small junction. (c) $T_1^{0\to1}$ limited by quasiparticles tunneling in the chain. (d) $T_1^{0\to2}$ limited by quasiparticles tunneling in the chain. (e) $T_1^{0\to1}$ limited by both quasiparticles processes in (a) and (c). (f) $T_1^{0\to2}$ limited by both quasiparticles processes in (b) and (d).

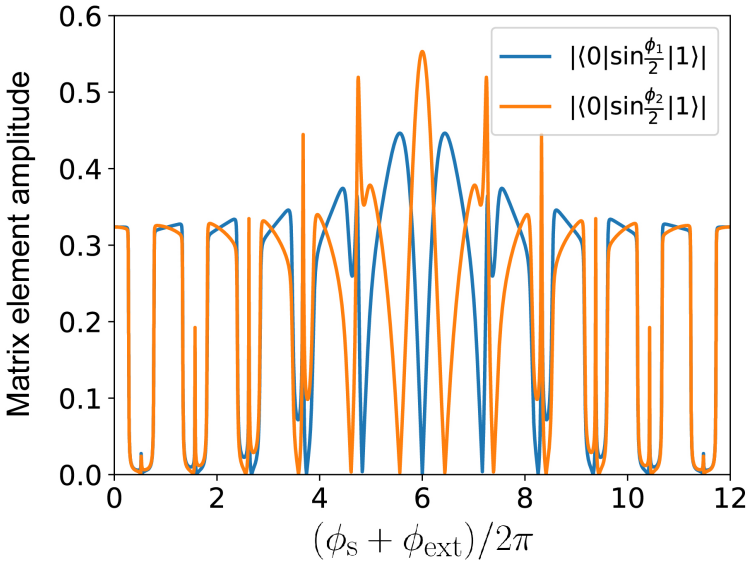

Figure 4.13: Matrix elements for quasiparticle relaxation in a split-junction device. Simulation of the $\sin\frac{\phi_{\{1,2\}}}{2}$ matrix elements in the split-junction device with the same parameters discussed in section 4.1.2. Due to the finite flux through the SQUID, the matrix elements never have the same vanishing values at the same flux. When the flux through the small loop reaches half-integer flux quantum value, one of the matrix elements reaches its maximum, making the circuit very sensitive to quasiparticles.

reverses. Therefore, if quasiparticles limit our relaxation time T_1, we should be able to observe the cross-overs near the small loop's half-integer flux quantum region. As reported in section 6.2, it is not the case, so we conclude that the device is not sensitive to quasiparticles, assuming that the theoretical model above is correct.

4.2.4 Thermal Photon Dephasing

Cavity Modes

It has been shown that in a cQED system, residual thermal photons inside the cavity can dephase the qubit by dispersively modifying its transition frequency [122, 54, 123]. Similar to any other superconducting circuit coupled to a resonator, fluxonium is also susceptible

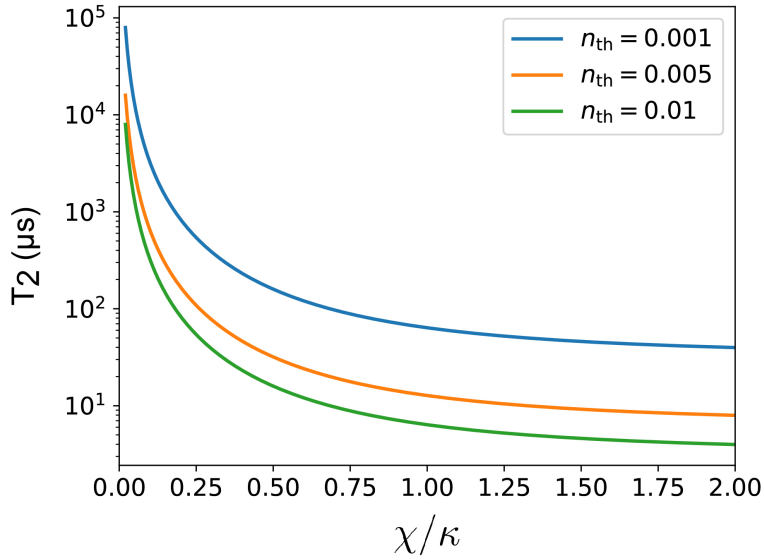

Figure 4.14: Simulation of T_2 limited by thermal photon in cavity. Coherence time limit from Eq. 3.51 for different average thermal photon numbers as a function of χ/κ, with $\kappa/2\pi = 5$ MHz.

to this dephasing mechanism. In high coherence devices reported in section 6.3, the small dispersive shifts (see Table 6.1) result in a very high coherence limit. This confirmed the approached used in previous studies to enhance coherence time limited by photon noise [102, 103]. However, we should consider strong dispersive case in future experiments. Specifically, from Eq. 3.51, the dephasing rate is

$$\Gamma_{\rm th} = \frac{n_{\rm th}^{\rm eff}\kappa\chi_{01}^2}{\kappa^2 + \chi_{01}^2}.$$

We can study the coherence limit of fluxonium with strong dispersive interaction by varying the dispersive shift χ_{01} and thermal photon numbers $n_{\rm th}^{\rm eff}$. The result corresponding to different average thermal photon numbers $n_{\rm th}$ is plotted in Fig. 4.14 for cavity coupling $\kappa/2\pi = 5$ MHz, which is the lower limit in our experiments. While the dephasing time is obviously bad for high photon numbers, large dispersive shift does not necessarily limit T_2

if we take care to lower the effective cavity photon temperature, which has been achieved in previous cQED experiments [124, 123, 125].

Recent experiments with fluxonium in our lab typically involve $\chi/\kappa \approx 1$, and the coherence time is high, $T_2 > 100\ \mu$s. This suggests that the effective thermal photon number is $n_{\rm th} \leq 0.001$ in our latest experiments.

Collective Modes

In fluxonium, the chain modes which couple to the qubit can be populated by thermal photons, therefore may contribute to decoherence. As discussed previously, the array of junctions can be considered a transmission line. In our fluxonium design, it is shorted at one end, and thus acts as a quarter-wavelength resonator [120, 121] with resonant microwave modes. These modes can be divided into even (superscripted as e) modes which interact with the qubit, and odd modes (superscripted as o) which interact among themselves. Changes in the occupation of the even modes can thus dephase the qubit. In addition, the nonlinearity of the array junctions gives rise to the dependence of the inductive energy E_L on the occupations of collective modes, creating another dephasing channel. We follow the formalism developed in ref. [126] to compute the possible dephasing rate due to the collective modes below.

The coupling coefficient of mode ρ is given by

$$g_{2\rho} = \frac{4}{\sqrt{2N}} \frac{E_C^{\phi} E_{C,\rho}^{e}}{E_g^{a}} \frac{c_{2\rho}}{s_{2\rho}^2}, \tag{4.15}$$

where N is the number of junctions in the chain, $c_{2\rho} = \cos\frac{\pi\rho}{N}$, $s_{2\rho} = \sin\frac{\pi\rho}{N}$, and $\tilde{E}_C^{\phi}$ is the qubit mode's charging energy normalized by the chain and ground capacitances (subscripted as g), and

$$\frac{1}{E_C^{\phi}} = \frac{1}{E_C^{b}} + \frac{1}{N E_C^{a}} + \frac{1}{4E_t}\left(1 - \frac{2}{3}\frac{N+1}{N}\lambda\right). \tag{4.16}$$

Table 4.1: Parameters for collective modes simulation.

E_C^b	E_L	E_J^b	E_J^a	C_g^a	C_a	C_c	g_q	$\kappa/2\pi$	N
1 GHz	1 GHz	3 GHz	150 GHz	36 aF	36 fF	1 fF	0.1 GHz	5 MHz	100

Here, the total capacitance that determines E_t is given as

$$C_t = 2(C_g^b + C_c) + (N-1)C_g^a, \tag{4.17}$$

and the dimensionless parameter λ is defined as

$$\lambda = \frac{(N-1)C_g^a}{C_t} = \frac{(N-1)E_t}{E_g^a}. \tag{4.18}$$

The normalized array junction charging energy for the even mode ρ is defined via

$$\frac{1}{E_{C,\rho}^e} = \frac{1}{E_C^a} + \frac{1}{4E_g^a s_\rho^2}. \tag{4.19}$$

These modes have frequencies

$$\omega_\rho = \sqrt{8E_{C,\rho}^e E_J^a}, \tag{4.20}$$

and would have dispersive shifts

$$\chi_\rho = \frac{1}{2}\sqrt{\frac{E_J^a}{8E_{C,\rho}^e}}g_\rho^2 \times \left[|\langle 0|\hat{n}|1\rangle|^2 \frac{2\omega_{10}}{\omega_{10}^2 - \omega_\rho^2} + \sum_{l\geq 2}|\langle 0|\hat{n}|l\rangle|^2 \frac{\omega_{l0}}{\omega_{l0}^2 - \omega_\rho^2} + \sum_{l\geq 2}|\langle 1|\hat{n}|l\rangle|^2 \frac{\omega_{l1}}{\omega_{l1}^2 - \omega_\rho^2}\right]. \tag{4.21}$$

In addition, if we take into account the nonlinearity of the junctions array, we would see a dependence of the inductive energy E_L on the collective modes' occupation. This leads to variation of the qubit frequency, and consequently qubit dephasing. We can model this

frequency dependence as a dispersive shift $\chi_\mu^{\delta E_L}$,

$$\chi_\rho^{\delta E_L} = \frac{1}{2}\frac{\partial \omega_{10}}{\partial E_L}\frac{E_L l_\rho^2}{2N}. \tag{4.22}$$

The photons occupying the collective modes can decay via the coupling of the qubit to the cavity mode. Considering the emission of the qubit excitation to the bath, we can use Fermi's golden rule to derive the Purcell decay rate,

$$\kappa_q = \frac{\kappa g_q^2}{(\omega_q - \omega_c)^2}, \tag{4.23}$$

where κ is the coupling rate of the cavity, and g_q is the cavity-qubit coupling,

$$g_q = 2eV\frac{E_c^\phi}{E_C^c}\langle 0|n|1\rangle. \tag{4.24}$$

The collective modes decay rate in the dispersive limit is given by

$$\kappa_\rho = \frac{\kappa}{(\omega_\rho - \omega_c)^2}\left[\frac{eV}{4E_C^c}g_\rho\frac{1}{\sqrt{2}l_\rho}\right]^2. \tag{4.25}$$

Using Eq. 4.24, we can write Eq. 4.25 in terms of g_q, g_ρ, and other known parameters.

We simulate the coupling coefficients g_ρ, mode frequencies ω_ρ, decay rates κ_ρ, dispersive shifts χ_ρ for even modes, and $\chi_\rho^{\delta E_L}$ resulted from nonlinear effect using the parameters provided in Table 4.1. Each mode would dephase the qubit at a rate given by Eq. 3.50. Assuming the effective occupation number of each mode to be equal, $n_\rho = 0.01$, we estimate the coherence time T_2 to be of order ≈ 100 ms. This long time scale is mostly due to the slow decay rate κ_ρ of the collective modes. We note that the rate given by Eq. 4.25 corresponds only to Purcell effect, and the photons may decay faster through other channels. Our simulation results suggest that the thermal photons in the chain modes at higher frequencies would unlikely contribute to dephasing in fluxonium. However, proper shielding

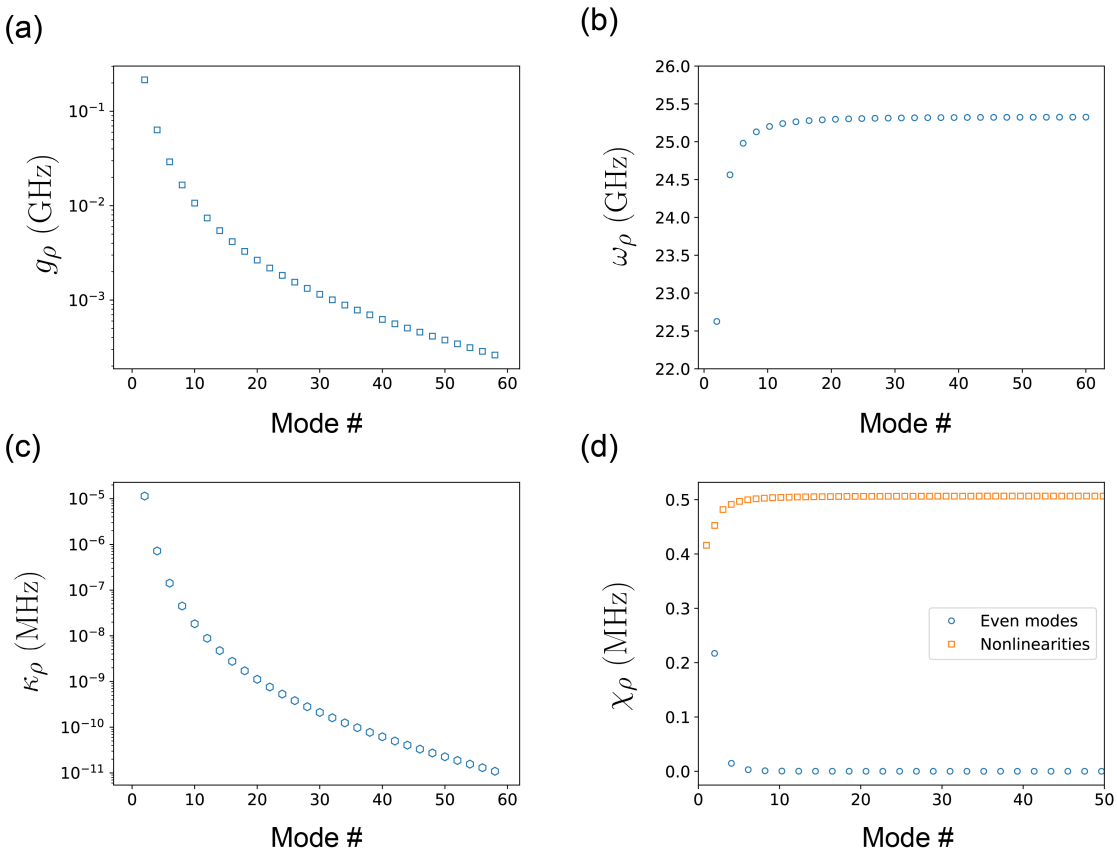

Figure 4.15: Simulation of dephasing by photons occupying collective modes. (a) Coupling coefficient $g_{2\rho}$ for even modes. (b) Frequencies $\omega_{2\rho}$ of even modes. (c) Decay rate of collective modes. (d) Dispersive shifts of even modes and changes in E_L resulted from array-junction nonlinearities.

and filtering techniques should still be employed to keep n_ρ low.

4.3 Fluxonium Readout

We discuss dispersive readout of fluxonium in this section. The dispersive shift between two different energy eigenstates $|i\rangle$ and $|j\rangle$ in fluxonium can be derived using second order

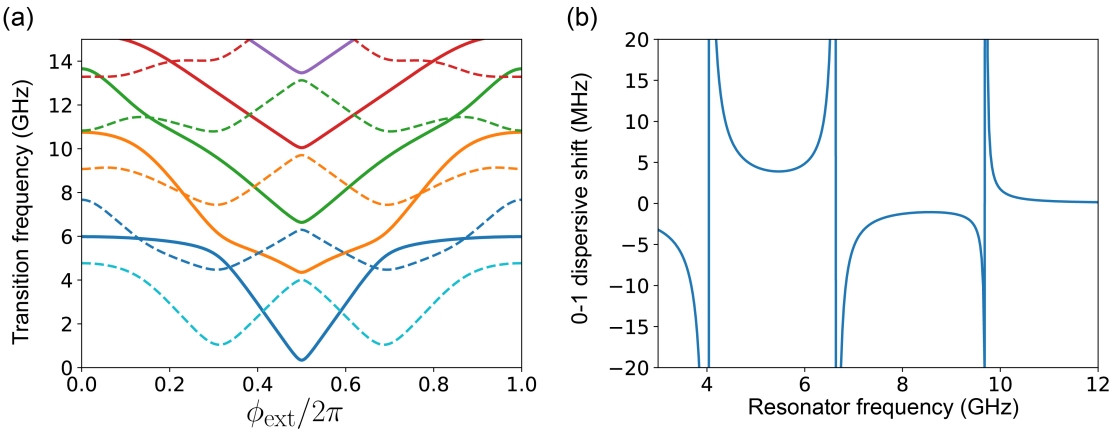

Figure 4.16: Simulation of dispersive shift. (a) Transition energy spectrum of a fluxonium circuit with $E_C = 1$ GHz, $E_L = 1$ GHz, and $E_J = 5$ GHz. Transitions from $|0\rangle$ are plotted in solid, and transitions from $|1\rangle$ are plotted in dashed lines. (b) Dispersive shift of the $0 \to 1$ transition as a function of resonator frequency at the half-integer flux quantum bias. Whenever a higher qubit transition crosses the cavity resonance, the dispersive shift given by Eq. 4.26 diverges.

perturbation [127],

$$\chi_{ij} = g_{qR}^2 \left(\sum_{k \neq i} |n_{ik}|^2 \frac{2f_{ik}}{f_{ik}^2 - f_r^2} - \sum_{k \neq j} |n_{jk}|^2 \frac{2f_{jk}}{f_{jk}^2 - f_r^2} \right), \tag{4.26}$$

where f_r is the resonator's resonant frequency. We can immediately deduce from this analytic formula that direct interaction between the transition $|i\rangle \to |j\rangle$ and the cavity is not important. In fact, the best strategy to enhance dispersive shifts in fluxonium circuits is to engineer the qubit to have a transition frequency f_{ik} near the cavity resonant frequency, as illustrated in Fig. 4.16 for a fluxonium circuit with parameters $E_C = 1$ GHz, $E_L = 1$ GHz, and $E_J = 5$ GHz. This strategy was used to enhance the readout in two-qubit devices where strong joint readout is required.

Increasing the coupling coefficient g_{qR} is the more straightforward strategy, however, as we cannot always engineer the spectrum of the qubit or choose an arbitrary cavity resonant

frequency. Design and simulation of 3D cavity and the cavity-qubit coupling are discussed in more details in section 5.2.

4.4 Multi-Fluxonium Circuits

4.4.1 Capacitively Coupled Fluxoniums

Two fluxonium circuits capacitively coupled via a capacitor C_M can be described by the Hamiltonian

$$H = H_A + H_B + J_C n_A n_B, \tag{4.27}$$

where n_α is the reduced charge on capacitor C_α, $J_C = 4e^2 C_M/(C_A C_B)$ in the limit $C_M \ll C_A,\ C_B$, and H_A, H_B are the uncoupled fluxonium Hamiltonians. We note that C_M also slightly renormalizes the charging energy E_C^α. Our analysis focuses on the half-integer flux quantum bias where the qubit transition $0 \to 1$ has high coherence.

From Fig. 4.5(a), we see that $n^\alpha_{0\to1}$ is smaller than the charge matrix elements of other transitions $n^\alpha_{i\to j}$ at the flux sweet spot. This reduces the interaction between the computational states compared to that of higher states. This can be illustrated by inspecting the energy levels of two fluxonium circuits with varying coupling constant J_C. For this purpose, we study two capacitively coupled fluxonium qubits (Fig. 4.17(a)) with $E_C^A = E_C^B = 1$ GHz, $E_L^A = 1$ GHz, $E_L^B = 1.5$ GHz, $E_J^A = 5$ GHz, and $E_J^B = 5.5$ GHz. We follow the notation convention $|kl\rangle_0 = |k_A\rangle|l_B\rangle$ for bare state and $|kl\rangle$ for dressed state.

In Fig. 4.17(b), we see that due to the small charge matrix elements associated with computational transitions, the computational states $|00\rangle$, $|10\rangle$, $|01\rangle$, $|11\rangle$ are minimally disturbed. Because $n_{1\to2} \gg n_{0\to1}$, the states $|12\rangle$ and $|21\rangle$ push each other strongly with increasing J_C. States $|02\rangle$ and $|20\rangle$ are relatively unperturbed because the uncoupled matrix elements $n_{0\to2}$ and $n_{2\to2}$ vanish at half-integer flux quantum. Here we emphasize that only eigenstates with similar eigenenergies would repel each other. For example, the pair

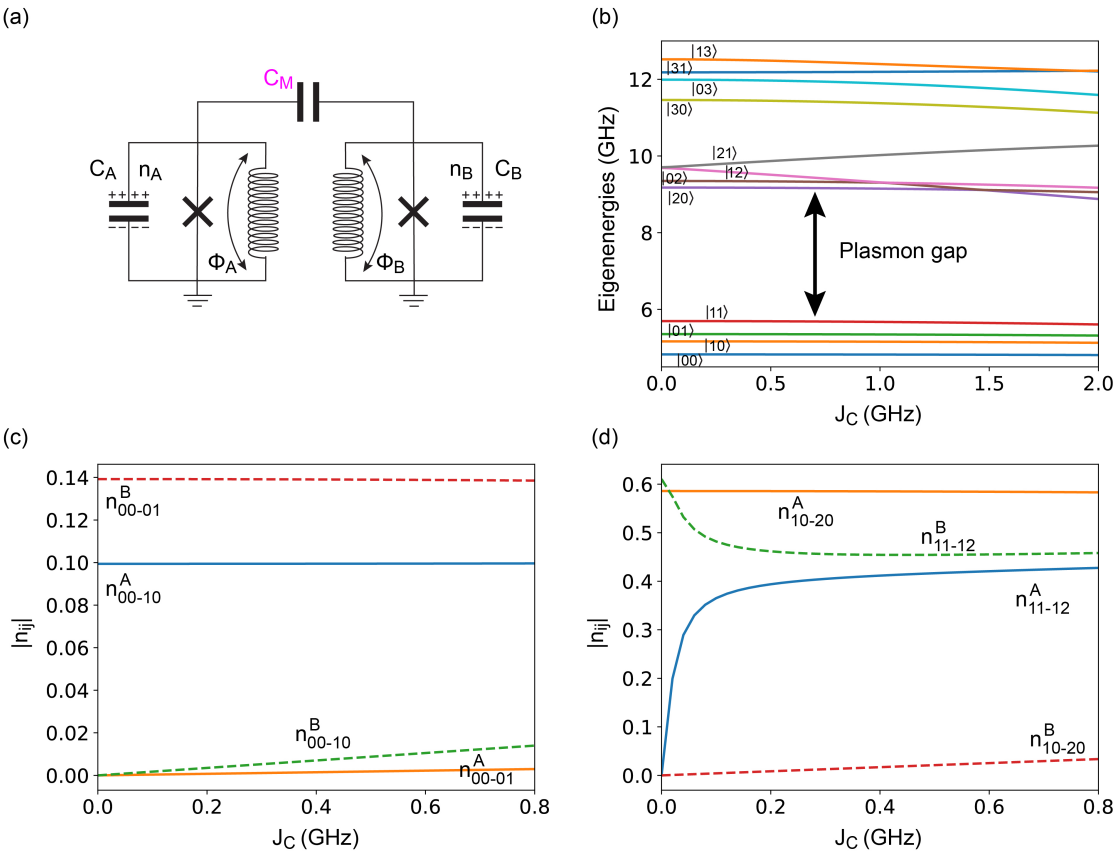

Figure 4.17: Capacitively coupled fluxoniums. (a) Circuit diagram of two capacitively coupled fluxonium qubits. In the small coupling limit, the ratio $C_M/(C_A C_B)$ determines the coupling strength. (b) Eigenenergies of the coupled system versus the coupling strength J_C at the half-integer flux bias. The computational states are minimally disturbed, while the $|12\rangle$ and $|21\rangle$ states push each other strongly. (c) Matrix elements of computational transitions versus the coupling strength J_C. n^A's are plotted in solid, and n^B's are plotted in dashed lines. $n^B_{00\to10}$ becomes non-zero due to mixing of $|00\rangle$ and $|10\rangle$ with higher states. $n^A_{00\to01}$ turns on much slower because the corresponding interference of all contributions is negative. (d) Matrix elements of higher transitions versus coupling strength J_C. States $|12\rangle$ and $|21\rangle$ interact strongly with increasing J_C, leading to the renormalization of $n^{A,B}_{11\to12}$.

of states $|20\rangle$ and $|13\rangle$ are not close, therefore do not repel each other despite having large matrix element between them.

Interestingly, due to the dressing of states, some matrix elements are renormalized. As shown in Fig. 4.17(c), the charge matrix element $n^B_{00\to10}$ becomes finite as the coupling

strength increases, due to the mixing of computational states. Roughly speaking, we can write

$$\begin{aligned}
|00\rangle &= a_{00}|00\rangle_0 + a_{11}|11\rangle_0 + a_{31}|31\rangle_0 + a_{13}|13\rangle_0 + \ldots, \\
|10\rangle &= b_{10}|10\rangle_0 + b_{01}|01\rangle_0 + b_{03}|03\rangle_0 + b_{21}|21\rangle_0 + \ldots, \\
|01\rangle &= c_{01}|01\rangle_0 + c_{10}|10\rangle_0 + c_{30}|30\rangle_0 + c_{12}|12\rangle_0 + \ldots, \\
|11\rangle &= d_{11}|11\rangle_0 + d_{00}|00\rangle_0 + d_{20}|20\rangle_0 + d_{02}|02\rangle_0 + \ldots,
\end{aligned} \tag{4.28}$$

which are perturbative to first order in J_C, with $a_{00} = b_{10} = c_{01} = d_{11} = 1$, and other coefficients depend linearly on J_C. As a result, $|00\rangle$ mixes with $|11\rangle_0$ and $|13\rangle_0$, while $|10\rangle$ mixes with $|01\rangle_0$ and $|03\rangle_0$ at finite J_C. All these contributions make $\langle 00|n_B|10\rangle$ increase with J_C. On the other hand, $\langle 00|n_A|01\rangle$ is relatively unaffected because the interference between the contributions is negative.

In Fig. 4.17(d), the direct interaction between $|12\rangle$ and $|21\rangle$ causes them to hybridize strongly and renormalizes $n^A_{11\to12}$ and $n^B_{11\to12}$. In addition, $n^B_{10\to20}$ also becomes finite when the coupling is turned on, due to the dressing of $|10\rangle$ and $|20\rangle$.

4.4.2 Inductively Coupled Fluxoniums

In a similar fashion, two fluxonium qubits coupled inductively via a mutual inductor L_M (Fig. 4.5(a)) can be described by the Hamiltonian

$$H = H_A + H_B - J_L \phi_A \phi_B, \tag{4.29}$$

where ϕ_α is the reduced flux across the inductor L_α, $J_L = \left(\frac{\hbar}{2e}\right)^2 \frac{L_M}{L_A L_B}$ is the qubit-qubit inductive coupling constant in the limit $L_M \ll L_A,\ L_B$, and H_A, H_B are the uncoupled fluxonium Hamiltonians. We note that L_M slightly modifies $E_{L\alpha}$.

From Fig. 4.5(b), we see that $\phi_{0\to1}$ is large at half flux quantum. This causes strong mixing of the computational states. We can confirm this by inspecting the eigenenergies of two inductively coupled fluxonium qubits biased at half flux quantum with parameters

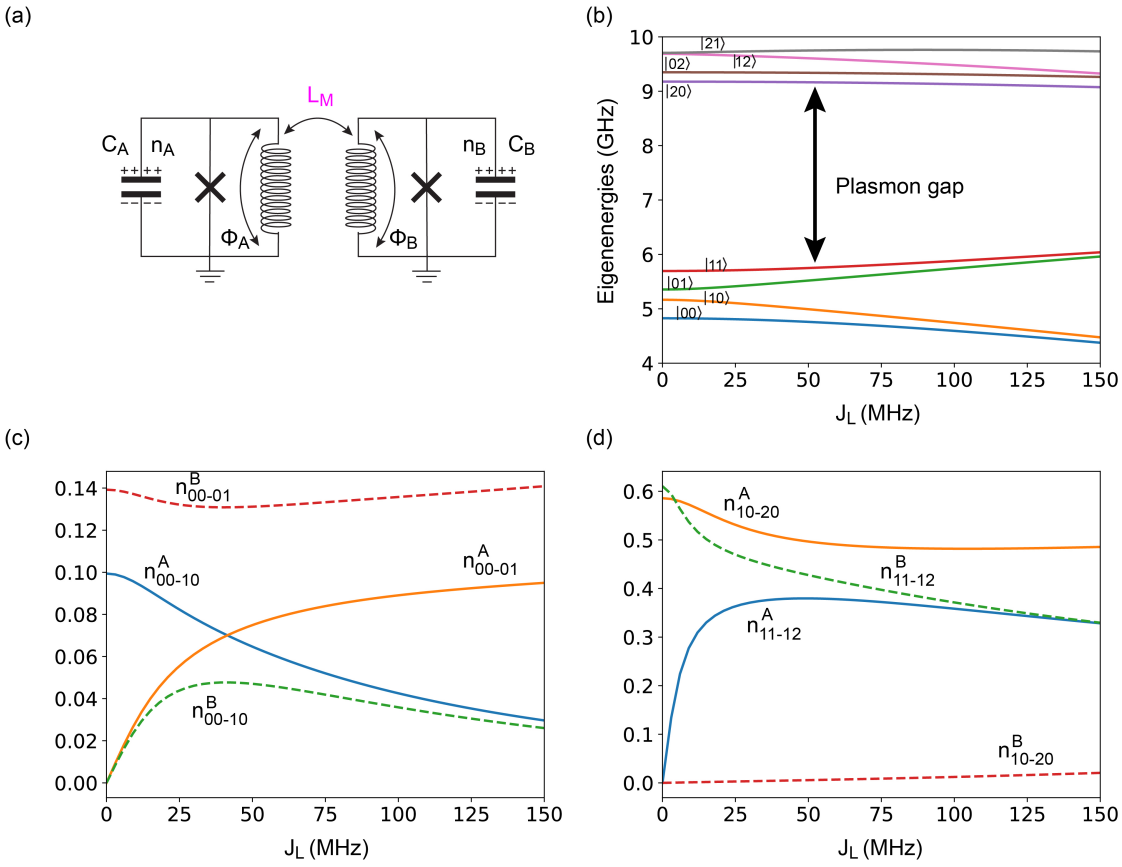

Figure 4.18: Inductively coupled fluxoniums. (a) Circuit model of two inductively coupled fluxonium qubits. In the small coupling limit, the ratio $L_M/(L_A L_B)$ determines the coupling strength. (b) Eigenenergies of the coupled system versus the coupling strength J_L at the half-integer flux bias. Due to the strong $0 \to 1$ phase matrix element, the computational eigenstates become strongly hybridized. (c) Charge matrix elements of computational transitions versus the coupling strength J_L. n^A's are plotted in solid, and n^B's are plotted in dashed lines. The strong mixing of the computational states results in large changes in the matrix elements with respect to J_L. (d) Charge matrix elements of higher transitions versus coupling strength J_L.

$E_C^A = E_C^B = 1$ GHz, $E_L^A = 1$ GHz, $E_L^B = 1.5$ GHz, $E_J^A = 5$ GHz, $E_J^B = 5.5$ GHz, and varying J_L (Fig. 4.18(b)). We observe that the $|01\rangle$ and $|10\rangle$ states push each other strongly even at small coupling value $J_L \approx 50$ MHz.

The mixing of these computational states leads to strong renormalization of the corresponding matrix elements, for example, $n^A_{00\to10}$ and $n^B_{00\to10}$, as shown in Fig. 4.18(c). The

mixing of higher states is not as dramatic, but still results in strongly dressed states at a modest coupling value $J_L \approx 100$ MHz (Fig. 4.18(b)). Consequently, $n^{A,B}_{11\to12}$ are renormalized rapidly with the coupling coefficient J_L. On the other hand, the negative interference between the relevant states leaves $n^{B}_{10\to20}$ relatively unchanged (Fig. 4.18(d)).

4.4.3 Microwave-Activated Controlled-Z Entangling Gate

In atomic systems, qubit states are protected from environmental noise and have long coherence, whereas quantum gates and readout are performed via transitions outside of the computational subspace. This separation of states in quantum information storage and processing allows both long coherence and fast operation. Since fluxonium has energy spectra and selection rules similar to natural atoms, recent experimental achievements in atomic systems motivate us to consider using higher levels to perform a two-qubit entangling operation. Simulations of two capacitively coupled fluxonium showing strong mixing of higher states and minimal perturbation to the computational space, illustrated in Fig. 4.17, further strengthens this idea.

Following this direction, a recent paper [128] proposes a controlled-Z gate for two fluxoniums with an always-on interaction. The gate is activated by a microwave pulse near the $|1\rangle \to |2\rangle$ transition of either qubit. Numerical simulations in the paper shows promising fidelity, above 99.9% for gate time below 100 ns when decoherence is neglected. Here, we focus on the capacitive coupling case which has been investigated in the lab. Preliminary experimental results are reported in section 6.4.

The main idea of the CZ gate is as follows. When there is no coupling, $\omega_{01\to02} = \omega_{11\to12} = \omega^{B}_{1\to2}$, and we cannot selectively drive $|11\rangle \leftrightarrow |12\rangle$. As the interaction J_C is turned on, $|12\rangle$ and $|21\rangle$ push each other apart due to the high single-qubit matrix element $n_{1\to2}$, while $|02\rangle$ and $|20\rangle$ remain relatively unperturbed. This lifts the degeneracy above. The CZ gate can then be realized by selectively driving $|11\rangle \leftrightarrow |12\rangle$ (or $|11\rangle \leftrightarrow |21\rangle$). One oscillation

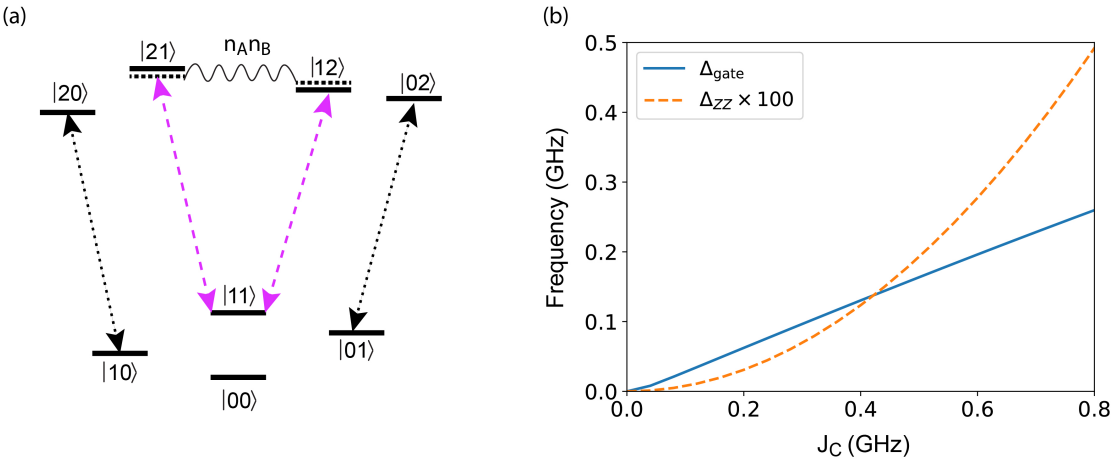

Figure 4.19: Microwave-activated controlled-Z gate. (a) Microwave-activated controlled-Z gate scheme. The large matrix elements $n^{A,B}_{1\to2}$ push the dressed states $|12\rangle$ and $|21\rangle$ apart, lifting the degeneracy. This allows us to selectively drive either $|11\rangle - |21\rangle$ or $|11\rangle - |12\rangle$ (magenta) to realize the CZ unitary. (b) Gate rate and spurious ZZ coupling versus J_C. The gate rate (solid) is typically much higher than the spurious coupling (dashed). We note that the ZZ coupling turns on rapidly with J_C, compared to the gate rate, so optimal configuration may be obtained in the region where $J_C < 200$ MHz for this pair of qubits.

$|11\rangle \to |12\rangle \to |11\rangle$ (or $|11\rangle \to |21\rangle \to |11\rangle$) results in a phase factor $e^{i\pi}$ for state $|11\rangle$. This operation is thus equivalent to applying the unitary operator $U_{\rm CZ} = \mathrm{diag}(1, 1, 1, -1)$ to the computational subspace. The idea is illustrated in Fig. 4.19(a).

We can define a gate rate [129], which is characterized by the frequency mismatch $\Delta_{\rm gate} = f_{01\to02} - f_{11\to12}$. It increases with decreasing $\delta = |f^A_{1\to2} - f^B_{1\to2}|$ and increasing J_C. This implies that smaller δ generally leads to better performing CZ gate.

On the other hand, the always on interaction introduces a spurious ZZ coupling $\Delta_{ZZ} = |f_{01\to11} - f_{00\to10}|$, which creates error during the entangling operation. The ZZ coupling also affects our single-qubit gate fidelity [130]. This can be interpreted as the dispersive shift between two qubits: the transition frequency of qubit A depends on the state of qubit B, and vice versa. We note that the ZZ coupling itself can be employed to realize an entangling gate. To examine the difference between the gate rate and the ZZ coupling rate, we simulate

Δ_{gate} and Δ_{ZZ} using the parameters from Fig. 4.17, and plot the results in Fig. 4.19(b).

To minimize this spurious effect, we can straightforwardly decrease the coupling strength J_C at the expense of slowing down the CZ gate rate. We note that for the pair of qubits being examined, the ZZ coupling turns on rapidly with J_C, compared to the gate rate, so having $J_C < 200$ MHz is preferable in this case. Another option is to engineer the precise spectrum of two fluxonium circuits to cancel out this effect, which will be the focus of future research.

Chapter 5

Experimental Techniques

He stepped down, trying not to look long at her, as if she were the sun, yet he saw her, like the sun, even without looking.

Leo Tolstoy

Exciting quantum phenomena can only be revealed once excellent engineering steps are taken to design and set up the experiments. This chapter describes our philosophies and approaches in cryogenic experimental setup (section 5.1), simulation and design of 3D cavities (section 5.2), practical considerations regarding microwave electronics (section 5.3), and fabrication techniques (section 5.4).

5.1 Cryogenic Setup

Cryogenic engineering lies at the heart of superconducting qubit experiments. In order to observe quantum mechanical behaviors in these macroscopic systems, it is necessary to get rid of thermal effects. For example, a body with mass m at temperature T radiates electromagnetic photon flux following Planck's law of black body radiation, which can easily smear out any quantum effect if T is high. A qubit with transition frequency of a few GHz is constantly excited to a mixed equilibrium state at room temperature. In order for

the system to display quantum behaviors, it is necessary to cool it down sufficiently and isolate it from external environment. In this section, we will review how to set up the experiment in a dilution refrigerator and the approaches we use to isolate our devices from the environment.

The ideal quantum experiment would take place at the absolute temperature of 0 kelvin, but it's not possible to reach this temperature with current technology. However, advances in cryogenic engineering currently allow construction of modern dilution refrigerators which can cool down to below 10 mK, two orders of magnitude colder than the interstellar vacuum space. The base plate of such a fridge is where the quantum phenomena in superconducting circuits occur.

5.1.1 Material Consideration

Setting up a cryogenic experiment requires the knowledge of relevant properties of materials at low temperatures, in particular their thermal expansion, thermal conductivity, and electrical conductivity.

The thermal vibration of atoms changes with temperature, resulting in a difference in these atoms' average separations. Materials subsequently expand at higher temperature and contract at lower temperature. Thermal expansion or contraction must be taken into account when choosing materials for parts in the experiment, especially for the nuts and screws used to connect different components together. Tight screw joints may become loose at low temperature if materials are chosen poorly. Thermal contact can generally be improved after cooldown by the addition of a washer with low thermal expansion coefficient under the screw/nut with higher expansion coefficient.

In cryogenic experiments, we typically use four different metals: copper, brass, stainless steel, and aluminum. In general, brass has a higher expansion coefficient than copper and stainless steel, so we typically use brass screws and stainless steel washer if possible. As

the temperature drops, brass screws contract more than the stainless steel or copper parts, and can create a pressing force to keep the parts together. Brass is also a decent thermal conductor, so using a brass screw to establish a direct thermal link between the fridge and the electrical component is another good approach to thermalize the components.

In solids, heat can be transported via two mechanisms. In insulators, only lattice vibrations are there to transport heat, while in conductors, free electrons from the conduction band near the Fermi energy can also carry heat. The characteristic velocity of phonons is the sound velocity, which is about three order of magnitudes lower than the Fermi velocity of free electrons. Therefore, insulators are generally poor thermal conductors at low temperature ($T < 1$ K), and metals are generally good thermal conductors [131]. However, we should keep in mind that certain metals can become superconducting below their critical temperatures. In the superconducting state, the free electrons form Cooper pairs which cannot carry heat. The thermal conductivity of a superconductor below T_c is thus only as good as that of an insulator.

For thermal conduction, copper is considered the king of all materials in cryogenic environment due to its high thermal conductivity at low temperature and its relatively low cost. Stainless steel is a poor thermal conductor, so it can be used when thermal isolation is desired. Alumninum becomes superconducting below $T_c = 1.2$ K, so it is a bad thermal conductor at mK range. Our general approach is to use copper where thermal conduction is desired, and stainless steel where thermal isolation is needed. Using insulators such as plastic tapes inside the fridge should generally be avoided, because they cool down very slowly

5.1.2 Shields

Another path through which heat can be carried inside the fridge is via black body radiation, where thermal photons are emitted from a stage at higher temperature and absorbed

by components at lower temperatures. This effect is small compared to heat transferred by solid or gas. While residual thermal photons may not heat up the fridge, they can affect qubits and cavities, so protection against thermal photons is crucial in achieving high coherence [132].

In practice, several metal cans are put together successively at each stage of the refrigerator to block the radiation from parts of the fridge at higher temperatures. In addition, a gold plated copper radiation shield can be custom-ordered from BlueFors to further protect the bottom part of the fridge. Despite the protection provided by the metal cans discussed above, hot photons may leak through crevasses between metal joints, and high energy radiation may pass through thin metal shields as well. We seal those small openings with copper tape before each cooldown.

In addition to the metal shields, a mixture of Stycast 2850 and carbon powder can be used to paint the inside of the radiation shield and absorb stray infrared photons [133]. We initially implemented this type of black paint but abandoned it after a few cooldowns to make room for more cryogenic components. Its effect on fluxonium's coherence thus remains inconclusive. A single layer of cryoperm magnetic shield surrounding the cold finger at 10 mK provides further protection against spacial electromagnetic radiation.

In recent experiments starting from Summer 2019, we have been using several layers of μ-metal shields at room temperature to minimize stray magnetic field from neighboring labs. Recent investigation has concluded that high energy radiation may be the source that generates quasiparticles, and room temperature shielding helps protect superconducting circuit systems [92]. Interestingly, this result is consistent with our best coherence data obtained from the setup with additional room temperature shields.

5.1.3 Filters

The experimental lines connecting the device under test (DUT) inside the fridge to the classical electronics equipment at room temperature may allow thermal photons to propagate and disturb the system. These measurement lines must therefore allow passage of applied microwave signal at a few GHZ range and at the same time block out the rest of the electromagnetic spectrum. For this purpose, we employ separate techniques for the input and output lines.

The complete setup of the fridge is shown in Fig 5.1. We change the specific placement of the components from time to time to accommodate new components and measurement lines.

Input Line

For the input line, since we can control the power of the drive signal to overcome dissipation along the way, the best general strategy in reducing hot photons from room temperature is to use commercial XMA cryogenic attenuators. This approach is generally cheap and reasonably effective. The total attenuation should be low enough to allow RF signal generated by electrical equipment at room temperature to reach the base plate with sufficient power. Three important details determine how well we actually isolate the system from thermal photons at higher temperatures: the placement of the attenuators, their thermalization, cooling powers, and working frequencies.

Electrically speaking, attenuators are simply resistors (or networks of resistors). Thus, they attenuate input photons, and also generate thermal photons corresponding to the temperatures of their bodies. The effective temperature of the output of an attenuator at a fixed frequency f is written as

$$T_{\text{out}} = T_a + A \times T_{\text{in}}, \tag{5.1}$$

where $T_{\text{in,out}}$ are the effective temperatures of the input and output photons, T_a is the

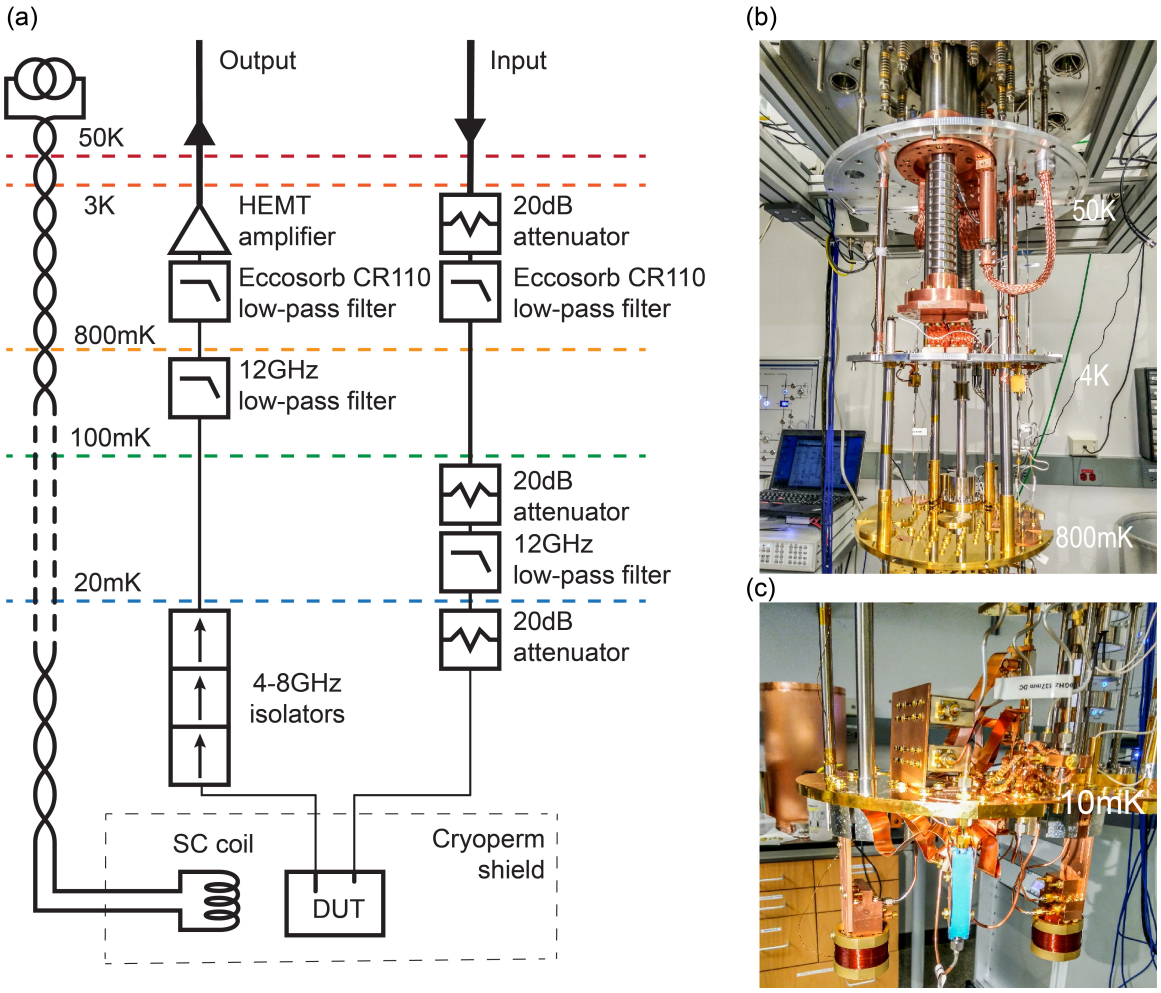

Figure 5.1: Cryogenic setup. (a) Typical experimental setup for high coherence fluxonium qubits. Recent addition of the TWPA at the base plate comes with an additional double-junction circulator, also in 4-8 GHz range. (b) Dilution fridge. (c) Base plate setup.

temperature of the attenuator, and $A = 1/G$ is the attenuation factor[1]. If the fridge had infinite cooling power at 10 mK, it would then be ideal to place all the attenuators there. Unfortunately, this is not the case, and the cooling power at different stages of the fridge has to be taken into account. For example, the cooling power at the cold plate of the BlueFors LD 250 fridge is around $300\ \mu$W while it is only around $14\ \mu$W at the base plate. As a result, it is better to distribute the attenuation. We can approximate the effective noise

[1]The attenuation A typically depends on frequency f.

temperature of the input line at the mixing chamber with an arbitrary configuration of attenuation distribution using

$$S_{\text{eff}} = S(10\ \text{mK}) + A_{10\ \text{mK}}(S(100\ \text{mK}) + A_{10\ \ \text{mK}}(S(4\ \text{K}) + A_{4\ \text{K}}S(300\ \text{K}))), \tag{5.2}$$

where $S(T)$ is the noise spectral density of a resistor at temperature T.

In our setup, 20 dB XMA cryogenic attenuators are placed at 4 K, 100 mK, and 10 mK plates, which should naively reduce the hot flux of photons at 300 K to a sufficiently low amount at the mixing plate [122, 123]. This approximation is only accurate if (i) the attenuators are thermalized to equilibrium at the expected temperatures, and (ii) the attenuators work at all frequencies. A broken and hot attenuator sitting next to the device being measured at 10 mK can easily become an experimentalist's nightmare.

To thermalize these hexagonal prism attenuators, we bolt two copper bars using brass screws and stainless steel washers to clamp copper strips to two opposite sides of the attenuators. The strips are then bolted to the plates of the fridge. The attenuators are positioned underneath the respective plates to avoid radiation from the higher temperature stage above them. The outer body of the XMA attenuators are made of stainless steel, while its resistive part is made of thin films, so it is unclear if they can be thermalized well. Recent studies have proposed novel cryogenic attenuators that thermalize better [124, 125].

Another weak point of these commercial attenuators is their working bandwidth. As shown in Fig. 5.2(a), the XMA attenuator may not work at high frequencies above 25 GHz. To block out radiation above this threshold, we employ a commercial low pass filter with cutoff frequency at 12 GHz from K&L, which works well up to 40 GHz (see Fig. 5.2(b)).

To protect the experiment from noise having frequencies above 40 GHz, we use a home-made Eccosorb CR110 low pass filter that gradually cutoffs at higher frequencies, as shown in Fig. 5.2(c). The design of our Eccosorb filter basically consists of SMA connectors attached to a section of Eccosorb CR110 transmission line, as shown in Fig. 5.3(a). The

dimensions of this section are designed such that it has 50 Ω characteristic impedance. Eccosorb CR110 is engineered to have $Z_0 = \sqrt{\mu/\epsilon} = 1$, and to attenuate heavily at high frequency, $> 100\text{GHz}$ range, while its insertion loss is small at 10 GHz [134, 135]. The attenuation per unit length of our homemade filters at 8 GHz is roughly 1 dB/cm, so a short section can even be placed on the output line. Using the same principle of spacing out the attenuators above, we place one Eccosorb filter at 4 K and one at 10 mK. High coherence results were achieved with the Eccosorb filters in place.

To transmit the signal through the input line from one stage to another, we use stainless steel coax cables, due to their excellent thermal isolation. Soldering stainless steel can be tricky, but it is possible if necessary steps are taken. In our lab, we mostly use direct-plug SMA connectors and solder the cables ourselves.

Output Line

The design philosophy for the output line is different. Resistors attenuate signals both ways, which does not work if we want to measure the small signal coming from the device. To allow the one-way transmission of the signal at the designated frequency, we can use RF cryogenic circulators or isolators.

A circulator consists of a strongly magnetic ferrite component, which directs the flow of RF signal inside. This interaction creates a magnetic field vortex inside the component, making the flow of signal possible only in one direction. This is analogous to a ship sailing around a whirlpool: it is prohibitively hard to go in the opposite direction of the flow. When one of the three ports of a circulator is terminated with a 50 Ω resistor, it becomes an isolator. Since this resistor also acts as a black body, it is important to thermalize it well.

In fluxonium experiments, we typically use a combination of three circulators/isolators from QuinStar, or a triple junctions circulators/isolators from Low Noise Factory. The performances of some circulators at liquid nitrogen temperature (77 K) are shown in Fig. 5.2(d). All circulators are placed at the 10 mK plate.

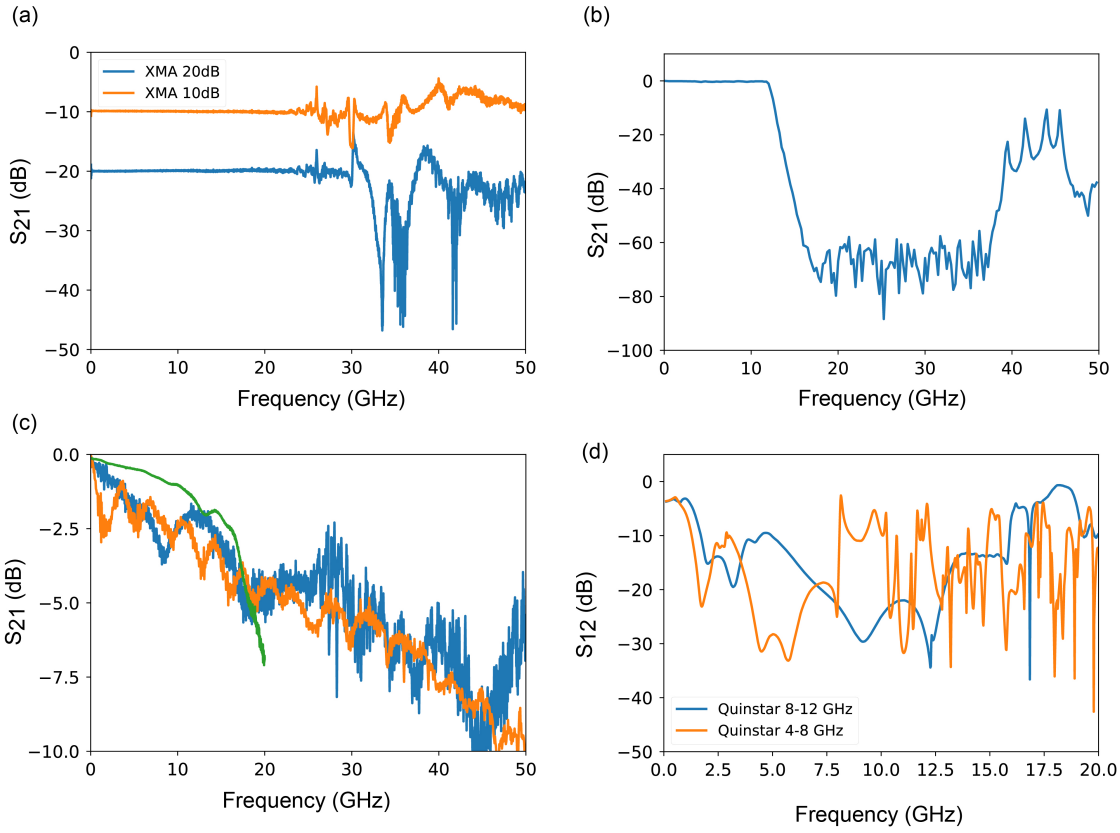

Figure 5.2: Performance of cryogenic components. (a) Transmission through commercial XMA attenuators. They do not work well above 25 GHz. (b) Transmission through K&L filter with cutoff at 12 GHz. It does not work well above 40 GHz. (c) Transmission through homemade Eccosorb CR110 filters which continue to attenuate signal at high frequencies. They are supposed to work well up to THz range. (d) Isolation measurement of QuinStar circulators. They only work well within the specified frequency range.

The bandwidth of the circulators has to cover the frequency of the output signal. Since it is relatively narrow compared to that of other components, the bandwidth of the circulator determines the bandwidth of the measurement line. We typically use components with 4-8 GHz or 8-12 GHz bandwidths. Some experiments requiring broad bandwidth are accommodated with 4-12 GHz circulators/isolators.

We recently added a traveling wave parametric amplifier (TWPA) [136] to the output, which enabled us to perform single-shot measurement of two-qubit systems. In the new

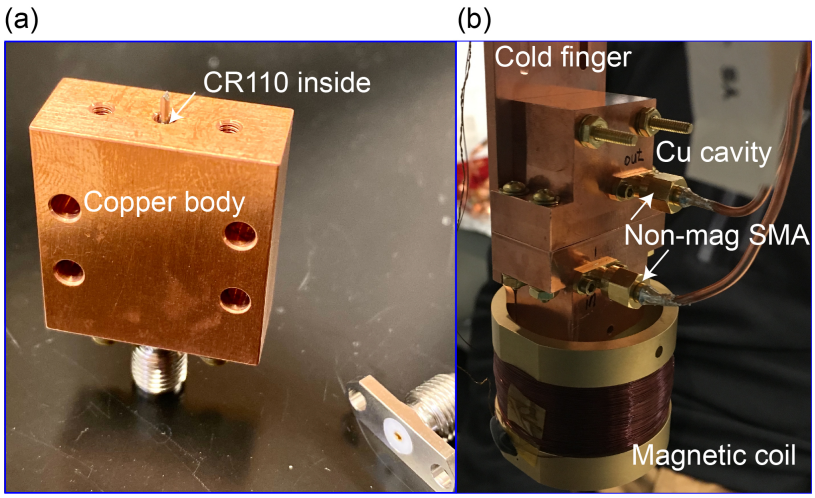

Figure 5.3: Cryogenic components. (a) Homemade Eccosorb CR110 low pass filter consisting of a transmission line section having $Z_0 = 50\ \Omega$ sandwiched between two SMA connectors. (b) The copper cavity is mounted on a cold finger. The input and output ports are connected to non-magnetic SMA connectors. The magnetic coil can be attached to the cold finger or directly to the cavity.

setup (not shown), the TWPA is sandwiched between a set of circulators in the 4-8 GHz range, three on the input, and two on the output side.

Unfortunately, these commercial circulators don't isolate well outside their bandwidth (see Fig. 5.2(c)). To cover the rest of the electromagnetic spectrum, we use a selection of K&L low pass filters and Eccosorb CR110 filters. The cryogenic amplifier is believed to be a good filter of thermal photons above 4 K, so we did not use any additional filters above the 4 K stage. To optimize the SNR of the output signal, the Eccosorb filter on the output line is small, with insertion loss less than 0.5 dB. Low frequency noise in the line is considered less important because the cold 3D cavity filters it out quite well (see Fig. 6.2). At the time of writing of this manuscript, we are designing both high pass and band pass filters to provide better protection at frequencies below 4 GHz.

As in the driving line, all components in the readout line are thermalized either by being attached directly to a cold finger, or via copper strips firmly clamped to their bodies to make as much metal-to-metal contact as possible. Apiezon cryogenic thermal grease was used in

a few cooldowns to thermalize components without flat surfaces, or to attach the chip to the cavity, but there was no apparent difference in the qubits' coherence. We stopped using this grease in 2018 because it increasingly made things messy after repeated cooldowns.

To transmit the signal from the device under test to the output port of the fridge, we initially used stainless steel coax cable as well, but then switched to CuNi in 2017, sacrificing thermal isolation for lower insertion loss. Starting with the two-qubit experiment, we used commercially-assembled superconducting NbTi cables below 4 K to minimize the signal loss. Small sections of copper coax are used to connect cryogenic components at the mixing chamber stage of the fridge, since thermal isolation between components sitting at the same temperature is undesirable. On the other hand, this last cable must be as cold as possible to minimize the effective thermal photon noise. Copper with its excellent thermal conductivity is thus a good material here. All connectors inside the cryoperm shield is made of non-magnetic material to achieve magnetic field hygiene around the sample, as shown in Fig. 5.3(b).

We tested the refrigerator input-output line by measuring the transmission signal at room temperature, during cooldown, and when the base plate reached 10 mK. We repeated the measurement after the installation of a cryogenic amplifier. The results are shown in Fig. 5.4. From this data, we could calibrate the total attenuation, which includes 50 dB of attenuation from the XMA commercial attenuators[2] and 10 dB from the coax cables. In addition, we could also check the performance of the cryogenic amplifier and the bandwidth of isolators.

Flux Bias Line

An important part of a fluxonium experimental setup is the flux bias line used to apply a magnetic field to the circuit. To construct the magnetic coil, we designed a brass hollow

[2]This measurement was performed in 2016. We added an additional 10 dB at the base plate in later experiments.

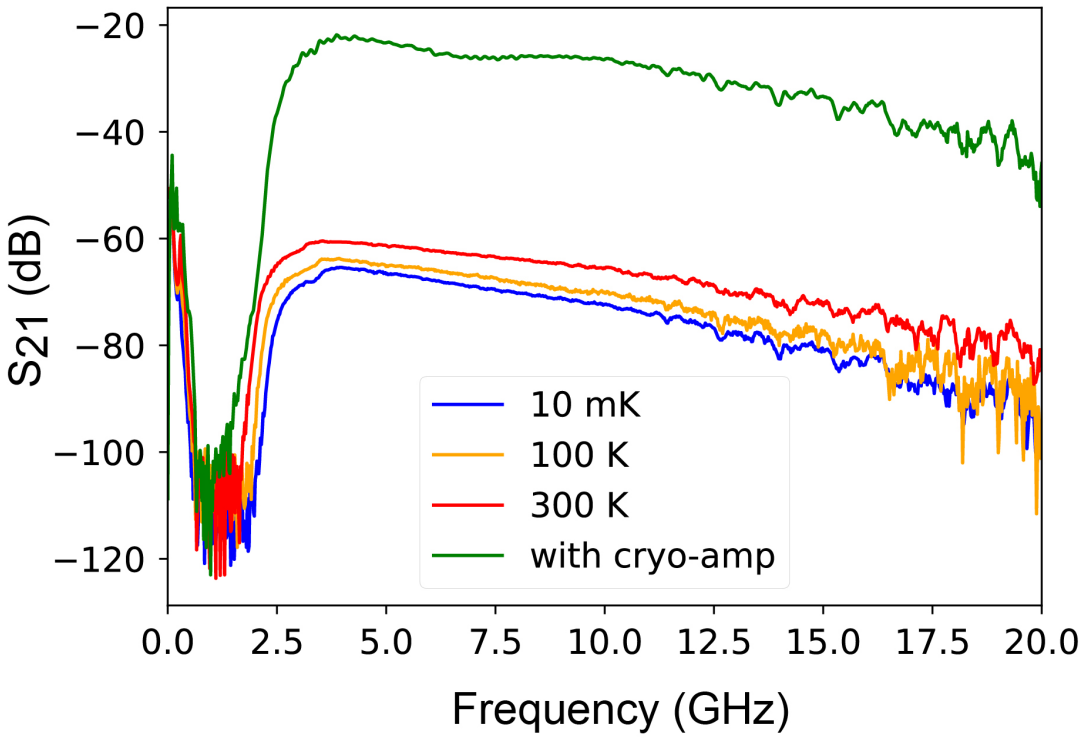

Figure 5.4: Refrigerator input-output transmission. Performance of the fridge line at various temperatures, and with the addition of a cryo-amplifier. At the time of the measurement, there were 50 dB attenuation from XMA commercial attenuators and 10 dB attenuation from the coax cables. Per manufacturer's specification, the cryo-amplifier provides 40 dB of gain from 4 to 16 GHz, which is consistent with our data.

cylinder to fit the body of the copper cavity and cold finger. It could be attached to the body of the cavity or the cold finger interchangibly, depending on how strong and homogeneous we would like the magnetic field at the chip to be (see Fig. 5.3(b)). The coil was made of NbTi, a superconducting material. The wire was coiled around the brass body using a drill. We then fixed the wire to the body using Stycast 2850. The superconducting coil eliminates dissipation caused by the applied current, and also helps with thermal isolation.

For input/output lead connecting to the coil, we used manganin wire. We thermalized this wire by attaching it to metal posts positioned at the 50 K and 4 K plates using GE

varnish. The manganin wire and the NbTi coil were soldered together at the 4 K stage.

We noticed that the addition of the coil corresponds to a rise in the temperature of the fridge's base plate, which implies that our thermalization of the wire is not perfect. This could be due to the copper cladding on the outside of the wire. In addition, whenever a large current (>100 mA) is applied to the coil, we see a sharp increase in the fridge's temperature, which can be due to the Joule heating of the manganin wire or the solder contact.

5.2 Cavity Simulation and Design

The purpose of the 3D cavity in fluxonium experiments is to readout the state of the qubit(s). In designing the cavity, three important properties have to be considered: the resonant modes of the cavity, the cavity-qubit coupling, and its coupling to the input/output transmission line.

5.2.1 Resonant Modes

The cavity's geometry must allow good thermal contact with a copper cold finger, mounting of a magnetic coil directly on the cavity's body, and it must fit inside a cylindrical cryoperm magnetic shield. Taking into account these conditions, we chose rectangular geometry and copper as the material for the body. A few aluminum cavities were used to test the shielding inside the dilution fridge (see section 6.1).

To protect the qubit's lower spectrum from decay via the cavity modes, we chose the fundamental mode TE_{101} for readout purpose [137, 51]. Since fluxonium has many levels which may interact with the cavity's higher modes, it is important to take them into account. The resonant frequencies of a rectangular 3D cavity follows [131]

$$f_{mnl} = \frac{c}{2\pi\sqrt{\mu_r \epsilon_r}} \sqrt{\left(\frac{m\pi}{a}\right)^2 + \left(\frac{n\pi}{b}\right)^2 + \left(\frac{l\pi}{d}\right)^2}, \tag{5.3}$$

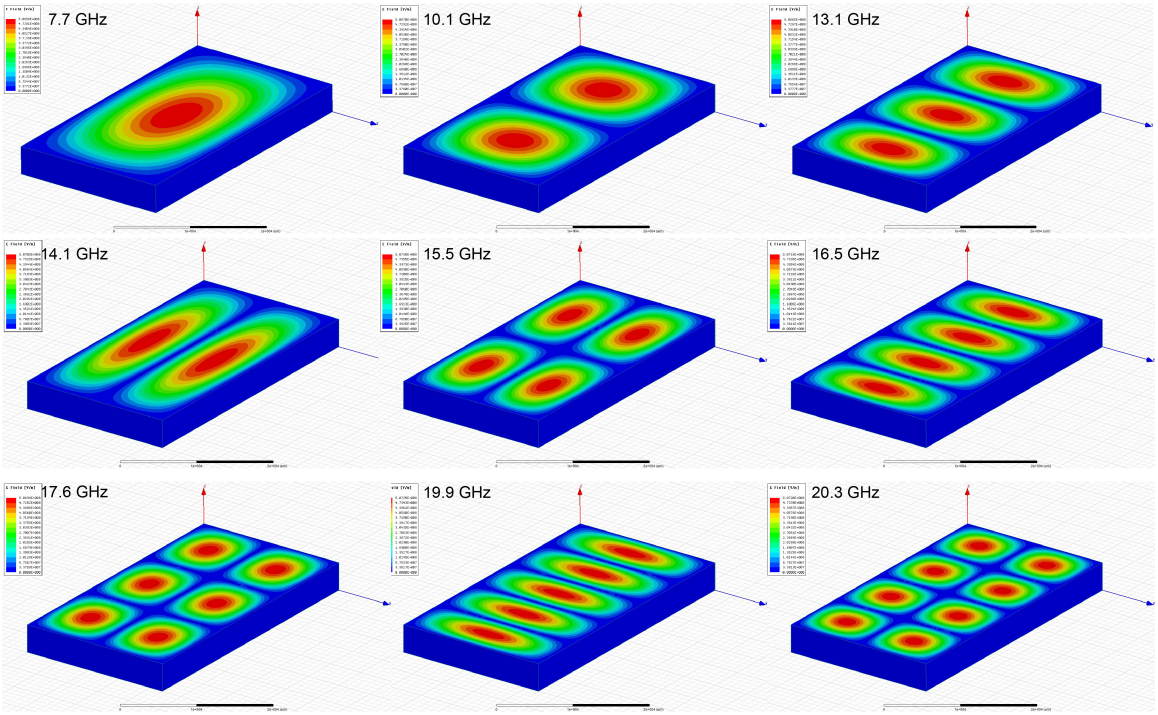

Figure 5.5: Electric field density of resonant modes in a rectangular cavity. Electric field density for higher modes of the 7.5 GHz cavity. Note that not all modes couple to the qubit, and higher modes would be occupied by fewer thermal photons, therefore contributing much less to the dephasing of the qubit.

where a, b, d (with $a > d > b$) are dimensions of the cavity, and m, n, l are integers, no more than one of which can be 0. They are used to identify the mode number of the cavity. For example, TE_{101} mode corresponds to $m = 1$, $n = 0$, $l = 1$.

We designed the cavity by first using Eq. 5.3 and then by checking the resonances and the corresponding electromagnetic fields on ANSYS Electronics Desktop. The dimensions of the cavity were chosen to give the fundamental resonance within the bandwidth of the measurement line. The lowest TE_{101} mode of a rectangular cavity and integration of a qubit has been studied in refs. [51, 138]. Here, we focus on the simulation of some higher modes up to 20 GHz. Their electric field density distributions on the surface of the cavity are shown in Fig. 5.5.

It is apparent that if we place the qubit along the electric field of the fundamental mode

in the middle of the cavity, we can protect it from coupling to most of the higher modes. On the other hand, the modes at higher frequencies are less populated by thermal photons due to Bose-Einstein statistics, so they should not be severely problematic, provided that our filters work well. Regardless, we should still take care to design qubits to have transition frequencies away from, for instance, the mode at 13.1 GHz. Direct excitation from the computational subspace via this mode may still dephase the qubit.

5.2.2 Cavity-Qubit Coupling

The height of the cavity (the smallest dimension, see Fig. 5.5) does not dictate the cavity's resonant frequencies, but it is important for the coupling between the cavity and the qubit. The smaller the height dimension, the larger the electric field across the qubit's antenna, and consequently the higher the coupling. This cavity-qubit coupling also depends on the size and shape of the dipole antenna. The shunting capacitance, which contributes significantly to the charging energy E_C of the qubit, comes from the antenna as well [51]. We simulated different cavity and qubit geometries on Ansys Desktop to search for the desired configuration.

To simulate the cavity-qubit coupling, we used the eigenmode solver. We assigned an LC boundary condition to the virtual circuit between the antenna. By varying the inductance value of this circuit and finding the resonant frequencies, we extracted the amplitude of the avoided crossing between the circuit mode and the cavity's fundamental mode that we used for readout, as shown in Fig. 5.6(b). Note that the coupling here has unit of Hz.

If desired, we could also check the LC circuit's coupling to higher modes, which is either zero or small compared to the coupling to the TE_{101} mode. The size and shape of the dipole antenna can be varied to meet our requirements for the coupling strength g and the shunting capacitance.

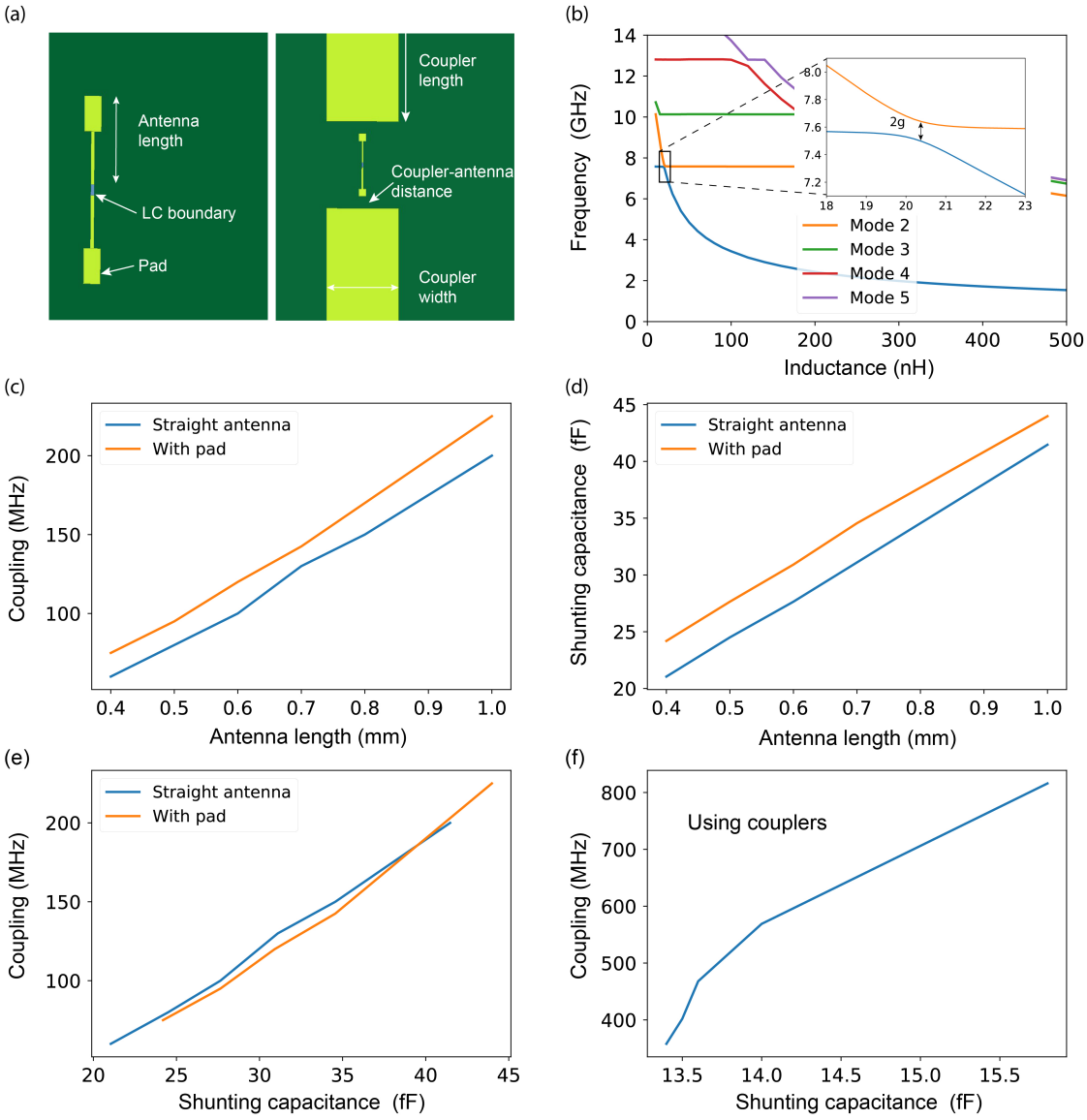

Figure 5.6: Simulation of cavity-qubit coupling. (a) Geometry of antenna and couplers. (b) Eigenmode simulation. The anti-crossing amplitude is twice the coupling constant $g/2\pi$. (c) Coupling constants simulation of two type of antennas. The length of the antenna is varied, resulting in different coupling. (d) Shunting capacitance simulation of two types of antennas. (e) Comparison of shunting capacitance versus coupling constant for both antenna geometries, showing their correlation. (f) Using the couplers allows us to enhance the coupling significantly with much less increase in the shunting capacitance, as compared to using only the symmetric dipole antenna.

We concluded that regardless of the size and shape of the antenna, increasing the coupling correlates with increasing the shunting capacitance, which is equivalent to decreasing the charging energy E_C (see Fig. 5.6(c-e)). This is unavoidable in any symmetric dipole antenna. To overcome this relation, we designed a pair of couplers to increase the coupling without increasing the shunting capacitiance (see Fig. 5.6(a)). The idea was to create an equipotential conducting element to concentrate the electric field corresponding to the TE_{101} mode of the cavity such that the voltage drop across the qubit's antenna is enhanced. These couplers are particularly useful in experiments requiring a strong coupling of qubit to cavity mode, or qubit to a traveling wave mode, without affecting the charging energy E_C. The simulation result for the couplers is shown in Fig. 5.6(f).

5.2.3 External Coupling to Cavity and Qubit

Next, we designed and engineered the coupling of the cavity to the $50\ \Omega$ transmission line, which involves a transition between a TE_{101} standing wave in the cavity and a TEM mode in the coax cable. The loss of energy from the cavity is characterized by the rate κ, where $Q = \omega_0/\kappa$ is the total quality factor of the cavity. The loss can be due to intrinsic loss inside the cavity, or due to the coupling of the cavity to the external transmission line.

In appendix A, we show that loss can be modeled as a shunting admittance with non vanishing real part. To simplify here for simulation, we can model the real part of the admittance as a pure conductor/resistor. The quality factor is then $Q = \omega_c RC$. When the loss is mostly intrinsic, $Q_{\mathrm{int}} < Q_{\mathrm{ext}}$, we say that the cavity is under-coupled, and when the loss is mostly extrinsic via coupling to input/output connection $Q_{\mathrm{int}} > Q_{\mathrm{ext}}$, we say that the cavity is over-coupled. In designing the input-output coupling, it is necessary for the signal to go to the output port instead of being lost inside the cavity or going back through the input. Thus, in a reflection measurement, we designed the port to be over-coupled, and in transmission measurement, we designed the input and output coupling such that

$Q_{\rm in},\ Q_{\rm int} \gg Q_{\rm out}$.

The capacitive external coupling of the cavity to the transmission line can be controlled by changing the length of the pin going through the ports. This can be verified by finite element method simulation. First, we assigned a boundary condition on the port $R_{\rm port} = 50\ \Omega$ and varied the length of the conductor going inside the cavity to check for $Q_{\rm ext}$. Then, we chose the length corresponding to a desired quality factor, and ran the simulation again with varying $R_{\rm port}$ to check for consistency. The results are shown in Fig. 5.7(a) and (b) for input and output ports, respectively.

Experimentally, the coupling was tuned using a feedback loop of measuring the external quality factor of the cavity and cutting the pin shorter until the desired coupling is attained. Fig. 5.8 shows the amplitude and phase of the reflection S_{11} parameter with various $Q_{\rm ext}/Q_{\rm int}$, following

$$S_{11}(f) = \frac{2i(f-f_0) - f_0/Q_{\rm ext} + f_0/Q_{\rm int}}{2i(f-f_0) + f_0/Q_{\rm ext} + f_0/Q_{\rm int}}. \tag{5.4}$$

The linewidth depends strongly on this ratio, and we can deduce that to get an accurate fit, it is better to bring the ratio closer to unity, which corresponds to a narrow linewidth. Typical cavity reflection measurement data is shown in Fig. 6.1.

One notable feature in our cavity design is the placement of the input port. Both the input and output ports were initially placed in symmetric positions along the diagonal of the cavity to minimize the perturbation to the surface current of the cavity's TE_{101} mode, as shown in Fig. 5.9(a). However, the microwave control of the qubit's transition becomes very slow due to the screening of the cavity in this design. We realized that at frequency far below the fundamental mode, the direct capacitive coupling between the qubit and the input pin becomes dominant. We subsequently designed the input port to be as close to the chip as possible, as shown in Fig. 5.9(a). Such placement of the input pin provides a substantial coupling enhancement between the microwave drive and the qubit, allowing us to drive

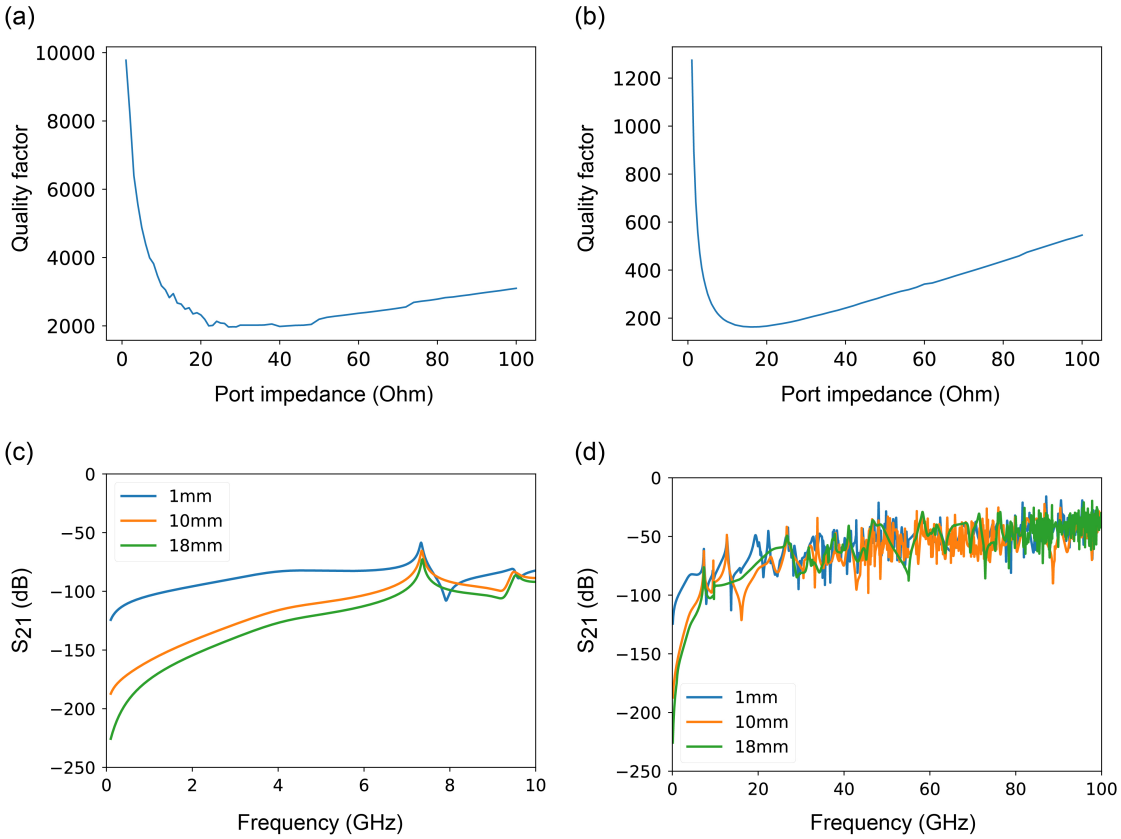

Figure 5.7: Simulation of external coupling to cavity and qubit. (a) and (b): Simulation of cavity's external coupling to the transmission line for the input and output ports, respectively. (c) Simulation of the capacitive coupling between the pin and the qubit, which is modeled as a lumped port. This shows the importance of the placement of the connector. As the connector is placed closer to the chip, the coupling is enhanced significantly. (d) Simulation of input pin - qubit coupling in a broad frequency range. Position of the port is not so important at frequencies higher than the cavity's fundamental resonance. This also explains how stray radiation can couple strongly to the qubit, despite the protection from a 3D cavity.

the low qubit transition frequency sufficiently fast. The simulation of this effect is shown in Fig. 5.7(c). Note that the cavity still filters out noise very well below its fundamental mode. We also measured qubit A coherence (see Table 6.1) using both types of cavities, and observed no difference in $0 \rightarrow 1$ transition's T_1 and T_2.

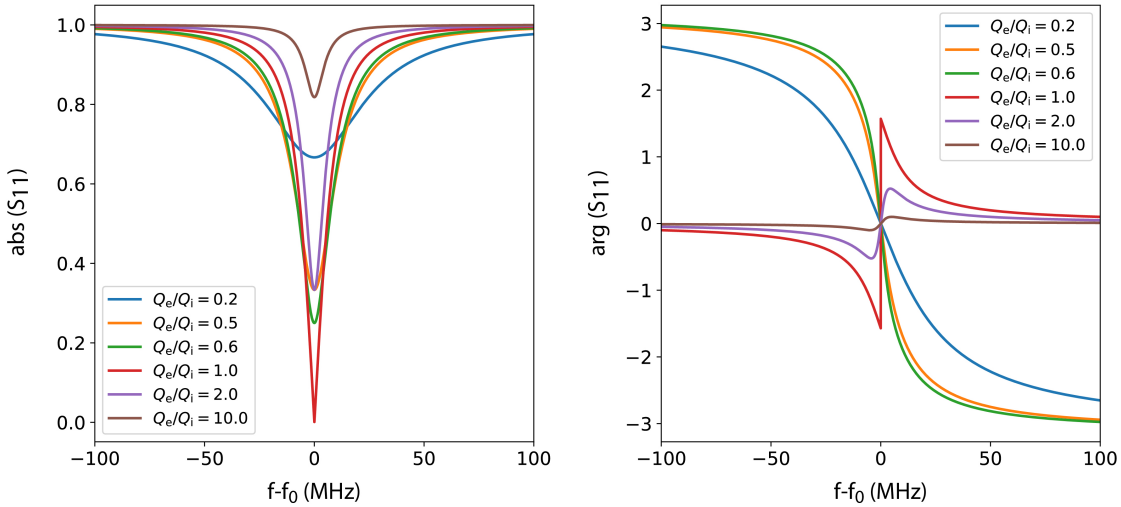

Figure 5.8: Simulation of cavity reflection. Amplitude and phase of reflection S_{11} given by Eq. 5.4. The linewidth depends strongly on the ratio between external and internal quality factor Q_e/Q_i. In order to get an accurate fit of high internal quality factor, we can tune the external coupling to be around the expected internal loss rate.

While the placement of the port strongly influences the direct capacitive coupling between the pin and the qubit at low frequency in the $0-6$ GHz range, it has little effect at high frequencies above the fundamental resonant mode (see Fig. 5.7(d)). This implies that stray radiation photons at high frequencies may couple to the qubit and create unwanted effect regardless of the position of the port and despite the protection from the cavity. This confirms that the position of the input port does not compromise qubit coherence, and shows the importance of shielding and filtering in our setup to protect the device under test from high frequency noise.

5.2.4 Cavity Preparation

Fig 5.9 shows the schematics of our cavity designs. The first few cavities were machined in the lab, and later ones were made by professional machine shops. We first designed the cavity to have high internal quality factor, which comes into play in our experiment with

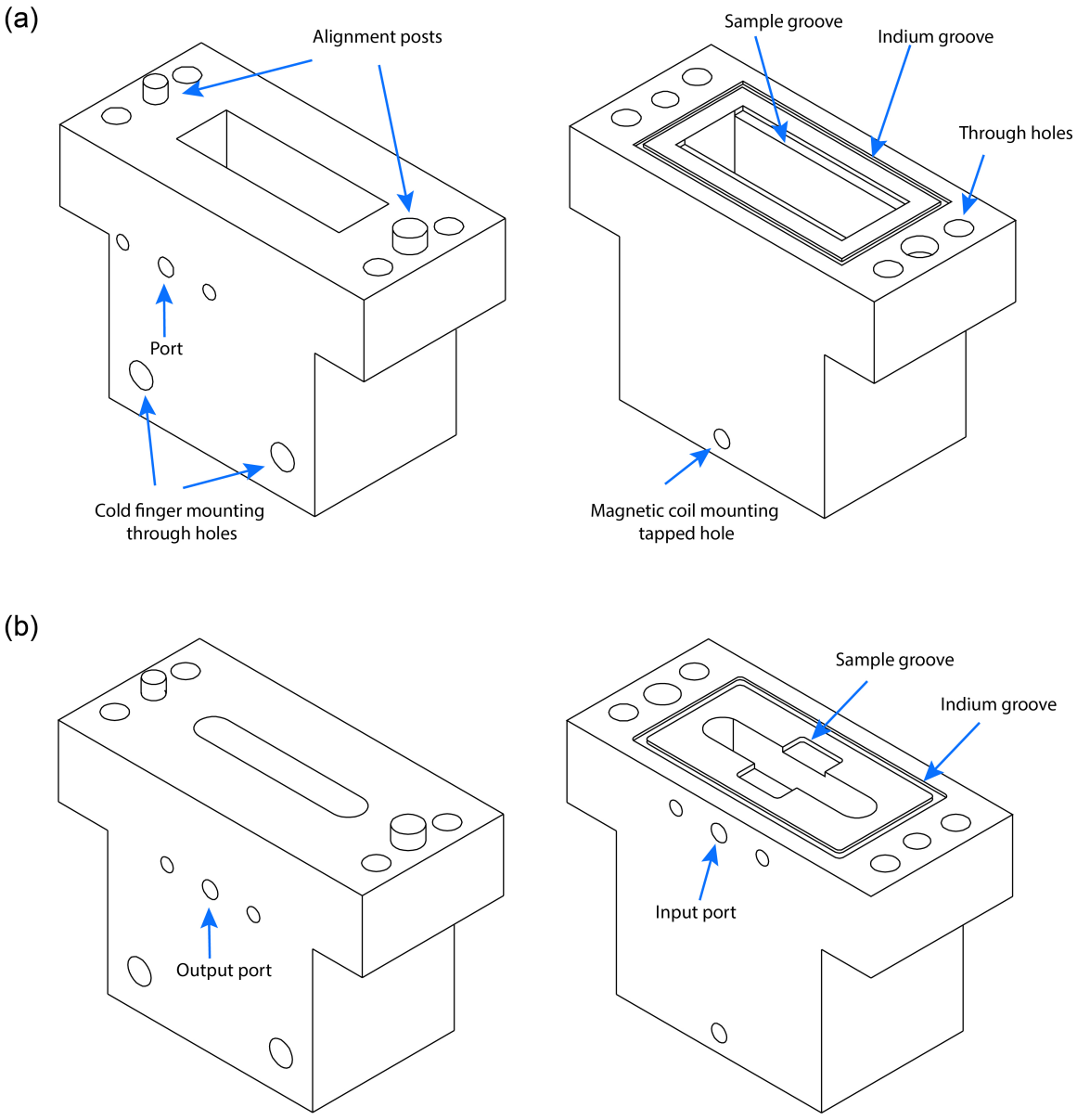

Figure 5.9: 3D cavity designs. These designs allow mounting of a magnetic coil onto the body of the cavity. (a) Design A has only one port place at in the middle of the diagonal line across the cavity. This placement minimally disturbs the surface current and results in higher internal quality factor. The sample groove was machined across the cavity's width, allowing customization of the chip's position. (b) Design B has asymmetric input/output port for transmission measurement. The input port is placed close to the chip to allow strong driving at low frequency. The third dimension of the cavity is decreased to enhance qubit-cavity coupling. The surface area of the sample groove is increased to allow better thermalization of the chip.

high-Q aluminum cavities (see section 6.1). The rest of the cavities are made from copper. The sample groove was made long, allowing us to customize the position of the chip. By moving the chip horizontally, we could tune the coupling between the qubit and cavity, as well as between qubit and driving port.

The later design prioritizes qubit's driving at low frequency, so the input port was made to be as close to the chip as possible. This allows us to apply fast gate on transition frequencies as low as 50 MHz. The output port is overcoupled to the readout line. Since the output pin is a little longer, this port is positioned further away to minimize direct coupling of low frequency noise to the qubit.

Both designs have through holes on the side for direct attachment to the cold finger on the base plate, and tapped holes for direct mounting of the coil. Alternatively, this tapped hole can be drilled through, and the coil can be mounted using a long screw. Table 5.1 shows a summary of different types of cavities mentioned in this thesis work.

After machining, the cavities are further polished with sandpapers, starting from a coarse grit, CAMI standard of 600, to a finer grit, CAMI standard of 1500. The copper cavities are then washed with soap and dipped in a solution of citric acid, commercially available as Citranox, for ten minutes. Finally, they are rinsed with DI water and sonicated with IPA for another ten minutes. When measured at 10 mK, the copper cavity has internal quality factor $Q_{\mathrm{int}} = 25000$. The interior of the cavity may contain impurity from machining which may not cooldown well and create thermal photons which can be detrimental to the qubit's coherence. The cleaning step is therefore essential, even if it does not result in a higher internal quality factor.

For reflection/hanger experiment setup, we used a single port with corresponding $Q_{\mathrm{out}} \approx 1000$. For transmission experiments, we set $Q_{\mathrm{out}} \approx 600$, $Q_{\mathrm{in}} \approx 3000$, so the linewidth for a 7.5 GHz cavity is approximately 15 MHz. Recent two-qubits experiments have increased quality factors to improve the dispersive shift over coupling rate χ_{01}/κ ratio, with $Q_{\mathrm{out}} \approx 2000$, $Q_{\mathrm{in}} \approx 6000$, corresponding to a linewidth of around 5 MHz.

Table 5.1: Summary of cavity features.

Cavity #	Material	Design feature
1	6061 Al	Design A
2	4N6 Al	Design A
3	C101 Cu	Design A
4	C101 Cu	Design B

Aluminum cavities become superconducting at low temperature so its internal quality factors can reach millions [139, 140]. To determine the Q_{int} more precisely in such case, we tuned the external quality factor Q_{ext} in aluminum cavities to at least 2×10^5. We also performed electro-polishing of these cavities to get the best possible quality factor. This allows us to test our filter and shielding, as discussed in section 6.1.

The qubit is mounted onto the cavity with pressed indium wire. Too much applied pressure can break the chip, so the best strategy is to apply just enough indium, then use the other half of the cavity to push on the chip. We usually perform a final check to see if the chip sticks well to the copper surface.

5.3 Microwave Electronics

The microwave electronic wiring, optical table, physical signal connections, and typical instruments are shown in Fig. 5.10. We will go into the details in this section. We discuss control and readout separately, as the former involves signal synthesis, and the later involves signal analysis.

5.3.1 Control

The pulses for controlling qubits and performing cavity readout are generated by an arbitrary waveform generator (AWG). In the lab, we mostly use a Tektronix 5014C AWG, which

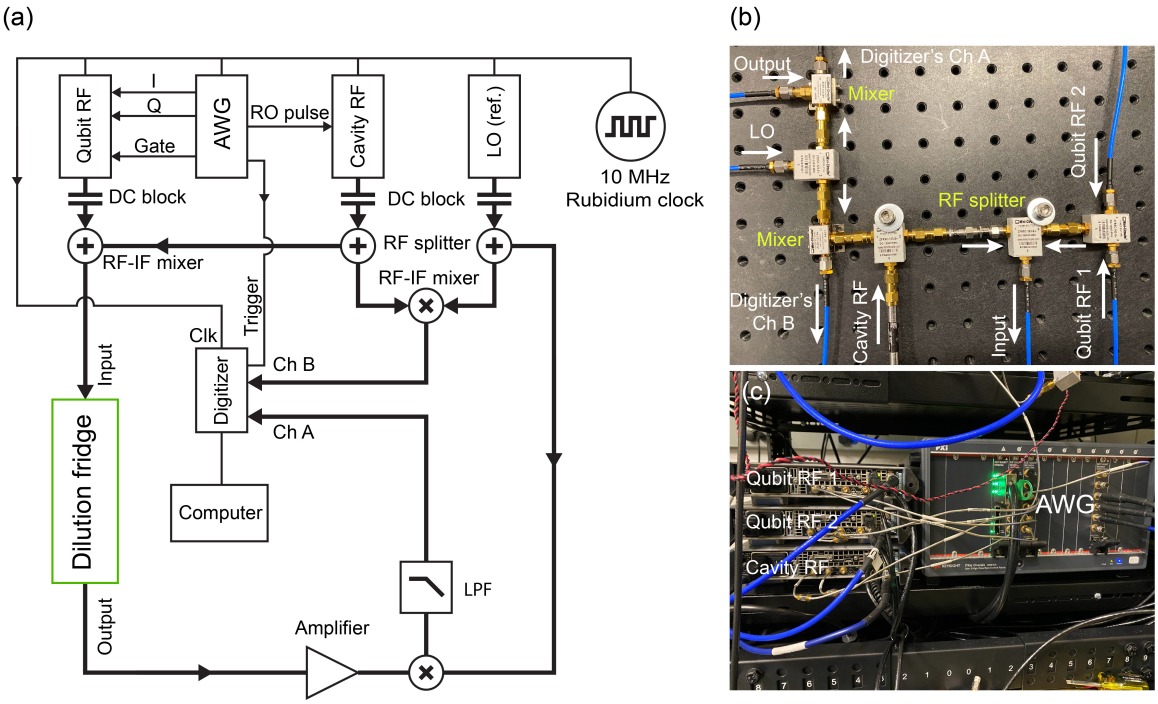

Figure 5.10: Room temperature electronics and microwave lines setup. (a) Wiring diagram. (b) Optical table setup. (c) IQ RF sources and Keysight AWG + digitizer PXI modules.

has 4 analog channels, each comes with 2 digital marker channels. These digital channels are useful for generating pulses to readout the cavity, gate the IQ generators to decrease carrier leakage, or to trigger other instruments. A single Tektronix AWG is usually good enough to perform most experiments.

We recently incorporated a more capable Keysight PXI 3202 AWG, which can be extended to have as many as 32 analog channels. However, it doesn't include digital channels, so we usually have to use the analog channels to generate simple square pulses to trigger the digitizer or to gate the IQ generators, which is not cost effective. The Keysight tends to crash less often than the Tektronix.

The Tektronix 5014C has maximum sampling rate of 1.2 GSa/s, whereas the Keysight sampling rate is 1 GSa/s. Both can reliably generate pulses with maximum resolution of

around 2 ns. Beyond that, there is distortion in the synthesized pulses which can be seen with a fast oscilloscope. The Tektronix can also generate RF pulses with frequency up to 250 MHz in normal mode, or up to 350 MHz in direct output mode at amplitudes below 0.5 V. We note that the practical performance of the AWGs we tested is often not as good as specified by the manufacturers. For example, there is distortion in the sinusoidal wave at 300 MHz, and there are also spurious modes coming from the AWG at higher frequencies, which can be seen in Fig. 5.11(e) and (f).

The cavity tone is generated by a Rohde & Schwarz SMB100A RF source in pulse modulation mode, with frequency range from 100 kHz up to 20 GHz, and on/off ratio higher than 100 dB.

We use Rohde & Schwarz SGS100A SGMA IQ vector signal generators to drive qubits. These generators can perform IQ modulation in a wide frequency range, from 80 MHz up to 12.75 GHz, and can output CW tone from 1 MHz to 12.75 GHz, so we can use them to scan the spectrum of fluxonium circuits conveniently. These small boxes can be stacked snugly on any shelving unit, so many of them can be easily added if any experiment demands additional drives. They may produce distortions when the input IQ pulses' amplitudes are too high, as shown in Fig. 5.12(b). When high fidelity operation is desired, it is best to double check the RF pulses both in frequency and time domain to confirm that the instruments generate the signal we expect.

For local oscillator, we use refurbished Agilent HP 8671a sources together with Mini-Circuits amplifiers at their outputs to increase the power needed to mix the signal down. We typically use a Mini-Circuits ZX05-153 frequency mixer which requires the LO power to be at least 10 dBm.

To generate signal at higher frequencies, we employ a Rohde & Schwarz SMW200A vector signal generator which can output RF signal at frequency up to 40 GHz. This instrument typically has better specifications, with up to 2 GHz IQ modulation bandwidth, higher on/off ratio, and better spectral purity. It can be programmed to work as an AWG as well,

although we have not utilized this function.

Microwave electronics are generally quite reliable, but we have to make sure to follow the specifications listed by the manufacturers. Occasionally, the experiment stops suddenly, and the first reasonable response is to check the microwave electronics to see if they output the signal with correct frequency, power, and modulation options or not. If there is indeed a problem with an RF source, it can often be fixed by simply power cycling the instrument and performing internal adjustment and calibration. In rare occasions, broken instruments have to be sent back to get fixed, in which case having an extra RF source on standby is not a bad idea.

When testing the instruments, we note the importance of the linewidth of the Gausssian pulses. Sharp pulses are wide spectrally, potentially creating leakages to other transitions, as shown in Fig 5.11(a). This can be verified by taking the Fourier transform of a Gausssian function. For example, for $f(t) = e^{-\alpha t^2}$, $F(\omega) = \sqrt{\frac{\pi}{\alpha}} e^{-\omega^2/4\alpha}$, so the linewidths in time domain and frequency domain are inversely proportional. A normal modulated Gaussian pulse is shown in Fig. 5.12(a). When short pulses are desired for a crowded spectrum, DRAG can be used to mitigate the problem [107, 108]. Note that there are some distortions in the spectrum of a short pulse at low frequency, due to the limitation in IQ modulation capability of the generator, as shown in Fig 5.11(b).

A common problem in RF electronics is the harmonics generated by the instruments, usually at twice the carrier frequency. A low pass filter with an appropriate cutoff frequency can be used to mitigate this problem. Other common problems include carrier leakage and asymmetric IQ modulation, shown in Fig 5.11(c).

When the frequencies are beyond the specification of the instrument, IF pulse leakage also appears. As shown in Fig 5.11(d), when we configured an IQ modulation with $\omega_{\mathrm{IF}}/2\pi = 100$ MHz, $\omega_{\mathrm{RF}}/2\pi = 180$ MHz using the Rohde & Schwarz SGS100A SGMA source, the IF tone leaked through and could be detected by the spectrum analyzer.

If the qubit transition frequencies are too low, beyond the range of the IQ source (below

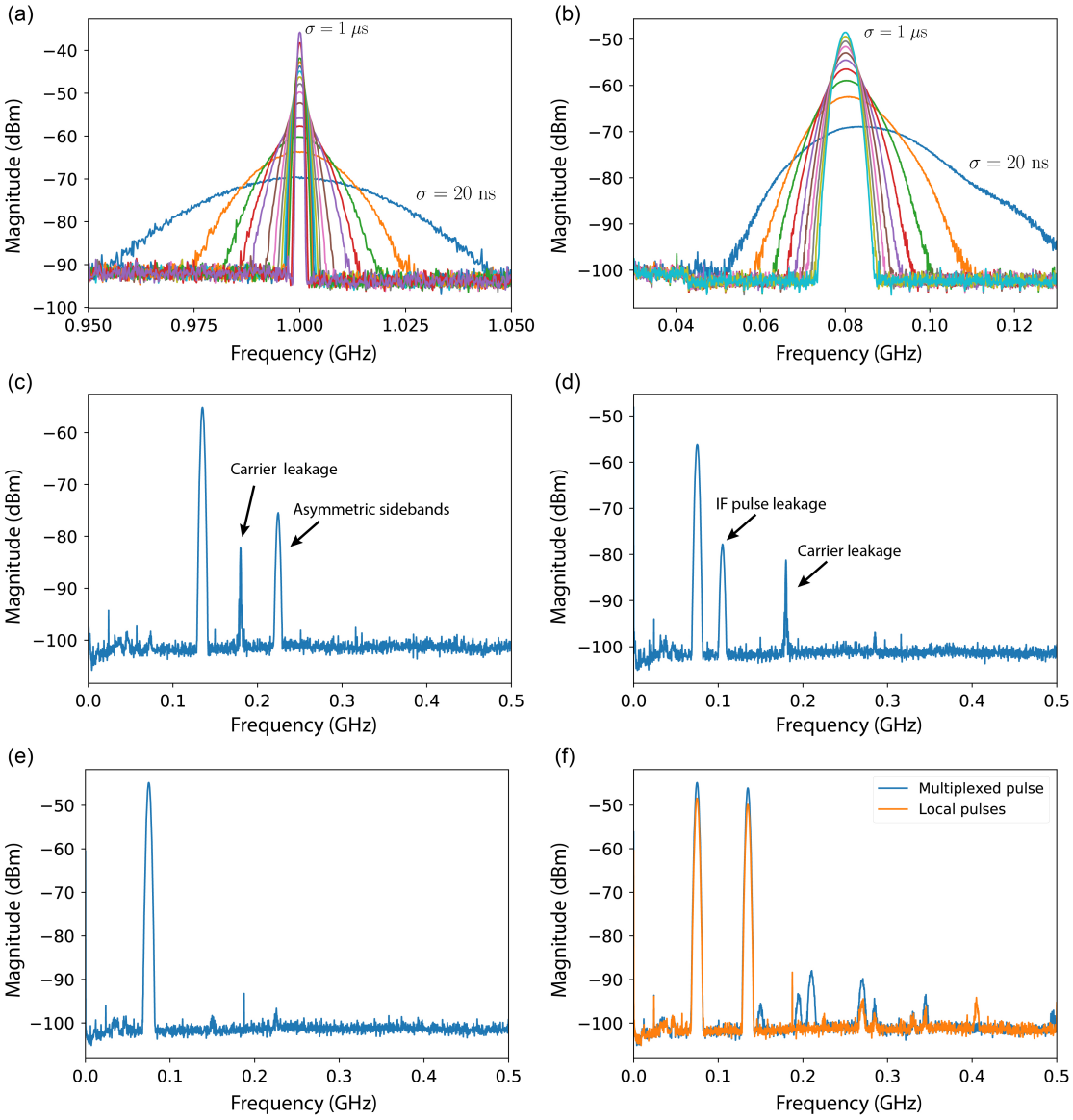

Figure 5.11: Frequency domain pulse testing. (a) The Gausssian pulses are generated by the AWG and feed into the IQ RF boxes. We see that the shorter the pulse, the wider the spectral width becomes. (b) There can be distortion at low frequency if the pulse profile exceeds the IQ RF source's specification. (c) IQ modulation imperfection, including carrier leakage and asymmetric sidebands. (d) When the carrier frequency is lower than specification, IF leakage is present. (e, f) Errors in AWG's generated pulses, namely noises at higher frequency, and lower pulse amplitude when both Channel 1 and Channel 2 are used.

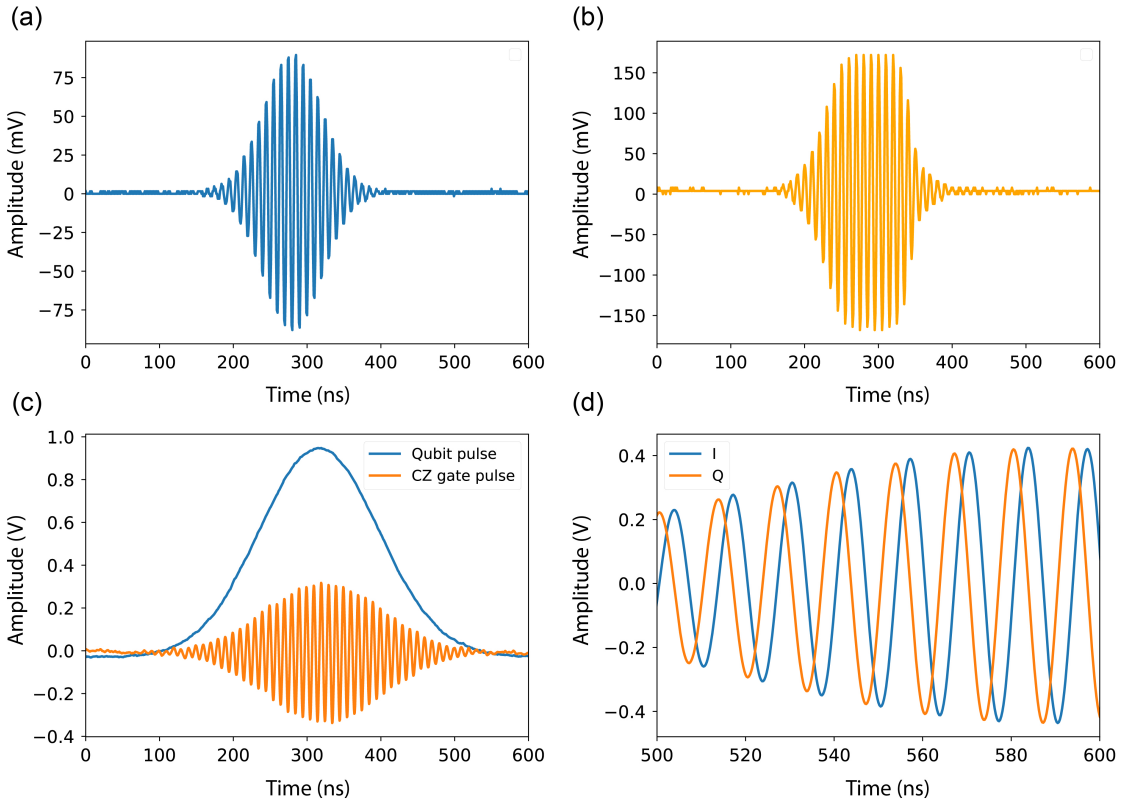

Figure 5.12: Time domain pulse testing. (a) A good Gausssian enveloped pulse. (b) A bad pulse caused by the input Gausssian pulse having an amplitude higher than the IQ RF source can handle. (c) Time delay checking. The blue pulse is about 5 ns ahead of the orange pulse. (d) Phase checking. The signals are fitted to a model and the phases can be compared. In this case, the phase difference between the I and Q signals is good.

80 MHz), we can apply an RF pulse directly from the AWG. We noted one subtle problem with the AWG used in fluxonium experiments. When there is a waveform loaded into channel 2, channel 1's pulse amplitude changes (see Fig. 5.11(f)). So if both channel 1 and channel 2 are used simultaneously, we have to calibrate the pulses when both channels are loaded with some waveform.

Note that pulse modulation usually well work only when the external pulse from the AWG has high amplitude. On the other hand, IQ modulation does not work well when the pulse's amplitude is too high, as shown in Fig. 5.12(b). Delays between pulses should also

be checked and compensated for if we do not want the pulses to overlap (see Fig. 5.12(c)).

Ideally, the IQ signal is generated such that its components are mathematically 90^o out of phase, but distortion can disturb this phase difference. Therefore, it is best to check the pulses with a fast oscilloscope and compensate for any mismatch (see Fig. 5.12(d)).

5.3.2 Readout

In the experiments reported in this thesis, we use heterodyne readout scheme as described in ref. [141]. The main signal going through the fridge and the reference signal going directly to the digitizer's other input are generated by the same RF source. Since electrical analog-to-digital converter (ADC) can only digitize at a maximum rate of a few giga-samples per second, the signal must be mixed down to intermediate frequency, which is 50 MHz in our experiments. We use a commercial RF mixer from Mini-Circuits for this purpose. The resulting signal $S(t)$ is then digitized by an analog-digital-converter (ADC) electronics card, and post-processed in IQ fashion,

$$\begin{aligned} I(t) &= \frac{1}{T_{\mathrm{IF}}} \int_t^{t+T_{\mathrm{IF}}} \cos(\omega_{\mathrm{IF}} t') S(t') dt', \\ Q(t) &= \frac{1}{T_{\mathrm{IF}}} \int_t^{t+T_{\mathrm{IF}}} \sin(\omega_{\mathrm{IF}} t') S(t') dt', \end{aligned} \tag{5.5}$$

which give us the IQ signals averaged over the demodulation period for both the main signal and the reference, denoted as A and B, respectively. The demodulated IQ signals can be written as

$$\begin{aligned} I_A(t) &= A_A(t) \cos(\phi_A(t) + \phi_0(t)), \\ Q_A(t) &= A_A(t) \sin(\phi_A(t) + \phi_0(t)), \\ I_B(t) &= A_B(t) \cos(\phi_B(t) + \phi_0(t)), \\ Q_B(t) &= A_B(t) \sin(\phi_B(t) + \phi_0(t)), \end{aligned} \tag{5.6}$$

from which we can cancel out the phase instability of the RF source ϕ_0, and record the phase difference between the signals, $\phi(t) \equiv \phi_A(t) - \phi_B(t)$, along with the amplitude of the main signal, $A_A(t) = \sqrt{I_A^2 + Q_A^2}$. Alternatively, heterodyne demodulation using single-sideband balanced IQ mixers can be used, which technically gives better SNR [80].

We noticed that the ADCs have large leakage from the trigger and the 10 MHz reference clock. This is usually not a big problem because (i) we use a reference signal and the setup is only sensitive to the phase difference between the signal coming from the fridge and the reference, and (ii) we only care about the change in the signal when the qubit shifts the cavity's resonance.

We may bypass these intrinsic RF noise by choosing the right configuration for the demodulation. First, the trigger duration should be multiples of the clock's period $T_{\mathrm{clk}} = 100\ \mathrm{ns}$ to avoid jitters in the demodulated signal. Second, we should choose an optimal IF frequency. In choosing this, we have to take into consideration the bandwidth of the digitizer, the timescale of dynamics we want to measure, noise spectrum from electronics at the card's input. To bypass the clock reference leakage, a frequency that is multiple of 10 MHz is preferable. In the end, we choose 50 MHz, although other frequencies would also work.

A small phase drift is often observed in long measurements. We speculated that this drift is due to the fluctuations inside the room temperature amplifier, since readout lines with different amplifiers consistently correspond to different amount of drift, and the measurement utilizing the best room temperature amplifier (LNF-LNR4-8C) has the smallest drift.

Depending on the specific dispersive shift of the cavity induced by the different qubit states, the shift can be clearer either in phase or magnitude. In general, one must check both at different cavity frequencies to find the optimal readout setting. For most of the experiments involved here, the dispersive shifts are substantially smaller than the cavity's linewidth, so we mainly readout the phase of the cavity. In recent experiments where the

dispersive shift is comparable to cavity's coupling rate, $\chi_{01} \approx \kappa$, we typically project the signal along the axis with highest separation in the IQ plane.

We use two different types of digitizers in the lab. The first one is the Alazar 9870, and the second one is the Keysight 3102. The advantage of the Alazar is its fast data transfer rate to the computer's memory at 1.6 GB/s with very good buffer management, lower noise at the input of the channel, and a faster digitization rate at 1 GSa/s. The Keysight lags behind in these areas with a slower data transfer rate at 200 MB/s, unknown noise at channel 1 and channel 4 inputs which can be due to internal leakage, and a slower 500 MSa/s sampling rate. However, the Keysight has 4 input channels, 2 GB of on-board RAM, and can be used together with other Keysight PXI cards to do FPGA-based feedback operations. Both of them exhibit noise from the 10 MHz reference clock and the trigger input mentioned above.

5.3.3 Other Equipment

We use a Yokogawa GS200 programmable DC voltage/current source to bias the magnetic flux. We initially used the instrument in voltage bias mode, but then noticed that the applied current fluctuated and drifted in time, causing significant flux instability. We have since then used the source in current bias mode. The instrument has a feedback loop that stabilizes the output current with high precision in this mode, $\delta I = \pm 0.003\%$ in one day.

For S-parameters measurement, we extensively use a Rohde & Schwarz ZNB20 vector network analyzer (VNA) that works up to 20 GHz. The VNA is also used to perform continuous wave (CW) spectroscopy. It generally takes data faster than a heterodyne setup because we only need to set the starting and stopping frequencies, together with the number of points to scan. The instrument's control then communicates with the generator internally, which is more efficient than the full heterodyne experimental scheme.

To check the spectral components of RF signals, we use a Rohde & Schwarz FSV30 signal analyzer that functions as both a spectrum and an IQ analyzer. It can analyze signal

at frequencies ranging from 10 Hz up to 30 GHz, and be configured to work as an ad-hoc oscilloscope of high frequency pulse as well.

We use a Rohde & Schwarz HMO2024 oscilloscope to check the pulses in time domain. It has a maximum sampling rate of 2 GSa/s and a bandwidth between 100 and 300 MHz, which is good for low frequency signals. Since the specification for the IQ RF source is generally better at frequencies above 1 GHz, there is generally no need to check for performance above 1 GHz if the signal purity is as good as expected below 1 GHz. We also use a Picoscope 9301 to check the instruments' performance at higher frequencies in time domain.

5.3.4 Data Acquisition Software

A few different generations of control softwares have been used in the course of this dissertation work as the lab evolved from its infancy. We started by using LabView to measure cavities and the first few fluxonium devices. In 2016, we developed the first control scripts using Python and a database to store data. We also developed a sequencer to transfer complex sequences to the Tektronix AWG more efficiently. Later that year, we began using the Python-based HQC software package developed at ENS Paris and combined it with our sequencing technique. We gradually switched to Labber starting in 2018. Certain capabilities of existing Labber drivers, such as the multi-qubit pulse generator, have been modified to meet our needs.

5.4 Fabrication

5.4.1 General Considerations

After constructing the cryogenic setup, connecting the microwave electronics, and machining the cavities, it comes time to prepare the device. Superconducting circuits can be designed and fabricated using standard lithography techniques. The fabricated devices must satisfy two demands: (i) the circuit parameters must be close to the values desired, and (ii) the surface of the chip must be as clean as possible to avoid unwanted dissipation in the form of dielectric loss.

In the lab, we choose silicon as the substrate and aluminum as the superconducting material. Silicon is currently the work horse in the semiconductor industry, and circuits based on silicon fabrication have been proven to have low loss [48]. In addition, silicon can be etched by plasma-chemical etching, which opens up new possibility for more complex fabrication techniques. Inspired by the long relaxation time of a borrowed transmon on sapphire sample, we recently started fabricating qubits on sapphire.

Aluminum is not only one of the most conventional superconductors, its behavior and properties well predicted by theory, but its native oxide can also be conveniently utilized to make Josephson junctions. Aluminum is thus far the best metal to build superconducting circuits with.

Our fabrication follows the Dolan Bridge technique [19], which allows small overlapping structures to be made with high accuracy and reproducibility using electron beam lithography.

First, a double layer of polymer called resist is spun on top of the substrate. Then, the sample is exposed to high energy electrons beam with a pre-defined design pattern. The exposed regions become soluble in a developer, and they are then washed away, yielding a mask. The two layers of polymer are chosen such that the lower layer is much thicker and softer than the top one, leading to the creation of undercut in a structure.

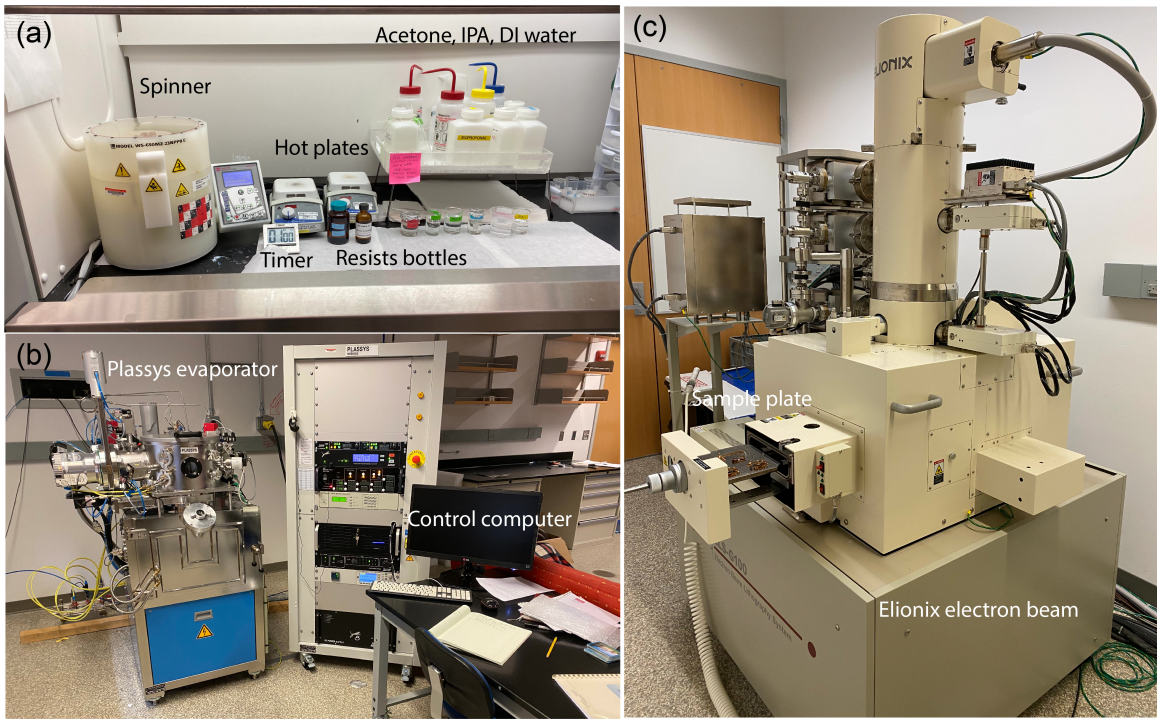

Figure 5.13: Fabrication facilities. Our fabrication facilities include (a) a chemical film hood, (b) a Plassys evaporator, and (c) an Elionix e-beam machine.

The effect of undercut is then used to form hanging bridges in the top layer. The metal film is then deposited in a metal evaporator. The exposed region allows patterning of the metal film onto the substrate surface, whereas the rest of the mask with the metal film on top is then removed using acetone.

The fabrication procedure essentially consists of six steps: chip preparation, resist application, electron beam writing, development, deposition, and liftoff. It is important that the details of the recipe are followed in an exact manner every time for consistency. The recipe is thus included below.

5.4.2 Fabrication Recipe

Chip Preparation

We first cut out the chip using a cleave such that its dimension must fit the cavity on which it is mounted. For fluxonium experiment, we use high resistivity undoped silicon wafer. We begin by spraying isopropanol (IPA) onto the wafer and blow dry it with nitrogen gas (N_2). We use a glass slide and a scribe to scratch out the part we want to cleave. We repeat the cleaning with IPA and N_2 between every step to ensure that the surface of the chip is free of debris, which is mostly silicon dust in this case. Once the cut on the chip is aligned with the cleaver, we can gently press it down to cleanly cut the chip away from the wafer. We repeat this as many times as needed to prepare the final chip with the exact dimensions.

The cutout chips are cleaned through solutions of acetone and IPA to get rid of any residue or dust on the surface. The chips are typically sonicated in said solution for 3 minutes each. We have to make sure that the chip is dropped from acetone into IPA solution right away to prevent acetone drying, otherwise some acetone residue may stick on. After removal from IPA, the chip is again blown dry with N_2. We then inspect the chip under the microscope for possible dust or defects and decide to proceed to the next step or prepare another chip.

Resist Application

Two layers of resists have to be put on the chip's surface, MMA EL 13 and 950 PMMA A3. First, we set the hot plate to 180^o C, then spin MMA EL 13 at 5000 RPM on the spinner for 1 minute. Once the spin is completed, we remove the chip and bake it on the hot plate at 180^o C for 1 minute. We then spin the 950 PMMA A3 on the spinner at 4000 RPM for 1 minute, and bake it on the plate for 30 minutes, also at 180^o C. We do chip inspection after every step to make sure the surface is clean and the resist spreads evenly across the area where the pattern will be written.

Electron Beam Writing

Electron beam writing was first done in the clean room using a Raith and then a Joel electron beam machine. We started using the Elionix ELS G100 electron beam lithography system in 2016 and subsequently increased the fabrication productivity. All the devices reported in this thesis, except for the double loop device, were fabricated using the Elionix.

The Auto CAD design file is first converted to a schedule file and loaded into the system. Specific settings must be chosen to calculate the right doses for the lithography. After all the parameteres have been set, the chip can be loaded into the machine. We then focus the beam and set the correct current (1 nA in this case) and execute the write. We check the pattern and parameters again after every step to make sure that nothing may go wrong. The big features are written with 100 nA current.

Development

Once the electron beam writing has been finished, the chip is dipped into a solution called the developer, which is 3:1 IPA:DI by volume. The solution is kept at 6^o C at all time. To make the development step more consistent, we use an ice bath with an exact ratio of water to ice every time, and the developer's beaker is immersed in the ice bath until the temperature reaches equilibrium, which typically takes 10 minutes. The chip is held by a pair of reverse-action tweezers and wiggled back and forth inside the developer for 2 minutes at a frequency of approximately 2 Hz. The chip is taken out immediately after the timer goes off and blown dry with N_2. The cold bath is a key feature of the development process.

Deposition

We load the chip into the Plassys evaporator and pump the loadlock for 20 hours before the deposition to get rid of possible contaminants. We check that the loadlock pressure reaches

1.3×10^{-7} mbar before beginning deposition. The deposition process include the following steps: (i) 20 s descum with argon at each deposition angle ($\pm 23.83^o$). (ii) Titanium evaporation at a rate of 0.1 nm/s for 2 min with the shutter closed to clean the chamber. (iii) First Al deposition at a rate of 1 nm/s at an angle of 23.83^o, resulting in approximately 20 nm of aluminum. (iv) 10 minutes static/dynamic oxidation at 100 mbar. (v) Second Al deposition at a rate of 1 nm/s at -23.83^o. Approximately 40 nm of aluminum is deposited. (vi) 20 minutes oxidation at 10 mbar.

Liftoff

We place the chip in acetone and put the beaker on a hot plate at 60^o C for 3 hours. We then sonicate it for 5 s and sonicate again in IPA for 10 s. Finally, we blow dry the chip with N_2

The device is generally considered completed at this stage. However, significant aging occurs in the first few hours after the chip is taken out of the evaporator, and the junctions continue to age for at least a month or two, but at an exponentially slower rate. Therefore, we usually fabricate the desired device about two weeks in advance of the intended cooldown to ensure that the parameters have settled down by the time they are extracted from measurement. That way, we can design our next device to meet the required specifications based on the previously measured ones.

Chapter 6

Fluxonium Experiments

Whatever it is you're seeking won't come in the form you're expecting.

Haruki Murakami

This chapter discusses the experiments with fluxonium superconducting artificial atoms in our lab at the University of Maryland. We start with rudimentary cavity characterization in section 6.1, namely determining the cavity resonance and quality factor. Then we focus on our primary results, showing the demonstration of protection from energy relaxation in section 6.2 and high coherence results in section 6.3. We report current progress on the microwave-activated controlled-Z entangling gate in two capacitively coupled fluxonium qubits in section 6.4. Finally, we review auxiliary experimental details in section 6.5.

6.1 Cavity Characterization

Before cooling down and measuring the qubit, the nominal first step is to characterize the cavity, determine the input/output coupling, and check for the resonant frequencies. We measured cavities in both 1-port reflection and 2-port transmission configurations using the

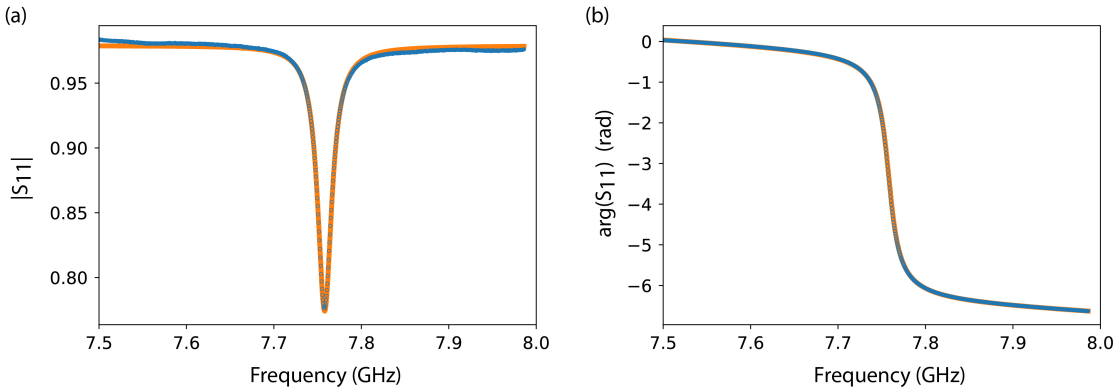

Figure 6.1: 1-port cavity reflection measurement. Fitting (solid orange) of the reflection S_{11} data (blue) using Eq. 5.4 for both (a) amplitude and (b) phase.

vector network analyzer. Typical results at room temperature are shown in Fig. 6.1 and Fig. 6.2.

In reflection measurements, both magnitude and phase data are used to extract the quality factors. In order to find the individual quality factor of each port, we use a port-less part for the other half of the cavity (see Fig. 5.9). For most copper cavities used for fluxonium readout, the input port $\mathrm{Q_{in}}$ is around 1000, and the output port $\mathrm{Q_{out}}$ is around 3000. As explained in section 5.2, the fit is more accurate when the external and internal quality factors are close, $\mathrm{Q_{int}} \approx \mathrm{Q_{ext}}$.

We also performed transmission measurement of our 3D cavities, first to check the total quality factor, and second, to record the presence of other resonances. The result in Fig. 6.2 shows the small transmission magnitude in the low frequency region of the 3D cavities. We deduced that this was due to direct capacitive coupling between the ports. The data suggests the importance of the pins' placement, and simulation has shown that placing the pin closer to the qubit enhances the coupling between the input port and the qubit mode at low frequencies (see Fig. 5.7(c) and (d)). This increased capacitive coupling to the dipole antenna allows fast gates for the low transition frequencies in our devices.

After setting up and testing the cryogenic lines, the very first experiment we performed

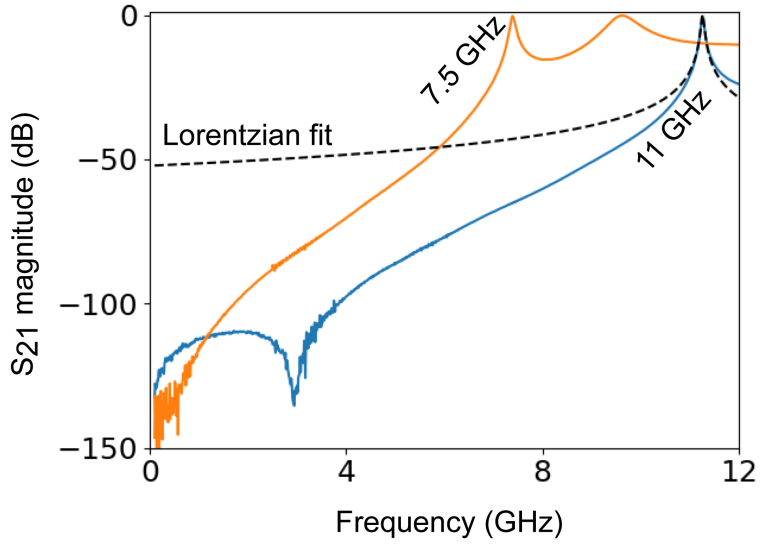

Figure 6.2: 2-port cavity transmission measurement. Transmission measurement result of cavities with resonant frequencies at 7.5 GHz and 11 GHz. Note that the transmission profile of a 3D cavity differs from that of an ideal LC oscillator away from resonance.

in the lab was measuring the quality factors of aluminum cavities across different cool-downs and shielding configurations to find the optimal setup. The changes in Q_{int} are summarized in Fig. 6.3. Both high-power (blue squares) and low-power (orange circles) probe tones were used, with higher power typically resulted in higher quality factors (Fig. 6.3, inset).

We started with a cavity made of 6061 aluminum alloy, the same material used in aircraft and yacht construction due to its good mechanical properties. The cavity was made in-house using a micro milling machine. Then we switched to a 4N6 aluminum cavity, also machined in-house. The design is shown in Fig. 5.9(a). The purer 4N6 aluminum cavity has higher quality factor. Since the cavities are superconducting below 1.2 K, their internal quality factor should naively approach infinity at 10 mK, but the data deviates from this expectation.

We first improved Q_{int} of the 4N6 aluminum cavity by etching it via electrochemical

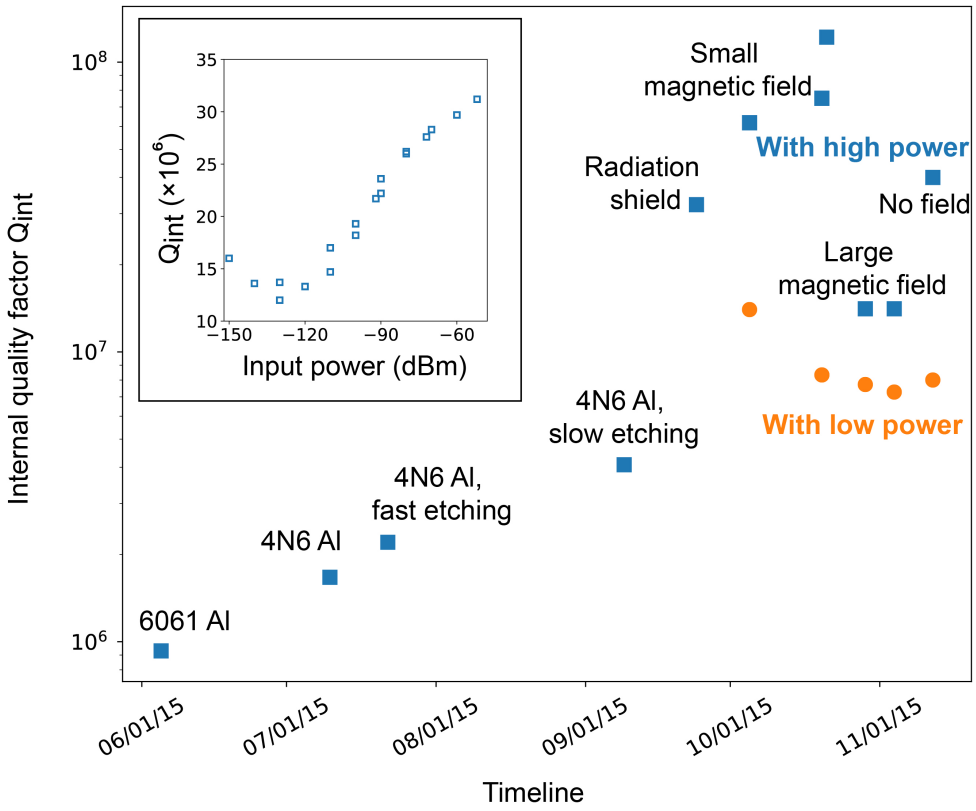

Figure 6.3: Change of internal quality factor. First, the cavity material was changed from 6061 Al to 4N6 Al. Etching process then improved the quality factor by a factor of two. The best improvement in Q_{int} was made by installing a gold-plated radiation shield underneath the base plate. Further increase in Q_{int} was made by applying a small magnetic field to the cavity (see text). (Inset) Variation of internal quality factor of the 4N6 cavity inside the extra radiation shield at 11 mK with respect to input power from the VNA.

polishing. The slow etching process [142] helped improve Q_{int} by more than a factor of two. The most notable change happened after we installed a gold-plated radiation shield underneath the base plate. This could be due to the lower radiation level which may create non-equilibrium quasiparticles in the superconducting cavity.

Further increase in Q_{int} was made by applying a small magnetic field to the cavity. The field was generated by a permanent magnet placed under the dilution fridge. We

varied the distance between its center of mass and the bottom of the fridge, then measured the corresponding cavity quality factors. When the magnet was placed right below the fridge, the quality factor dropped. As we removed the magnet completely, the quality factor returned to its initial value after we installed the radiation shield. While experiments with magnetic fields were not rigorous, the result shows that the presence of such a field can mitigate dissipation, which is likely due to residual non-equilibrium quasiparticles. This suggests that further filtering and shielding should be employed in our initial setup.

6.2 Selection Rules Engineering in Fluxonium

6.2.1 Introduction

The principle behind protection of a quantum system from energy relaxation is as follows [143, 144]. The two qubit states involved must have weakly overlapping wave functions, such that the transition matrix element of all local operator, called transition dipoles in atomic physics, is suppressed. This mechanism plays a crucial role in atomic clock [145], but it is not clear if this can help extend the lifetime of macroscopic superconducting systems, since cQED in the metastable regime involving forbidden transitions has not been explored experimentally. Fluxonium is especially suited to demonstrate this selection rules, since there are both forbidden transitions with small dipole associated with suppressed flux tunneling, and allowed transitions with large dipole associated with plasma oscillations in the circuit.

This section shows the accomplishment of this key step in a superconducting artificial atom. We designed circuit parameters to combine both forbidden and allowed transitions. The transition dipoles are flux tunable while the transition frequencies are minimally modified. The forbidden transitions can still dispersively interact with a cavity mode even if its transition dipole vanishes, due to the virtual excitations of the allowed transitions to higher states in the circuit.

6.2.2 Forbidden Transitions in Fluxonium

To achieve the necessary tunability, we replace the single weak Josephson junction with a split-junction, also referred to as SQUID-junction in literature. The circuit is coupled capacitively to a 3D copper cavity via a large dipole antenna. The resulting circuit, shown in Fig. 6.4 (a) and (b), can be viewed as a 3D split transmon shunted by a large linear inductance. The circuit Hamiltonian is defined by the inductive energy of the chain E_L, the the charging energy of the total capacitance E_C, and the variable Josephson energy of the split-junction $E_J(\phi_1)$. The circuit can be tuned by the fluxes ϕ_1 and ϕ_2 threading the two loops. The reduced flux ϕ in the inductance is the position-like quantum degree of freedom of the circuit. It moves in an effective potential given by $U(\phi) = E_L\phi^2/2 - E_J(\phi_1)\cos(\phi + \phi_J(\phi_1) - \phi_2$, where $E_J(\phi_1)$ and $\phi_J(\phi_1)$ are derived in Appendix B (see Eq. B.13 and Eq. B.14). The kinetic energy is given by $4E_Cn^2$ where n is the momentum-like continuous variable conjugate to ϕ.

In the regime where $E_J/E_L \gg 1$ and $E_J/E_C \geq 10$, there are two distinct types of transitions in fluxonium circuit. The former condition ensures that the potential consists of multiple Josephson wells whose depth and tilt are controlled by the fluxes ϕ_1 and ϕ_2. The latter condition weakens quantum tunneling between states localized in different wells. The intrawell transitions are called plasmons by analogy with plasma oscillations in junctions, similar to transitions found in a transmon [49]. The difference here is that a plasmon is insensitive to charge noise due to the inductive shunt [118]. The interwell transitions are called fluxons. They are accompanied by a 2π phase twist in the superconducting phase along the circuit's main loop. A fluxon is analogous to the transition of a flux qubit [146, 55, 54], but with two to three orders decrease in sensitivity to flux noise due to the large number of junctions in the loop [114]. When the two wells are offset against each other, the two localized states have vanishing overlap. Thus, a fluxon is a forbidden transition with an exponentially small matrix element for sufficiently large E_J/E_C ratio

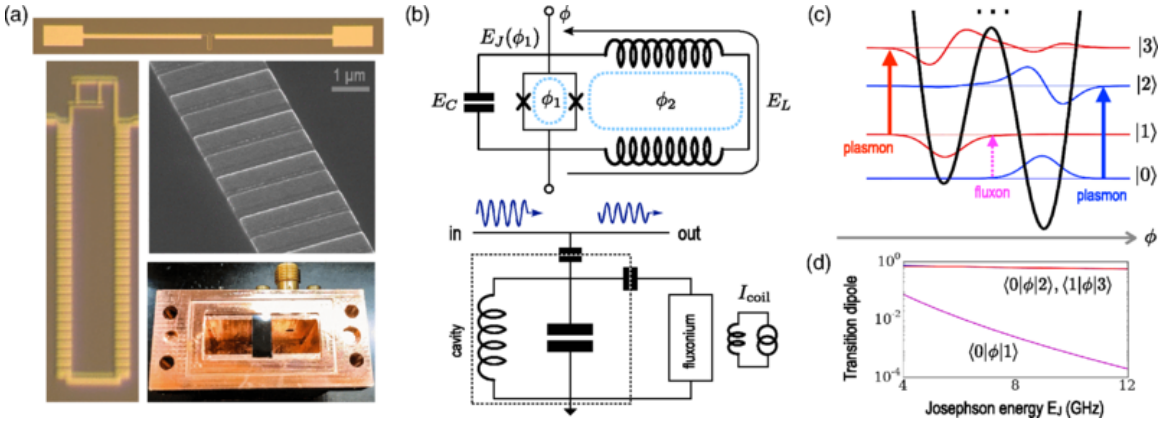

Figure 6.4: Idea for selection rules engineering. (a) Images of a double-loop fluxonium device in a 3D cavity. The antenna is directly connected to the split-junction. (b) Circuit models of a double-loop fluxonium atom and its coupling to a 3D copper cavity. (c) Lowest four energy levels of the atom accurately positioned in the double-well potential profile $U(\phi)$, along with their calculated wave functions. (d) The interwell fluxon transition 0-1 (magenta) has a vanishing transition dipole and hence is forbidden. The intrawell plasmon transition 0-2 and 1-3 (blue and red) by contrast have transition dipoles of the order of unity and are thus allowed.

[147]. By contrast, plasmons are allowed because their transition dipoles are near unity across a broad flux range (see Fig. 4.5).

As mentioned earlier, readout of the forbidden fluxon transition is possible through the virtual plasmon excitations (Eq. 4.26). The origin of the nonzero dispersive shift can be understood as follows. When the qubit is in state $|0\rangle$, the cavity is shifted by an amount χ_0 due to its interaction with plasmon modes of the circuit. This ground state dispersive shift value is large as the plasmon frequency approaches the cavity resonance, similar to the case in transmon qubits [49]. State $|1\rangle$ localized in the other potential well shifts the cavity via the same mechanism. The difference in the plasmon frequencies, blue vs. red in Fig. 6.4(c), thus results in a non zero dispersive shift $\chi_{01} = \chi_1 - \chi_0$. Quantitatively, the dispersive shifts are found by taking into account all the contributions from other states starting from $|0\rangle$ or $|1\rangle$, and is in general non-vanishing [127].

6.2.3 Spectral Features

Two-tone spectroscopy as a function of coil current and frequency reveals the spectrum of our device (Fig. 6.5). The cavity is irradiated near resonance at 10 GHz. The coil current can be converted to the total flux through the circuit in a linear fashion, $\phi_{1,2} = \beta_{1,2} I_{\text{coil}}$, where I_{coil} is the coil current and $\beta_{1,2}$ are the flux coupling constants. The observed resonances vary with the coil current in a quasi-periodic manner. They fit remarkably well to the analytical model using only six adjustable parameters: E_C, E_L, E_{J1}, E_{J2}, β_1, β_2 (see Eq. 4.1 and Eq. 4.2). From this excellent fit, we can confidently calculate the corresponding matrix elements of charge and flux operators at every flux point.

The spectrum shown in Fig. 6.5 contains interesting features. First, the quasiperiodicity of the spectrum as a function of the coil current corresponds to changing the external flux in the big loop by a flux quantum, $\phi_2 \to \phi_2 + 2\pi$. The SQUID loop has a much smaller area, and hence a much larger flux period. The point of inversion symmetry of the spectrum at $I_{\text{coil}} \approx 45.5\ \text{mA}$ corresponds to biasing the SQUID loop with a half flux quantum, $\phi_1 = \pi$, and the effective Josephson energy reaches its minimum. Note that the minimum value is nonzero due to the asymmetry of the split-junction, $E_{J1} \neq E_{J2}$.

The separation of the spectrum into plasmons and fluxons is apparent in the region $38\ \text{mA} < I_{\text{coil}} < 42\ \text{mA}$. The weakly flux-independent transition with multiple sweet spots is the lower-well plasmon. Because of the presence of the inductive shunt, the plasmon's frequency is not a monotonic function of E_J, although it reduces with E_J on average (see Eq. B.13). The transition that changes linearly with the coil current in a zigzag pattern is a fluxon. The avoided crossings correspond to a full hybridization of a fluxon with a plasmon (Fig. 6.5, left inset). The frequency splitting quantifies the strength of interwell transitions, varying from 100 MHz at $I_{\text{coil}} = 38.56\ \text{mA}$, where a fluxon is well-defined, to over 1 GHz near the spectral inversion point, where fluxon-plasmon strongly mix. Fig. 6.5's top right inset illustrates that at sufficiently large E_J value, the logarithm of the anti-crossing frequency

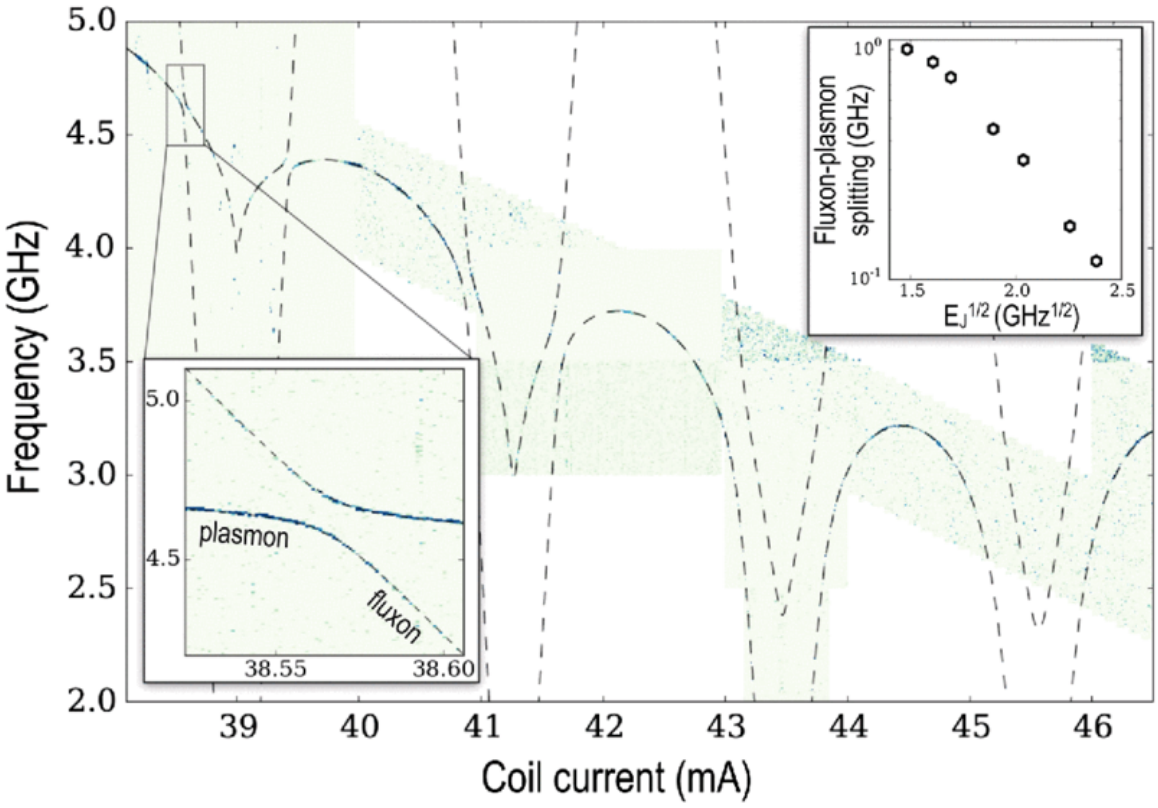

Figure 6.5: Spectrum of a split-junction fluxonium. Transmission signal near cavity resonance as a function of the coil current and spectroscopy tone frequency. Cavity resonance is off the graph at about 10 GHz (Fig. 6.24). Dashed lines represent a fit to the circuit model in Fig. 6.4 using Eq. 4.1. (Bottom inset) Enlargement of the smallest fluxon-plasmon splitting region. (Top inset) measured values of the seven splittings visible in the plot vs the extracted value of $E_J^{1/2}$ in frequency units (see Eq. B.13).

scales as $E_J^{1/2}$, in agreement with the WKB description of tunneling [141].

6.2.4 Demonstration of Protection

Controlled inhibition of energy decay in our circuit is most clearly demonstrated by measuring the lifetime of the lowest $|0\rangle \rightarrow |1\rangle$ transition as we tune the coil current through the plasmon-fluxon anti-crossing, shown in the lower inset in Fig. 6.5. Indeed, we observe a drastic enhancement of energy relaxation time T_1 time from $T_1 < 10\ \mu$s at the plasmon side to $T_1 > 1$ ms at the fluxon side (Fig. 6.6(a)). To interpret the data quantitatively, we

turned to the model of dielectric loss, common in superconducting circuits [18]. This model is consistent with the observed enhancement of T_1 and requires the bounds on the effective loss tangent $\tan\delta$ of the total capacitance shunting the qubit to be between 2×10^{-5} and 2×10^{-6}. For the same range of coil currents, we plot the calculated dispersive shift χ, which remarkably does not drop significantly at the fluxon side of the anticrossing (see Fig. 6.6(b)). The measured dispersive shift, extracted from the Rabi oscillation amplitude, agrees well with a theoretical expression without adjustable parameters. In sharp contrast, the dispersive shift calculated using only states $|0\rangle$ and $|1\rangle$ drops rapidly with the enhancement in T_1, emphasizing the importance of plasmons in creating the finite dispersive shift for fluxons.

Rabi oscillations along with echo experiments demonstrate that a fluxon remains coherent even when its transition dipole is suppressed to the extent that $T_1 > 1.5\,\mathrm{ms}$ (Fig. 6.6(c)). The coherence time T_2, given by the characeteristic decay time of the echo signal, is given by $T_2 \approx 4\ \mu\mathrm{s}$ and is limited by the first-order flux noise with amplitude of approximately $10^{-6}\Phi_0/\sqrt{\mathrm{Hz}}$ at 1 Hz. The decay of the readout signal following a π pulse on a qubit fits the exponential function well, and repeated experiments did not produce more than a factor of two variations of T_1 within about one hour (Fig. 6.6(c)). This leads us to believe that the fluctuation of T_1 values in Fig. 6.6(a) occur on a longer than a one-hour timescale.

The central feature of our work is the collection of energy decay times for the qubit transition at a number of values of the coil current such that the transition dipole, given by $d_{01} = \langle 0|\phi|1\rangle$, vastly varies, while the transition frequency is confined to a narrow interval of 3.5-4.5 GHz. These transitions lose energy to essentially identical environmental factors. Therefore, Fermi's golden rule predicts that at zero temperature, the relaxation rate scales quadratically with the transition dipole for an arbitrary linearly coupled environment. Our data obey this simple scaling for the values of T_1 spanning a remarkable range of over 2 orders of magnitude (Fig. 6.7(a)). Despite some fluctuations, the data clearly show that the dramatic enhancement of T_1 of a qubit occurs solely due to the reduction of its transition

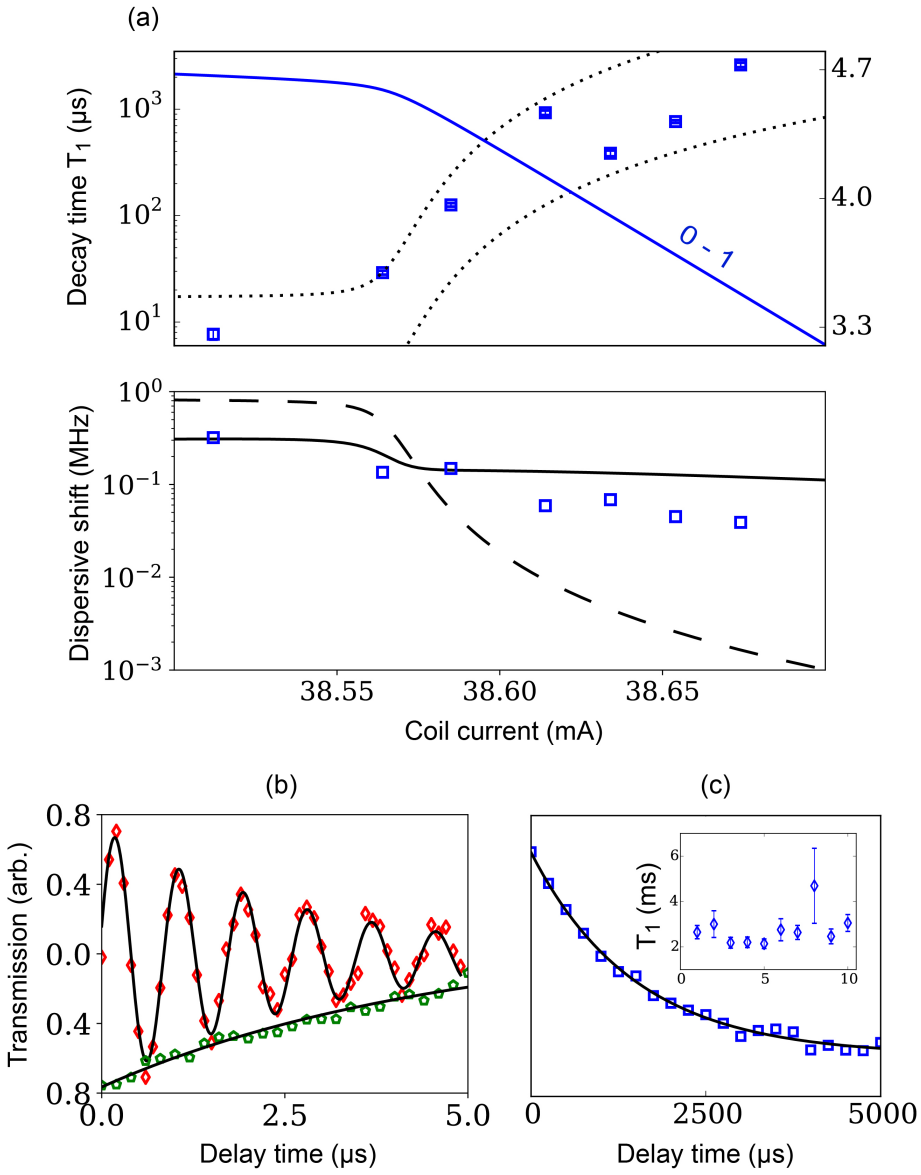

Figure 6.6: Data around the anti-crossing at $38\ \mathrm{mA}$. (a) The measured lifetime T_1 of the $|0\rangle \rightarrow |1\rangle$ transition (square marker) and its frequency (solid line). Dotted lines are the dielectric loss prediction corresponding to the loss tangent values of 2×10^{-5} and 2×10^{-6}. (b) Measured dispersive shift (square marker) and calculated dispersive shifts, taking into account all transitions to higher levels (solid line) and only states 0 and 1 (dashed line). Note that χ decreases much slower than T_1 grows. (c) Examples of time-domain measurement data: Rabi oscillation trace (red), echo trace (green), and energy relaxation trace (blue). The inset shows the variation of relaxation time T_1 over a period of about one hour.

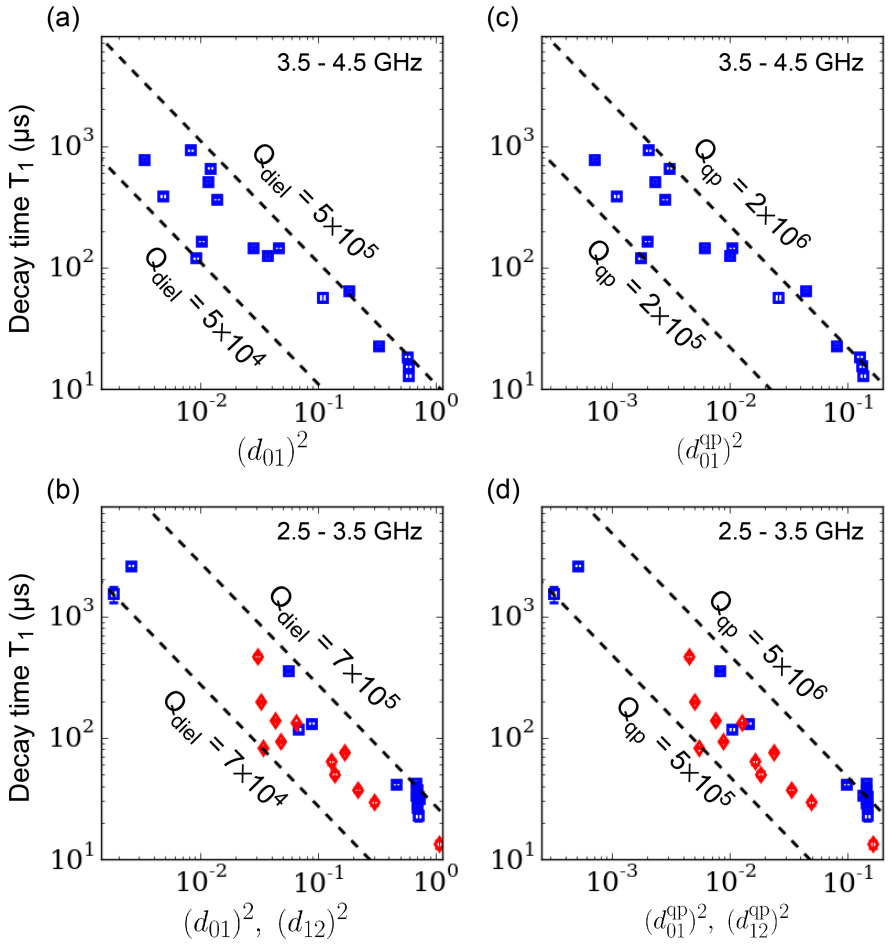

Figure 6.7: Demonstration of protection. Measured energy decay times for transitions $|0\rangle \rightarrow |1\rangle$ (blue) and $|1\rangle \rightarrow |2\rangle$ (red) taken from a narrow range of frequencies plotted against the calculated values of the corresponding transition dipole squared. Dashed lines illustrate Fermi's golden rule predictions for dielectric loss (a, b) and quasiparticle loss (c, d) using the expressions for their respective quality factors (Eq. 4.3 and Eq. 4.12, respectively).

dipole. Because the suppression of the matrix element in the fluxon regime has no classical analog, the observed scaling evidences that the energy decay occurs by a spontaneous emission rather than by a thermal activation. Data for the 2.5-3.5 GHz frequency range, including relaxation of the $|1\rangle \rightarrow |2\rangle$ transition confirms our conclusion (Fig. 6.7(b)).

The only known nonlinear loss mechanism in which coupling to the bath cannot be described using the matrix elements of ϕ is quasiparticle tunneling across the small junction

[90, 91]. The effective transition dipole d_{ij}^{qp} corresponding to the coupling to quasiparticles involves a complex function of ϕ and depends on external flux. However, replotting the energy decay times against this quantity (Fig. 6.7(c) and (d)) shows that coupling to quasiparticles is suppressed in similar fashion. This is simply due to the fact that the fluxon transition is forbidden from any local bath by the vanishing overlap of the qubit states wavefunctions.

6.2.5 Metastable Regime

Additionally, by increasing the energy ratio E_J/E_C, we reached the metastable regime, where the fluxon state's lifetime becomes immeasurably long. The spectrum corresponding to max E_J/E_C in the device is shown in Fig. 6.8. The main feature here is the plasmon transition spectrum. Because tunneling is strongly suppressed, we could not coherently manipulate fluxon transitions. Even at strong qubit tone power which is enough to clearly reveal the $|0\rangle \rightarrow |2\rangle$ two photon plasmon transitions, the fluxon line is still obscure.

While it was not possible to address the fluxon transition directly, we could observe state $|1\rangle$ being populated by an incoherent pumping process, shown in Fig. 6.9. The cavity tone effectively becomes a pump at high power, transferring the qubit's population to the first excited state which is localized in the higher potential well (Fig. 6.5(c)). This mechanism is possibly similar to the measurement induced transition discussed in ref. [148]. When the population in the first excited state is higher than in the ground state, the $|1\rangle - |3\rangle$ spectral line appears with better contrast than the $|0\rangle - |2\rangle$ line. As we turned down the cavity power, the population reverted back to the ground state.

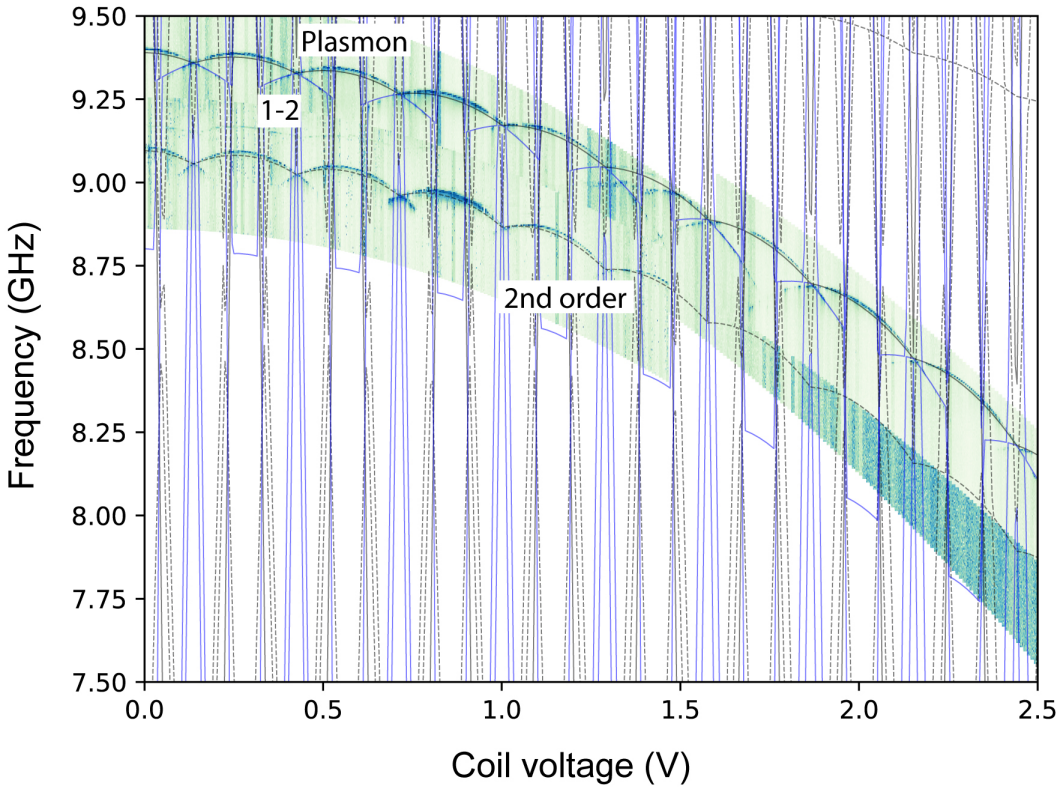

Figure 6.8: Top spectrum of split-junction device. Spectrum corresponding to the highest E_J range in the split-junction device (device C in Table 6.1). Fluxon transitions are strongly forbidden here, and only plasmon transitions are visible. The data still fits remarkably well to the simple model. Using a high power qubit tone, we could reveal the two-photon plasmon transitions at half of the $|0\rangle \rightarrow |2\rangle$ transition frequencies (fitted to dashed lines), which allows extraction of the anharmonicity. Another special feature visible here is the $|1\rangle \rightarrow |3\rangle$ transition in blue lines.

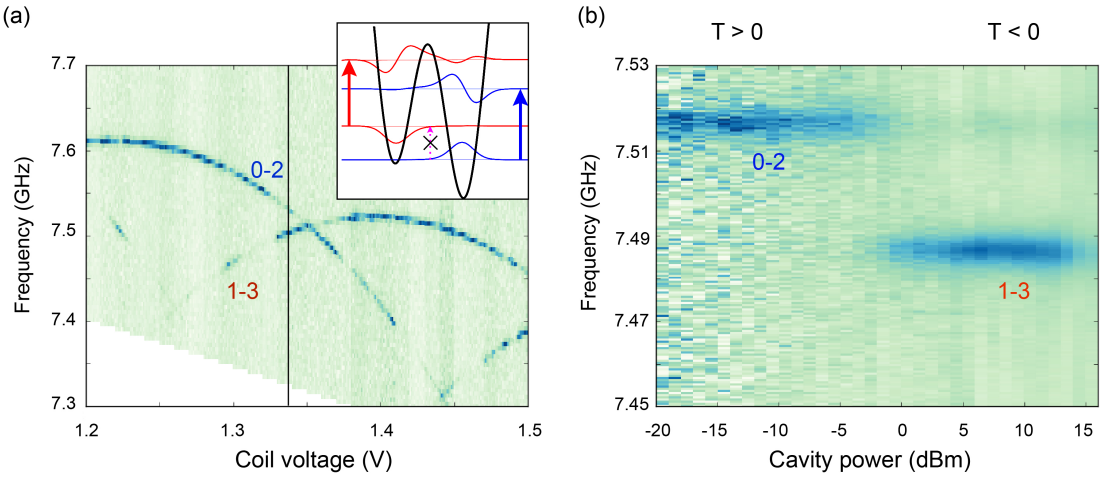

Figure 6.9: Metastable regime spectroscopy. (a) Zoomed-in of the spectrum showing the visible $|0\rangle \rightarrow |2\rangle$ and $|1\rangle \rightarrow |3\rangle$ transitions. (b) Qubit's effective temperature depends on cavity tone power. At low cavity power, the qubit is predominantly is the ground state, thus $|0\rangle \rightarrow |2\rangle$ transition is visible. At high cavity power, qubit localizes more in the excited state, thus $|1\rangle \rightarrow |3\rangle$ transition is visible, while $|0\rangle \rightarrow |2\rangle$ transition becomes obscure.

6.3 High Coherence Fluxonium Qubits

6.3.1 Introduction

In this section, we describe fluxonium superconducting qubits designed to evade decoherence due to dielectric loss and flux noise without sacrificing anharmonicity, flux-tuning range, or controllable interactions. The geometry of the qubit is shown in Fig. 6.10(a), and its circuit diagram is drawn in Fig. 6.10(b).

In this experiment, we operate the qubit near the $\phi_{\text{ext}} = \pi$ "sweet spot", where the first order sensitivity of the transition frequency to flux vanishes by symmetry (Fig. 6.10e). The qubit states $|0\rangle$ and $|1\rangle$ correspond to the tunnel splitting of the two-fold degenerate classical ground state. The circuit parameters are such that the qubit transition frequency is about an order of magnitude lower than that at $\phi_{\text{ext}} = 0$. The non-computational states $|2\rangle$, $|3\rangle$, etc., are separated by a plasmon gap (Fig. 6.10e) and they form an anharmonic spectrum with a rich selection rule structure.

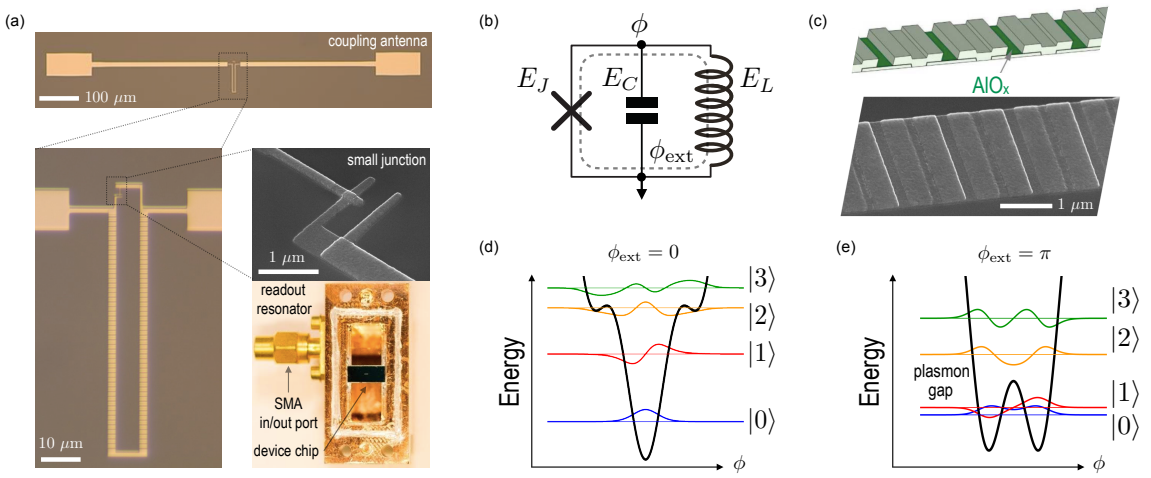

Figure 6.10: Description of high coherence fluxonium experiment. (a) Images of a single-junction fluxonium device indicating the antenna, the loop, the small junction, and the chip mounted in a copper resonator. (b) The three-element circuit model of fluxonium. (c) Implementation of a large-value inductance L using a linear chain of Josephson junctions. (d, e) The particle-in-a-box potential energy, the spectrum, and the eigenstates for the circuit model in (b) in the cases $\phi_{\text{ext}} = 0$ (d) and $\phi_{\text{ext}} = \pi$ (e), which is the focus of the present work.

By reducing qubit frequency tenfold from typical $4 - 8$ GHz range, the energy relaxation rate is expected to naturally slow down without the need for improving materials (see Eq. 4.3). One might think this trick would inevitably slow down interactions too, as it happens with weakly anhamonic oscillators. Fortunately, this is not the case with fluxoniums. For example, the dispersive coupling to a cavity mode can be as large as it is in a typical transmon setup owing to the high frequencies and dipoles of transitions outside the computational space. Furthermore, inductive coupling can be made large even within the computational subspace, as it was experimentally demonstrated by the molecular binding spectra of two fluxoniums with shared chain junctions [149].

6.3.2 Results

Similar to the original fluxonium design, here we attach an external capacitance in the form of a simple dipolar antenna directly to the small junction. The capacitance is mainly due

to this antenna. Device C is used to demonstrate protection in the previous experiment described in section 6.2. It contains a split-junction (DC superconducting quantum interference device). It is now measured at the simultaneous sweet spot (the so-called double sweet-spot) of both loops, which were fabricated to have commensurate areas. In all other devices we used a single junction for simplicity. The qubits were capacitively coupled to a 3D copper box readout mode with a frequency of 7.5 GHz and a linewidth $\kappa/2\pi \approx 15$ MHz (this is equivalent to a rather low external quality factor $Q = 500$). The state of the qubit was monitored in a basic two-port cavity transmission measurement. For consistency, all devices were measured at a small external magnetic field. The precise effect of this field remains inconclusive at this stage.

Cryogenic setups are described in section 5.1. The robust Dolan bridge technique is used in fabrication. It yields the smallest possible stray capacitance in a planar geometry. We can fabricate up to 40000-junction long chains without any fault. The advantage of such chain geometry is the lack of need for resist mask's precision tuning. The substrate is high-resistivity silicon covered by native oxide. Our fabrication procedure is discussed in more details in section 5.4.

The measured spectrum of device A together with the fitted theory lines is shown in Fig. 6.11. The data was obtained by conventional two-tone spectroscopy [63]. The theory is a result of numerical diagonalization of the simple Hamiltonian (Eq. 3.17) with E_J, E_C, E_L, and flux to coil current conversion as fit parameters. Note that in addition to fitting the two lowest frequency transitions, the theory precisely matches the red sideband of the readout mode with the transition between states $|0\rangle$ and $|4\rangle$. This indicates that there are no stray chain modes at frequencies below 10 GHz and the simple Hamiltonian is an accurate model of our complex device. At $\phi_{\text{ext}} = 0$ the qubit transition (labeled '$0-1$') corresponds to anharmonic oscillations in the central Josephson well. The nature of this transition, along with its frequency at about 4.5 GHz and the value of the transition dipole $\langle 0|\phi|1\rangle$ is similar to that of a typical transmon qubit. The difference here is that the Josephson

well is slightly deformed by the shunting inductance (Fig. 6.10(c)) and the anharmonicity, approximately given by $E_C \approx 0.8$ GHz, is considerably enhanced owing to the reduced value of the shunting capacitance.

As the flux is tuned toward the sweet-spot at $\phi_{\text{ext}} = \pi$, the qubit transition monotonically drops to about 800 MHz. Already with the naked eye it is evident that the sensitivity of the qubit transition to flux does not exceed about 20 GHz per flux quantum, while the frequency is tuned by over two octaves. Due to the thermal occupation of the $|1\rangle$-state one can see the transition '$1-2$' in the small vicinity of $\phi_{\text{ext}} = \pi$. The transition '$0-2$' is parity-forbidden exactly at $\phi_{\text{ext}} = \pi$, which is correctly reflected by the continuous reduction of its power-broadened linewidth (in a fixed power experiment) upon tuning the flux towards the sweet spot. The large anharmonicity of the qubit at the sweet spot can be characterized by the ratio $\omega_{12}/\omega_{01} \approx 3-10$ for our typical circuit parameters. Finally, we note that no two-level defects were spotted in the spectrum near $\phi_{\text{ext}} = \pi$ with anticrossings larger than a few MHz.

The frequency dependence of energy relaxation time T_1, covering several frequency octaves, was measured by flux-tuning the qubit transition between $\phi_{\text{ext}} = 0$ and $\phi_{\text{ext}} = \pi$. The T_1 values were obtained by a standard time-domain experiment recording the evolution of the cavity transmission following a π-pulse to a qubit. The majority of relaxation signals fit well to an exponential function and the characteristic decay time is quoted as T_1. We observed infrequent instances of a double-exponential decay, and those cases were not included in extracting the qubits' T_1 values.

To extract the noise spectral density $S_\phi(\omega)$, we normalized the measured relaxation lifetimes by the square of the matrix element and plotted the quantity $T_1 \times |\langle 0|\phi|1\rangle|^2$ as a function of qubit frequency $\omega_{01}/2\pi$ (Fig. 6.12, top). According to Fermi's golden rule, this quantity is inversely proportional to the spectral density of the noise coupled to the phase variable ϕ at the qubit frequency ω.

At frequencies above 1 GHz, the data follows a simple model $S_\phi(\omega) = \hbar C \omega^2 \tan\delta_C$,

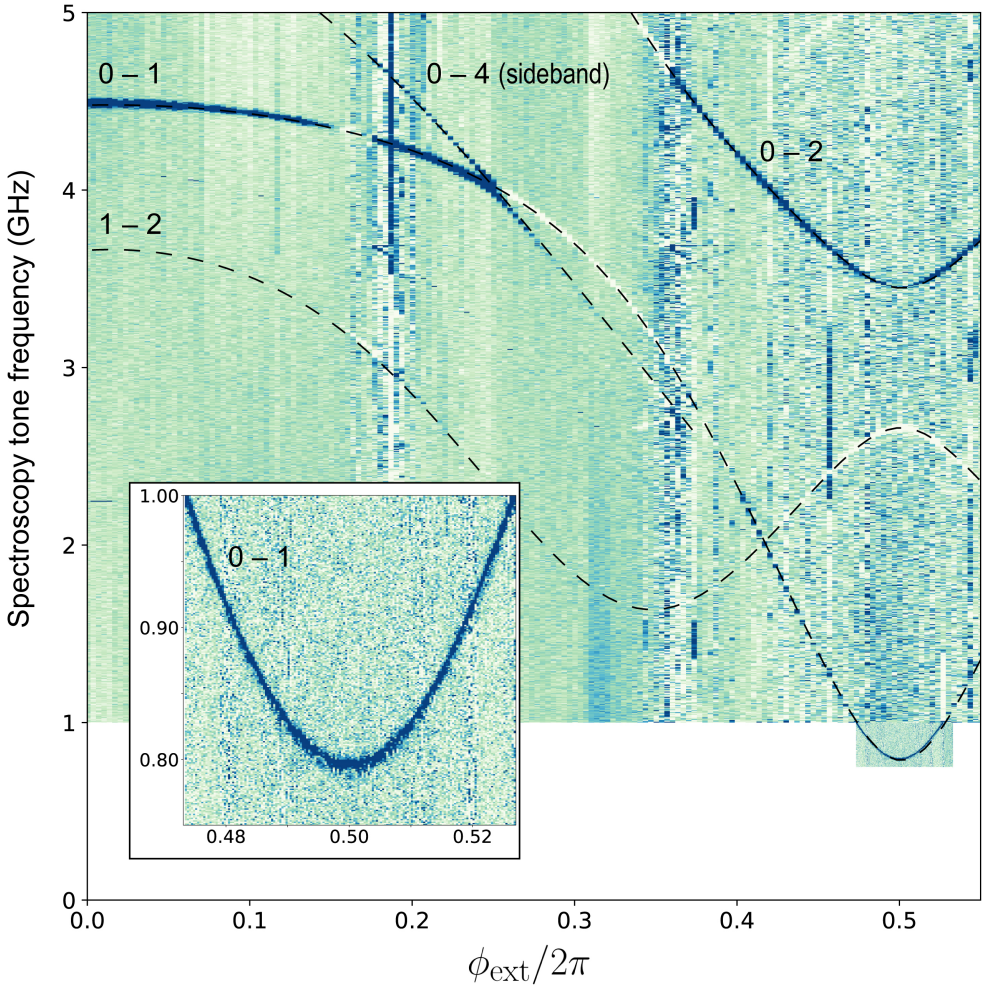

Figure 6.11: Two-tone spectroscopy of a fluxonium qubit. Two-tone spectroscopy transmission signal (arbitrary units) as a function of spectroscopy frequency and flux through the loop for device A. The contrast was optimized piecewise to maximize the visibility of the resonances. Lines indicate a fit to the spectrum of the Hamiltonian. The extra resonance line crossing (not anticrossing) the qubit transition $0-1$ is the red sideband of the $0-4$ transition and the readout at 7.5 GHz

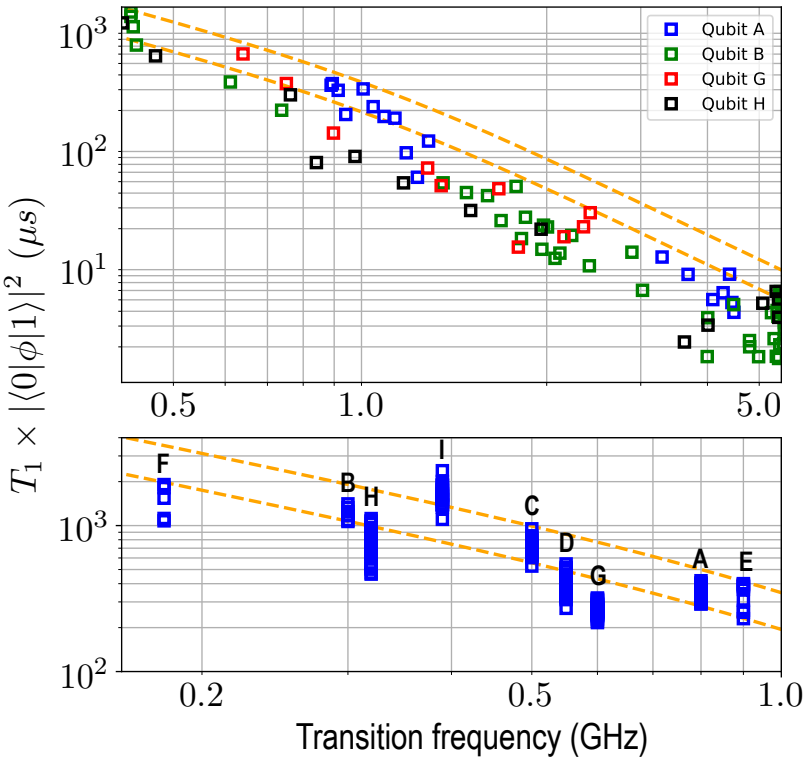

Figure 6.12: Relaxation data. (top) Normalized energy relaxation time (a quantity inversely proportional to the spectral density of noise coupled to the ϕ-variable) as a function of qubit transition frequency, measured by tuning flux in devices A, B, G, H. (bottom) Same quantity, including repeated in time measurements, for all devices A-I biased at their half-integer flux sweet-spots. Dashed lines represent a dielectric loss theory (see text).

assuming an effective frequency-independent dielectric loss tangent $\tan\delta_C$ of the total capacitance C across the weak junction. At lower frequencies we have to account for the stimulated emission by thermal photons in the environmental modes and a possible frequency dependence of the dielectric loss tangent (Eq. 4.3). The latter is modeled empirically as $\tan\delta_C \propto \omega^\epsilon$, $\epsilon > 0$. Using $T = 20$ mK (base temperature of the dilution refrigerator), $\epsilon = 0.15$, and an interval $\tan\delta_C(\omega = 2\pi \times 6\text{ GHz}) = (2.0 - 3.6) \times 10^{-6}$, we obtain a good agreement between theory and the measured T_1 times for all devices biased at their sweet spots (Fig. 6.12, bottom).

The coherence time measurement was performed using a standard single π-pulse echo

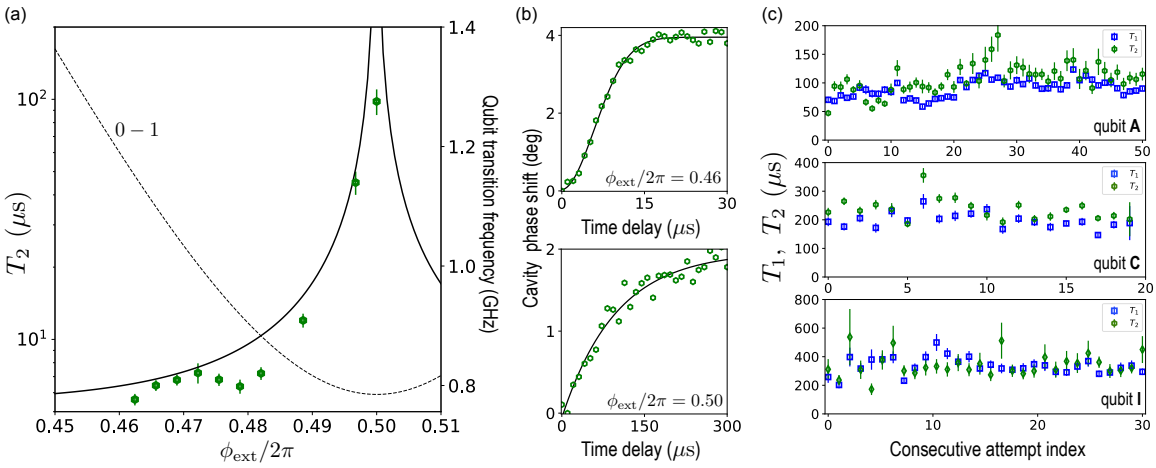

Figure 6.13: Coherence time data. (a) Coherence time T_2 (markers) and the qubit frequency (dashed line) as a function of flux. Solid line indicates a prediction for the first-order coupling to a $1/f$ flux noise. (b) Gaussian echo signal away from the sweet spot (top) and an exponential echo signal at the sweet spot (bottom).(c) Interleaved measurement of temporal fluctuations of T_1 (blue markers) and T_2 (green markers) at $\phi_{\rm ext} = \pi$ over a time interval of approximately 12 hours.

sequence [33] in order to eliminate the uninformative low-frequency (minutes-scale) drifts in the setup. This protocol choice was also dictated by the relatively low readout efficiency in this particular setup, which required minutes of averaging time. The measured coherence times T_2 as a function of flux for device A are shown in Fig. 6.13(a). Away from the sweet spot, where the qubit transition is maximally sensitive to flux, we typically measure $T_2 \approx 3-6$ μs and the echo signal has a distinct Gaussian shape (Fig. 6.13(b), top). This confirms that decoherence is due to pure dephasing. Tuning the flux towards the sweet spot, we observe a monotonic rise in the coherence time to about $T_2 \approx 100$ μs $\geq T_1$. Here the echo signal is exponential, which is consistent with relaxation-dominated decoherence (Fig. 6.13(b), bottom). The flux dependence of T_2 agrees with the first-order coupling to the $1/f$ flux noise with the amplitude $2 \times 10^{-6}(h/2e)/\sqrt{\text{Hz}}$ at 1 Hz.

To understand the robustness of measured T_2 values at the sweet spot, we have performed repeated interleaved measurements of times T_1 and T_2. The results for the representative devices A, C, and I are shown in Fig. 6.13(c). Each attempt took approximately

30 min of data acquisition. Both the values of T_1 and T_2 drift in time, but their variation typically does not exceed a factor of two over about a half-day. In some attempts we have observed $T_2 \approx 2T_1$, but a typical situation is $T_1 < T_2 < 2T_1$. We believe that the difference between $2T_1$ and T_2 may be caused by a combination of imperfect tuning of echo pulses, possible flux drifts due to imperfect magnetic shielding, and long averaging times. However, fluctuations in pure dephasing time, formally defined as $1/(1/T_2 - 1/2T_1)$ could not be fully excluded at this stage. A setup involving a quantum-limited amplifier would clarify the details of the temporal drift of coherence times in future experiments. However, it is clear that the coherence is already largely limited by energy relaxation.

The longest reliably measured values of T_2 together with the accompanying value of T_1 are quoted for all devices in Table 6.1. Indeed, the worst (best) coherence device D (I) has $T_2 = 90$ μs ($T_2 > 400$ μs) and corresponds to a slightly lower (higher) than usual value of T_1 (Table 6.1). Interestingly, the second longest coherence time ($T_2 > 300$ μs) was observed in the device C, which contains a spit-junction, and it is thus sensitive to flux noise in two loops. This strengthens the conclusion that flux-noise is not a limiting decoherence mechanism in our devices at the sweet spot.

6.3.3 Discussion of Decoherence Channels

The summary of measured coherence times along with the extracted device parameters is given in Table 6.1. Using this information we can place important bounds on various decoherence mechanisms, which are summarized in the table and discussed below.

Flux Noise

Decoherence times measured away from the sweet spot as a function of flux agree with a $1/f$ flux noise model with the amplitude approximately equal to $2 \times 10^{-6}(h/2e)/\mathrm{Hz}^{1/2}$ at 1 Hz (see Eq. 3.43), which is similar to the noise level in flux qubits. However, here the

Table 6.1: Summary of relevant device parameters. The values of E_J, E_C, E_L were obtained from spectroscopy fits; loss mechanism limit estimates are discussed in the text. * denotes effective E_J of the split-junction device biased at the double sweet-spot.

Qubit	E_J	E_C	E_L	N	T_1	T_2	$\frac{\omega_{01}}{2\pi}$	$\frac{\omega_{12}}{\omega_{01}}$	$\frac{\chi_{01}}{2\pi}$	$\tan\delta_C$	$\tan\delta_{\mathrm{AlOx}}$	x	$\tan\delta_L$
	GHz	GHz	GHz	-	μs	μs	GHz	-	MHz	$\times 10^{-6}$	$\times 10^{-4}$	$\times 10^{-8}$	$\times 10^{-8}$
A	3	0.84	1	100	110	160	0.78	3.4	0.27	1.7	1.1	3.84	15.4
B	4.86	0.84	1.14	136	250	150	0.32	11.1	0.57	1.5	1.3	0.52	2.03
C	2.2*	0.55	0.72	102	260	350	0.48	3.8	0.08	1.23	0.9	1.77	5.75
D	2.2	0.83	0.52	196	70	90	0.56	4.1	0.1	3.12	4.0	7	28.25
E	1.6	0.86	0.5	100	108	140	0.83	2.5	0.05	1.52	1.0	7.8	30.22
F	3.4	0.8	0.41	348	270	165	0.17	18.3	0.28	1.94	4.5	0.63	2.1
G	1.65	1.14	0.19	400	110	140	0.55	4.1	0.03	2	3.8	8.65	34.9
H	4.43	1	0.79	100	230	235	0.32	11.8	0.1	1.68	0.9	0.72	2.85
I	3.43	1	0.58	144	500	510	0.395	8.2	0.08	0.63	0.5	0.53	2.11

off-sweet-spot coherence time is 2-3 orders of magnitude longer (a few microseconds), due to the large number of junctions N and hence the proportionally reduced first-order flux sensitivity, whose maximal value is given by $2\pi E_L \times 2e/h \propto 1/N$. Having measured both the transition frequency vs. flux and the flux noise amplitude, we can estimate the limit on coherence time at the sweet-spot due to the second order coupling. The coupling can be approximated by $(2\pi)^4 E_L^2/f_{01} \times (2e/h)^2$, which gives a range of coherence times $10-100$ ms for the typical devices presented here. Such long times are possible entirely due to the $1/N^2$ scaling of the second-order flux sensitivity.

Interestingly, the data shows no signatures of flux noise induced energy relaxation, reported in recent experiments on flux qubits. Formally, the relaxation rate is given by the familiar Fermi's golden rule expression where the spectral density of the bath is replaced by that of the flux noise, such that it grows at low frequencies (see Eq. 3.22). In the case of a fluxonium, the relaxation rate scales as $E_L^2 \sim 1/N^2$ (the square of the energy matrix

element in the Fermi's golden rule). This gives a protection against the suggested energy relaxation by a factor $10^2 - 10^4$ in comparison to flux qubits. Such a large protection factor may explain the dramatic difference between the T_1 vs qubit frequency data reported in and that shown here.

Quasiparticles

A qubit can relax by emitting a photon which is absorbed by an unpaired quasiparticle tunneling across a junction. Assuming that the T_1 values in Table 6.1 are limited by the tunneling of out-of-equilibrium quasiparticles across the chain junctions, we conclude that their normalized density $x_{\rm qp}$ can be below 10^{-8}. Given the device dimensions, this number corresponds to less than one quasiparticle in the entire chain.

According to theory, the tunneling across the weak junction is coherently suppressed at $\phi_{\rm ext} = \pi$ by the destructive electron-hole interference [90, 91]. The interpretation of a previous fluxonium experiment in terms of this effect implied a two orders of magnitude difference between the values of x for the weak junction and for the chain junctions [85], which seems unlikely. In our experiment, an estimate of the quasiparticle density near the small junction can be obtained from device C which has a double-loop. There, the coherent suppression of tunneling is absent even at the double sweet spot of both loops because one of the two weak junctions is always away from the π-phase bias. Yet, the measured relaxation rate is similar to those of the single-loop devices. Its value requires the absence of quasiparticles near the weak junction, consistent with the above conclusion regarding the absence of quasiparticles in the chains. We cautiously speculate that vortices may be efficient at trapping quasiparticles in our specific device geometry, although further experimental results are needed to verify this hypothesis.

Thermal Photons

Every qubit undergoing a dispersive readout will experience dephasing due to photon shot noise if the readout mode is not properly thermalized [63] (Eq. 3.51). In this work we deliberately avoided this issue by making the readout mode linewidth κ much larger than the dispersive shift χ. As Table 6.1 illustrates, there is no obvious correlation between χ and T_2 which is evidence that thermal photons in the readout mode are indeed irrelevant.

Of more importance is the photon shot noise in the $N-1$ collective modes of the Josephson chain. Their frequencies bunch near the junction's plasma frequency, which in our case is around 20 GHz. Because of the non-linearity of the plasma modes, occupation of one such mode by a single photon introduces a dispersive shift of about 10^{-4} of the qubit frequency. Such a shift is much larger than the qubit's natural linewidth. Hence, in order for the qubit to have a coherence time T_2, the average time for the absence of an out-of-equilibrium photon excitation in each mode must be longer than $N \times T_2$. Given numbers in Table 6.1, we estimate this time to be longer than 50 ms, which means that the chain is practically empty of out-of-equilibrium photons. The thermalization of plasma modes in our chains is intriguing because the microwave environment at such high frequencies is poorly characterized. On one hand, with the external quality factor $Q \approx 500$, our cavity is an order of magnitude more open to the readout line than those typically used in high-coherence transmon experiments. Hence the circuit modes are well exposed to the environment of the readout line. On the other hand, losses in coaxial components in this line are substantially higher at 20 GHz and this might lead to a better thermalization of the high-frequency modes.

Dielectric Loss

Because our devices have capacitive antennas, they are exposed to surface loss in the same way as any other capacitively-shunted junction qubit. Small temporal fluctuations of T_1 may be consistent with the recent data on the X-mon qubits, explained by the drifts in the

value of $\tan\delta_C$ due to the dynamics of the weakly-coupled two-level defects [150]. Fluctuations aside, the relaxation time T_1 grows upon reducing the qubit frequency in agreement with the model of a weakly frequency-dependent dielectric loss tangent $\tan\delta_C \propto \omega^\epsilon$ of the total capacitance C across the weak junction. Let us first comment on this frequency dependence. Unlike most energy relaxation measurements of superconducting qubits, the data in Fig. 6.12 spans a remarkable 6 octaves of frequency, which makes it more sensitive to the possible frequency-dependence of $\tan\delta_C$. We used the values $\epsilon = 0.15$ and $T = 20$ mK (the base temperature of our dilution refrigerator) to match theory and data in Fig. 6.12. However, it is likely that the device temperature is higher and this would require a larger value of ϵ. More accurate experiments are required to establish bounds on the value of ϵ to clarify the underlying mechanism. Note that having $\epsilon > 0$ is a fortunate circumstance because it helps to increase the energy relaxation time towards lower frequencies.

The absolute values of T_1 at the sweet spot can be explained assuming a narrow range of $\tan\delta_C \approx (2.0 - 3.6) \times 10^{-6}$ taken at the frequency of 6 GHz (Fig. 6.12). Importantly, these numbers are nearly an order of magnitude larger than those extracted for optimally designed 3D-transmons [30], where $\tan\delta_C$ reaches down to $\tan\delta_C \approx 3 \times 10^{-7}$. Given that our antenna has a similar geometry, we expect it to have a similar surface participation ratio. Therefore, our relaxation data strongly suggest that losses in the interface layers of our devices are significantly stronger than those of optimally-fabricated transmons. This is not unexpected, given that our simplistic Al on Si fabrication procedure does not involve any advance surface preparation steps. In fact, the production of device I, which corresponds to a notably smaller value of $\tan\delta_C$ (Fig. 6.12 (bottom) and Table 6.1), included an extra step of dipping the chip into buffer oxide etching solution prior to spinning resist (see 5.4). This is an additional evidence of surface loss dominating the energy relaxation.

Dielectric loss in the tunnel oxide of the chain junctions is another potentially important energy relaxation mechanism. Assuming that each junction's capacitance has a non-zero loss tangent, we can estimate its average value as $\tan\delta_{\mathrm{AlOx}} < 10^{-3}$. Fortunately, the large

number of junctions in the chain helps to reduce the relaxation rate proportionally to $1/N$. This is because the alternating voltage across the antenna is divided by N for each junction of the chain [114]. Our estimate on the loss tangent of AlOx (10^{-4}) is about an order of magnitude smaller than the previously reported bulk value [151]. It is possible that the area of each chain junction (about $1\ \mu\mathrm{m}^2$) is sufficiently low to make encountering a strongly-coupled charge defect statistically unlikely. This effect can be explored in future devices upon varying the chain junction area.

Inductive Loss

By analogy with the effective dielectric loss tangent $\tan\delta_C$ of the capacitance C we can introduce an empirical inductive loss tangent $\tan\delta_L = \mathrm{Im}[L]/\mathrm{Re}[L]$ for the inductance L. One can show that the two loss tangents leading to the same value of T_1 are related according to $\tan\delta_L/\tan\delta_C = \omega_{01}^2 LC$. For a harmonic oscillator, the ratio above is a unity, which means that T_1 is determined by the mechanism with the largest loss tangent. By contrast, our devices are much more sensitive to the absolute value of the inductive loss tangent rather than to an absolute value of the capacitive loss tangent, because for our parameters $\omega_{01}^2 LC \sim 10^{-1} - 10^{-2}$. Given that for the quasiparticles loss $\tan\delta_L \approx x$, one can qualitatively understand the nearly two orders of magnitude difference between the bounds on $\tan\delta_C$ and x in Table 6.1.

6.4 Microwave-Activated Controlled-Z Entangling Gate

6.4.1 Introduction

A crucial step toward constructing a fault tolerant quantum computer is the implementation of a universal set of high-fidelity single- and multi-qubit gates. In a typical fluxonium circuit with high coherence and high anharmonicity [61], single-qubit gates are expected

to be nearly perfect. The evolution of fluxonium-based quantum processing technology has therefore reached the second stage, where multi-qubit gates are explored and optimized.

In fluxonium-based architectures, a microwave-activated entangling gate has multiple advantages. First, the qubits can be fixed at their flux sweet spots, so they remain highly coherent throughout the entire operation. Second, the microwave control is analogous to that of single-qubit gates, where an RF tone at a certain frequency is applied for a specific amount of time. Moreover, the spectra of fluxonium devices can be engineered with more freedom since the Hamiltonian involves three energy parameters E_C, E_J, and E_L. As discussed in section 4.1, fluxonium's spectrum at half-integer flux is less sensitive to fluctuations in E_J and E_L than to changes in the ratio E_J/E_L. This robustness against fabrication errors makes scalable optimization of the microwave-activated interaction in fluxonium practical.

In this section, we describe the experimental progress in implementing the controlled-Z two-qubit entangling gate introduced in section 4.4 and ref. [128]. Due to the small matrix element in the computational space, $n_{0\to1} \ll n_{1\to2}$, we can implement a fast entangling operation and at the same time limit the unwanted interaction in the computational space to achieve a high-fidelity two-qubit gate. To realize the gate, we employed two capacitively coupled fluxonium qubits. To bias both qubits simultaneously at their sweet spots using the magnetic coil shown in Fig. 5.3, we placed the two loops close to each other. To satisfy the requirements on the qubit-qubit capacitive coupling constant J_C, the qubit-cavity couling constant g, and the charging energy E_C, we designed the dipole antenna to be asymmetric as shown in Fig. 6.14(a). The qubits are mounted on a copper cavity and readout jointly [112, 111].

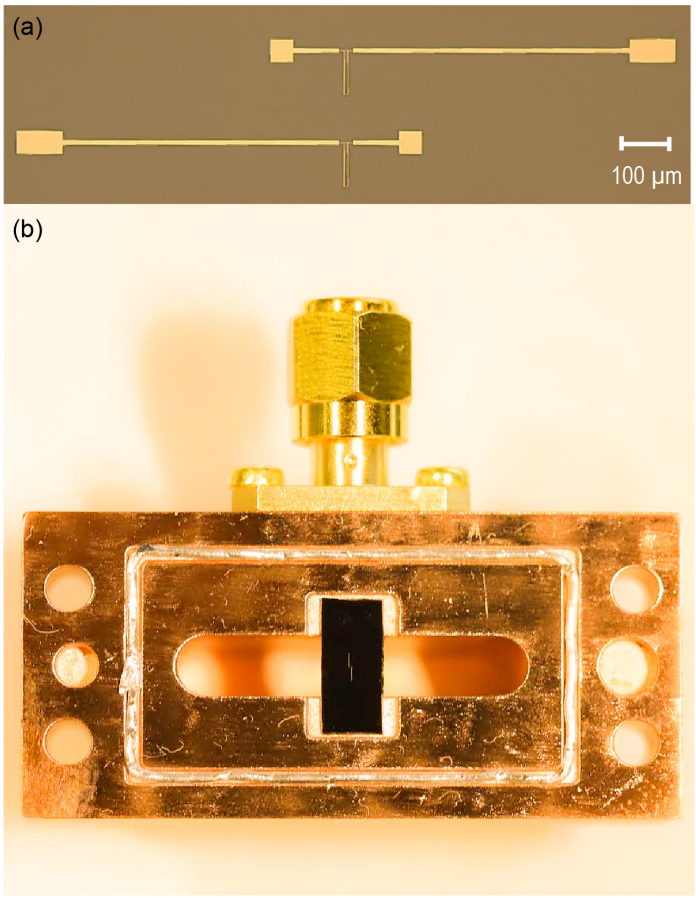

Figure 6.14: Two-qubit device. (a) Optical image of two capacitively coupled fluxoniums. (b) Joint readout setup using a copper cavity with linewidth $\kappa/2\pi \approx 4.5$ MHz.

6.4.2 Spectrum

To characterize the two-qubit device, we first performed a two-tone spectroscopy scan to get its spectrum, which was then fitted using the simple model to extract the qubits' parameters. The fitting procedure consisted of two steps. First, we fitted the $0 \to 1$ and $0 \to 2$ transitions of each qubit, assuming they are uncoupled. This allowed us to obtain the initial guess, and to identify the coupled transition energies for the next step. Then, the spectrum was fitted to a capacitively coupled fluxonium model (Eq. 4.27) utilizing up to seven transitions across two flux periods. The extracted parameters can be used to simulate the spectrum to

Table 6.2: Extracted parameters for two capacitively coupled fluxonium circuits.

E_C^A	E_L^A	E_J^A	E_C^B	E_L^B	E_J^B	J_C	g	unit
0.972	0.456	5.899	1.027	0.683	5.768	0.224	0.1	GHz

Table 6.3: Charge matrix elements for computational transitions.

	$\|00\rangle \rightarrow \|10\rangle$	$\|00\rangle \rightarrow \|01\rangle$	$\|10\rangle \rightarrow \|11\rangle$	$\|01\rangle \rightarrow \|11\rangle$
n_A	-0.0252j	-0.001j	0.0015j	0.0252j
n_B	0.0007j	0.0446j	-0.0446j	-0.0006j

compare with the data as shown in Fig. 6.15(a).

For the specific two-qubit device reported in this thesis, the parameters including the qubit-cavity coupling constant g are listed in Table 6.2. The spectrum contains many features, but we only have to pay attention to the half integer flux quantum region. The extracted computational transition frequencies are: $f_{00\rightarrow01} = 136.3$ MHz, $f_{00\rightarrow10} = 72.4$ MHz, and the gate transition frequencies are $f_{11\rightarrow12} = 4.902$ GHz, $f_{11\rightarrow21} = 5.198$ GHz. We extracted the ZZ coupling rate $\Delta_{ZZ} \approx 28$ kHz and the gate rates $f_{11\rightarrow21} - f_{10\rightarrow20} = 22$ MHz, $f_{01\rightarrow02} - f_{11\rightarrow12} = 15$ MHz. The reduced charge matrix elements corresponding to transitions within the computational space are computed and shown in Table 6.3.

Although the applied external fluxes for the two qubits were not perfectly aligned, we could still choose a flux bias close to the two sweet spots which gave us a decent coherence time $T_2^{\text{echo}} \approx 40$ μs and relaxation time $T_1 \approx 300$ μs for both qubits. The rest of this section describes experiments done at this flux bias.

6.4.3 Single-Shot Joint Readout

We used a TWPA [136] in this experiment to improve the SNR of the cavity signal. This allowed us to readout the qubit states in single-shot manner. To obtain the data shown in

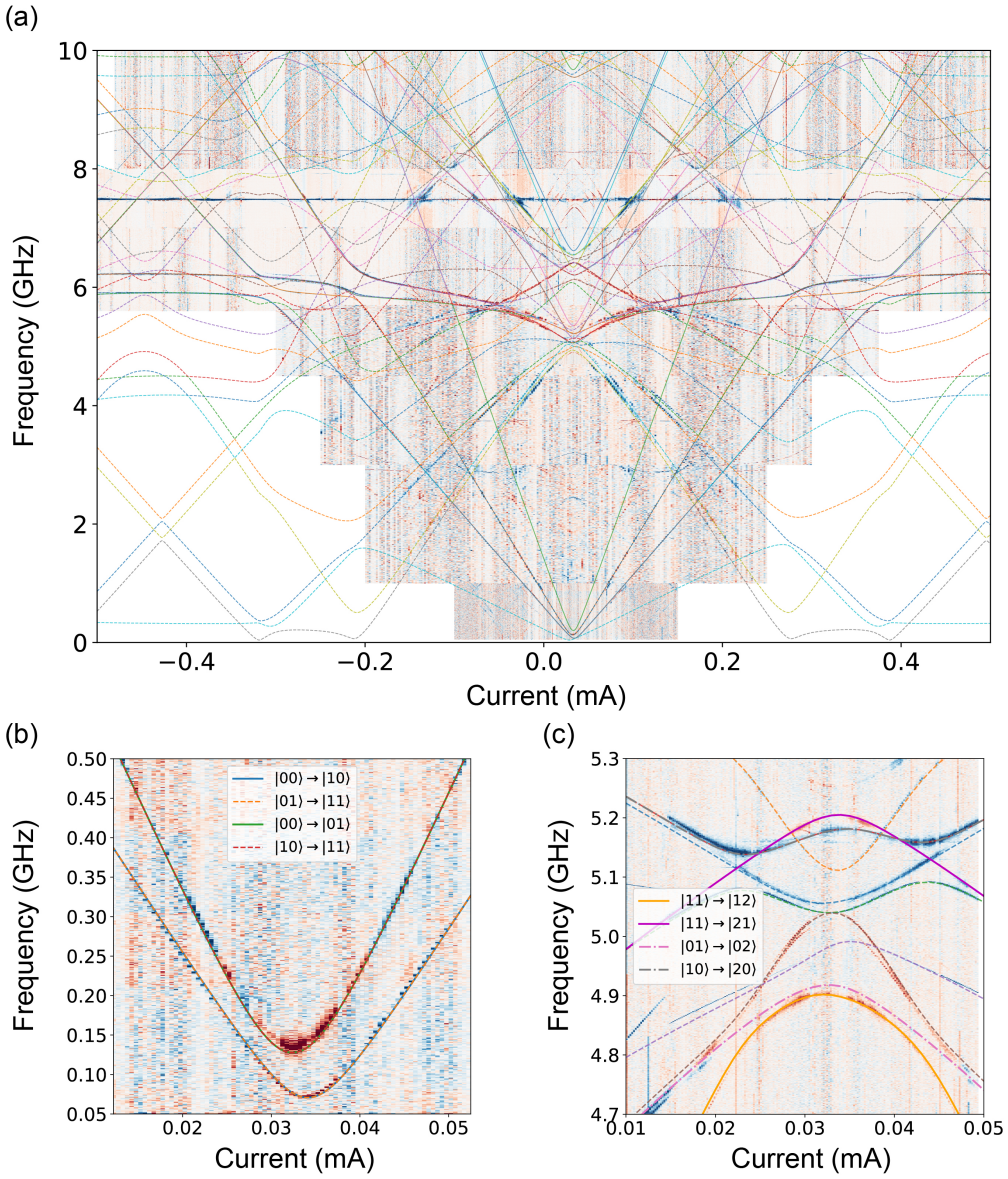

Figure 6.15: Spectrum of two capacitively coupled fluxonium qubits. (a) Spectrum with fit from the simple model. (b) Zoomed-in spectrum showing the computational subspace with $\omega_{00\to10}/2\pi = 72.4$ MHz, $\omega_{00\to01}/2\pi = 136.3$ MHz. The ZZ coupling rate is $\Delta_{ZZ} = 28$ MHz. (c) Zoomed-in spectrum showing the CZ gate subspace, with $\omega_{11\to12}/2\pi = 4.902$ GHz, $\omega_{11\to21}/2\pi = 5.198$ GHz. The gate rates are $f_{01\to02} - f_{11\to12} = 15$ MHz, $f_{11\to21} - f_{10\to20} = 22$ MHz.

Fig. 6.16(a), we first optimized the TWPA pump parameters, namely the pump frequency and power, then swept the cavity power and frequency until the four blobs corresponding to the computational states $|00\rangle$, $|10\rangle$, $|01\rangle$, and $|11\rangle$ became well-resolved in a 2D IQ histogram plot. We also swept the integration time separately to find the optimal readout configuration. The blobs were identified at a later stage by Rabi driving the higher transitions $|11\rangle \leftrightarrow |12\rangle$, $|01\rangle \leftrightarrow |02\rangle$, $|11\rangle \leftrightarrow |21\rangle$, $|10\rangle \leftrightarrow |20\rangle$ after preselection. Additional preselected Rabi experiments for $|00\rangle \leftrightarrow |01\rangle$ and $|00\rangle \leftrightarrow |10\rangle$ were used to check for consistency.

We fitted a sum of four Gaussian functions to the projected single-shot histogram data and extracted the populations of the computational states, as shown in Fig. 6.16(b). We estimated the effective temperatures for the qubit A and qubit B assuming Boltzmann statistics (see Eq. 2.76). For example, we made the assumption that the ground and excited state populations of qubit A are $P_{00} + P_{01}$ and $P_{10} + P_{11}$, respectively. We found that these effective temperatures depended strongly on the cavity and TWPA pump tones' power. We do not understand this effect fully at the moment, and further research is required to unveil the underlying physics behind this behavior. With the optimal readout configuration, the extracted populations are $P_{|00\rangle} = 0.3$, $P_{|10\rangle} = 0.35$, $P_{|01\rangle} = 0.11$, $P_{|11\rangle} = 0.24$. These correspond to effective temperatures $T_A \approx -9$ mK, $T_B \approx 10$ mK for qubit A and qubit B. We emphasize again that these are effective, rather than physical, temperatures.

Our ability to readout the qubits in single-shot manner allowed initialization by preselection technique [152]. This was achieved by including in the pulse sequence another pulse at the cavity frequency referred to as the *heralding* pulse, and a delay time $\tau = 5/\kappa$ after the heralding pulse. The delay allows the cavity photons to decay before any qubit gate operations. The result in Fig. 6.17 shows that we could initialize the qubit to the $|00\rangle$ state with fidelity ≈ 0.9, corresponding to the effective temperatures $T_A \approx 1.3$ mK, $T_B \approx 2.1$ mK. The initialization error comes from the fact that the readout is not perfectly QND.

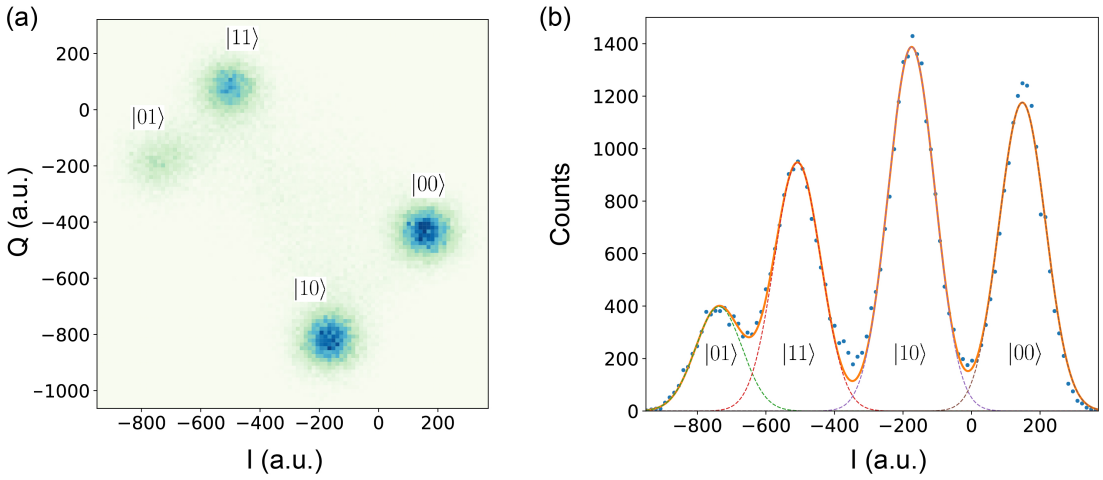

Figure 6.16: Single-shot joint readout of qubits' thermal states (a) 2D histogram of cavity signal showing the four blobs corresponding to the qubit in four computational states. (b) Projection of data in plot (a) onto the I-axis. Fitting of the 1D histogram to four Gaussian curves allowed us to determine the populations, and subsequently estimate the temperatures of the qubits: $T_A \approx -9$ mK, $T_B \approx 10$ mK.

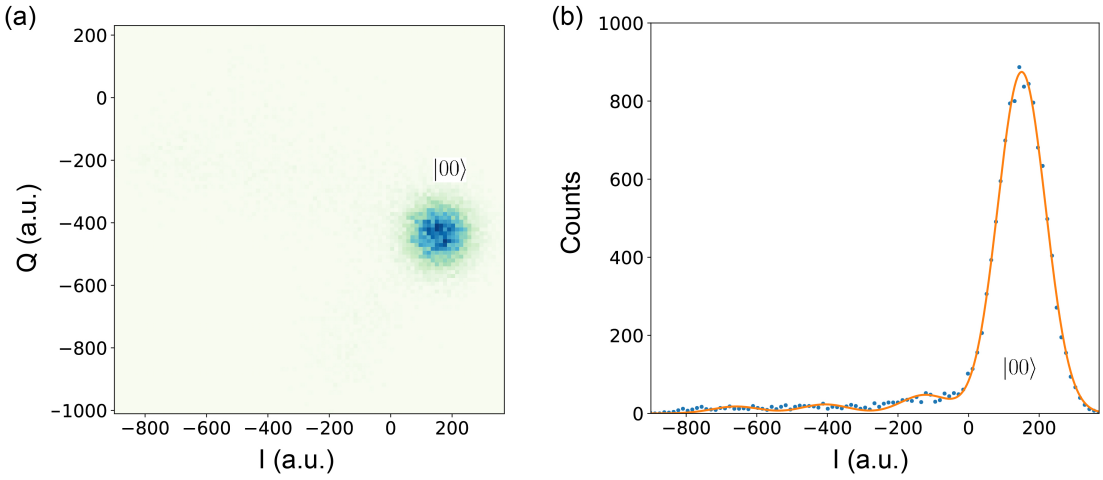

Figure 6.17: Initialization by preselection. (a) 2D histogram of cavity signal after preselection showing only one blob corresponding to the ground state $|00\rangle$. (b) Projected data from (a) onto the I-axis. The temperatures after initialization were $T_A \approx 1.3$ mK, $T_B \approx 2.1$ mK.

6.4.4 Single-Qubit Gates

Although the qubits' transition frequencies are low and the computational states' thermal populations are substantial, the high fidelity initialization procedure allowed us to improve the signal contrast significantly, and we could readout the states of the qubits much more reliably. Qubits having low transition frequency pose yet another problem: no commercial IQ mixer that we are aware of works below 80 MHz. Therefore, to control the qubits at such low frequencies, we resorted to using the AWG's ability to synthesize RF signal up to 300 MHz.

We observed Rabi oscillations in both qubits by driving them directly with the AWG (Fig. 6.18(a) and (b)). The qubit frequencies were found with Ramsey experiments (see section 6.5). The pulses have Gaussian shape with width $\sigma = 150\ \mathrm{ns}$ and cutoff boundary at 4σ. We further tuned up the gates by applying a sequence consisting of an odd number of $\pi/2$ pulses in either quadrature with varying pulse amplitude, and selecting the amplitude corresponding to the curve that varied the least with respect to the number of pulses [153].

Using this pulse configuration, we prepared different single-qubit states and performed quantum state tomography. The single-qubit density matrices were reconstructed using linear inversion (see section 2.3). The results are shown in Fig. 6.18(c), with the average single-qubit state fidelity $\mathcal{F} = 0.98$ using Eq. 2.69.

We measured the single-qubit gates' fidelities using interleaved randomized benchmarking (RB) [154], which works as follows. First, a regular RB measurement is performed by applying a random sequence of m Clifford gates C_i, chosen randomly from the Clifford group Cliff_1 (Fig. 6.19(a), top). The $(m+1)\mathrm{th}$ gate is chosen to effectively turn the entire sequence into identity operation. The measurement is randomized $K = 11$ times, and the

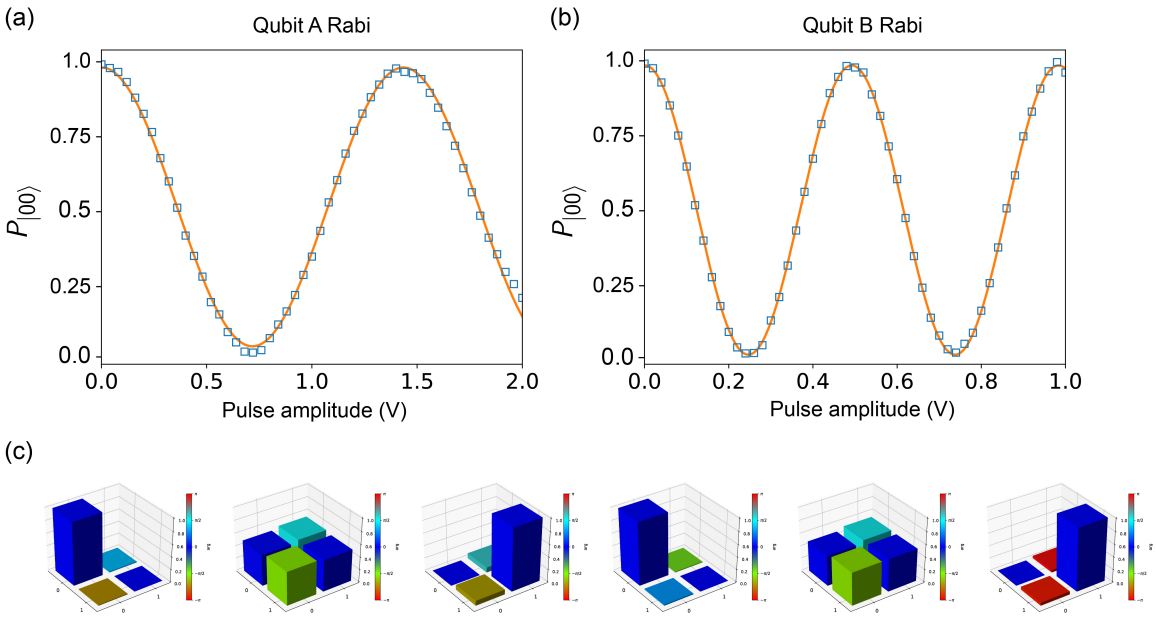

Figure 6.18: Control of low frequency qubit transitions. (a) Rabi oscillation between $|00\rangle$ and $|10\rangle$. (b) Rabi oscillation between $|00\rangle$ and $|01\rangle$. Both qubits were driven using the AWG's direct outputs. (c) Single-qubit state tomography results showing the density matrices of the (from left to right) ground, superposition, and excited states of qubits A and B.

averaged result is fitted to either the zeroth or first order model:

$$\begin{aligned} F^{(0)}(m) &= A_0 p^m + B_0, \\ F^{(1)}(m) &= A_1 p^m + C_1 (m-1) p^{m-2} + B_1, \end{aligned} \tag{6.1}$$

to extract the depolarizing parameter p. The average error rate over the entire Clifford gate sequence is given by

$$r = \frac{1-p}{2} \tag{6.2}$$

Then, an interleaved RB measurement is performed by inserting an additional gate of choice $\mathcal{C}$ after every Clifford gate $\mathcal{C}_i$, up to the mth random gate (Fig. 6.19(a), bottom). Again, the $(m+1)$th gate is chosen to be the inverse of the combination of the previous m gates. The measurement is repeated to realized $K = 11$ randomizations, and the averaged

Table 6.4: Single-qubit gate fidelities.

Gate	Cliff_1	I	X	-X	X/2	- X/2	Y	-Y	Y/2	-Y/2
A, 0th	0.976	0.989	0.982	0.982	0.987	0.988	0.982	0.982	0.987	0.985
B, 0th	0.987	0.9925	0.9886	0.9885	0.9927	0.9921	0.9889	0.9881	0.9927	0.9915
A, 1st	0.954	0.981	0.961	0.962	0.973	0.973	0.959	0.961	0.972	0.969
B, 1st	0.993	0.994	0.9924	0.9924	0.9948	0.9941	0.9924	0.9918	0.9949	0.994

result is fitted to Eq. 6.1 to extract the depolarizing parameter $p_{\mathcal{C}}$. The error rate $r_{\mathcal{C}}$ of the interleaved gate $\mathcal{C}$ is estimated as

$$r_{\mathcal{C}} = \frac{1 - p_{\mathcal{C}}/p}{2}. \tag{6.3}$$

Randomized benchmarking results for single-qubit gates are shown in Fig. 6.19(b) and (c) for qubits A and B, respectively. The fidelities are summarized in Table 6.4 for both zeroth and first orders fit. Gate errors are likely due to a combination of decoherence, spurious ZZ coupling, and microwave cross-talks. Further improvements would involve shorter gate times, composite pulses to cancel out the crosstalks, and pulse shaping techniques such as DRAG [107, 108]. Future 2D integration of individual microwave controls should make the crosstalks negligible.

6.4.5 Two-Qubit Controlled-Z Gate

Characterization of the controlled-Z gate is discussed below. First, we performed two-tone spectroscopy to locate the gate transition frequency and Rabi experiments to find the right pulse parameters. To avoid state leakage, we simply used a Gaussian pulse with width $\sigma = 150$ ns and total duration equal to 4σ. The gate transition has $T_1 \sim 10$ μs Rabi oscillation between $|11\rangle \leftrightarrow |21\rangle$ and $|11\rangle \leftrightarrow |21\rangle$ are shown in Fig. 6.20(a) and (b), respectively. We used a Gaussian pulse with total duration equal to 600 ns.

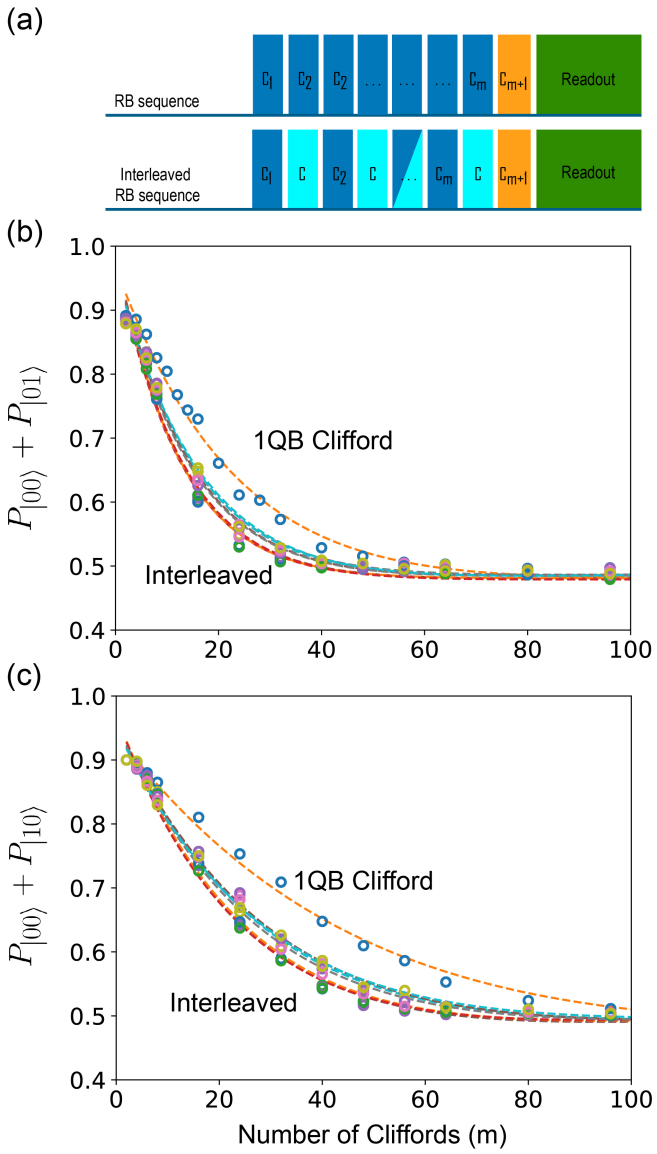

Figure 6.19: Benchmarking single-qubit gates. (a) Randomized benchmarking sequence (top), and interleaved randomized benchmarking sequence (bottom). Normal RB sequence gives us the average fidelity for the entire set of Clifford gates. The interleaved RB sequence gives us the error for specific gates. The target gate $\mathcal{C}$ (light blue) is interleaved with random gates (dark blue) chosen from the Clifford group. In both cases, a final gate (orange) is used to make the sequence equivalent to the identity operation. (b) Interleaved randomized benchmarking results for qubit A. (c) Interleaved randomized benchmarking results for qubit B.

After tuning up the gate, we used the sequence described in Fig. 2.3 to create Bell states and then characterized them using quantum state tomography. To ensure that the resulting density matrices are physical, we used maximum likelihood estimation (MLE) to determine the output state (see Eq. 6.8). Since we measured starting with a thermal state and could initialize to any computational state using preselection, we could essentially create four different Bell states in a single measurement. Results for $|\beta_{10}\rangle$ and $|\beta_{00}\rangle$ are plotted in Fig. 6.20 (c-d).

We computed the concurrences and fidelities for these states. Concurrence is a simple entanglement monotone measure [155]. The procedure to determine it is as follows. First, we compute the product $R = \rho(Y \otimes Y)\rho^*(Y \otimes Y)$, then take the eigenvalues of R and arrange them in decreasing order as $\{\lambda_1, \lambda_2, \lambda_3, \lambda_4\}$. The concurrence is then defined as $C(\rho) = \max(0, \sqrt{\lambda_1} - \sqrt{\lambda_2} - \sqrt{\lambda_3} - \sqrt{\lambda_4})$. We found $C = 0.915$ for $|\beta_{10}\rangle$ and $C = 0.88$ for $|\beta_{00}\rangle$, indicating that the states we created are highly entangled. The state fidelities computed using Eq. 2.69 are $\mathcal{F}_{|\beta_{10}\rangle} = 0.956$ and $\mathcal{F}_{|\beta_{00}\rangle} = 0.915$.

We next performed quantum process tomography for the CZ gate by preparing 16 independent input states, applying the gate, and utilizing quantum state tomography via MLE to determine each output state. The resulting χ matrix based on the $\{I, X, Y, Z\}^{\otimes 2}$ operator set was computed using linear inversion (see Eq. 2.84) and shown in Fig. 6.21(a). The corresponding process fidelity computed using Eq. 2.85 is $\mathcal{F} = 0.88$, which is likely dominated by SPAM errors.

Finally, we extracted the CZ gate fidelity using interleaved RB. The procedure for two-qubit case is similar to the single-qubit one. First, the regular RB result is fitted to Eq. 6.1 to extract the depolarlizing parameter p_{2QB}, and the average error for the two-qubit Clifford group is

$$r = \frac{3}{4}(1 - p). \tag{6.4}$$

The interleaved RB result is then fitted to extract p_{CZ}, which gives us the error of the gate

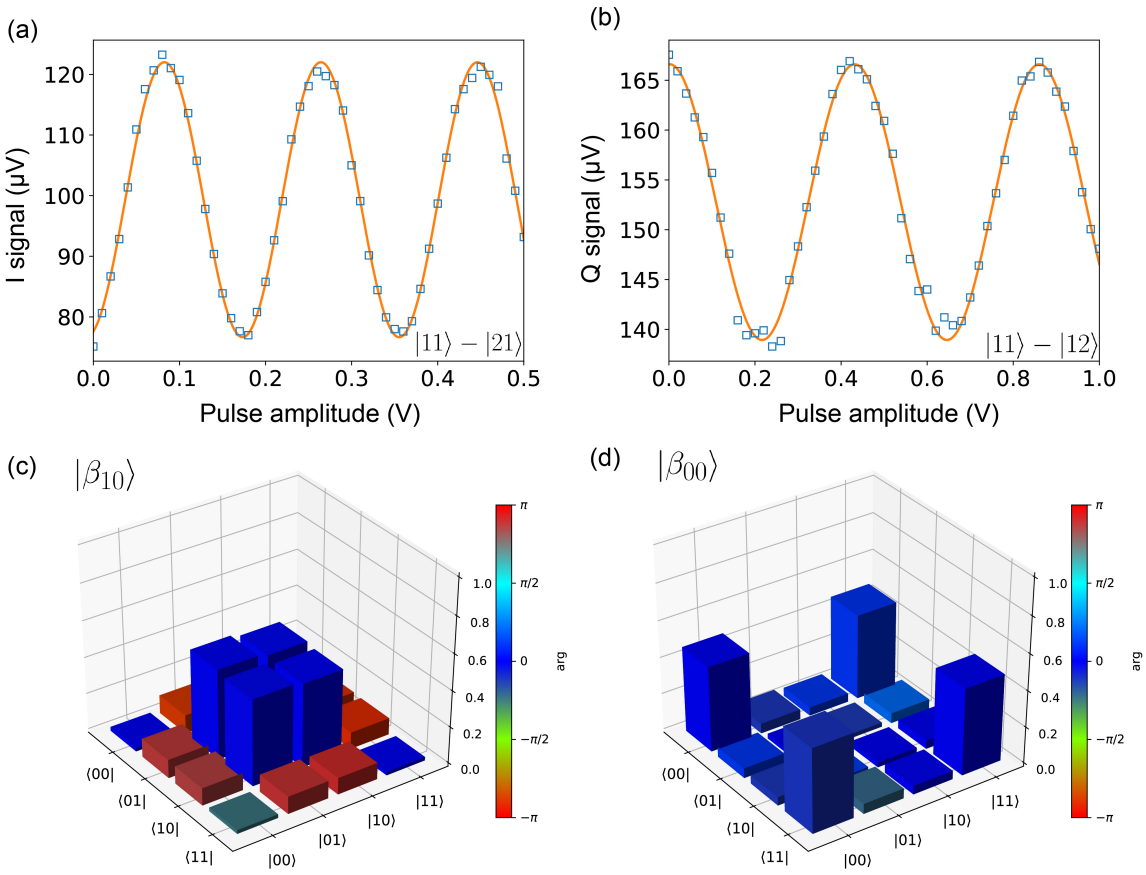

Figure 6.20: Entangling operation. (a) Rabi oscillation between $|11\rangle$ and $|21\rangle$, realized by applying a Gaussian-shaped pulse at the exact transition frequency and varying the pulse amplitude. (b) Rabi oscillation between $|11\rangle$ and $|12\rangle$, also realized by varying the Gaussian pulse's amplitude. (c) Bell state $|\beta_{10}\rangle$ created by using the sequence in Fig. 2.3 and $|00\rangle$ as initial state. (d) Bell state $|\beta_{00}\rangle$ created by using the sequence in Fig. 2.3 and $|11\rangle$ as initial state.

as

$$r_{\mathrm{CZ}} = \frac{3}{4}\left(1 - \frac{p_{\mathrm{CZ}}}{p_{\mathrm{2QB}}}\right). \tag{6.5}$$

We typically observed $\mathcal{F}_{\mathrm{CZ}} = 1 - r_{\mathrm{CZ}} = 0.96 \pm 0.02$ (Fig. 6.21(b)), and the best fidelity achieved was 0.975 ± 0.015. The current result is most likely limited by a combination of ZZ coupling, dephasing, and AC Stark shifts of nearby transitions. The uncertainty in characterizing the two-qubit gate is mostly due to errors from single-qubit gates. Further

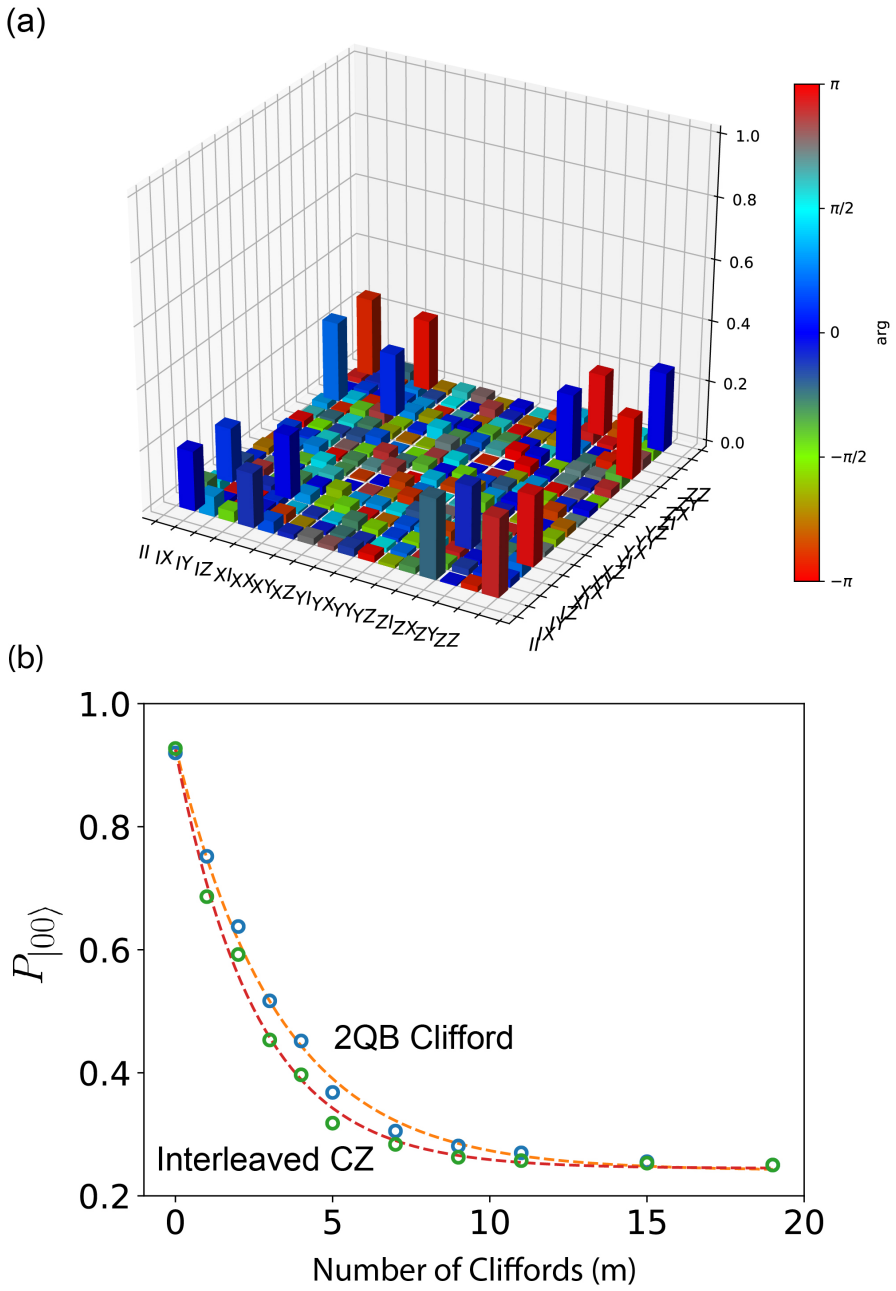

Figure 6.21: Benchmarking two-qubit gate. (a) Quantum process tomography of the CZ entangling gate, with process fidelity $\mathcal{F} = 0.88$. The infidelity is likely dominated by SPAM errors. (b) Interleaved RB result with $F_{\mathrm{CZ}} = 0.96 \pm 0.02$.

improvement in single-qubit gates would reduce this uncertainty. Alternatively, using iterative RB [153] should allow us to extract the small gate error more confidently. Improving the CZ gate should be possible by using shorter gate with pulse shaping techniques such as DRAG [107, 108]. Optimization techniques such as one proposed in ref. [156] would be necessary to find the optimal pulse shape and detuning.

6.5 Tune-up Experiments

This section describes typical fluxonium measurements we performed in the lab. We focus on discussing the techniques and experimental details which are essentials to obtaining the results in the previous sections.

6.5.1 Spectroscopy

Cavity: One-Tone Spectroscopy

One may be tempted to measure the cavity at room temperature when the qubit has been mounted, but care must be taken because a high-amplitude electric field across the small Josephson junctions can kill it. To avoid destruction from electrostatic discharge, we should wear anti-static straps upon handling the chip or cavity. A $50\ \Omega$ load resistor is connected to the cavity port to avoid accidentally shocking the device. It is usually safe to check the cavity with the VNA after mounting it onto the cold finger and connecting the coax cables, since there is now at least $60\ \mathrm{dB}$ of attenuation between the cavity and the VNA.

After cooling-down, the very first measurement is to check the cavity resonance. Next, we must determine at which power we should readout the cavity and qubit system, so a one-tone experiment with power variation must be done. The result typically shows a change in cavity resonance across a threshold value, as shown in Fig. 6.22. The cavity power must generally be chosen to be lower than the threshold for the qubit to shift the resonance.

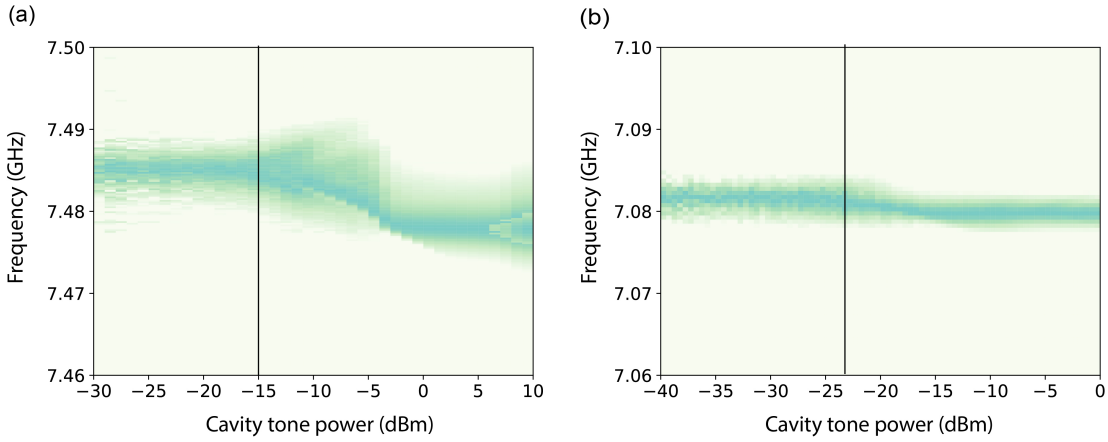

Figure 6.22: One-tone versus power. Cavity resonance versus probe tone power with data along the y-axis normalized to the mean value. The power should be lower than the threshold (black vertical line) where the cavity resonance starts going back to its bare value. (a) The dispersive shift is large, so the change in cavity resonance is obvious. (b) The dispersive shift is small, so we can do a finer scan to find the threshold.

Choosing a cavity tone power that is too high may make the cavity insensitive to the state of the fluxonium qubit, preventing us from reading it out. On the other hand, if we choose a power that is too low, the SNR would be too small, and the measurement would take a long time to average out the noise. Therefore, the best strategy is to pick the power right below or at the threshold value (black vertical line in Fig. 6.22).

After choosing the appropriate power, we can perform a quick measurement where we sweep the flux and keep the cavity tone frequency fixed. This helps us to quickly check if the qubit is alive because a typical fluxonium qubit modulates the cavity resonance with flux. This also helps us determine the flux periodicity of the device, as shown in Fig. 6.23(a). A full one tone spectroscopy can now be started using the appropriate power, frequency, and flux range. The cavity-qubit anti-crossing can be fitted to extract the coupling coefficient. The fitting, however, is best done after we have acquired some knowledge about the qubit spectrum, and identified which transitions actually cross the cavity (see Fig. 6.23 (b)).

In the case when the anti-crossing is too small, such as when the matrix elements of the corresponding transition is small due to large E_J/E_C ratio, the small modulation of

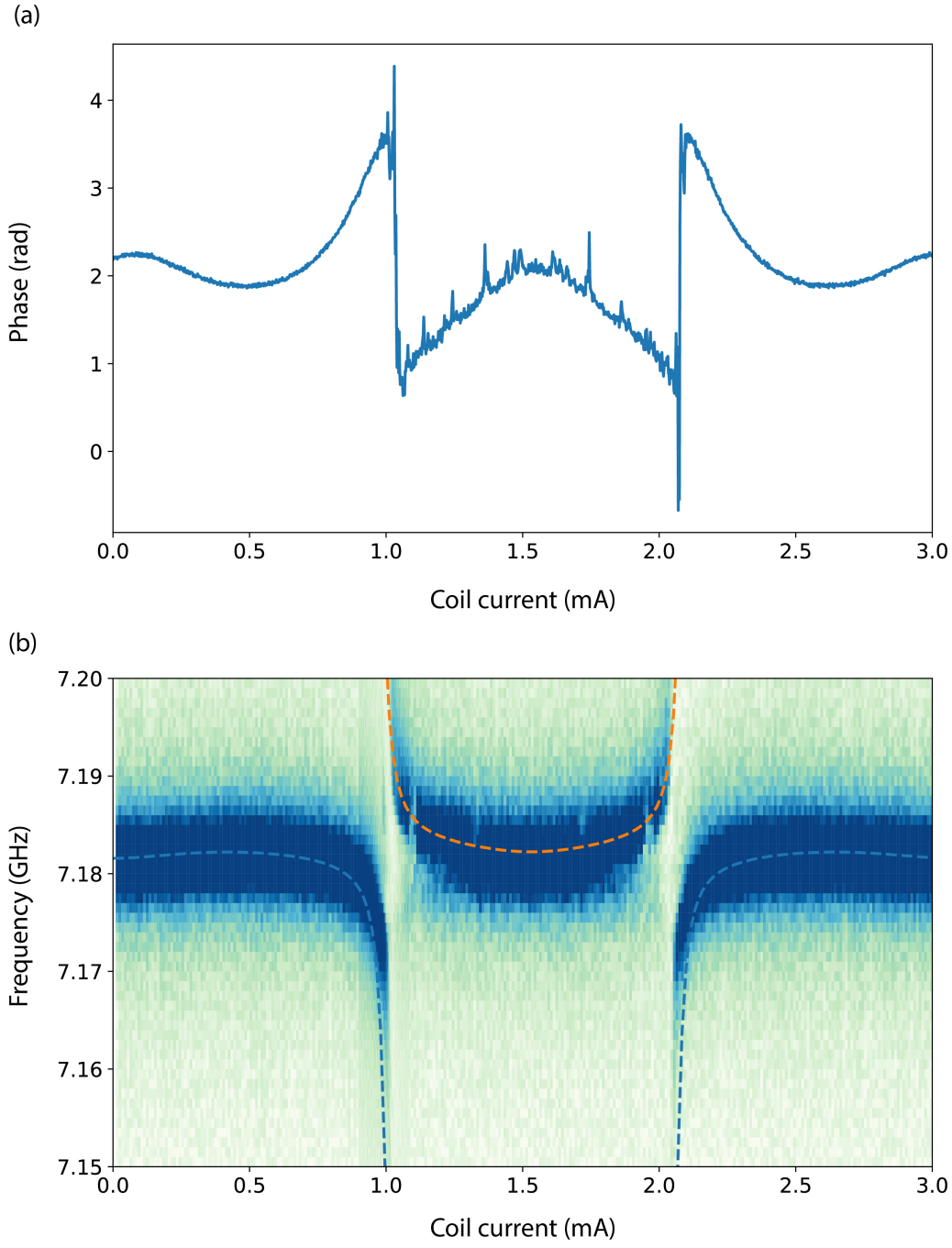

Figure 6.23: One-tone versus flux. (a) Cavity resonance versus flux. The measurement helps us confirm if the qubit is *alive*, and allows the extraction of flux periodicity. (b) One-tone spectroscopy showing the cavity anticrossing with qubit transition. The data can be used to extract the qubit-cavity coupling coefficient.

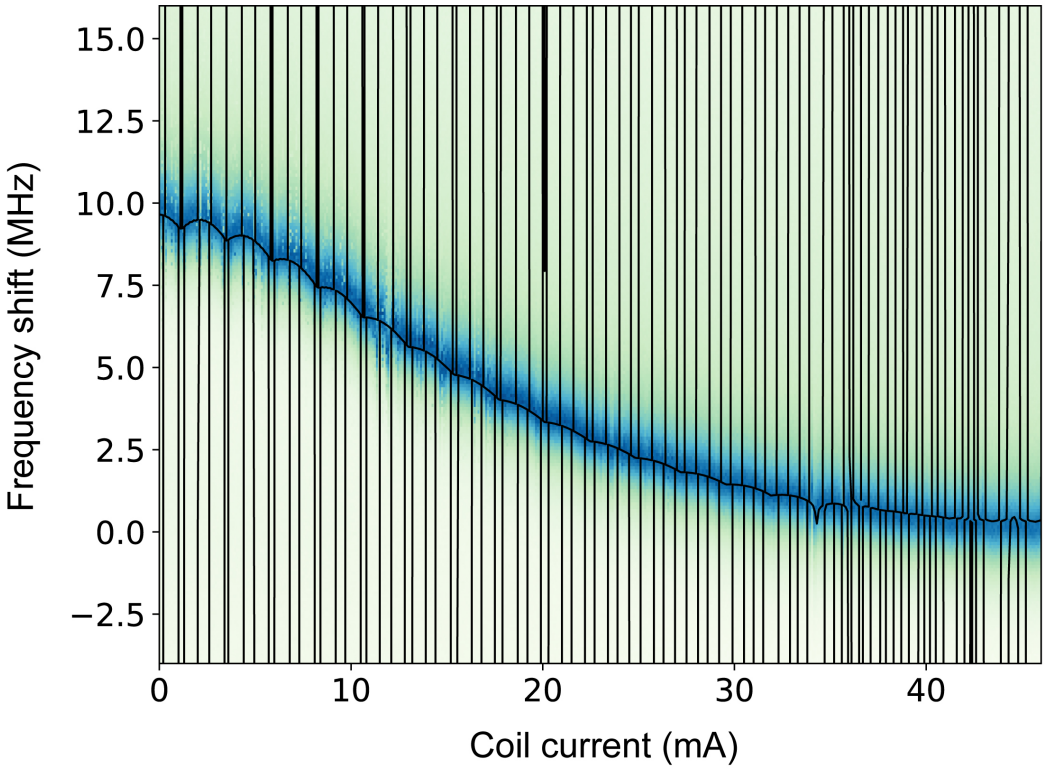

Figure 6.24: One-tone spectrum of the split-junction device. The cavity resonance is modulated slightly by the qubit as the plasmon changes with E_J. In this case, the coupling coefficient can also be extracted by fitting the cavity resonance across the entire flux period. The vertical black lines are fitted theoretical lines corresponding to the fluxon transitions (data not visible).

the cavity by the plasmon in flux can also be fitted to extract coupling coefficient g. For example, in the selection rules experiment discussed in section 6.2, the variation in E_J with flux effectively changes the cavity frequency. There is a large change over the small loop's flux period, but also a small change in cavity frequency over the big loop's flux period, as shown in Fig. 6.24. This fitting procedure is more efficient if the qubit spectrum has been measured and the qubit's parameters have been extracted, so the coupling coefficient is the only fitting parameter.

Qubit: Two-Tone Spectroscopy

After measuring the cavity, we proceed to scan the qubit spectrum by performing two-tone spectroscopy. This is typically done in pulse mode, where the qubit pulse is first applied, and the cavity readout pulse is applied right after. If the qubit tone excites the qubit, the cavity resonance would be shifted, with the value of the shift dependent on the dispersive shift at that particular flux bias. By measuring the cavity before the qubit decays back to its equilibrium state, we can record the qubit frequency. Then, we can get the qubit spectrum by sweeping the coil current.

Since fluxonium has transition frequencies across a very broad range, while the 3D cavity filters out the input signal at low frequencies, we have to perform spectroscopy using different qubit tone powers in different frequency ranges. The rule of thumb is to use qubit tone power at -30 dB less than cavity power in the region ± 3 GHz away from cavity resonance. If time allows, a power sweep can be done to check for the best option. The power should be increased approximately 5 dB per GHz as we move lower in frequency, depending on the distance between the chip and the input port. We used this strategy to obtain the spectroscopy data in Fig. 6.25 for a representative fluxonium sample. We can fit spectroscopy data to the Hamiltonian model (Eq. 3.17) to extract the parameters and calculate relevant properties of the qubit. Further interpretation of spectroscopy data is discussed in section 6.3.

As shown in the previous chapter (see Fig. 5.11(a)), a pulse with sharp rising time has a wide spectral bandwidth, and may excite additional transitions, blurring the main line. To avoid this, we often use a Gaussian pulse for qubit spectroscopy. In general, a wider Gaussian pulse in time domain results in cleaner spectral features. While pulse spectroscopy is typically used to obtain a clean spectrum, it requires synchronization between the qubit and cavity RF tones, which is most conveniently done using an AWG.

When there is no AWG available, it is also possible to perform a continuous wave (CW)

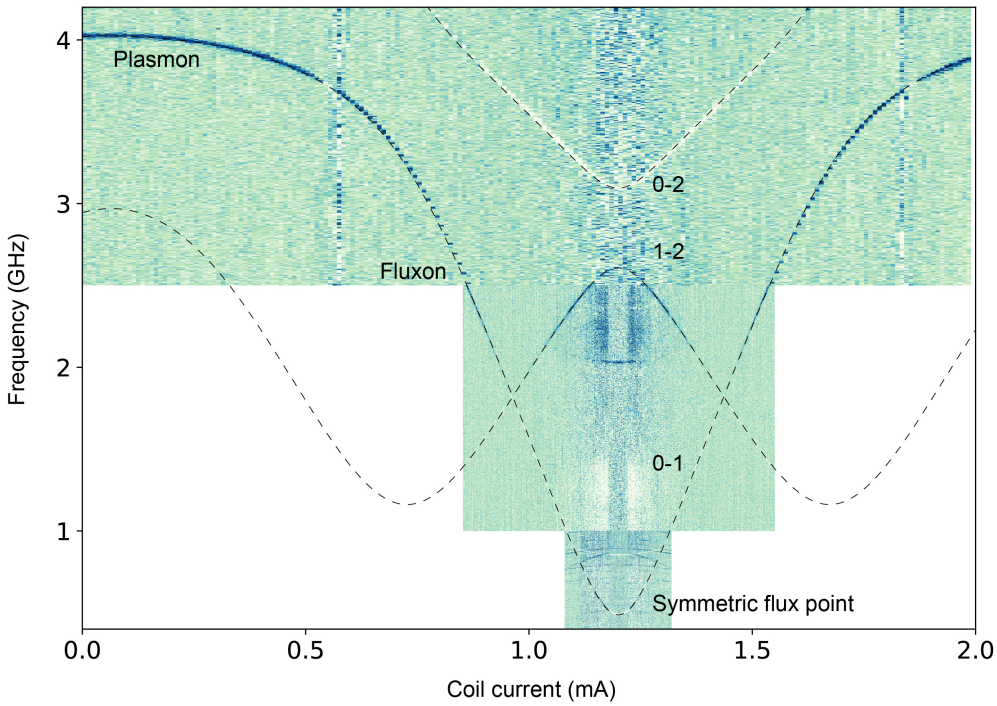

Figure 6.25: Two-tone spectrum. Two-tone spectroscopy result of a typical fluxonium sample showing the $0-1$, $0-2$, $1-2$ transition energies. The scan is typically completed in 3 stages. First, the plasmon region is scanned using 10 MHz frequency step and $10\ \mu$A flux step. Then, the fluxon region is scanned using 10 times finer resolution in both frequency and flux. Finally, the half flux spectrum region is scanned at a higher power or longer qubit pulse.

measurement where both cavity and qubit tones are applied simultaneously. This results in faster measurement time at the cost of a spectrum with many lines corresponding to higher order processes. While these lines may also appear in pulse spectroscopy when high qubit tone power is used, their number is fewer. CW is most conveniently used in a VNA setup, where two ports of the VNA are used to measure the S parameter of the cavity, and an additional port or an external RF source is used as the qubit tone.

In CW spectroscopy, the qubit is measured in the presence of cavity photons, so its frequency may not be that of the bare qubit, due to the AC Stark shift introduced in section

2.2. On the other hand, this shift helps us determine the number of photons present in the cavity. For this experiment, we can measure the qubit spectrum at a fixed flux bias and vary the cavity power. An example is shown in Fig. 6.26(a). If the dispersive shift per photon has been determined, it is then straightforward to calibrate the photon number based on the frequency shift. At the same time, the fluctuation of the photon number scales with its square root, so more photons in the cavity would result in faster dephasing, effectively broadening the qubit's linewidth. This effect is shown in Fig. 6.26(b).

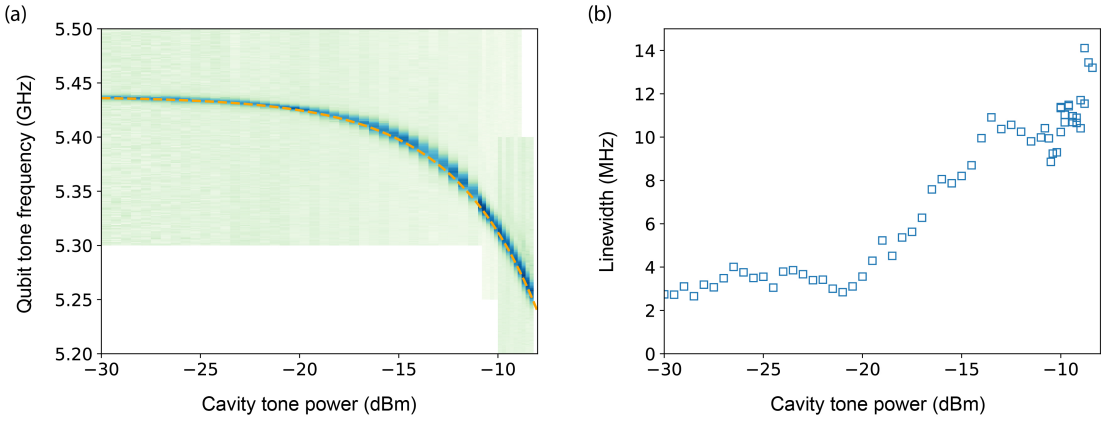

Figure 6.26: AC Stark shift in spectral domain. (a) As the cavity power increases, the qubit frequency is shifted by photons occupying the cavity. (b) The qubit linewidth broadens as the number of cavity photons increases, due to the measurement back action dephasing. At low cavity power, the linewidth is not well resolved due to the finite frequency step.

6.5.2 Time Domain Measurements

Rabi Oscillations

The qubit is not proven quantum until we can successfully perform a Rabi oscillation experiment on it, and the linear dependence of the Rabi frequency on the applied power validates the two-level system approximation. In fact, the birth of the field of superconducting circuits is sometimes considered to be the demonstration of coherent oscillation in the charge qubit in 1999 [16], almost two decades after macroscopic tunneling and discrete energy

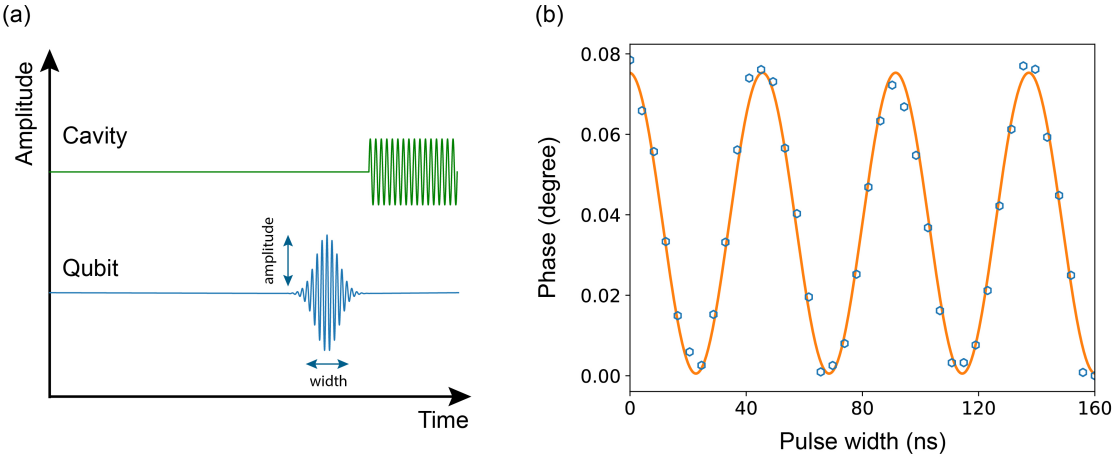

Figure 6.27: Rabi measurement. Rabi sequence (a) and data (b). The experiment was perform by varying the qubit pulse's width.

levels were observed in Josephson junction devices [13, 14].

To perform a Rabi experiment, we first apply a pulse with varying amplitude or duration at the qubit frequency, and then readout. Those two techniques are referred to as amplitude-Rabi and time-Rabi, respectively. The projection of the rotating state vector on the Bloch sphere along the Z-axis results in a sinusoidal signal, as shown in Fig. 6.27.

Rabi oscillations can be used to measure relevant noise in the rotating frame [67]. To determine the dephasing rate in the rotating frame, a time-Rabi must be used. More importantly, Rabi experiments let us determine the parameters for the microwave gates we need to perform further experiments such as T_1, Ramsey fringes, and T_2 echo, as well as to do quantum computation.

To get high resolution Rabi data, amplitude-Rabi is usually a better choise, since the AWG's analog channel has 14-bit amplitude resolution. Another advantage of amplitude-Rabi is at the software level. Measurement software's pulse generator driver generates the $\pi/2$ pulse by dividing the π pulse amplitude in half, so the amplitude-Rabi data can be used to check if this approach is valid.

Ramsey Fringes

After the parameters for qubit gates have been determined, we can perform Ramsey experiment. The sequence is shown in Fig.6.28(a). It involves two $\pi/2$ pulses applied at a frequency a little bit detuned from the qubit, and their separation in time is varied. The first pulse rotates the qubit state vector to the Bloch sphere's XY-plane, where it precesses around Z (in the rotating frame) at the detuning frequency during the delay time between the pulses. The second $\pi/2$ pulse projects the qubit to an axis whose direction depends on the angle around Z that the qubit has rotated. The qubit is measured along Z right after, resulting in a sinusoidal signal whose frequency is the difference between the applied RF tone and the qubit transition frequency. Moreover, decoherence would make us lose track of the qubit's rotation angle, and averaging an ensemble of measurement data would result in a decaying envelope for the oscillations.

Ramsey data gives us two important parameters. First, it reveals very precisely how large the detuning between the applied RF tone and the qubit transition is. This property of the Ramsey technique has made it the gold standard in finding atomic systems' frequencies. Second, it gives us the dephasing time of the qubit, often referred to as the free induction decay time. As argued in section 3.2, because the qubit transition frequency can fluctuate or simply drift over a long time scale during which we perform the measurement, the Ramsey decay time we achieve depends on the measurement time and long time scale fluctuation statistics. Thus, the coherence time T_2^* measured using Ramsey is not the actual time scale we are usually interested in. We confirmed this by varying the averaging time, and for longer measurement time, the resulting Ramsey decay becomes shorter. We note that when measured with a TWPA, the Ramsey time of qubit I was about two times smaller than the echo time, whereas it was three to five times smaller than the echo time in experiments that needed long averaging time to resolve the qubit states.

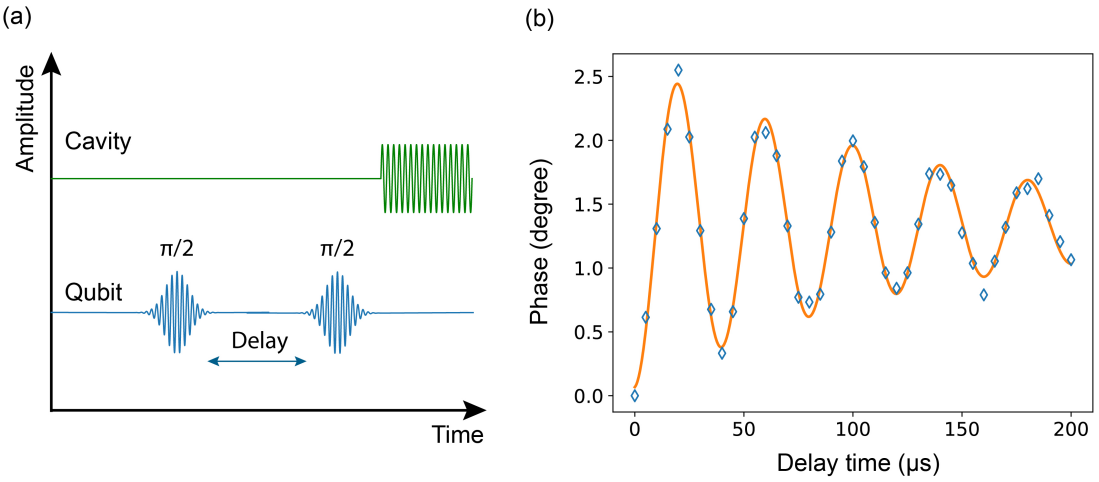

Figure 6.28: Ramsey measurement. (a) Ramsey sequence. (b) Ramsey fringe data showing a decaying sinusoidal. The oscillation frequency is equal to the difference between the applied RF tone and the qubit transition frequency, while the decay envelope gives us information about the free induction dephasing time $T_2^* \approx 140\ \mu s$.

Relaxation Time T_1

To measure the relaxation time, a π pulse is first applied at the qubit frequency to drive it to the excited state. This is followed by a varied delay time during which the qubit decays back to the ground state, or more precisely, to equilibrium. The state of the qubit is then measured by applying a readout pulse at the cavity frequency. The typical T_1 sequence and decay data are shown in Fig. 6.29.

Alternatively, a long saturation pulse can be used instead of a π-pulse to simply drive the qubit out of equilibrium to a mixed state. However, we notice that sometimes the Rabi oscillation does not decay to its median point. In addition, T_1 measured with the saturation pulse is usually longer than the T_1 measured with the π-pulse. We speculate that the longer T_1 may be due to the effective decay from other states being pumped by the long saturation pulse. Other possible reasons for the effect include quasiparticle dynamics around the small junctions and two-levels defects causing dielectric loss. Quasiparticle density can be changed, and two-level defects can be saturated by such long pulses. For

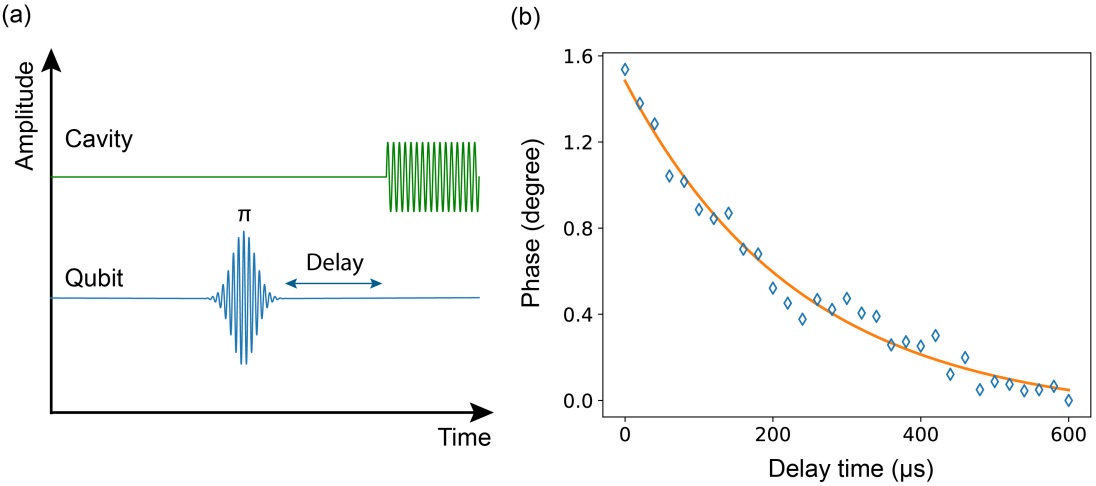

Figure 6.29: T_1 measurement. (a) T_1 sequence. (b) Data showing the relaxation rate of qubit excited state to equilibrium with $T_1 \approx 238\ \mu$s.

these reasons, we only consider T_1 data measured using π-pulse.

Dynamical Decoupling

As explained in section 3.2, we can partially cancel out dephasing from the low frequency noise affecting long measurement time by applying a π pulse between the $\pi/2$ pulses, effectively shifting the window function to a higher frequency. The pulse sequence and typical result for echo are shown in Fig. 6.30.

The echo technique can be visualized in an intuitive manner. After the applied $\pi/2$ pulse, the qubit is projected on the XY-plane, and its precession trajectory can be affected by the environment via certain noise channels. If after time $\tau/2$, we flip the qubit by π, and let the same noise channels reverse the qubit trajectory in another time period $\tau/2$, we can effectively cancel out the previous phase drift. The π pulse inserted in between is thus often called the *refocusing* pulse, and the name "echo" comes from the refocused output appearing after time τ [94].

This technique can be generalized to one involving an odd number of π pulses in between the $\pi/2$ pulses. The technique is called CP (Carr-Purcell) if the refocusing pulses flip

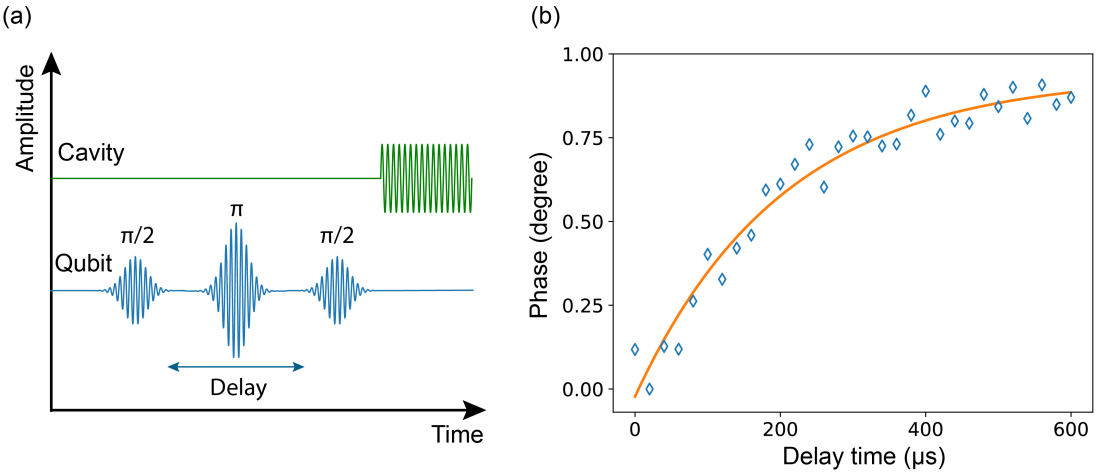

Figure 6.30: T_2^{echo} measurement. (a) T_2^{echo} sequence. The π-pulse is in the same quadrature as the $\pi/2$-pulses in our measurements. (b) Data showing the exponential decay used to extract decoherence time $T_2 \approx 205\ \mu$s.

the qubit around the same axis as the $\pi/2$ pulses do, and CPMG (Carr-Purcell-Meiboom-Gill) if the refocusing pulses flip the qubit around the perpendicular axis. It has been demonstrated that performing the CPMG technique effectively increases the qubit coherece time if the dominant dephasing mechanism is due to 1/f flux noise [81].

There are other techniques to probe the noise spectrum affecting coherence times, such as the strong Rabi driving technique [67], and the spin-locking technique [157]. Both of them give information about the noise spectrum at the rotating frequencies. Future experiments utilizing these techniques to study noise in fluxonium qubits would be helpful in obtaining further information about noise in multi-junction circuits.

6.5.3 Preliminary Trace of Quasiparticle

At the start of the coherence study described in section 6.3, we measured T_1 along the $0-1$ spectrum of device A in Table 6.1 across the first flux period, and at an applied magnetic field of around 2 gauss, corresponding to the 20th flux period. The data are shown in Fig. 6.31. T_1 away from the sweet spot is longer at a higher magnetic field. Theoretical

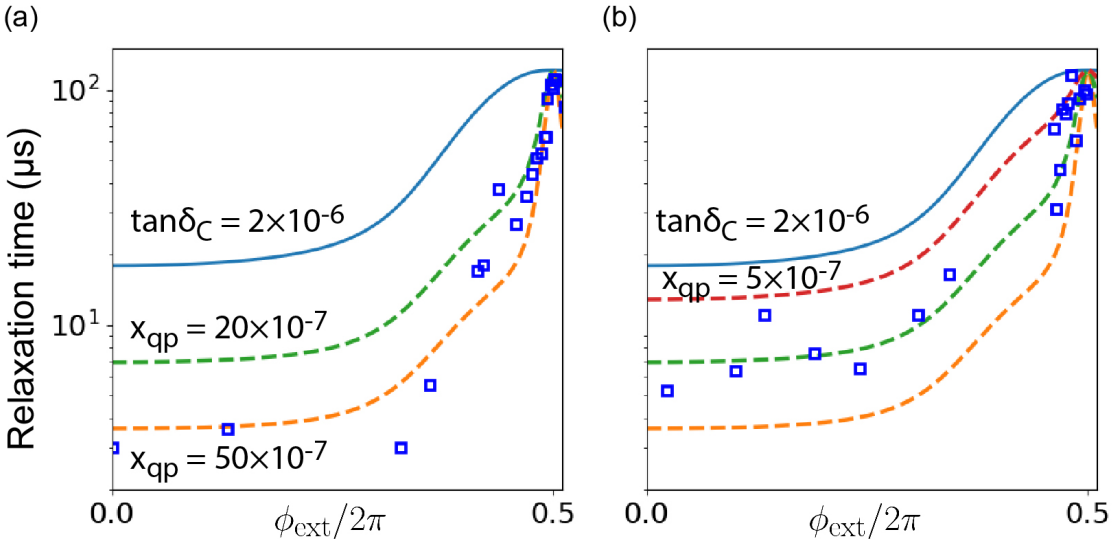

Figure 6.31: Possible effect from quasiparticles. T_1 relaxation data (blue square) measured along the $0 \rightarrow 1$ spectrum of device A at (a) zero magnetic field and (b) approximately 2 G. Solid line corresponds to theoretical dielectric loss limit, and dash lines correspond to addition of dissipation due to quasiparticles tunneling across the small junction (see text).

lines are plotted for comparison in these plots. They were computed as follows. First, a dielectric loss limit with corresponding loss tangent $\tan\delta_C = 2 \times 10^{-6}$ (see Eq. 4.3) was assumed (blue solid line). We then added to this limit the dissipation due to quasiparticle tunneling across the small junction (Eq. 4.10), using different normalized quasiparticle density $x_{\rm qp}$'s (dashed lines).

The filtering and shielding setup was minimal at the time of this measurement. In later experiments, we made several improvements in our cryogenic setup, and observed no noticeable enhancement in T_1 near integer flux when a magnetic field of the same amplitude ≈ 2 G was applied.

6.5.4 Quantum Tomography

Quantum State Tomography

We briefly outline the procedure to mathematically reconstruct a density matrix describing a two-level system and extend it to a two-qubit system in section 2.3. In practice, what we measure is the signal in units of voltage, and we have to post-process the data into expectation values of Pauli operators. We describe our experimental quantum state tomography procedures for single-qubit and two-qubit systems below.

The measurement of a two-level system in the ground state can be described by a measurement operator $M = |0\rangle\langle 0| = \frac{1}{2}(I + Z)$. We get $\langle M \rangle = 1$ for qubit in the ground state, and $\langle M \rangle = 0$ for qubit in the excited state. To convert the measured data in physical unit to expectation values, we use the β-coefficients and write $M = \beta_I I + \beta_Z Z$, where β_I and β_Z have units of voltage. The conversion between voltage and expectation values then involves precise calibration of these coefficients. Note that the factor $1/2$ has been absorbed into the β's coefficients, which is valid as long as our calibration and post-processing consistently take this into account.

If the measurement is ideal and strong enough to give us single-shot readout, the β-coefficients can be determined most directly from the IQ single-shot histogram data. However, in cases when the measurement is not strong enough, or not QND, we can calibrate these coefficients by measuring the signal after preparing the qubit in the ground and excited state to get $V_I = \beta_I + \beta_Z$ and $V_Z = \beta_I - \beta_Z$, respectively. This helps us bypass systematic state preparation and measurement errors, with the dominant errors in the reconstructed states originating from imperfect gates. This approach has been employed to benchmark gates in superconducting qubits [112, 111].

After calibrating the β-coefficients, we can perform qubit rotations before reading out the cavity to determine the corresponding expectation values, as outlined in Table 6.5. Since the density matrix has 4 entries and must satisfy 1 constraint $\mathrm{Tr}(\rho) = 1$, we need at least

Table 6.5: Gate sequence for single-qubit state tomography.

Measurement #	Rotation	Outcome
1	I	$\beta_I + \beta_Z\langle Z\rangle$
2	$X/2$	$\beta_I + \beta_Z\langle Y\rangle$
3	$-Y/2$	$\beta_I + \beta_Z\langle X\rangle$

3 different measurements. Instead of the unit trace constraint, we use $\langle I\rangle = 1$. Following Eq. 2.64, the density matrix can then be reconstructed from the expectation values $\langle X\rangle$, $\langle Y\rangle$, and $\langle Z\rangle$.

Two-qubit quantum state tomography follows the same procedure. To calibrate the β-coefficients in $M = \beta_{II}II + \beta_{ZI}ZI + \beta_{IZ}IZ + \beta_{ZZ}ZZ$, we measure the cavity signals $V_{II} = \beta_{II} + \beta_{ZI} + \beta_{IZ} + \beta_{ZZ}$, $V_{ZI} = \beta_{II} - \beta_{ZI} + \beta_{IZ} - \beta_{ZZ}$, $V_{IZ} = \beta_{II} + \beta_{ZI} - \beta_{IZ} - \beta_{ZZ}$, and $V_{ZZ} = \beta_{II} - \beta_{ZI} - \beta_{IZ} + \beta_{ZZ}$, where V_{IZ}, for example, is the measured signal after flipping the second qubit to excited state while keeping the first qubit in the ground state.

Once the β-coefficients calibration has been completed, we can extract the expectation values for all the relevant Pauli operators. With the density matrix describing a two-qubit system having 16 entries and satisfying 1 constraint, we need at least 15 measurements in two-qubit state tomography. By performing 15 different combinations of rotations on the qubits and using the constraint $\langle II\rangle = 1$, we can extract the necessary expectation values via linear algebra. The measurement outcomes, as shown in Table 6.6, are organized into matrix form, and a simple matrix inversion can be used to compute the expectation values.

For two-qubit state tomography, we found that the reconstructed matrix is often not physical, since our linear reconstruction neglect the Hermiticity and positivity properties of a density matrix. To account for these constraints, we use MLE technique [158, 159]. It works as follows. First, we note that the density matrix can be decomposed into Cholesky

Table 6.6: Gate sequence for two-qubit state tomography.

Measurement #	Rotation on A	Rotation on B	Outcome
1	I	I	$\beta_{II}+\beta_{ZI}\langle ZI\rangle+\beta_{IZ}\langle IZ\rangle+\beta_{ZZ}\langle ZZ\rangle$
2	X	I	$\beta_{II}-\beta_{ZI}\langle ZI\rangle+\beta_{IZ}\langle IZ\rangle-\beta_{ZZ}\langle ZZ\rangle$
3	I	X	$\beta_{II}+\beta_{ZI}\langle ZI\rangle-\beta_{IZ}\langle IZ\rangle-\beta_{ZZ}\langle ZZ\rangle$
4	$X/2$	I	$\beta_{II}+\beta_{ZI}\langle YI\rangle+\beta_{IZ}\langle IZ\rangle+\beta_{ZZ}\langle YZ\rangle$
5	$X/2$	$X/2$	$\beta_{II}+\beta_{ZI}\langle YI\rangle+\beta_{IZ}\langle IY\rangle+\beta_{ZZ}\langle YY\rangle$
6	$X/2$	$Y/2$	$\beta_{II}+\beta_{ZI}\langle YI\rangle-\beta_{IZ}\langle IX\rangle-\beta_{ZZ}\langle YX\rangle$
7	$X/2$	X	$\beta_{II}+\beta_{ZI}\langle YI\rangle-\beta_{IZ}\langle IZ\rangle-\beta_{ZZ}\langle YZ\rangle$
8	$Y/2$	I	$\beta_{II}-\beta_{ZI}\langle XI\rangle+\beta_{IZ}\langle IZ\rangle-\beta_{ZZ}\langle XZ\rangle$
9	$Y/2$	$X/2$	$\beta_{II}-\beta_{ZI}\langle XI\rangle+\beta_{IZ}\langle IY\rangle-\beta_{ZZ}\langle XY\rangle$
10	$Y/2$	$Y/2$	$\beta_{II}-\beta_{ZI}\langle XI\rangle-\beta_{IZ}\langle IX\rangle+\beta_{ZZ}\langle XX\rangle$
11	$Y/2$	X	$\beta_{II}-\beta_{ZI}\langle XI\rangle-\beta_{IZ}\langle IZ\rangle+\beta_{ZZ}\langle XZ\rangle$
12	I	$X/2$	$\beta_{II}+\beta_{ZI}\langle ZI\rangle+\beta_{IZ}\langle IY\rangle+\beta_{ZZ}\langle ZY\rangle$
13	X	$X/2$	$\beta_{II}-\beta_{ZI}\langle ZI\rangle+\beta_{IZ}\langle IY\rangle-\beta_{ZZ}\langle ZY\rangle$
14	I	$Y/2$	$\beta_{II}+\beta_{ZI}\langle ZI\rangle-\beta_{IZ}\langle IX\rangle-\beta_{ZZ}\langle ZX\rangle$
15	X	$Y/2$	$\beta_{II}-\beta_{ZI}\langle ZI\rangle-\beta_{IZ}\langle IX\rangle+\beta_{ZZ}\langle ZX\rangle$

form

$$\rho=\frac{T^\dagger T}{\mathrm{Tr}(T^\dagger T)}, \tag{6.6}$$

where the upper triangular matrix T for a two-qubit system is

$$T=\begin{pmatrix} t_1 & t_5+it_6 & t_{11}+it_{12} & t_{15}+it_{16}\\ 0 & t_2 & t_7+it_8 & t_{13}+it_{14}\\ 0 & 0 & t_3 & t_9+it_{10}\\ 0 & 0 & 0 & t_4 \end{pmatrix}. \tag{6.7}$$

The matrix entries $\{t_i\}$ can be found from minimization of the likelihood function

$$\mathcal{L} = \sum_{i=1}^{15} (m_i - \mathrm{Tr}(M_i \rho))^2, \tag{6.8}$$

where m_i and M_i are respectively the measured signal and measurement operator corresponding to measurement i. By keeping track of the list of rotations, and thus the measurement operators, we can post-process the m_i data to reconstruct the density matrix. Unlike the linear reconstruction approach, we may want to use an over-complete set of measurements to estimate the density matrix more precisely using MLE. For example, a set of 30 or 36 measurements can be extended from the one shown in Table 6.6 by using negative-angle rotations such as $-X/2$ and $-Y/2$.

Quantum Process Tomography

With quantum state tomography procedure described, we now move on to discuss quantum process tomography, the procedure to identify the quantum operation map $\mathcal{E}$ [68, 160]. The technical outline is described at the end of section 2.3. Below we discuss the experimental procedure to find the χ matrix.

First, we prepare a set of pulse sequences, each one comprises (i) a pre-pulse preparing the initial state ρ_i, (ii) the intended gate(s) we use to realize the intended quantum operation, and finally (iii) a post-pulse used for state tomography. For single-qubit process tomography, we use the pre-pulse set $\{I,\ X,\ Y/2,\ -X/2\}$, and the post-pulse set shown in Table 6.5, resulting in 12 different measurements. For two-qubit process tomography, we use the pre-pulse set $\{I\otimes I,\ I\otimes X,\ I\otimes Y/2,\ I\otimes -X/2,\ X\otimes I,\ X\otimes X,\ X\otimes Y/2,\ X\otimes -X/2,\ Y/2\otimes I,\ Y/2\otimes X,\ Y/2\otimes Y/2,\ Y/2\otimes -X/2,\ -X/2\otimes I, -X/2\otimes X,\ -X/2\otimes Y/2,\ -X/2\otimes -X/2\}$, and the post-pulse set shown in Table 6.6, resulting in 240 different measurements.

Then, quantum states tomography is used to reconstruct the 16 output density matrices $\{\rho_j\}$, preferably by using maximum-likelihood estimation. By keeping track of the pulse

sequence order, and thus the initial states, we can reconstruct the χ matrix based on the $\{I,\ X,\ Y,\ Z\}^{\otimes 2}$ operator basis using Eq. 2.84. Note that this linear conversion produces χ as a vector, and we must reshape it into a $d^2 \times d^2$ matrix. Alternative to χ, the Pauli transfer matrix $\mathcal{R}$, which maps an input Pauli state vector to an output Pauli state vector, can be used to characterize a quantum process as well [130]. We may obtain both maps and check for consistency, for example, by comparing the fidelities extracted from the two different methods.

6.5.5 Randomized Benchmarking

Although quantum process tomography is the standard technique for characterizing a quantum operation, it is subjected to two drawbacks. First, the procedure is increasingly tedious for large systems comprising of multiple qubits. The number of measurements scales as $d^4 - d^2$ where $d = 2^n$ is the dimension of the Hilbert space, and n is the number of qubits. As outlined above, while process tomography involves only 12 measurements for a single qubit, that number goes up to 240 for two qubits, and would be 4032 for three qubits. Second, the result is sensitive to SPAM errors. For instance, our current single-qubit gates are not much better than the entangling gate, so the extracted fidelity is prominently due to single-qubit gate errors.

One method for characterizing qubit gates that overcomes these shortcomings is randomized benchmarking (RB) [161, 154]. This technique involves the generation of random sequence of gates, with the last gate computed to make the total sequence equivalent to an identity operation. Averaging over different randomized sequence results give us a decay that scales with the average fidelity of our gates, which we can fit to a simple model. The process is independent of SPAM errors.

We describe the RB and interleaved RB protocols below, following ref. [154]. They are restricted to gates within the Clifford group, denoted as $\mathrm{Clif_n}$ for n qubits. For a single

qubit, the Clif_1 group consists of 24 elements, each Clifford gate has an average length of 1.875 pulses. For two qubits, the Clif_2 group consists of 11520 elements, with each Clifford gate containing on average 1.5 CZ gates and 8.25 single-qubit gates [35, 162]. The gate sequences are shown in Fig. 6.19(a). An interleaved RB sequence includes an additional gate $\mathcal{C}$ of interest after each random gate $\mathcal{C}_i$, in a sequence of m gates. The regular RB decay is fitted to either the zeroth or first order model in Eq. 6.1 to extract the depolarizing parameter p. The average error rate over all Clifford gates is given by

$$r = (d-1)(1-p)/d, \tag{6.9}$$

where $d = 2^n$ is the dimension of the system.

In interleaved RB, the decay is fitted to extract the depolarizing parameters $p_{\mathcal{C}}$. Because of addition of the interleaved gate, the fidelity curve decays faster, corresponding to $p_{\mathcal{C}} < p$. The average error of this interleaved gate is estimated by

$$r_{\mathcal{C}} = \frac{(d-1)(1-p_{\mathcal{C}}/p)}{d}, \tag{6.10}$$

and must be within the range $[r_{\mathcal{C}} - E, r_{\mathcal{C}} + E]$, where $E = \min\{(d-1)(|p - p_{\mathcal{C}}/p| + (1-p))/d,\ 2(d^2-1)(1-p)/pd^2 + 4\sqrt{1-p}\sqrt{d^2-1}/p\}$.

In experiments where the change in qubit populations can be described by the projection of the demodulated signal onto its I or Q quadrature (or magnitude/phase), the change in the signal can be used to fit the decay. When a joint readout is used for two-qubit devices, cross-correlation between the measurements of qubit A and qubit B may make the projected signal to scale non-linearly with the populations. In this case, single-shot histogram readout data should be used to extract the populations $\{P_i\}$ of all the states after each randomized sequence m. The change in the populations can then be used to fit the RB data. For single-qubit RB in a two-qubit device, we fit the data set $P_{|00\rangle}(m) + P_{|01\rangle}(m)$ for qubit A, and

$P_{|00\rangle}(m) + P_{|10\rangle}(m)$ for qubit B, where $|\mathrm{AB}\rangle$ denotes the qubit state. For two-qubit RB, we fit the data set $P_{|00\rangle}(m)$.

Chapter 7

Summary and Outlook

I dream of painting and then I paint my dream.

Vincent van Gogh

7.1 Summary of Results

7.1.1 Selection Rules Engineering

Our experiment described in section 6.2 demonstrated for the first time that the energy decay time in a macroscopic artificial atom can be extended into the millisecond range by a controlled suppression of the overlap of the qubit state wave functions. We measured the energy decay time T_1 of a qubit and observed a textbook enhancement of T_1 as a function of dipole moment. The energy decay quality factor Q_1 reached the value of 4×10^7, corresponding to $T_1 = 2$ ms for qubit frequency of 3.3 GHz, without sign of saturation. We have also shown evidence of the metastable fluxonium dynamics. The result was confirmed in an independent experiment by Earnest et al. [163].

7.1.2 High Coherence Fluxonium

In the experiments reported in section 6.3, we presented a specific design of fluxonium qubits which repeatedly yielded high coherence times T_2 at the half-integer flux bias, with the best device satisfying $T_2 > 400$ μs. To our knowledge, this is the longest coherence time found in a superconducting qubit today. Compared to a typical flux qubit, the effect of $1/f$ flux noise is practically eliminated by the large loop inductance ($L \sim 10^2$ nH) of the Josephson chain. The qubit transition frequency can still be flux-tuned by many octaves while keeping coherence time above a few *microseconds*, limited by first-order coupling to flux noise. Our fluxoniums are compatible with transmon-based scaling architectures, which require connecting an external coupling capacitance (antenna) to the small junction. This connection comes at the price of energy relaxation induced by the surface loss in the antenna. The surface loss problem was largely (but not completely) bypassed by reducing the qubit frequency to around $\omega_{01}/2\pi \approx 500$ MHz. Because the spectral density of noise associated with surface loss drops rapidly with frequency, the relaxation time of our qubits exceeded that of the best capacitively-shunted junction circuits despite a sub-optimal Al on Si fabrication procedure.

Several design features possibly contributed to the dramatic improvement of coherence compared to previous fluxonium experiments. The original design was severely limited by the surface loss ($T_2 \sim T_1 \leq 10$ μs) in the finger capacitors attached to the small junction [59, 114]. In a subsequent series of experiments this capacitance was removed and the readout was done through the inductive coupling to a low quality factor chain mode dressed by an external capacitance [85, 87, 149, 164]. This expectedly eliminated the surface loss and dramatically improved T_1 but not T_2. In the present work we went back to the original design [59, 114], including the Dolan bridge fabrication and (i) used a better geometry of the antenna to minimize the surface participation ratio the way it is done in modern transmons [30] and (ii) used the fundamental mode of a simple copper box for readout [102].

Finally, the geometry of our Josephson chain might be favorable for trapping quasiparticles in the background magnetic field.

Importantly, the approximately tenfold reduction of the qubit frequency compared to the traditional 5 GHz value does not prevent fast gate operations or strong interactions. This is because the spectrum of a typical fluxonium has a rich structure of excited states reminiscent of the fine structure in the spectrum of conventional atoms. Transitions outside the computational subspace belong to a traditional frequency and transition dipole range, which can be utilized for creating fast flux- or microwave- activated quantum gates. Moreover, the inductive connection of fluxoniums via shared junctions can make the exchange coupling comparable to the qubit frequency without leaving the computational subspace. These large exchange couplings combined with the exceptional coherence times can be especially useful for constructing coherent quantum annealers. The next steps towards quantum computing with fluxoniums consist of demonstrating high coherence in combination with fast single-shot readout, fast flux tuning, and fast two-qubit gates, which we are currently working on.

Following the common viewpoint of minimizing the number of junctions per qubit, one may be tempted to replace the discrete chain by a patterned film of a highly-disordered superconductor with a comparable kinetic inductance. It is important to realize that the effective loss tangent of the inductance must be in the $10^{-7} - 10^{-8}$ range in order to reach the coherence times reported in this experiment. Whether such a low loss can be reached with dirty superconductors is an interesting question [165, 166, 167, 168]. Our specific Josephson tunnel junction chain design was primarily motivated by the maximal simplicity of the qubit fabrication procedure: it is single step and does not require high-contrast lithography. The high coherence was made possible, in part, by the remarkably good thermalization of both quasiparticles and collective modes in the chains. Understanding this effect in future experiments may have high impact on quantum circuit design. In the meantime, our experiment demonstrated for the first time that coherence time of superconducting qubits can be

extended beyond the state-of-the art by increasing circuit complexity.

7.1.3 Microwave-Activated Two-Qubit Gate

We reported current progress on the microwave-activated entangling gate in section 6.4, showing that two high coherence fluxonium qubits can be entangled with high fidelity. In one single device, we successfully demonstrated single-shot readout capability, initialization by preselection, precise single-qubit controls at very low frequencies, and high fidelity two-qubit gate. The computational states are at around 100 MHz and have high coherence, yet the multi-qubit interaction is quite fast, especially compared to the decoherence time and spurious ZZ coupling.

Our preliminary results show that fluxonium is a promising qubit in the quest to build quantum computers. The experimental procedures described can be readily applied to study other microwave-activated gate such as the cross-resonance gate [169, 130] or the bSWAP gate [170] using fluxonium qubits. Improving the gate past fault-tolerance threshold is currently being explored. This includes utilizing composite pulses [107, 108] and numerical "last-mile" optimization [156]. The next step in scaling up fluxonium devices would involve the development of 2D architecture along with local microwave control and readout integration, similar to the progress already made on transmon qubits (see refs. [35, 26], for example).

7.2 Quantum Computing with Fluxoniums

Here we outline how fluxoniums can be integrated into existing schemes of scalable quantum computing. This outlook discussion is largely based on already published theoretical and experimental work on interacting fluxoniums.

7.2.1 Capacitive Coupling

Viewing fluxoniums as inductively-shunted charge qubits, one can understand the effect of connecting two such devices by a mutual capacitance C_C using the charge qubit expressions. Assuming that $C_C \ll C$, the effective interaction term is given by $H_{\text{int}} = J_C n_1 n_2$, where $J_C = 2E_C \times (C_C/C)$ and $n_{1,2}$ are the charge operators of the two devices. Given that in our design $E_C \sim 1$ GHz, and choosing a moderate ratio $C_C/C = 10$ one can readily get an exchange constant $J_C \sim 200$ MHz, which is similar to what is possible with capacitive coupling of transmons. Note that the repulsion of qubit frequencies by the term H_{int} is significantly reduced by the small value of the charge matrix elements $\langle 0|n_{1,2}|1\rangle$. Fortunately, this is not the case for transitions outside the computational subspace, where matrix elements are large and one can use them to perform, e.g. microwave-activated two-qubit gates [128].

7.2.2 Inductive Coupling

In contrast with capacitive coupling, a proper inductive coupling of fluxoniums allows for extremely strong interactions already within the computational subspace. Viewing fluxoniums as superconducting loops with a weak link, two such devices can be inductively coupled by sharing one or several junctions between the two loops. Assuming that the fraction of the shared junctions is $m \ll 1$, the interaction term is given by $H_{\text{int}} = J_L(\phi_1/\pi)(\phi_2/\pi)$, where $J_L = m\pi^2 E_L$ and $\phi_{1,2}$ are the phase operators of the two devices. Normalization of the phase operators by π is convenient because $\langle 0|\phi_{1,2}|1\rangle \approx \pi$ at the sweet spot. Therefore, even for a modest $m = 0.1$ (about 10-20 shared junctions), we get the frequency repulsion of qubit transitions on the order of $J_L \approx 0.5$ GHz, i.e. it is comparable to transition frequencies. In fact, by making $m \sim 1$, a molecular-type binding of two fluxoniums has already been experimentally demonstrated [149].

7.2.3 Dispersive Qubit-Cavity Interaction

Circuit quantum electrodynamics with fluxonium qubits was described in Ref 31. The most useful strong dispersive regime of cQED corresponds to $\chi \gg \kappa$. Introducing the dimensionless photon creation (annihilation) operator $a^\dagger(a)$, the coupling term is $H_{\text{int}} = g_C ni(a - a^\dagger)$ for capacitive coupling and $H_{\text{int}} = g_L \phi(a + a^\dagger)$ for inductive coupling. Given the discussion of inductive and capacitive coupling above, it is straightforward to achieve the values $g_C/2\pi, g_L/2\pi \approx 100$ MHz, typical of conventional qubits [164, 60]. However, here the qubit frequency (typically 500 MHz) is far detuned from the photon frequency (typically above 5 GHz). Nevertheless, the shifts χ can be large due to the virtual transitions connecting states $|0\rangle$ and $|1\rangle$ to the non-computational states [127]. In fact, it was shown experimentally [60] that dispersive shift is non-zero even for a vanishing qubit transition dipole, i.e. $\langle 0|\phi, n|1\rangle \to 0$.

7.2.4 Flux-Controlled Gates

Since fluxonium's spectrum can be tuned by flux it is tempting to consider flux-controlled gate operations. Perhaps the simplest such gate is the analog of a C-phase gate for transmons [71], relying on the repulsion of the two-qubit states $|11\rangle$ and $|20\rangle$ or $|02\rangle$. The states repulsion can be generated by a direct capacitive or inductive connection of fluxoniums. In fact, one may expect an enhancement of gate fidelity because fluxoniums maintain a relatively high coherence time $T_2 \approx 5\ \mu$s while biased outside the sweet spot during the gate operation.

7.2.5 Fixed-Frequency Gates

In section 4.4, we describe a fast CZ gate between two capacitively fluxoniums obtained by applying a 2π-pulse at a frequency near the $|1\rangle - |2\rangle$ of the target qubit [128]. In general, the quantum state leakage during such gate operations was shown to be remarkably low

owing to the large anharmonicity of the non-computational part of the spectrum. Although microwave-activated gates still require static flux-biasing of qubits at their sweet spots, their advantage is that they are compatible with the 3D circuit QED architecture used in this thesis.

The experimental results shown in section (6.4) are promising, and further steps should be taken to minimize spurious interactions and optimize the gate fidelity. For example, the unwanted ZZ coupling is particularly large in a few devices, which is linked to the interactions between higher levels.

Other microwave-activated gates, such as the cross-resonance gate [169] and bSWAP gate [170] can also be used to entangle two fluxoniums by directly driving transitions residing within the computational subspace. The advantage of these gates compared to the CZ gate comes from the long coherence of the $|0\rangle$ and $|1\rangle$ computational states. Preliminary simulation results are promising for both, and future theoretical description of these gates in fluxonium-based systems will be available soon.

7.2.6 Quantum Adiabatic Optimization

A network of interconnected fluxoniums, after the projection to the computational subspace, can implement a generic quantum spin-$1/2$ Hamiltonian:

$$H = \sum_{i,j} h_i^Z \sigma_{Z_i} + h_i^X \sigma_{X_i} - J_{i,j}^{XX} \sigma_{X_i} \sigma_{X_j}. \tag{7.1}$$

Here the field h^Z is the qubit transition frequency at the sweet spot, field h^X is the detuning from the sweet spot, and J^{XX} is the nearest neighbor coupling constant. The field h^Z can also be tuned independently from h^X by replacing a single weak junction by a split junction, as it was done in device C. Such a Hamiltonian is typically implemented using a system of semi-classical SQUID circuits to explore quantum annealing algorithms [171].

Our devices can provide a previously unavailable realization of this model. (i) Owing

to the extremely large anharmonicity, $\omega_{12}/\omega_{01} \gg 1$, a network of fluxoniums remains in its computational subspace even in the presence of multiple spin-flips, i.e. projecting to the computational subspace remains valid. (ii) Even far away from the sweet spot, we get $T_2 \sim 5\ \mu$s, which translates into the level broadening of about 30 kHz. This number in principle allows resolving the many-body level spacing in a system of 10 locally coupled spins. (iii) Inductive connection allows a local coupling to multiple neighbors with the condition $J^{XX} \sim h^Z$. These three conditions are simultaneously required for exploring the most intriguing scenarios of quantum many-body physics of spin systems. Fluxoniums are therefore well positioned for constructing the next generation of quantum annealers operating in a highly-coherent regime where quantum speed up is expected from theory [37].

7.2.7 Optimal Qubit Frequency

It is interesting to discuss the choice of the optimal qubit frequency as the design, in principle, allows to reduce it to an arbitrary low value. We believe that the presented qubit frequency range around 500 MHz is currently the optimal for a number of reasons.

The first concern is the finite temperature of the qubit. Already at 500 MHz, which translates to a temperature of 25 mK, a significant population of state $|1\rangle$ is expected. In principle, this is not a problem for a quantum processor as long as the energy relaxation time T_1 is sufficiently long. The qubits anyway need to be initialized with a high-fidelity. However, it is convenient to be able to characterize low-frequency devices without the need to do so, hence keeping the qubit frequency not far below the temperature is advantageous. More importantly, for $\hbar\omega \ll k_B T$, the relaxation time T_1 must be rescaled compared to its zero-temperature value due to the stimulated emission factor $T_1 \approx T_1(T=0) \times (k_B T/\hbar\omega)$ (see Eq. 4.9 and Fig. 4.11).

From a technical viewpoint, the chosen frequency range appears particularly convenient for scaling: there is room to frequency-resolve neighboring qubits by spreading them by a

few hundred MHz; Rabi-driving with a frequency up to 50 MHz can be applied even within the 3D circuit QED architectures, which can provide 10 ns-long single-qubit pulses; cross-talks are in general expected to be reduced at lower frequencies. Last but not least, qubit pulses can be done using cheaper digital electronics which can significantly reduce scaling costs.

Appendices

Appendix A

Noise and Energy Relaxation

Winter is coming.

George R.R. Martin

In this appendix, we connect noise described by the noise spectral density to energy relaxation via Fermi's golden rule.

A.1 Noise Correlation and Spectral Density

First, we explore how to characterize noise in quantum systems, following ref. [83]. Consider a classical voltage noise signal $v(t)$ that fluctuates randomly in time and have zero mean value, $\langle v(t) \rangle = 0$. The frequency spectrum of this noise is defined via the Fourier transform

$$V(\omega) = \int_{-\infty}^{\infty} v(t) e^{i\omega t} dt. \tag{A.1}$$

The cycle averaged intensity of the noise at frequency ω is proportional to

$$\langle |V(\omega)|^2 \rangle = \int_{-\infty}^{\infty} dt \int_{-\infty}^{\infty} dt' \langle v(t) v(t') \rangle e^{i\omega(t-t')}. \tag{A.2}$$

In a real experiment, the data is taken over a period of time T, so the relations above should be redefined via a 'windowed' Fourier transform :

$$V(\omega) = \frac{1}{\sqrt{T}} \int_0^T v(t) e^{i\omega t} dt, \tag{A.3}$$

$$\langle |V(\omega)|^2 \rangle = \frac{1}{T} \int_0^T dt \int_0^T dt' \langle v(t)v(t') \rangle e^{i\omega(t-t')}. \tag{A.4}$$

Note that the unit of the noise in frequency domain is $\mathrm{volts}/\sqrt{\mathrm{Hz}}$. This allows us to normalize $V(\omega)$ to be independent of the sampling time T. The spectral density of the noise $v(t)$ is defined to be

$$S_V(\omega) \equiv \lim_{T\to\infty} \langle |V(\omega)|^2 \rangle. \tag{A.5}$$

In the time domain, the noise $v(t)$ can be characterized by its correlation function

$$G_v(\tau) = \langle v(t)v(t-\tau) \rangle = \frac{1}{T} \int_0^T v(t)v(t-\tau) dt, \tag{A.6}$$

which tells us how the voltage fluctuations are correlated within the time scale $\tau = t - t'$. The correlation function can be assumed to decay to zero in a finite characteristic correlation time τ_c.

We now work to establish the relation between $S_V(\omega)$ and $G_v(\tau)$. We first rewrite Eq. A.4,

$$\begin{aligned} \langle |V(\omega)|^2 \rangle &= \frac{1}{T} \int_0^T dt \int_0^T dt' \langle v(t)v(t') \rangle e^{i\omega(t-t')} \\ &= \frac{1}{T} \int_0^T dt \int_{-T}^T d\tau \langle v(t)v(t-\tau) \rangle e^{i\omega\tau}. \end{aligned} \tag{A.7}$$

In the limit $T \gg \tau_c$, we can approximate

$$\begin{aligned} S_V(\omega) &= \frac{1}{T}\int_0^T dt \int_{-\infty}^{\infty} d\tau \langle v(t)v(t-\tau)\rangle e^{i\omega\tau} \\ &= \int_{-\infty}^{\infty} d\tau G_v(\tau) e^{i\omega\tau}, \end{aligned} \tag{A.8}$$

which tells us that the spectral density is simply the Fourier transform of the correlation function. This gives the intensity of the noise at certain frequencies. The inverse transform subsequently gives

$$G_V(\tau) = \frac{1}{2\pi}\int_{-\infty}^{\infty} d\omega S_V(\omega) e^{-i\omega\tau}. \tag{A.9}$$

We note that noise with short correlation time is broadband in frequency. For example, the white noise correlation function is

$$G_V(t) = \alpha\delta(t), \tag{A.10}$$

which corresponds to a flat spectrum

$$S_V(\omega) = \alpha. \tag{A.11}$$

Noise having correlation time $\tau_c \ll T$ corresponds to *Markovian* processes, where the disturbance from the noise is random, uncorrelated, and independent of each other. Noise not satisfying this condition is classified as *non-Markovian*.

Fluctuation-Dissipation Theorem

At first, the Hamiltonian formalism seems to be powerless in treating dissipation which is an irreversible process. Our approach in modeling dissipation quantum-mechanically is to consider an infinite collection of harmonic oscillators which consists of inductors and capacitors with purely imaginary admittances. The real part of the total admittance accounts

for noise that dissipates the qubit's energy [70].

For instance, a resistor can be modeled as a semi-infinite transmission line. The impedance seen by the qubit is precisely the characteristic impedance of the line $Z_o = \sqrt{l/c}$. In electrical engineering language, the energy absorbed by this line travels in one direction away from the qubit and is never reflected back. We can then write the associated Lagrangian and define the noise spectral density for such dissipative element.

First consider a single lossless LC resonant mode with Hamiltonian

$$H = \frac{Q^2}{2C} + \frac{\Phi^2}{2L}.$$

Introducing the creation and annihilation operators as usual with commutation relation $[a, a^\dagger] = 1$, we have

$$\begin{aligned} \Phi &= \sqrt{\frac{\hbar Z_o}{2}}(a^\dagger + a), \\ Q &= i\sqrt{\frac{\hbar}{2Z_o}}(a^\dagger - a), \\ H &= \frac{\hbar\omega_o}{2}(a^\dagger a + \frac{1}{2}), \end{aligned} \tag{A.12}$$

and the charge at time t is

$$Q(t) = e^{iHt/\hbar}Q(0)e^{-iHt/\hbar}. \tag{A.13}$$

The current correlation function for a mode at frequency $\omega_o = (LC)^{-1/2}$ is

$$\langle i(t)i(0)\rangle = -\frac{d^2}{dt^2}\langle Q(t)Q(0)\rangle = \frac{\hbar\omega_o}{2L}(\langle a^\dagger a\rangle e^{i\omega_o t} + \langle aa^\dagger\rangle e^{-i\omega_o t}). \tag{A.14}$$

At thermal equilibrium, the distribution of photons follows Bose-Einstein statistics,

$$\begin{aligned}\langle a^\dagger a\rangle &= \frac{1}{e^{\hbar\omega_o/k_BT}-1} = \frac{1}{2}\left[\coth\left(\frac{\hbar\omega_o}{2k_BT}\right)-1\right],\\ \langle aa^\dagger\rangle &= \langle a^\dagger a\rangle + 1 = \frac{1}{2}\left[\coth\left(\frac{\hbar\omega_o}{2k_BT}\right)+1\right],\end{aligned} \tag{A.15}$$

from which we get

$$\langle i(t)i(0)\rangle = \frac{\hbar\omega_o}{2L}\left[\coth\left(\frac{\hbar\omega_o}{2k_BT}\right)\cos(\omega_o t) - i\sin(\omega_o t)\right]. \tag{A.16}$$

Next, consider a frequency-dependent admittance $Y(\omega)$ with Fourier transform

$$Y(\omega) = \int_\infty^\infty y(t)e^{i\omega t}dt, \tag{A.17}$$

which can be extended to the complex plane as

$$Y(\omega+i\eta) = \int_\infty^\infty y(t)e^{i(\omega+i\eta)t}dt. \tag{A.18}$$

We can then define the generalized admittance function

$$Y(\omega) = \lim_{\eta\to 0} Y(\omega+i\eta). \tag{A.19}$$

The asymptotic expression for the nth oscillator's admittance is

$$Y_n(\omega) = y_n\left\{\frac{\pi}{2}\omega_n\left[\delta(\omega-\omega_n)+\delta(\omega+\omega_n)\right] + \frac{i}{2}\left[\mathrm{p.p}\left(\frac{\omega_n}{\omega-\omega_n}\right)+\mathrm{p.p}\left(\frac{\omega_n}{\omega+\omega_n}\right)\right]\right\}, \tag{A.20}$$

where $y_n = \sqrt{C_n/L_n}$ and $\omega_n = 1/\sqrt{L_nC_n}$. The generalized admittance has both real and imaginary parts, and the smooth $\mathrm{ReY}(\omega)$ function is replaced by an infinitely dense comb of δ functions. Using the Caldeira-Leggett representation, we can add up all the modes to obtain the correlation of the noise. Note that the model does not specify the internal

working of a dissipative element.

We can then rewrite Eq. A.16 for a collection of harmonic oscillators as

$$\langle i(t)i(0)\rangle = \frac{\hbar}{2\pi}\int_{-\infty}^{\infty}\omega d\omega\left[\coth\left(\frac{\hbar\omega_o}{2k_BT}\right)+1\right]\mathrm{ReY}(\omega)e^{-i\omega t}. \tag{A.21}$$

And with the definition of the spectral density $S_I(\omega)=\int_{-\infty}^{\infty}dt\langle i(t)i(0)\rangle e^{i\omega t}$, we get

$$S_I(\omega)=\hbar\omega\mathrm{ReY}(\omega)\left[\coth\left(\frac{\hbar\omega}{2k_BT}\right)+1\right]. \tag{A.22}$$

On the other hand, we can also define the voltage noise spectral density as

$$S_V(\omega)=\hbar\omega\mathrm{ReZ}(\omega)\left[\coth\left(\frac{\hbar\omega}{2k_BT}\right)+1\right]. \tag{A.23}$$

For example, the spectral density of voltage fluctuations from a resistor R following the equation above is

$$S_V(\omega)=\frac{2R\hbar\omega}{1-e^{-\hbar\omega/k_BT}}. \tag{A.24}$$

In the limit $k_BT\gg\hbar\omega$, the noise reaches the classical limit

$$S_V(\omega)=2Rk_BT. \tag{A.25}$$

In the quantum limit, which is achieved by freezing the resistor to absolute zero, the noise spectral property becomes

$$S_V(\omega)=2R\hbar\omega\Theta(\omega), \tag{A.26}$$

where $\Theta(\omega)=1$ for $\omega>0$ and $\Theta(\omega)=0$, otherwise.

Let us connect the plot shown in Fig. A.1 to Bose-Einstein statistics. The positve frequency part of the noise spectral density corresponds to the absorption of energy by the resistor, and the negative part to its emission of energy. From this, we learn that in the

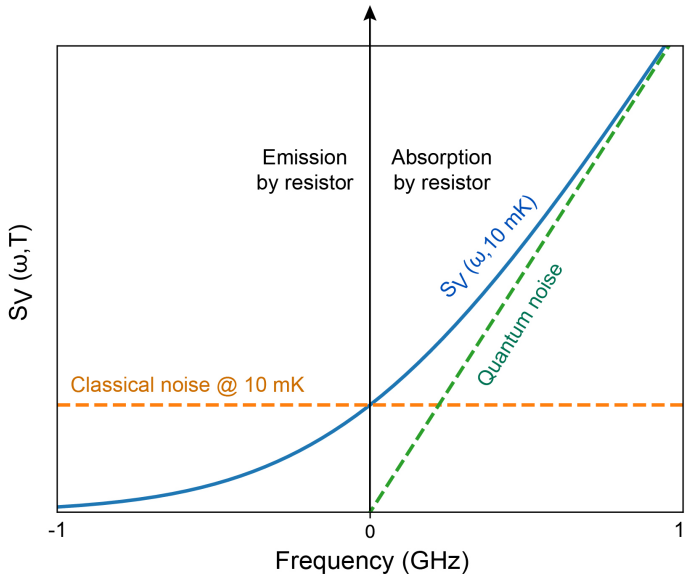

Figure A.1: Voltage noise. Voltage noise spectral density from a resistor at $T = 10$ mK. The classical noise at 10mK and the quantum noise are shown for comparison.

classical limit, the resistor emits as much as it absorbs, whereas in the quantum limit, the resistor only absorbs energy from the quantum system it connects to. We will see next that this also explains why we cannot observe quantum behavior in the classical limit where the noise is symmetric, $\Gamma_\uparrow = \Gamma_\downarrow$, and in the quantum limit, only decay process happens.

A.2 Fermi's Golden Rule

Consider a two-level quantum system with transition energy $E_{eg} = \hbar\omega_{eg}$, which is perturbed by a noise source with amplitude $f(t)$ and coupling efficiency A

$$\mathbf{H}_1(t) = Af(t)\sigma_X. \tag{A.27}$$

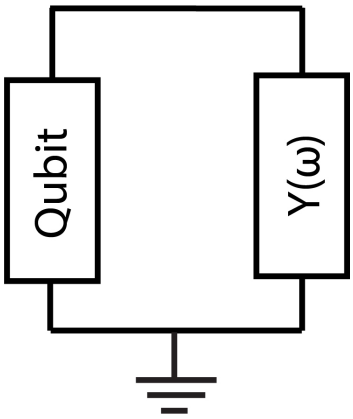

Figure A.2: Circuit dissipation model. Dissipation in superconducting circuits can be modeled using a complex shunting admittance $Y(\omega)$ which has a finite real part [70].

We assume for now that the perturbation is small and linearize it to first order. In the interaction picture the state of the system evolves as

$$|\psi_I(T)\rangle = |\psi(0)\rangle - \frac{i}{\hbar}\int_0^T dt \mathbf{H}_{1,I}(t)|\psi(0)\rangle, \tag{A.28}$$

which can be cast into matrix form as [172]:

$$i\hbar \begin{pmatrix} \dot{c_g} \\ \dot{c_e} \end{pmatrix} = Af(t) \begin{pmatrix} 0 & e^{i\omega_{ge}t} \\ e^{i\omega_{eg}t} & 0 \end{pmatrix} \begin{pmatrix} c_g \\ c_e \end{pmatrix}. \tag{A.29}$$

If we prepare the system in the ground state, the excited state coefficient at time T is

$$c_e(T) = -\frac{iA}{\hbar}\int_0^T dt e^{i\omega_{eg}t} f(t), \tag{A.30}$$

and the probability of the system to be in the excited state is

$$|c_e(T)|^2 = \frac{A^2}{\hbar^2}\int_0^T \int_0^T dt dt' e^{-i\omega_{eg}(t-t')} f(t) f(t') \tag{A.31}$$

Taking an ensemble average with time long compared to noise correlation time, $T \gg \tau_c$,

and changing variables $\tau = t - t'$, we have

$$\langle p_e(T)\rangle = \frac{A^2}{\hbar^2}\int_0^T dt \int_{-\infty}^{\infty} d\tau e^{-i\omega_{eg}\tau}\langle f(t)f(t-\tau)\rangle. \tag{A.32}$$

Writing the noise spectral density describing process $f(\tau)$ as

$$S_f(\omega) = \int_{-\infty}^{\infty} d\tau e^{i\omega_{eg}\tau}\langle f(t)f(t-\tau)\rangle, \tag{A.33}$$

and using time translational invariance to change the average brackets quantity to $\langle f(\tau)f(0)\rangle$, we can write the probability as a linear function of time T,

$$\langle p_e(T)\rangle = \frac{A^2}{\hbar^2}S_f(-\omega_{eg})T. \tag{A.34}$$

The time derivative of the averaged probability gives the transition rate

$$\Gamma_\uparrow = \frac{A^2}{\hbar^2}S_f(-\omega_{eg}). \tag{A.35}$$

If the system is prepared in the excited state, the same algebraic steps give us the decay rate

$$\Gamma_\downarrow = \frac{A^2}{\hbar^2}S_f(+\omega_{eg}). \tag{A.36}$$

In thermal equilibrium, the transition rates obey detailed balance relation $\Gamma_\downarrow/\Gamma_\uparrow = e^{\hbar\omega_{eg}/k_BT}$. This implies

$$S_f(+\omega_{eg}) = e^{\hbar\omega_{eg}/k_BT}S_f(-\omega_{eg}). \tag{A.37}$$

We see again that in the classical limit, $\hbar\omega_{eg}/k_BT \to 0$, the noise is symmetric, and the two transition rates are equal. This effectively blurs all quantum effects. In the quantum limit $T = 0$, $\Gamma_\uparrow$ and $S_f(-\omega_{eg})$ would vanish, and no energy is transferred to the system from the bath.

The relaxation rate from state i to j caused by source α follows the Fermi Golden rule derived above as

$$\Gamma_{ij}^{\alpha} = \frac{1}{\hbar^2}|\langle j|\hat{O}|i\rangle|^2 S_{\alpha}(\omega_{ij}). \tag{A.38}$$

where $S_{\alpha}(\omega_{ij})$ is the noise spectral density of source α that causes the decay at transition frequency ω_{ij}. If the noise source is modeled as a shunting admittance, then the relevant operator is flux, corresponding to the matrix element $\phi_o\langle j|\phi|i\rangle$, with $\phi_o = \hbar/2e$, and the noise spectral density is given as

$$S_{\alpha}(\omega) = \hbar\omega \mathrm{ReY}_{\alpha}(\omega)\left[\coth\left(\frac{\hbar\omega}{2k_BT}\right)+1\right]. \tag{A.39}$$

Appendix B

Effective Josephson Energy in SQUID

One Ring to rule them all, One Ring to find them,
One Ring to bring them all, and in the darkness bind them.

John R. R. Tolkien

First, let us consider a SQUID circuit consisting of two Josephson junctions. The physics is similar to that of the Cooper-pair-box since the Josephson junctions form islands on each side. The flux threading the SQUID loop may however effectively change the Josephson energy. The Hamiltonian of the circuit is

$$H = 4E_C n^2 - E_{J_1} \cos\phi_1 - E_{J_2} \cos\phi_2, \tag{B.1}$$

where $\phi_{1,2}$ are the respective gauge invariant phase differences across the two junctions. The relation between N individual phase differences around the loop and the magnetic flux $\Phi_{\rm s}$ threading the loop must obey Kirchoff's voltage law and flux quantization constraint [49],

$$\sum_i^N \phi_i = 2\pi \left(N + \frac{\Phi_{\rm ext}}{\Phi_o} \right) \equiv \phi_{\rm ext}, \tag{B.2}$$

where N is an integer, $\Phi_o = h/2e$ is the flux quantum, and ϕ_{ext} is the reduced external magnetic flux. If the phases $\phi_{1,2}$ are defined with respect to ground , with ϕ_2 going against the direction of the external flux, Eq. B.2 can be used to write

$$\phi_1 - \phi_2 = \phi_{\text{ext}}. \tag{B.3}$$

For a SQUID circuit, replace notation ϕ_{ext} with ϕ_s, we can write the Hamiltonian in Eq. B.1 as

$$H = 4E_C n^2 - E_{J_1} \cos\phi_1 - E_{J_2} \cos(\phi_1 - \phi_{\text{s}}). \tag{B.4}$$

Therefore, there is only one degree of freedom in the circuit. To derive the effective Josephson energy, we define the sum and difference between the individual Josephson energies as

$$\begin{aligned} E_{J_\Sigma} &= E_{J_1} + E_{J_2}, \\ d &= \frac{E_{J_1} - E_{J_2}}{E_{J_\Sigma}}, \end{aligned} \tag{B.5}$$

which are equivalent to

$$\begin{aligned} E_{J_1} &= \frac{1}{2} E_{J_\Sigma}(1+d), \\ E_{J_2} &= \frac{1}{2} E_{J_\Sigma}(1-d). \end{aligned} \tag{B.6}$$

The potential term in the Hamiltonian can then be written

$$V_J = E_{J_\Sigma} \left[\cos\left(\frac{\phi_1+\phi_2}{2}\right) \cos\left(\frac{\phi_{\text{s}}}{2}\right) - \text{d} \sin\left(\frac{\phi_1+\phi_2}{2}\right) \sin\left(\frac{\phi_{\text{s}}}{2}\right) \right] \tag{B.7}$$

$$= E_{J_\Sigma} \cos\left(\frac{\phi_1+\phi_2}{2}\right) \cos\left(\frac{\phi_{\text{s}}}{2}\right) \left[1 - \text{d} \tan\left(\frac{\phi_1+\phi_2}{2}\right) \tan\left(\frac{\phi_{\text{s}}}{2}\right) \right]. \tag{B.8}$$

We can redefine the phase degree of freedom $(\phi_1 + \phi_2)/2 = \phi$, effectively changing the degree of freedom to ϕ, and use a parameter θ such that $\tan\theta = \text{d}\tan(\phi_{\text{ext}}/2)$. Simplifying

the potential further, we get

$$\begin{aligned} V_J &= E_{J_\Sigma} \frac{\cos\left(\frac{\phi_s}{2}\right)\cos\left(\phi+\theta\right)}{\cos\theta} \\ &= E_{J_\Sigma}\cos\left(\frac{\phi_s}{2}\right)\sqrt{1+\tan^2\theta}\cos\left(\phi+\theta\right). \end{aligned} \tag{B.9}$$

We can redefine the phase degree of freedom again $\phi+\theta \rightarrow \phi$ and write the effective Josephson energy E_J as

$$E_{J\text{eff}} \equiv E_{J_\Sigma}\cos\left(\frac{\phi_s}{2}\right)\sqrt{1+\mathrm{d}^2\tan^2\left(\frac{\phi_s}{2}\right)}. \tag{B.10}$$

The Hamiltonian can thus be written as

$$H = 4E_C n^2 - E_J\cos\phi. \tag{B.11}$$

Note that for the Hamiltonian given by Eq. B.11 to be equivalent to the one given by Eq. B.1, the phase definition is $\phi = \phi_1 - \phi_s/2 + \theta$.

For a SQUID loop shunted by an inductor (Fig. 4.6), we can follow the same procedure, noting that $\phi_1 = \phi - \phi_{\text{ext}}$, where ϕ is the phase across the inductor. We can rewrite the Josephson terms in the Hamiltonian given by Eq. 4.1 as

$$\begin{aligned} V_J &= E_{J_\Sigma}\cos\left(\frac{\phi_1+\phi_2}{2}\right)\cos\left(\frac{\phi_1-\phi_2}{2}\right)\left\{1-\mathrm{d}\tan\left(\frac{\phi_1+\phi_2}{2}\right)\tan\left(\frac{\phi_1-\phi_2}{2}\right)\right\} \\ &= E_{J_\Sigma}\cos\left(\phi_1-\frac{\phi_s}{2}\right)\cos\left(\frac{\phi_s}{2}\right)\left\{1-\mathrm{d}\tan\left(\phi_1-\frac{\phi_s}{2}\right)\tan\left(\frac{\phi_s}{2}\right)\right\}. \end{aligned} \tag{B.12}$$

Define a variable θ as before, with $\tan\theta = \mathrm{d}\tan(\phi_s/2)$, we have

$$\begin{aligned} V_J &= E_{J_\Sigma}\frac{\cos\left(\phi_s/2\right)}{\cos\theta}\cos\left(\phi_1 - \phi_s/2 + \theta\right) \\ &= E_{J_\Sigma}\cos\left(\phi_s/2\right)\sqrt{1+\mathrm{d}^2\tan^2\left(\frac{\phi_s}{2}\right)}\cos\left(\phi_1 - \phi_s/2 + \theta\right) \\ &= E_{J_{\mathrm{eff}}}\cos\left(\phi_1 - \frac{\phi_s}{2} + \theta\right). \end{aligned} \tag{B.13}$$

The flux through SQUID loop simply tunes the effective Josephson energy of the circuit. The split-junction fluxonium Hamiltonian can thus be rewritten as

$$H = 4E_C n^2 + \frac{1}{2}E_L\phi^2 - E_{J\mathrm{eff}}\cos\left(\phi - \phi_{\mathrm{ext}} - \frac{\phi_s}{2} + \theta\right). \tag{B.14}$$

Appendix C

Coupled Circuits Hamiltonians

Call me Ishmael.

Herman Melville

C.1 Capacitive Coupling

Consider two coupled LC oscillators with resonant frequencies $\omega_1 = 1/\sqrt{L_1 C_1}$ and $\omega_2 = 1/\sqrt{L_2 C_2}$ as shown in Fig. C.1(a). If we wish to turn one of them into a qubit, we can conveniently add the Josephson energy term in the final step. The Lagrangian for two capacitively coupled LC circuits with coupling capacitance C_c is

$$\mathcal{L} = \frac{1}{2}C_1\dot{\Phi}_1^2 - \frac{\Phi_1^2}{2L_1} + \frac{1}{2}C_2\dot{\Phi}_2^2 - \frac{\Phi_2^2}{2L_2} + \frac{1}{2}C_c(\dot{\Phi}_1 - \dot{\Phi}_2)^2. \tag{C.1}$$

Using the transformation given by Eq. 3.7, we get

$$H = \frac{Q_1^2}{2C_1'} + \frac{\Phi_1^2}{2L_1} + \frac{Q_2^2}{2C_2'} + \frac{\Phi_2^2}{2L_2} + \frac{C_c}{C_1 C_2}Q_1 Q_2, \tag{C.2}$$

where $C_1' = (C_1C_2 + C_1C_c + C_2C_c)/(C_2 + C_c)$ and $C_2' = (C_1C_2 + C_1C_c + C_2C_c)/(C_1 + C_c)$. The

coupling capacitance C_c thus slightly renormalizes the shunting capacitances [70]. Writing the Q operators in terms of ladder operators (see section 3.1), we get

$$H_c = -\frac{\hbar}{2}\frac{C_c}{C_1C_2}\left(\frac{C_1C_2}{L_1L_2}\right)^{1/4}(a^\dagger - a)(b^\dagger - b) = -\hbar g_{RR}(a^\dagger - a)(b^\dagger - b). \tag{C.3}$$

For qubit-resonator coupling, the convention is to write $Q_1 = 2en$ for qubit, $Q_2 = i\sqrt{\frac{\hbar}{2Z_R}}(a^\dagger - a)$, so the coupling Hamiltonian takes the form

$$H_c = i2e\frac{C_c}{C_qC_R}\sqrt{\frac{\hbar}{2}\sqrt{\frac{C_R}{L_R}}}n(a^\dagger - a) = \hbar g_{qR}n(a^\dagger - a). \tag{C.4}$$

For qubit-qubit coupling, we often write

$$H_c = 4e^2\frac{C_c}{C_1C_2}n_1n_2 = J_Cn_1n_2. \tag{C.5}$$

The coupling constant g_{qR} is used to simulate the dispersive shift [127], and J_C is used to compute qubit spectrum. The coupling constant g_{RR} can be simulated in Ansys Desktop (section 5.2) by assigning a lump circuit boundary condition to the qubit mode, making it behave like an LC oscillator. We can extract the vacuum coupling coefficient $2g_{RR}$, which equals to the anti-crossing amplitude. This can then be converted to g_{qR} and J_C. A spectroscopy fit in the qubit-cavity anti-crossing region is used to experimentally extract the coupling constant g_{qR}, as shown in Fig. 6.23(b). Two-qubit spectrum can be used to fit and extract J_C, as shown in Fig. 6.15.

C.2 Inductive Coupling

Here we consider two harmonic oscillators coupled via a mutual inductance L_3 as shown in Fig. C.1(b). Defining the flux Φ_1, Φ_2, and Φ_3 as shown in Fig. C.1(b), we can write the

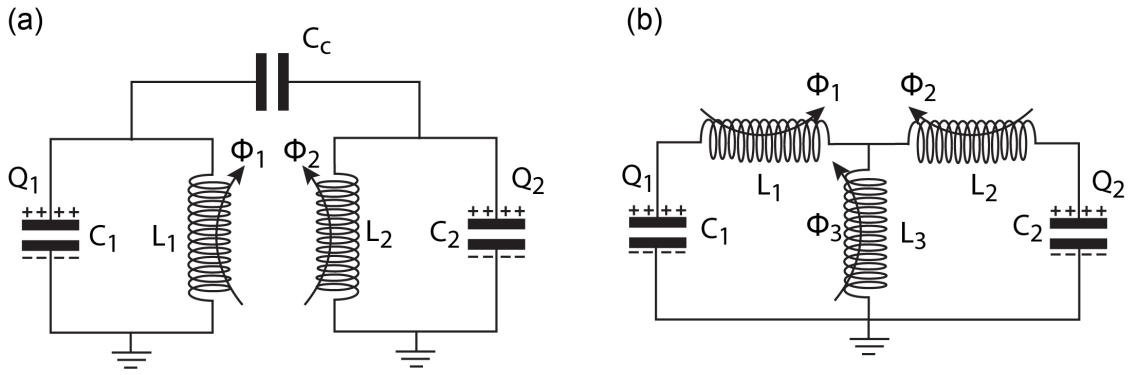

Figure C.1: Coupled circuits diagrams (a) Capacitively coupled LC circuits. (b) Inductively coupled LC circuit.

Lagrangian of the circuit as

$$\mathcal{L} = \frac{1}{2}C_1\dot{\Phi}_1^2 + \frac{1}{2}C_2\dot{\Phi}_2^2 - \frac{(\Phi_1 - \Phi_3)^2}{2L_1} - \frac{(\Phi_2 - \Phi_3)^2}{2L_2} - \frac{\Phi_3^2}{2L_3}. \tag{C.6}$$

We can write the potential part as a function of only Φ_1 and Φ_2 by using the condition on the current going through the mutual inductor L_3,

$$I_3 = \frac{\Phi_3}{L_3} = \frac{\Phi_1 - \Phi_3}{L_1} + \frac{\Phi_2 - \Phi_3}{L_2}. \tag{C.7}$$

Let $L_3/L_1 = r_1$ and $L_3/L_2 = r_2$, we get

$$\Phi_3 = \frac{r_1\Phi_1 + r_2\Phi_2}{1 + r_1 + r_2}. \tag{C.8}$$

Replacing Φ_3 in Eq. C.6 gives us

$$\mathcal{L}_P = \frac{1}{(1 + r_1 + r_2)^2}\left\{\frac{1}{2L_1}\left[(1 + r_2)\Phi_1 - r_2\Phi_2\right]^2 + \frac{1}{2L_2}\left[(1 + r_1)\Phi_2 - r_1\Phi_1\right]^2 + \frac{1}{2L_3}\left[r_1\Phi_1 + r_2\Phi_2\right]^2\right\}. \tag{C.9}$$

The Hamiltonian of the coupled systems is

$$H = H_1 + H_2 + H_c, \tag{C.10}$$

where the individual uncoupled terms H_1, H_2 each has a normalized inductance, and the coupling term H_c involves $\Phi_1\Phi_2$. By grouping terms with Φ_1^2, Φ_2^2, and $\Phi_1\Phi_2$ in Eq. C.9, we can write

$$\begin{aligned}
H_1 &= \frac{Q_1^2}{2C_1} + \frac{1}{2(1+r_1+r_2)^2}\left[\frac{1}{L_1}(1+r_2)^2 + \left(\frac{1}{L_2}+\frac{1}{L_3}\right)r_1^2\right]\Phi_1^2, \\
H_2 &= \frac{Q_2^2}{2C_2} + \frac{1}{2(1+r_1+r_2)^2}\left[\frac{1}{L_2}(1+r_1)^2 + \left(\frac{1}{L_1}+\frac{1}{L_3}\right)r_2^2\right]\Phi_2^2, \\
H_c &= -\frac{1}{(1+r_1+r_2)^2}\left[\frac{r_2(1+r_2)}{L_1} + \frac{r_1(1+r_1)}{L_2} - \frac{r_1 r_2}{L_3}\right]\Phi_1\Phi_2.
\end{aligned} \tag{C.11}$$

These are the general expressions for the Hamiltonians. In the weak coupling limit, $L_1,\ L_2 \gg L_3$, H_1 and H_2 are modified by L_3 by a negligible amount, while the coupling term H_c becomes [128]

$$H_c = -\frac{L_3}{L_1 L_2}\Phi_1\Phi_2 = -\left(\frac{\hbar}{2e}\right)^2 \frac{L_3}{L_1 L_2}\phi_1\phi_2. \tag{C.12}$$

For inductively coupled qubit-cavity system [173], we can add a Josephson energy term to H_1. For fluxonium, we can take the limit $L_1 \gg L_2, L_3$, so $r_1 = L_3/L_1 \approx 0$. The Hamiltonians in Eqs. C.11 become

$$\begin{aligned}
H_1 &= \frac{Q_1^2}{2C_1} + \frac{\Phi_1^2}{2L_1} - E_J\cos(\phi_1 - \phi_{\text{ext}}), \\
H_2 &= \frac{Q_2^2}{2C_2} + \frac{\Phi_2^2}{2(L_2+L_3)}, \\
H_c &= -\frac{L_3}{L_1(L_2+L_3)}\Phi_1\Phi_2 = -g_{qR}\phi_1(a+a^\dagger).
\end{aligned} \tag{C.13}$$

Bibliography

[1] Y. N. Harari, *Sapiens: A brief history of humankind*. Random House, 2014.

[2] P. Kaye, R. Laflamme, and M. Mosca, *An introduction to quantum computing*. Oxford university press, 2007.

[3] D. Deutsch, "Quantum theory, the church–turing principle and the universal quantum computer," *Proceedings of the Royal Society of London. A. Mathematical and Physical Sciences*, vol. 400, no. 1818, pp. 97–117, 1985.

[4] P. W. Shor, "Algorithms for quantum computation: discrete logarithms and factoring," in *Proceedings 35th annual symposium on foundations of computer science*, pp. 124–134, Ieee, 1994.

[5] M. A. Nielsen and I. L. Chuang, *Quantum computation and quantum information*. Cambridge University Press, 2016.

[6] L. K. Grover, "A fast quantum mechanical algorithm for database search," in *Proceedings of the twenty-eighth annual ACM symposium on Theory of computing*, pp. 212–219, 1996.

[7] A. Montanaro, "Quantum algorithms: an overview," *npj Quantum Information*, vol. 2, no. 1, pp. 1–8, 2016.

[8] J. Biamonte, P. Wittek, N. Pancotti, P. Rebentrost, N. Wiebe, and S. Lloyd, "Quantum machine learning," *Nature*, vol. 549, no. 7671, pp. 195–202, 2017.

[9] I. Bloch, "Quantum simulations come of age," *Nature Physics*, vol. 14, no. 12, pp. 1159–1161, 2018.

[10] S. Haroche and J.-M. Raimond, *Exploring the quantum: atoms, cavities, and photons*. Oxford university press, 2006.

[11] S. A. Huettel, A. W. Song, G. McCarthy, *et al.*, *Functional magnetic resonance imaging*, vol. 1. Sinauer Associates Sunderland, MA, 2004.

[12] T. D. Ladd, F. Jelezko, R. Laflamme, Y. Nakamura, C. Monroe, and J. L. OBrien, "Quantum computers," *Nature*, vol. 464, no. 7285, pp. 45–53, 2010.

[13] M. H. Devoret, J. M. Martinis, and J. Clarke, "Measurements of macroscopic quantum tunneling out of the zero-voltage state of a current-biased josephson junction," *Physical Review Letters*, vol. 55, no. 18, p. 1908, 1985.

[14] J. M. Martinis, M. H. Devoret, and J. Clarke, "Energy-level quantization in the zero-voltage state of a current-biased josephson junction," *Physical Review Letters*, vol. 55, no. 15, p. 1543, 1985.

[15] V. Bouchiat, D. Vion, P. Joyez, D. Esteve, and M. Devoret, "Quantum coherence with a single cooper pair," *Physica Scripta*, vol. 1998, no. T76, p. 165, 1998.

[16] Y. Nakamura, Y. A. Pashkin, and J. S. Tsai, "Coherent control of macroscopic quantum states in a single-cooper-pair box," *Nature*, vol. 398, no. 6730, pp. 786–788, 1999.

[17] J. Clarke and F. K. Wilhelm, "Superconducting quantum bits," *Nature*, vol. 453, no. 7198, pp. 1031–1042, 2008.

[18] M. H. Devoret and R. J. Schoelkopf, "Superconducting circuits for quantum information: an outlook," *Science*, vol. 339, no. 6124, pp. 1169–1174, 2013.

[19] G. Dolan, "Offset masks for lift-off photoprocessing," *Applied Physics Letters*, vol. 31, no. 5, pp. 337–339, 1977.

[20] L. Frunzio, A. Wallraff, D. Schuster, J. Majer, and R. Schoelkopf, "Fabrication and characterization of superconducting circuit qed devices for quantum computation," *IEEE transactions on applied superconductivity*, vol. 15, no. 2, pp. 860–863, 2005.

[21] R. Schoelkopf and S. Girvin, "Wiring up quantum systems," *Nature*, vol. 451, no. 7179, pp. 664–669, 2008.

[22] A. Blais, R.-S. Huang, A. Wallraff, S. M. Girvin, and R. J. Schoelkopf, "Cavity quantum electrodynamics for superconducting electrical circuits: An architecture for quantum computation," *Phys. Rev. A*, vol. 69, p. 062320, Jun 2004.

[23] A. Blais, J. Gambetta, A. Wallraff, D. I. Schuster, S. M. Girvin, M. H. Devoret, and R. J. Schoelkopf, "Quantum-information processing with circuit quantum electrodynamics," *Phys. Rev. A*, vol. 75, p. 032329, Mar 2007.

[24] J. Preskill, "Quantum computing in the nisq era and beyond," *Quantum*, vol. 2, p. 79, 2018.

[25] J. Preskill, "Quantum computing and the entanglement frontier," *ArXiv preprint ArXiv:1203.5813*, 2012.

[26] F. Arute, K. Arya, R. Babbush, D. Bacon, J. C. Bardin, R. Barends, R. Biswas, S. Boixo, F. G. Brandao, D. A. Buell, *et al.*, "Quantum supremacy using a programmable superconducting processor," *Nature*, vol. 574, no. 7779, pp. 505–510, 2019.

[27] R. Schoelkopf, A. Clerk, S. Girvin, K. Lehnert, and M. Devoret, "Qubits as spectrometers of quantum noise," in *Quantum noise in mesoscopic physics*, pp. 175–203, Springer, 2003.

[28] J. M. Martinis, S. Nam, J. Aumentado, K. Lang, and C. Urbina, "Decoherence of a superconducting qubit due to bias noise," *Physical Review B*, vol. 67, no. 9, p. 094510, 2003.

[29] J. M. Martinis, K. B. Cooper, R. McDermott, M. Steffen, M. Ansmann, K. Osborn, K. Cicak, S. Oh, D. P. Pappas, R. W. Simmonds, *et al.*, "Decoherence in josephson qubits from dielectric loss," *Physical Review Letters*, vol. 95, no. 21, p. 210503, 2005.

[30] C. Wang, C. Axline, Y. Y. Gao, T. Brecht, Y. Chu, L. Frunzio, M. Devoret, and R. J. Schoelkopf, "Surface participation and dielectric loss in superconducting qubits," *Applied Physics Letters*, vol. 107, no. 16, p. 162601, 2015.

[31] P. Bertet, I. Chiorescu, G. Burkard, K. Semba, C. Harmans, D. P. DiVincenzo, and J. Mooij, "Dephasing of a superconducting qubit induced by photon noise," *Physical Review Letters*, vol. 95, no. 25, p. 257002, 2005.

[32] R. H. Koch, D. P. DiVincenzo, and J. Clarke, "Model for 1/f flux noise in squids and qubits," *Physical Review Letters*, vol. 98, no. 26, p. 267003, 2007.

[33] F. Yoshihara, K. Harrabi, A. O. Niskanen, Y. Nakamura, and J. S. Tsai, "Decoherence of flux qubits due to $1/f$ flux noise," *Phys. Rev. Lett.*, vol. 97, p. 167001, Oct 2006.

[34] A. Streltsov, G. Adesso, and M. B. Plenio, "Colloquium: Quantum coherence as a resource," *Reviews of Modern Physics*, vol. 89, no. 4, p. 041003, 2017.

[35] R. Barends, J. Kelly, A. Megrant, A. Veitia, D. Sank, E. Jeffrey, T. C. White, J. Mutus, A. G. Fowler, B. Campbell, *et al.*, "Superconducting quantum circuits at the surface code threshold for fault tolerance," *Nature*, vol. 508, no. 7497, pp. 500–503, 2014.

[36] T. Albash and D. A. Lidar, "Decoherence in adiabatic quantum computation," *Physical Review A*, vol. 91, no. 6, p. 062320, 2015.

[37] S. Boixo, V. N. Smelyanskiy, A. Shabani, S. V. Isakov, M. Dykman, V. S. Denchev, M. H. Amin, A. Y. Smirnov, M. Mohseni, and H. Neven, "Computational multiqubit tunnelling in programmable quantum annealers," *Nature Communications*, vol. 7, p. 10327, 2016.

[38] A. Kandala, A. Mezzacapo, K. Temme, M. Takita, M. Brink, J. M. Chow, and J. M. Gambetta, "Hardware-efficient variational quantum eigensolver for small molecules and quantum magnets," *Nature*, vol. 549, no. 7671, pp. 242–246, 2017.

[39] R. Versluis, S. Poletto, N. Khammassi, B. Tarasinski, N. Haider, D. J. Michalak, A. Bruno, K. Bertels, and L. DiCarlo, "Scalable quantum circuit and control for a superconducting surface code," *Physical Review Applied*, vol. 8, no. 3, p. 034021, 2017.

[40] C. Song, K. Xu, W. Liu, C.-p. Yang, S.-B. Zheng, H. Deng, Q. Xie, K. Huang, Q. Guo, L. Zhang, *et al.*, "10-qubit entanglement and parallel logic operations with a superconducting circuit," *Physical Review Letters*, vol. 119, no. 18, p. 180511, 2017.

[41] J. Otterbach, R. Manenti, N. Alidoust, A. Bestwick, M. Block, B. Bloom, S. Caldwell, N. Didier, E. S. Fried, S. Hong, *et al.*, "Unsupervised machine learning on a hybrid quantum computer," *ArXiv preprint ArXiv:1712.05771*, 2017.

[42] C. Neill, P. Roushan, K. Kechedzhi, S. Boixo, S. V. Isakov, V. Smelyanskiy, A. Megrant, B. Chiaro, A. Dunsworth, K. Arya, *et al.*, "A blueprint for demonstrating quantum supremacy with superconducting qubits," *Science*, vol. 360, no. 6385, pp. 195–199, 2018.

[43] S. Boixo, S. V. Isakov, V. N. Smelyanskiy, R. Babbush, N. Ding, Z. Jiang, M. J. Bremner, J. M. Martinis, and H. Neven, "Characterizing quantum supremacy in near-term devices," *Nature Physics*, vol. 14, no. 6, pp. 595–600, 2018.

[44] J. S. Kline, M. R. Vissers, F. C. da Silva, D. S. Wisbey, M. Weides, T. J. Weir, B. Turek, D. A. Braje, W. D. Oliver, Y. Shalibo, *et al.*, "Sub-micrometer epitaxial josephson junctions for quantum circuits," *Superconductor Science and Technology*, vol. 25, no. 2, p. 025005, 2011.

[45] P. Kumar, S. Sendelbach, M. Beck, J. Freeland, Z. Wang, H. Wang, C. Y. Clare, R. Wu, D. Pappas, and R. McDermott, "Origin and reduction of 1/f magnetic flux noise in superconducting devices," *Physical Review Applied*, vol. 6, no. 4, p. 041001, 2016.

[46] C. Quintana, A. Megrant, Z. Chen, A. Dunsworth, B. Chiaro, R. Barends, B. Campbell, Y. Chen, I.-C. Hoi, E. Jeffrey, *et al.*, "Characterization and reduction of microfabrication-induced decoherence in superconducting quantum circuits," *Applied Physics Letters*, vol. 105, no. 6, p. 062601, 2014.

[47] A. Dunsworth, A. Megrant, C. Quintana, Z. Chen, R. Barends, B. Burkett, B. Foxen, Y. Chen, B. Chiaro, A. Fowler, *et al.*, "Characterization and reduction of capacitive loss induced by sub-micron josephson junction fabrication in superconducting qubits," *Applied Physics Letters*, vol. 111, no. 2, p. 022601, 2017.

[48] A. Kamal, J. L. Yoder, F. Yan, T. J. Gudmundsen, D. Hover, A. P. Sears, P. Welander, T. P. Orlando, S. Gustavsson, and W. D. Oliver, "Improved superconducting qubit coherence with high-temperature substrate annealing," *ArXiv preprint ArXiv:1606.09262*, 2016.

[49] J. Koch, M. Y. Terri, J. Gambetta, A. A. Houck, D. Schuster, J. Majer, A. Blais, M. H. Devoret, S. M. Girvin, and R. J. Schoelkopf, "Charge-insensitive qubit design derived from the cooper pair box," *Physical Review A*, vol. 76, no. 4, p. 042319, 2007.

[50] J. Schreier, A. A. Houck, J. Koch, D. I. Schuster, B. Johnson, J. Chow, J. M. Gambetta, J. Majer, L. Frunzio, M. H. Devoret, *et al.*, "Suppressing charge noise decoherence in superconducting charge qubits," *Physical Review B*, vol. 77, no. 18, p. 180502, 2008.

[51] H. Paik, D. Schuster, L. S. Bishop, G. Kirchmair, G. Catelani, A. Sears, B. Johnson, M. Reagor, L. Frunzio, L. Glazman, *et al.*, "Observation of high coherence in josephson junction qubits measured in a three-dimensional circuit qed architecture," *Physical Review Letters*, vol. 107, no. 24, p. 240501, 2011.

[52] J. You, X. Hu, S. Ashhab, and F. Nori, "Low-decoherence flux qubit," *Physical Review B*, vol. 75, no. 14, p. 140515, 2007.

[53] M. Steffen, S. Kumar, D. P. DiVincenzo, J. Rozen, G. A. Keefe, M. B. Rothwell, and M. B. Ketchen, "High-coherence hybrid superconducting qubit," *Physical Review Letters*, vol. 105, no. 10, p. 100502, 2010.

[54] F. Yan, S. Gustavsson, A. Kamal, J. Birenbaum, A. P. Sears, D. Hover, T. J. Gudmundsen, D. Rosenberg, G. Samach, S. Weber, *et al.*, "The flux qubit revisited to enhance coherence and reproducibility," *Nature Communications*, vol. 7, no. 1, pp. 1–9, 2016.

[55] C. H. Van Der Wal, A. Ter Haar, F. Wilhelm, R. Schouten, C. Harmans, T. Orlando, S. Lloyd, and J. Mooij, "Quantum superposition of macroscopic persistent-current states," *Science*, vol. 290, no. 5492, pp. 773–777, 2000.

[56] J. R. Friedman, V. Patel, W. Chen, S. Tolpygo, and J. E. Lukens, "Quantum superposition of distinct macroscopic states," *Nature*, vol. 406, no. 6791, pp. 43–46, 2000.

[57] J. Mooij, T. Orlando, L. Levitov, L. Tian, C. H. Van der Wal, and S. Lloyd, "Josephson persistent-current qubit," *Science*, vol. 285, no. 5430, pp. 1036–1039, 1999.

[58] Z. Chen, J. Kelly, C. Quintana, R. Barends, B. Campbell, Y. Chen, B. Chiaro, A. Dunsworth, A. Fowler, E. Lucero, *et al.*, "Measuring and suppressing quantum

state leakage in a superconducting qubit," *Physical Review Letters*, vol. 116, no. 2, p. 020501, 2016.

[59] V. E. Manucharyan, J. Koch, L. I. Glazman, and M. H. Devoret, "Fluxonium: Single cooper-pair circuit free of charge offsets," *Science*, vol. 326, no. 5949, pp. 113–116, 2009.

[60] Y.-H. Lin, L. B. Nguyen, N. Grabon, J. San Miguel, N. Pankratova, and V. E. Manucharyan, "Demonstration of protection of a superconducting qubit from energy decay," *Physical Review Letters*, vol. 120, no. 15, p. 150503, 2018.

[61] L. B. Nguyen, Y.-H. Lin, A. Somoroff, R. Mencia, N. Grabon, and V. E. Manucharyan, "High-coherence fluxonium qubit," *Physical Review X*, vol. 9, no. 4, p. 041041, 2019.

[62] A. Wallraff, D. I. Schuster, A. Blais, L. Frunzio, R.-S. Huang, J. Majer, S. Kumar, S. M. Girvin, and R. J. Schoelkopf, "Strong coupling of a single photon to a superconducting qubit using circuit quantum electrodynamics," *Nature*, vol. 431, no. 7005, p. 162, 2004.

[63] D. I. Schuster, A. Wallraff, A. Blais, L. Frunzio, R.-S. Huang, J. Majer, S. Girvin, and R. J. Schoelkopf, "ac stark shift and dephasing of a superconducting qubit strongly coupled to a cavity field," *Physical Review Letters*, vol. 94, no. 12, p. 123602, 2005.

[64] D. Schuster, A. A. Houck, J. Schreier, A. Wallraff, J. Gambetta, A. Blais, L. Frunzio, J. Majer, B. Johnson, M. Devoret, *et al.*, "Resolving photon number states in a superconducting circuit," *Nature*, vol. 445, no. 7127, pp. 515–518, 2007.

[65] J. Gambetta, A. Blais, D. I. Schuster, A. Wallraff, L. Frunzio, J. Majer, M. H. Devoret, S. M. Girvin, and R. J. Schoelkopf, "Qubit-photon interactions in a cavity: Measurement-induced dephasing and number splitting," *Physical Review A*, vol. 74, no. 4, p. 042318, 2006.

[66] B. Johnson, M. Reed, A. A. Houck, D. Schuster, L. S. Bishop, E. Ginossar, J. Gambetta, L. DiCarlo, L. Frunzio, S. Girvin, *et al.*, "Quantum non-demolition detection of single microwave photons in a circuit," *Nature Physics*, vol. 6, no. 9, pp. 663–667, 2010.

[67] F. Yoshihara, Y. Nakamura, F. Yan, S. Gustavsson, J. Bylander, W. D. Oliver, and J.-S. Tsai, "Flux qubit noise spectroscopy using rabi oscillations under strong driving conditions," *Physical Review B*, vol. 89, no. 2, p. 020503, 2014.

[68] I. L. Chuang and M. A. Nielsen, "Prescription for experimental determination of the dynamics of a quantum black box," *Journal of Modern Optics*, vol. 44, no. 11-12, pp. 2455–2467, 1997.

[69] M. Mohseni, A. Rezakhani, and D. Lidar, "Quantum-process tomography: Resource analysis of different strategies," *Physical Review A*, vol. 77, no. 3, p. 032322, 2008.

[70] M. H. Devoret *et al.*, "Quantum fluctuations in electrical circuits," *Les Houches, Session LXIII*, vol. 7, no. 8, 1995.

[71] L. DiCarlo, J. M. Chow, J. M. Gambetta, L. S. Bishop, B. R. Johnson, D. Schuster, J. Majer, A. Blais, L. Frunzio, S. Girvin, *et al.*, "Demonstration of two-qubit algorithms with a superconducting quantum processor," *Nature*, vol. 460, no. 7252, pp. 240–244, 2009.

[72] M. Mariantoni, H. Wang, T. Yamamoto, M. Neeley, R. C. Bialczak, Y. Chen, M. Lenander, E. Lucero, A. D. OConnell, D. Sank, *et al.*, "Implementing the quantum von neumann architecture with superconducting circuits," *Science*, vol. 334, no. 6052, pp. 61–65, 2011.

[73] A. W. Cross, L. S. Bishop, S. Sheldon, P. D. Nation, and J. M. Gambetta, "Validating quantum computers using randomized model circuits," *Physical Review A*, vol. 100, no. 3, p. 032328, 2019.

[74] V. V. Schmidt, *The physics of superconductors: Introduction to fundamentals and applications*. Springer Science & Business Media, 2013.

[75] M. Tinkham, *Introduction to superconductivity*. Courier Corporation, 2004.

[76] F. London and H. London, "The electromagnetic equations of the supraconductor," *Proceedings of the Royal Society of London. Series A-Mathematical and Physical Sciences*, vol. 149, no. 866, pp. 71–88, 1935.

[77] J. Schmalian, "Failed theories of superconductivity," *Modern Physics Letters B*, vol. 24, no. 27, pp. 2679–2691, 2010.

[78] J. Bardeen, L. N. Cooper, and J. R. Schrieffer, "Microscopic theory of superconductivity," *Physical Review*, vol. 106, no. 1, p. 162, 1957.

[79] B. Joesphson, "Possible new effects in superconductive tunneling," *Phys. Lett*, vol. 1, no. 7, p. 251, 1962.

[80] P. Krantz, M. Kjaergaard, F. Yan, T. P. Orlando, S. Gustavsson, and W. D. Oliver, "A quantum engineer's guide to superconducting qubits," *Applied Physics Reviews*, vol. 6, no. 2, p. 021318, 2019.

[81] J. Bylander, S. Gustavsson, F. Yan, F. Yoshihara, K. Harrabi, G. Fitch, D. G. Cory, Y. Nakamura, J.-S. Tsai, and W. D. Oliver, "Noise spectroscopy through dynamical decoupling with a superconducting flux qubit," *Nature Physics*, vol. 7, no. 7, pp. 565–570, 2011.

[82] D. M. Pozar, *Microwave Engineering 3e*. Wiley, 2006.

[83] A. A. Clerk, M. H. Devoret, S. M. Girvin, F. Marquardt, and R. J. Schoelkopf, "Introduction to quantum noise, measurement, and amplification," *Reviews of Modern Physics*, vol. 82, no. 2, p. 1155, 2010.

[84] C. Quintana, Y. Chen, D. Sank, A. Petukhov, T. White, D. Kafri, B. Chiaro, A. Megrant, R. Barends, B. Campbell, *et al.*, "Observation of classical-quantum crossover of 1/f flux noise and its paramagnetic temperature dependence," *Physical Review Letters*, vol. 118, no. 5, p. 057702, 2017.

[85] I. M. Pop, K. Geerlings, G. Catelani, R. J. Schoelkopf, L. I. Glazman, and M. H. Devoret, "Coherent suppression of electromagnetic dissipation due to superconducting quasiparticles," *Nature*, vol. 508, no. 7496, p. 369, 2014.

[86] C. Wang, Y. Y. Gao, I. M. Pop, U. Vool, C. Axline, T. Brecht, R. W. Heeres, L. Frunzio, M. H. Devoret, G. Catelani, *et al.*, "Measurement and control of quasiparticle dynamics in a superconducting qubit," *Nature Communications*, vol. 5, p. 5836, 2014.

[87] U. Vool, I. M. Pop, K. Sliwa, B. Abdo, C. Wang, T. Brecht, Y. Y. Gao, S. Shankar, M. Hatridge, G. Catelani, *et al.*, "Non-poissonian quantum jumps of a fluxonium qubit due to quasiparticle excitations," *Physical Review Letters*, vol. 113, no. 24, p. 247001, 2014.

[88] K. Serniak, M. Hays, G. de Lange, S. Diamond, S. Shankar, L. D. Burkhart, L. Frunzio, M. Houzet, and M. H. Devoret, "Hot nonequilibrium quasiparticles in transmon qubits," *Phys. Rev. Lett.*, vol. 121, p. 157701, Oct 2018.

[89] K. Serniak, S. Diamond, M. Hays, V. Fatemi, S. Shankar, L. Frunzio, R. Schoelkopf, and M. Devoret, "Direct dispersive monitoring of charge parity in offset-charge-sensitive transmons," *Phys. Rev. Applied*, vol. 12, p. 014052, Jul 2019.

[90] G. Catelani, J. Koch, L. Frunzio, R. Schoelkopf, M. H. Devoret, and L. Glazman, "Quasiparticle relaxation of superconducting qubits in the presence of flux," *Physical Review Letters*, vol. 106, no. 7, p. 077002, 2011.

[91] G. Catelani, R. J. Schoelkopf, M. H. Devoret, and L. I. Glazman, "Relaxation and frequency shifts induced by quasiparticles in superconducting qubits," *Physical Review B*, vol. 84, no. 6, p. 064517, 2011.

[92] A. Vepsäläinen, A. H. Karamlou, J. L. Orrell, A. S. Dogra, B. Loer, F. Vasconcelos, D. K. Kim, A. J. Melville, B. M. Niedzielski, J. L. Yoder, *et al.*, "Impact of ionizing radiation on superconducting qubit coherence," *ArXiv preprint ArXiv:2001.09190*, 2020.

[93] J. Preskill, "Lecture notes for physics 229: Quantum information and computation," *California Institute of Technology*, vol. 16, 1998.

[94] E. L. Hahn, "Spin echoes," *Physical review*, vol. 80, no. 4, p. 580, 1950.

[95] H. Y. Carr and E. M. Purcell, "Effects of diffusion on free precession in nuclear magnetic resonance experiments," *Physical review*, vol. 94, no. 3, p. 630, 1954.

[96] S. Meiboom and D. Gill, "Modified spin-echo method for measuring nuclear relaxation times," *Review of scientific instruments*, vol. 29, no. 8, pp. 688–691, 1958.

[97] E. Paladino, Y. Galperin, G. Falci, and B. Altshuler, "1/f noise: Implications for solid-state quantum information," *Reviews of Modern Physics*, vol. 86, no. 2, p. 361, 2014.

[98] G. Ithier, E. Collin, P. Joyez, P. J. Meeson, D. Vion, D. Esteve, F. Chiarello, A. Shnirman, Y. Makhlin, J. Schriefl, and G. Schön, "Decoherence in a superconducting quantum bit circuit," *Phys. Rev. B*, vol. 72, p. 134519, Oct 2005.

[99] M. Weissman, "1 f noise and other slow, nonexponential kinetics in condensed matter," *Reviews of modern physics*, vol. 60, no. 2, p. 537, 1988.

[100] S. Kogan, "1/f noise and random telegraph noise," *Electronic noise and fluctuations in solids*, p. 206, 1996.

[101] Y. Makhlin and A. Shnirman, "Dephasing of solid-state qubits at optimal points," *Physical Review Letters*, vol. 92, no. 17, p. 178301, 2004.

[102] C. Rigetti, J. M. Gambetta, S. Poletto, B. Plourde, J. M. Chow, A. Córcoles, J. A. Smolin, S. T. Merkel, J. Rozen, G. A. Keefe, *et al.*, "Superconducting qubit in a waveguide cavity with a coherence time approaching 0.1 ms," *Physical Review B*, vol. 86, no. 10, p. 100506, 2012.

[103] G. Zhang, Y. Liu, J. J. Raftery, and A. A. Houck, "Suppression of photon shot noise dephasing in a tunable coupling superconducting qubit," *npj Quantum Information*, vol. 3, no. 1, pp. 1–4, 2017.

[104] D. J. Van Harlingen, T. L. Robertson, B. L. T. Plourde, P. A. Reichardt, T. A. Crane, and J. Clarke, "Decoherence in josephson-junction qubits due to critical-current fluctuations," *Phys. Rev. B*, vol. 70, p. 064517, Aug 2004.

[105] J. Eroms, L. C. van Schaarenburg, E. F. C. Driessen, J. H. Plantenberg, C. M. Huizinga, R. N. Schouten, A. H. Verbruggen, C. J. P. M. Harmans, and J. E. Mooij, "Low-frequency noise in josephson junctions for superconducting qubits," *Applied Physics Letters*, vol. 89, no. 12, p. 122516, 2006.

[106] C. D. Nugroho, V. Orlyanchik, and D. J. Van Harlingen, "Low frequency resistance and critical current fluctuations in al-based josephson junctions," *Applied Physics Letters*, vol. 102, no. 14, p. 142602, 2013.

[107] F. Motzoi, J. M. Gambetta, P. Rebentrost, and F. K. Wilhelm, "Simple pulses for elimination of leakage in weakly nonlinear qubits," *Physical Review Letters*, vol. 103, no. 11, p. 110501, 2009.

[108] J. M. Chow, L. DiCarlo, J. M. Gambetta, F. Motzoi, L. Frunzio, S. M. Girvin, and R. J. Schoelkopf, "Optimized driving of superconducting artificial atoms for improved single-qubit gates," *Physical Review A*, vol. 82, no. 4, p. 040305, 2010.

[109] D. C. McKay, C. J. Wood, S. Sheldon, J. M. Chow, and J. M. Gambetta, "Efficient z gates for quantum computing," *Physical Review A*, vol. 96, no. 2, p. 022330, 2017.

[110] R. Bianchetti, S. Filipp, M. Baur, J. M. Fink, C. Lang, L. Steffen, M. Boissonneault, A. Blais, and A. Wallraff, "Control and tomography of a three level superconducting artificial atom," *Physical Review Letters*, vol. 105, no. 22, p. 223601, 2010.

[111] J. Chow, L. DiCarlo, J. Gambetta, A. Nunnenkamp, L. S. Bishop, L. Frunzio, M. Devoret, S. Girvin, and R. Schoelkopf, "Detecting highly entangled states with a joint qubit readout," *Physical Review A*, vol. 81, no. 6, p. 062325, 2010.

[112] S. Filipp, P. Maurer, P. Leek, M. Baur, R. Bianchetti, J. Fink, M. Göppl, L. Steffen, J. Gambetta, A. Blais, *et al.*, "Two-qubit state tomography using a joint dispersive readout," *Physical Review Letters*, vol. 102, no. 20, p. 200402, 2009.

[113] A. Roy and M. Devoret, "Introduction to parametric amplification of quantum signals with josephson circuits," *Comptes Rendus Physique*, vol. 17, no. 7, pp. 740–755, 2016.

[114] V. E. Manucharyan, N. A. Masluk, A. Kamal, J. Koch, L. I. Glazman, and M. H. Devoret, "Evidence for coherent quantum phase slips across a josephson junction array," *Physical Review B*, vol. 85, no. 2, p. 024521, 2012.

[115] J. R. Johansson, P. Nation, and F. Nori, "Qutip: An open-source python framework for the dynamics of open quantum systems," *Computer Physics Communications*, vol. 183, no. 8, pp. 1760–1772, 2012.

[116] J. R. Johansson, P. D. Nation, and F. Nori, "Qutip 2: A python framework for the dynamics of open quantum systems," *Computer Physics Communications*, vol. 184, no. 4, pp. 1234–1240, 2013.

[117] G. Zhu and J. Koch, "Asymptotic expressions for charge-matrix elements of the fluxonium circuit," *Physical Review B*, vol. 87, no. 14, p. 144518, 2013.

[118] J. Koch, V. Manucharyan, M. Devoret, and L. Glazman, "Charging effects in the inductively shunted josephson junction," *Physical Review Letters*, vol. 103, no. 21, p. 217004, 2009.

[119] V. Braginsky, V. Ilchenko, and K. S. Bagdassarov, "Experimental observation of fundamental microwave absorption in high-quality dielectric crystals," *Physics Letters A*, vol. 120, no. 6, pp. 300–305, 1987.

[120] R. Kuzmin, R. Mencia, N. Grabon, N. Mehta, Y.-H. Lin, and V. E. Manucharyan, "Quantum electrodynamics of a superconductor–insulator phase transition," *Nature Physics*, vol. 15, no. 9, pp. 930–934, 2019.

[121] R. Kuzmin, N. Mehta, N. Grabon, R. Mencia, and V. E. Manucharyan, "Superstrong coupling in circuit quantum electrodynamics," *npj Quantum Information*, vol. 5, no. 1, pp. 1–6, 2019.

[122] A. Sears, A. Petrenko, G. Catelani, L. Sun, H. Paik, G. Kirchmair, L. Frunzio, L. Glazman, S. Girvin, and R. Schoelkopf, "Photon shot noise dephasing in the strong-dispersive limit of circuit qed," *Physical Review B*, vol. 86, no. 18, p. 180504, 2012.

[123] F. Yan, D. Campbell, P. Krantz, M. Kjaergaard, D. Kim, J. L. Yoder, D. Hover, A. Sears, A. J. Kerman, T. P. Orlando, *et al.*, "Distinguishing coherent and thermal photon noise in a circuit quantum electrodynamical system," *Physical Review Letters*, vol. 120, no. 26, p. 260504, 2018.

[124] J.-H. Yeh, J. LeFebvre, S. Premaratne, F. Wellstood, and B. Palmer, "Microwave attenuators for use with quantum devices below 100 mk," *Journal of Applied Physics*, vol. 121, no. 22, p. 224501, 2017.

[125] Z. Wang, S. Shankar, Z. Minev, P. Campagne-Ibarcq, A. Narla, and M. H. Devoret, "Cavity attenuators for superconducting qubits," *Physical Review Applied*, vol. 11, no. 1, p. 014031, 2019.

[126] G. Viola and G. Catelani, "Collective modes in the fluxonium qubit," *Physical Review B*, vol. 92, no. 22, p. 224511, 2015.

[127] G. Zhu, D. G. Ferguson, V. E. Manucharyan, and J. Koch, "Circuit qed with fluxonium qubits: Theory of the dispersive regime," *Physical Review B*, vol. 87, no. 2, p. 024510, 2013.

[128] K. N. Nesterov, I. V. Pechenezhskiy, C. Wang, V. E. Manucharyan, and M. G. Vavilov, "Microwave-activated controlled-z gate for fixed-frequency fluxonium qubits," *Physical Review A*, vol. 98, no. 3, p. 030301, 2018.

[129] J. M. Chow, J. M. Gambetta, A. W. Cross, S. T. Merkel, C. Rigetti, and M. Steffen, "Microwave-activated conditional-phase gate for superconducting qubits," *New Journal of Physics*, vol. 15, no. 11, p. 115012, 2013.

[130] J. M. Chow, J. M. Gambetta, A. Córcoles, S. T. Merkel, J. A. Smolin, C. Rigetti, S. Poletto, G. A. Keefe, M. B. Rothwell, J. Rozen, *et al.*, "Universal quantum gate set approaching fault-tolerant thresholds with superconducting qubits," *Physical Review Letters*, vol. 109, no. 6, p. 060501, 2012.

[131] F. Pobell, *Matter and methods at low temperatures*. Springer-Verlag, 2007.

[132] A. D. Córcoles, J. M. Chow, J. M. Gambetta, C. Rigetti, J. R. Rozen, G. A. Keefe, M. Beth Rothwell, M. B. Ketchen, and M. Steffen, "Protecting superconducting qubits from radiation," *Applied Physics Letters*, vol. 99, no. 18, p. 181906, 2011.

[133] J. Wenner, Y. Yin, E. Lucero, R. Barends, Y. Chen, B. Chiaro, J. Kelly, M. Lenander, M. Mariantoni, A. Megrant, *et al.*, "Excitation of superconducting qubits from hot nonequilibrium quasiparticles," *Physical Review Letters*, vol. 110, no. 15, p. 150502, 2013.

[134] M. Halpern, H. P. Gush, E. Wishnow, and V. De Cosmo, "Far infrared transmission of dielectrics at cryogenic and room temperatures: glass, fluorogold, eccosorb, stycast, and various plastics," *Applied Optics*, vol. 25, no. 4, pp. 565–570, 1986.

[135] H. Hemmati, J. C. Mather, and W. L. Eichhorn, "Submillimeter and millimeter wave characterization of absorbing materials," *Applied Optics*, vol. 24, no. 24, pp. 4489–4492, 1985.

[136] C. Macklin, K. OBrien, D. Hover, M. Schwartz, V. Bolkhovsky, X. Zhang, W. Oliver, and I. Siddiqi, "A near–quantum-limited josephson traveling-wave parametric amplifier," *Science*, vol. 350, no. 6258, pp. 307–310, 2015.

[137] A. A. Houck, J. Schreier, B. Johnson, J. Chow, J. Koch, J. Gambetta, D. Schuster, L. Frunzio, M. Devoret, S. Girvin, *et al.*, "Controlling the spontaneous emission of a superconducting transmon qubit," *Physical Review Letters*, vol. 101, no. 8, p. 080502, 2008.

[138] T. Brecht, M. Reagor, Y. Chu, W. Pfaff, C. Wang, L. Frunzio, M. H. Devoret, and R. J. Schoelkopf, "Demonstration of superconducting micromachined cavities," *Applied Physics Letters*, vol. 107, no. 19, p. 192603, 2015.

[139] M. Reagor, H. Paik, G. Catelani, L. Sun, C. Axline, E. Holland, I. M. Pop, N. A. Masluk, T. Brecht, L. Frunzio, *et al.*, "Reaching 10 ms single photon lifetimes for superconducting aluminum cavities," *Applied Physics Letters*, vol. 102, no. 19, p. 192604, 2013.

[140] M. Reagor, W. Pfaff, C. Axline, R. W. Heeres, N. Ofek, K. Sliwa, E. Holland, C. Wang, J. Blumoff, K. Chou, *et al.*, "Quantum memory with millisecond coherence in circuit qed," *Physical Review B*, vol. 94, no. 1, p. 014506, 2016.

[141] V. Manucharyan, *Superinductance Ph. D*. PhD thesis, thesis Yale University, 2012.

[142] M. J. Reagor, *Superconducting Cavities forCircuit Quantum Electrodynamics*. Yale University, 2016.

[143] A. Y. Kitaev, "Fault-tolerant quantum computation by anyons," *Annals of Physics*, vol. 303, no. 1, pp. 2–30, 2003.

[144] L. Ioffe, M. Feigel'man, A. Ioselevich, D. Ivanov, M. Troyer, and G. Blatter, "Topologically protected quantum bits using josephson junction arrays," *Nature*, vol. 415, no. 6871, pp. 503–506, 2002.

[145] A. D. Ludlow, M. M. Boyd, J. Ye, E. Peik, and P. O. Schmidt, "Optical atomic clocks," *Reviews of Modern Physics*, vol. 87, no. 2, p. 637, 2015.

[146] F. Paauw, A. Fedorov, C. M. Harmans, and J. Mooij, "Tuning the gap of a superconducting flux qubit," *Physical Review Letters*, vol. 102, no. 9, p. 090501, 2009.

[147] A. J. Kerman, "Metastable superconducting qubit," *Physical Review Letters*, vol. 104, no. 2, p. 027002, 2010.

[148] D. Sank, Z. Chen, M. Khezri, J. Kelly, R. Barends, B. Campbell, Y. Chen, B. Chiaro, A. Dunsworth, A. Fowler, *et al.*, "Measurement-induced state transitions in a superconducting qubit: Beyond the rotating wave approximation," *Physical Review Letters*, vol. 117, no. 19, p. 190503, 2016.

[149] A. Kou, W. Smith, U. Vool, R. Brierley, H. Meier, L. Frunzio, S. Girvin, L. Glazman, and M. Devoret, "Fluxonium-based artificial molecule with a tunable magnetic moment," *Physical Review X*, vol. 7, no. 3, p. 031037, 2017.

[150] P. Klimov, J. Kelly, Z. Chen, M. Neeley, A. Megrant, B. Burkett, R. Barends, K. Arya, B. Chiaro, Y. Chen, *et al.*, "Fluctuations of energy-relaxation times in superconducting qubits," *Physical Review Letters*, vol. 121, no. 9, p. 090502, 2018.

[151] D. P. Pappas, M. R. Vissers, D. S. Wisbey, J. S. Kline, and J. Gao, "Two level system loss in superconducting microwave resonators," *IEEE Transactions on Applied Superconductivity*, vol. 21, no. 3, pp. 871–874, 2011.

[152] T. Walter, P. Kurpiers, S. Gasparinetti, P. Magnard, A. Potočnik, Y. Salathé, M. Pechal, M. Mondal, M. Oppliger, C. Eichler, *et al.*, "Rapid high-fidelity single-shot dispersive readout of superconducting qubits," *Physical Review Applied*, vol. 7, no. 5, p. 054020, 2017.

[153] S. Sheldon, L. S. Bishop, E. Magesan, S. Filipp, J. M. Chow, and J. M. Gambetta, "Characterizing errors on qubit operations via iterative randomized benchmarking," *Physical Review A*, vol. 93, no. 1, p. 012301, 2016.

[154] E. Magesan, J. M. Gambetta, B. R. Johnson, C. A. Ryan, J. M. Chow, S. T. Merkel, M. P. Da Silva, G. A. Keefe, M. B. Rothwell, T. A. Ohki, *et al.*, "Efficient measurement of quantum gate error by interleaved randomized benchmarking," *Physical Review Letters*, vol. 109, no. 8, p. 080505, 2012.

[155] S. Hill and W. K. Wootters, "Entanglement of a pair of quantum bits," *Physical review letters*, vol. 78, no. 26, p. 5022, 1997.

[156] J. Kelly, R. Barends, B. Campbell, Y. Chen, Z. Chen, B. Chiaro, A. Dunsworth, A. G. Fowler, I.-C. Hoi, E. Jeffrey, *et al.*, "Optimal quantum control using randomized benchmarking," *Physical Review Letters*, vol. 112, no. 24, p. 240504, 2014.

[157] F. Yan, S. Gustavsson, J. Bylander, X. Jin, F. Yoshihara, D. G. Cory, Y. Nakamura, T. P. Orlando, and W. D. Oliver, "Rotating-frame relaxation as a noise spectrum analyser of a superconducting qubit undergoing driven evolution," *Nature Communications*, vol. 4, p. 2337, 2013.

[158] Z. Hradil, "Quantum-state estimation," *Physical Review A*, vol. 55, no. 3, p. R1561, 1997.

[159] K. Banaszek, G. Dariano, M. Paris, and M. Sacchi, "Maximum-likelihood estimation of the density matrix," *Physical Review A*, vol. 61, no. 1, p. 010304, 1999.

[160] J. Poyatos, J. I. Cirac, and P. Zoller, "Complete characterization of a quantum process: the two-bit quantum gate," *Physical Review Letters*, vol. 78, no. 2, p. 390, 1997.

[161] E. Knill, D. Leibfried, R. Reichle, J. Britton, R. B. Blakestad, J. D. Jost, C. Langer, R. Ozeri, S. Seidelin, and D. J. Wineland, "Randomized benchmarking of quantum gates," *Physical Review A*, vol. 77, no. 1, p. 012307, 2008.

[162] A. D. Córcoles, J. M. Gambetta, J. M. Chow, J. A. Smolin, M. Ware, J. Strand, B. L. Plourde, and M. Steffen, "Process verification of two-qubit quantum gates by randomized benchmarking," *Physical Review A*, vol. 87, no. 3, p. 030301, 2013.

[163] N. Earnest, S. Chakram, Y. Lu, N. Irons, R. K. Naik, N. Leung, L. Ocola, D. A. Czaplewski, B. Baker, J. Lawrence, *et al.*, "Realization of a λ system with metastable

states of a capacitively shunted fluxonium," *Physical Review Letters*, vol. 120, no. 15, p. 150504, 2018.

[164] A. Kou, W. Smith, U. Vool, I. Pop, K. Sliwa, M. Hatridge, L. Frunzio, and M. Devoret, "Simultaneous monitoring of fluxonium qubits in a waveguide," *Physical Review Applied*, vol. 9, no. 6, p. 064022, 2018.

[165] T. Hazard, A. Gyenis, A. Di Paolo, A. Asfaw, S. A. Lyon, A. Blais, and A. A. Houck, "Nanowire superinductance fluxonium qubit," *Physical Review Letters*, vol. 122, no. 1, p. 010504, 2019.

[166] L. Grünhaupt, M. Spiecker, D. Gusenkova, N. Maleeva, S. T. Skacel, I. Takmakov, F. Valenti, P. Winkel, H. Rotzinger, W. Wernsdorfer, *et al.*, "Granular aluminium as a superconducting material for high-impedance quantum circuits," *Nature materials*, vol. 18, no. 8, pp. 816–819, 2019.

[167] W. Zhang, K. Kalashnikov, W.-S. Lu, P. Kamenov, T. DiNapoli, and M. Gershenson, "Microresonators fabricated from high-kinetic-inductance aluminum films," *Physical Review Applied*, vol. 11, no. 1, p. 011003, 2019.

[168] A. Shearrow, G. Koolstra, S. J. Whiteley, N. Earnest, P. S. Barry, F. J. Heremans, D. D. Awschalom, E. Shirokoff, and D. I. Schuster, "Atomic layer deposition of titanium nitride for quantum circuits," *Applied Physics Letters*, vol. 113, no. 21, p. 212601, 2018.

[169] J. M. Chow, A. Córcoles, J. M. Gambetta, C. Rigetti, B. Johnson, J. A. Smolin, J. Rozen, G. A. Keefe, M. B. Rothwell, M. B. Ketchen, *et al.*, "Simple all-microwave entangling gate for fixed-frequency superconducting qubits," *Physical Review Letters*, vol. 107, no. 8, p. 080502, 2011.

[170] S. Poletto, J. M. Gambetta, S. T. Merkel, J. A. Smolin, J. M. Chow, A. Córcoles, G. A. Keefe, M. B. Rothwell, J. Rozen, D. Abraham, *et al.*, "Entanglement of two superconducting qubits in a waveguide cavity via monochromatic two-photon excitation," *Physical Review Letters*, vol. 109, no. 24, p. 240505, 2012.

[171] M. W. Johnson, M. H. Amin, S. Gildert, T. Lanting, F. Hamze, N. Dickson, R. Harris, A. J. Berkley, J. Johansson, P. Bunyk, *et al.*, "Quantum annealing with manufactured spins," *Nature*, vol. 473, no. 7346, pp. 194–198, 2011.

[172] J. J. Sakurai, J. Napolitano, *et al.*, *Modern quantum mechanics*, vol. 185. Pearson Harlow, 2014.

[173] I. V. Pechenezhskiy, R. A. Mencia, L. B. Nguyen, Y.-H. Lin, and V. E. Manucharyan, "Quantum dynamics of quasicharge in an ultrahigh-impedance superconducting circuit," *ArXiv preprint ArXiv:1907.02937*, 2019.